The University Of Sheffield.

Analysis and Design of Radial Mode Piezoelectric Transformers for Resonant Converter Applications

Jack Forrester

A thesis submitted for the degree of PhD

The University of Sheffield

Faculty of Engineering

Department of Electronic and Electrical Engineering

September 2021

Abstract

The demand for electronic devices is increasing thus as is the need for power dense, efficient power converters. Piezoelectric transformers (PTs) are an alternative to traditional magnetic transformers, offering several advantages over magnetic devices and are ideal for use in low-to-medium power resonant converters. These advantages include desirable material properties, such as being non-ferromagnetic (thus reducing EMI) and the ability to operate in high ambient temperatures, high efficiency, and an integrated resonant tank circuit. However, to date, these devices have seen minimal commercial adoption, owing to the complexity and multidisciplinary nature of their design.

In the first part of this thesis, several mathematical models are developed which allow the characterisation of PTs (Chapter 3), allow the designer to avoid issues with spurious vibrations (Chapter 4) and allow the estimation of electrical equivalent circuit component values for radial mode PT topologies (Chapters 5-8). A full derivation of each model is presented and then subsequently verified against experimental and simulated results.

Chapter 9 investigates the use of BSPT ($BiScO_3$-$PbTiO_3$) as a high-temperature piezoelectric material for use in high-temperature PTs. A design is formulated using the mathematical models developed throughout the thesis and the performance of the BSPT PT is characterised using a both impedance analysis and power converter measurements. The results of this analysis are compared against a high performance PZT material, with promising results.

Finally, building on the work in the previous chapters, a genetic algorithm approach to PT design is then presented. This approach incorporates the modelling performed in the first part of the thesis to allow optimised designs to be generated based on a converter specification. Unlike previous approaches, this method considers a wide range of metrics, including device efficiency, vibration velocity, zero voltage switching performance and spurious mode avoidance when designing the device.

The work in this thesis provides a method of generating optimised designs for radial mode PTs for specific power converter applications, without expert knowledge or FEA tools. This will provide an excellent starting point for PT designs and will help to increase the commercial adoption of PTs.

Acknowledgements

I would first like to greatly thank my supervisors, Dr. Jonathan Davidson and Prof. Martin Foster for their support, guidance, and encouragement throughout this work. Also, I would like to thank Prof. Dave Stone for his advice, and along with Jonathan and Martin, thank you for providing excellent company to conferences in both Germany and Italy. I would like to thank EPSRC for funding this work and the FPeT project.

I thank our colleagues from the materials science department, Prof. Ian Reaney, Prof. Derek Sinclair and Dr. Linhao Li for their expertise on the materials science elements of this work. I would also like to thank Dr. Linhao Li for his work developing and fabricating several prototype PTs, which have been vital in facilitating several elements of this work.

I would also like to thank Zijiang Yang for providing his knowledge and control circuit, which was used to control the resonant converter described in Chapter 9. I would also like to thank my colleagues working on the FPeT project for their company during the many hours spent in the lab and their advice and ideas on my work.

I am deeply grateful for the encouragement and support from my parents, brother, and grandparents. I am deeply grateful to my partner Charlotte for her encouragement, patience, and support throughout this work. I am also thankful to my friends and those at Appleby Frodingham CC for their support throughout the duration of my PhD.

Without this support, I would not have been able to complete this work and so I am deeply grateful.

Nomenclature

Piezoelectric

Symbol	Description	Units
s^{E}	Elastic compliance, measured at constant electric field	m^2/N
d	Piezoelectric strain constant	$\mathrm{m/V}$
σ	Poisson's ratio	-
ρ	Density	$\mathrm{kg/m}^3$
ε^{T}	Dielectric constant, measured at constant stress	-
E	Electric field	$\mathrm{V/m}$
D	Electric displacement	$\mathrm{C/m}^2$
$T_{r,\theta}$	Stress	$\mathrm{N/m}^2$
$S_{r,\theta}$	Strain	-
Q	Q Factor	-
k_n^2	Coupling factor	-

Equivalent circuit

Symbol	Description	Units
R	Resistance, Root of a Bessel function used to determine resonant frequencies with a governing equation, Rotary-inertia coefficient	Ω, -, m^2
L	Inductance	H
C	Capacitance	F
A_{in}, A_{out}	Force factors	N/V
N	Turn ratio	-
V_{in}	Voltage between input electrodes and ground	V
V_{out}	Voltage between output electrodes and ground	V
P_{in}	Input power	W
P_{out}	Output power	W
i, I	Current	A
v	Vibration velocity	m/s
F	Force	N
Z	Impedance	Ω
D	Flexural rigidity	Nm
β, ζ	Impedance of L and C at resonance in a series LC circuit	Ω
$\omega, \omega_{\mathrm{n}}$	Frequency, Resonant frequency of the n^{th} mode	rad/s
f, f_{n}	Frequency, Resonant frequency of the n^{th} mode	Hz

η	Efficiency	%, -
X	Reactance	Ω
w, W	Transverse displacement	m
ψ, u_r	Radial displacement	m
M	Flexural moments	m^2
Q	Transverse shear force	N
q, Q	Charge	C
E	Electric field	$\mathrm{V/m}$
r, θ, z	Cylindrical coordinates	-
λ, δ	Non-dimensional frequency	-
S	Shear deformation coefficient	m^2
k^2	Shear correction factor	-

Dimensions

Symbol	Description	Units
a	Disc radius	m
T	Thickness	m
r_a	Dot radius in the ring-dot PT model	m
r_b	Inner-ring radius in the ring-dot PT model	m
$N_{\mathrm{in}}, N_{\mathrm{out}}$	Number of layers in the input/output section in the radial mode Transoner PT model	-

Genetic algorithm

Symbol	Description	Units
P	Number of devices per generation	-
X	The percentage of devices that are retained from a generation	%
γ	A uniformly distributed random number between (0-1) describing the percentage of a child's variables that comes from the first parents	-
α	A uniformly distributed random number between -1-1 determining the amount of mutation added/subtracted to a child device's variable	-
c	Child device	-
p	Parent device	-
V_c, V_p	Variable from either a child or parent device	-
MutAm	The maximum mutation amount added/subtracted to each of a child's variables	-
Gen	Current generation	-
MaxGen	Maximum number of generations	-
BestDevice	The fittest device for each generation	-
MaxFail	Maximum number of loops without a valid device before an error is returned	-

MutRate	Percentage chance of a child device mutating	%
ShouldMut	A Boolean variable describing if a child device should mutate	-

Maths

Symbol	Description	Units
j	Complex number, $\sqrt{-1}$	-
F	Cost function	-
J	Bessel function of the first kind	-
Y	Bessel function of the second kind	-
I	Modified Bessel function of the first kind	-
K	Modified Bessel function of the second kind	-
∇^2	Laplacian operator	-

Table of Contents

Table of Figures

Chapter 1 - Introduction

1.1 Introduction

Power converters are a vital component of almost all electrical devices. Converters are tasked with converting a supply from either AC or DC to either AC or DC at a different voltage level, whilst allowing sufficient current to pass through. They are found at all scales, from large multi-kilovolt, multi-kilowatt converters to small 5W mobile phone chargers. Over the past few decades, electrical devices have become smaller, more efficient and lower in cost. As a result, power electronic engineers have had to develop new power converter technologies to keep up with this trend.

50Hz, 15VA 12Vout toroidal mains transformer

330g

$100\ \mu m^3$ Volume

60-150kHz, 13W 12Vout SMPS transformer

7.8g

$4.6\ \mu m^3$ Volume

Fig. 1.1 – Comparison between mains and SMPS transformers [1.1], [1.2]

Traditionally, power converters consisted of a large, heavy mains transformer which stepped the voltage up or down depending on the application, as shown in Fig. 1.1. The voltage is then rectified to DC and finally regulated to the correct output voltage using a linear regulator. This

approach has several issues, firstly being its size and weight and, as linear regulators control the output voltage by dissipating power and wasting it as heat, they can be very inefficient.

These issues brought about the advent of switched mode power supplies (SMPS). SMPS solve the two main issues with linear regulators, by chopping the main voltage into a waveform at a much higher frequency, allows the circuit components to be reduced in size and thus weight, as shown in Fig. 1.1. Additionally, by controlling the duty cycle of this high frequency waveform, the output voltage level can be controlled in response to changes in supply or load, without wasting additional voltage as heat.

Building upon the SMPS principle, the resonant converter was then introduced, by adding a resonant circuit to the converter, allowing the switching elements to be soft-switched (i.e. zero voltage switched (ZVS)). This reduces switching losses and allows even higher frequencies to be used efficiently, thus further reducing converter size and increasing efficiency. This technique allows converters to be produced with efficiencies greater than 99%.

However, with increases in popularity and availability of IOT (Internet of things) devices, electronics in everyday appliances (fridges, washing machines, hairdryers, etc…), electric vehicles, monitoring systems and more, the demand for compact efficient converters is only going to rise in the coming years.

Whilst traditional magnetic transformers have been and are currently the obvious choice up for power converters, it is well discussed that improvement to magnetic components (transformers, inductors) are required for further innovation in power converter technology. Piezoelectric transformers (PT) provide an exciting alternative to traditional magnetic transformers. PTs are highly power dense and highly efficient, making them excellent for small, low to medium (<50W) power applications.

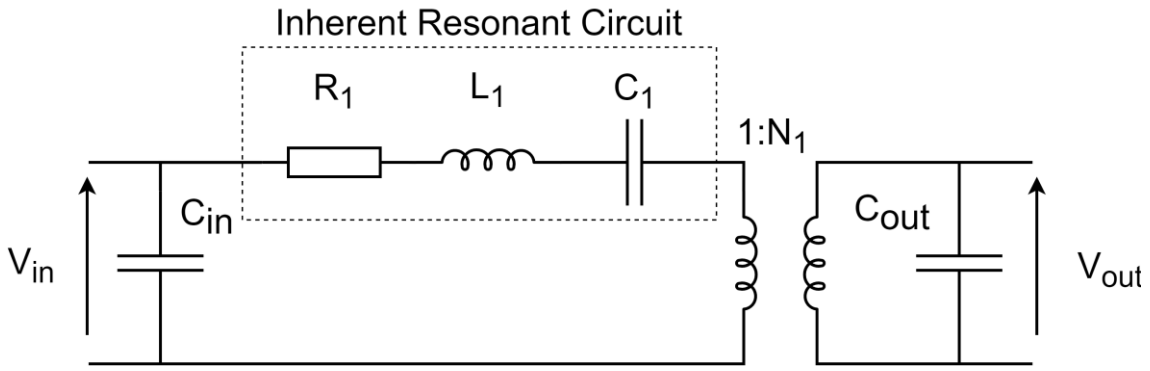

Fig. 1.2 – PT equivalent circuit

The key advantage of PTs is that they contain an inherent resonant circuit (see Fig. 1.2), allowing a resonant converter to be made with minimal additional passive components, significantly reducing converter size and complexity. Additionally, PTs are easily manufactured, are non-flammable and as they lack magnetic components, avoid EMI (electromagnetic interference) and EMC (electromagnetic compatibility) issues. Finally, PTs can be built to have unique properties that are not possible in magnetic transformers, such as the ability to operate in a high temperature environment and/or in high magnetic fields.

Fig. 1.3 – Rosen PT [1.3]

PTs have been around for over half a century and have already seen some commercial success. The Rosen PT is the most popular topology and in the early 2000s was frequently used as part of step-up converters in CCFL backlight circuits. The Rosen PT was ideal for this application owing to its small size, high efficiency, and high voltage gain. However, as backlighting technology moved to LED and due to the relatively low power output of the Rosen PT, in general, they have seen a dwindling interest.

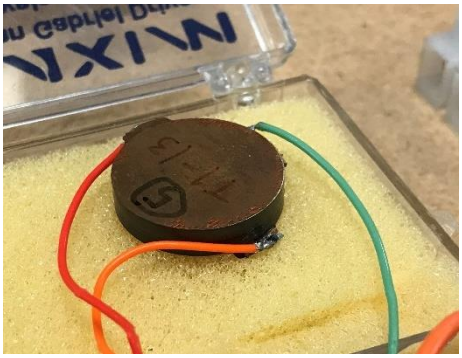

Fig. 1.4 – Radial mode Transoner PT

However, in recent years, owing to improvements in materials and the development of new PT topologies, higher power PTs have been developed. The most popular high-power topology, the radial mode Transoner PT (Fig. 1.4), has enabled small PT based converters to achieve output powers of up to 50W and as a result, has led to a resurgence of interest in the research community. Whilst it is unlikely that PTs will be a direct replacement to magnetic transformers in all applications, there are several industries and applications where PTs could be either more cost-effective than magnetic transformers or could be the only viable solution. Industries such as aerospace, construction and medical often require devices to operate in harsh environments such as high temperature or high magnetic fields (such as in MRI machines) which lend themselves perfectly to PTs. Similarly, with the introduction and commercial adoption of GaN and SiC transistors, that can operate at higher temperatures and in unique situations, PTs could be vital in unlocking the full potential of these devices, as part of gate drive circuitry.

However, higher power PTs have yet to see any commercial adoption. The main reason for this is the difficultly in designing PTs. The design process is complex as it requires knowledge of both material design and power electronics to be able to build, construct and design a PT and associated converter. This research and development phase can incur significant expense, as it often requires specific software tools such as finite element analysis software, which can cost upwards of £10,000 a year. Additionally, the lack of available design methodology for PTs specifically for resonant converter applications, means that the process requires trial and error. These reasons have meant that there are very few commercial PTs being sold currently and those that are available, cost significantly more than similar magnetic transformers.

Therefore, the motivation for the research presented in this thesis was to help reduce the difficulty in designing higher power PTs for resonant converter applications and to try and increase their commercial adoption. This research involves the development of novel electromechanical models for higher power PTs, new characterisation techniques, and the development of novel genetic algorithm-based PT design software, which uses the newly derived models as part of it design methodology. Additionally, this knowledge is applied to the design, construction, and testing of a novel high temperature PT.

1.2 Achievements

- Four equivalent circuit extraction algorithms, including a method designed specifically for high damping PTs such as high temperature PTs
- Detailed sensitivity analysis of the impact of spurious modes on all PT topologies, using equivalent circuit representations of spurious modes
- Two lumped equivalent circuit models for the spurious modes occurring in the radial mode Transoner PT, based on both Kirchhoff and Mindlin plate models
- Lumped equivalent circuit model for the ring-dot PT based on the Kirchhoff plate model
- Construction and evaluation of high temperature PTs made from bismuth scandium lead titanate
- Genetic algorithm approach to PT design for resonant converters, based on equations for the lumped equivalent circuit components. This algorithm includes spurious mode avoidance and optimises efficiency and vibration velocity, unlike previous approaches.

1.3 Novelty

From a power electronics engineers' standpoint, it is much easier to consider PTs as an equivalent electrical circuit rather than a complex electromechanical device. Therefore, the focus of the initial chapters of this thesis will be around extracting equivalent circuit component values from a PT or to estimate these values based on a physical PT design.

Chapter 3 describes three new general-purpose methods for extracting the equivalent circuit components of low loss (damping) PTs, from impedance measurements. Whilst the first two presented methods provide improvements over previously published work, increasing

accuracy and reliability of the methods, the third method is a novel approach. The accuracy of each method is then verified against experimental measurements from PTs and the noise resilience of each method analysed.

Whilst these methods are excellent for low loss PTs, for higher damping PTs or for analysing spurious modes, the increased loss causes inaccuracies in the previous three methods. To overcome this problem a fourth method is devised, combining two of the previous approaches with a more accurate model of the PTs loss, to increase accuracy when extracting components from a high damping PT. A comparison of the high damping and the general-purpose methods is presented, using simulated measurements and experimental PT measurements. Finally, a noise resilience analysis is presented for the high damping method, including a comparison to the general-purpose methods.

One of the key issues in the design of PTs is the existence of unwanted, spurious vibration modes. These modes often require expensive simulation tools to model, which is critical to avoid adverse effects. In Chapter 4, an analysis is performed to help determine methods of designing PTs in such a way that spurious modes have negligible effect on performance. The analysis will be aimed at giving a PT designer the information required, given some knowledge of the equivalent circuit of the PT, to determine whether a PT will avoid performance issues from spurious modes.

Initially, the efficiency of the idealised single-mode PT is analysed and the elements of its equivalent circuit that influence this efficiency are determined. The equivalent circuit model of the PT is then extended to include another resonant branch (i.e. a spurious mode) and the efficiency of this modified equivalent circuit examined. This allows the efficiency degradation from the interaction between the optimum and spurious modes, when the PT is driven at the optimum (operating) mode, to be analysed through multiple sensitivity analyses. Using the results of this analysis, the key factors that affect the efficiency degradation are highlighted. Further, quantitative restrictions on the design space, in terms of equivalent circuit parameter values, are proposed. Observing this restriction will result in minimal degradation in efficiency for each specific PT as a result of spurious modes. Finally, the results are verified by experimental measurements.

Chapter 5 and Chapter 6 present equivalent circuit models for the flexural vibration modes occurring in the radial mode Transoner PT, thus allowing the resulting analysis presented in Chapter 4 to be applied to the design of Transoner PTs. Firstly, a lumped equivalent circuit model will be derived using the classic Kirchhoff plate theory in Chapter 5. However, unlike previous lumped equivalent models for PTs which have used the Kirchhoff plate theory, the simplifications used in this theory have a significant effect on the accuracy of the model. Therefore, a second model is derived using the more complex Mindlin Plate theory in Chapter 6. Finally, the resulting models will be verified against COMSOL simulations and experimentally measured PTs in Chapter 7.

Similarly, Chapter 8 presents the derivation of a lumped equivalent circuit model for the radial vibration mode occurring in the ring-dot PT. Whilst previous attempts have been made at performing such an analysis, this chapter extends previous analyses by incorporating a model of the 'gap' region between ring and dot electrodes, increasing accuracy. Additionally, equations for the lumped equivalent circuit parameters are presented unlike previous published work. Finally, these models are combined and simplified to the standard Mason form. This model is then further extended to include a more complex electric field model for the 'gap' region, increasing accuracy when modelling non-ideal devices. These models are then verified using COMSOL and experimental measurements.

Chapter 9 details the design, construction and testing of a PT made from bismuth scandium lead titanate (BSPT) a high-temperature piezoelectric material. Whilst high temperature piezoelectrics have been used both in research and in commercial applications, they have not been applied to PTs. BSPT is a high performance, hard piezoelectric material with similar performance characteristics to the state-of-the-art lead zirconium titanate (PZT) materials. A simple design for a high temperature ring-dot PT is formulated using the analysis in Chapter 8. A PZT ring-dot PT is also built to the same design for comparison. Both PTs are then characterised at various ambient temperatures, extracting the equivalent values using the high damping method presented in Chapter 3. Finally, both PTs are integrated into a simple inductor less half-bridge resonant converter and again tested at various ambient temperatures. The results are then analysed and discussed.

Combining the work in the previous chapters, Chapter 10 presents a novel genetic algorithm approach to designing both ring-dot and radial mode Transoner PTs for use in inductor-less

half-bridge converters. Genetic algorithm approaches have several advantages over previous methods, as previous approaches reduce the design search space early in the process, without fully evaluating the impact of that choice. This can often mean the final designed PT will be the 'local' optimum device (i.e. best device with some parameters fixed at certain values) and not the desired 'global' optimum device (i.e. the overall best device) for the application.

To overcome this limitation, this work proposes randomly choosing device dimensions based strictly on physical limitations (i.e. max/min layer thickness, radius, etc…), determining how 'fit' the resulting device is for the application and then iterating and improving upon this design based on these findings. Unlike previous genetic algorithm approaches, this model takes advantage of the newly developed lumped equivalent circuit models presented in Chapter 5, Chapter 6 and Chapter 8. These models combined with a previously developed model for the radial mode of the Transoner PT, allow the physical design of a PT to be translated into an equivalent circuit model without having to use relatively slow and expensive FEA tools as done in previous genetic algorithm approaches. This novel method allows faster computation or alternatively allows the number of devices analysed to significantly increase in a similar timeframe. Another improvement over previous approaches, is that the fitness of the PT will be evaluated based on electrical quantities such as efficiency, output voltage and the ability to achieve zero voltage switching (ZVS), rather than piezoelectric parameters such as coupling factor. Therefore, the chosen PT design will not only be for an optimised PT in general (high coupling factor, low losses) but also a PT optimised for the desired application (achieves desired output voltage, achieves zero voltage switching, highly electrically efficient at the chosen operating point). Additionally, the algorithm will apply the spurious mode analysis presented in Chapter 4, unlike any previous design method, and as a result allows spurious mode interaction to be accounted for in the design.

A detailed description of the genetic algorithm is presented, highlighting the nuances in both ring-dot and radial mode PTs implementations. The algorithm is built into a user-friendly web application, allowing users to achieve optimal PT designs based on detailed specifications with minimal prior PT knowledge. Finally, an example design produced by the algorithm is verified with COMSOL and LTSpice simulations.

1.4 Publication summary

Several elements of the work presented in this thesis have been published in peer review journals or conferences. The high damping equivalent circuit extraction methods presented in Chapter 3 has been peer reviewed and published in IET Electronic letters, however, owing to the short length of the letter format, the work in Chapter 3 provides greater analysis of the accuracy and the noise resilience of this method. Additionally, the 3 general purpose methods in Chapter 3 have been presented at EPE 2019 conference in Genoa, Italy. The analysis of the impact of spurious modes of PT performance presented in Chapter 4, has been peer reviewed and published in the IEEE Transactions on Power Electronics journal. Similarly, a paper was presented at PCIM 2018 conference in Nuremburg, Germany, which discusses the topic of spurious mode-based efficiency loss and presents an initial analysis of the resonant frequencies of the spurious modes occurring in the radial mode Transoner PT. Finally, as a preamble to the genetic algorithm-based PT designer presented in Chapter 10, a more simplistic design algorithm was presented at PEMD 2018 in Liverpool, UK and then published in The Journal of Engineering.

1.5 Publications arising from this research

1.5.1 Journal publications

A) J. Forrester, J. N. Davidson, M. P. Foster, and D. A. Stone, 'Influence of Spurious Modes on the Efficiency of Piezoelectric Transformers: a Sensitivity Analysis', *IEEE Transactions on Power Electronics*, 2020, doi: 10.1109/TPEL.2020.3001486

B) Forrester, J., Li, L., Davidson, J., Foster, M., Stone, D., Sinclair, D. and Reaney, I. (2020), Equivalent circuit parameter extraction of low-capacitance high-damping PTs. Electron. Lett., pp. 347-350, 2020, doi: 10.1049/el.2019.3887

C) J. Forrester, J. N. Davidson, M. P. Foster, E. L. Horsley, and D. A. Stone, 'Automated design tools for piezoelectric transformer-based power supplies', *The Journal of Engineering*, vol. 2019, no. 17, pp. 4163–4166, 2019, doi: 10.1049/joe.2018.8065.

D) Z. Yang, J. Forrester, J. N. Davidson, M. P. Foster, and D. A. Stone, 'Resonant Current Estimation and Phase-Locked Loop Feedback Design for Piezoelectric Transformer-Based Power Supplies', *IEEE Trans. Power Electron.*, vol. 35, no. 10, pp. 10466–10476, Oct. 2020, doi: 10.1109/TPEL.2020.2976206

1.5.2 Conference publications

E) J. Forrester, J. Davidson, M. Foster and D. Stone, "Equivalent Circuit Parameter Extraction Methods for Piezoelectric Transformers," *2019 21st European Conference on Power Electronics and Applications (EPE '19 ECCE Europe)*, Genova, Italy, 2019, doi: 10.23919/EPE.2019.8915189.

F) J. Forrester, J. Davidson and M. Foster, "Effect of Spurious Resonant Modes on the Operation of Radial Mode Piezoelectric Transformers," *PCIM Europe 2018; International Exhibition and Conference for Power Electronics, Intelligent Motion, Renewable Energy and Energy Management*, Nuremberg, Germany, 2018

1.6 References

[1.1] 'SMPS Transformer, Universal Offline Standard, 550 mA, 16 W, 1.5 kV, 85V to 265V'. https://uk.farnell.com/wurth-elektronik/760871135/isolation-transformer-136-13-13/dp/3584511RL (accessed Jul. 06, 2021).

[1.2] '2 x 15V 15 VA Toroidal Transformer | MCTA015/15 Farnell UK'. https://uk.farnell.com/multicomp/mcta015-15/transformer-toroidal-2-x-15v-15va/dp/9530266 (accessed Jul. 06, 2021).

[1.3] V. Carazo and Alfredo, 'Piezoelectric Transformers: An Historical Review', *Actuators*, vol. 5, no. 2, p. 12, Apr. 2016, doi: 10.3390/act5020012.

Chapter 2 - Review of piezoelectric transformers

2.1 Introduction to piezoelectric devices

Due to the electromechanical nature of piezoelectric devices, the analysis of such systems involves the introduction of several new concepts for electronic engineers. In this section, these new concepts will be defined and introduced to give context to the following thesis. The discussed concepts include coordinate systems and tensors; fundamental piezoelectric equations; discussion of the piezoelectric physics and the measurement of piezoelectric devices.

2.1.1 Coordinate systems

One of the main challenges when working with piezoelectric systems is that piezoelectric materials are typically anisotropic, meaning they have differing properties in different directions. Therefore, carefully defining the coordinate system is vital to ensure the correct properties are used during analysis. It is common when working with piezoelectric materials to use a numbered axis coordinate system, called compressed matrix notation, with numbers going from 1-6 [2.1]. This coordinate system is often notated using a ‘p or ‘q’. An example of this system is shown in Fig. 2.1 with cartesian coordinates also displayed.

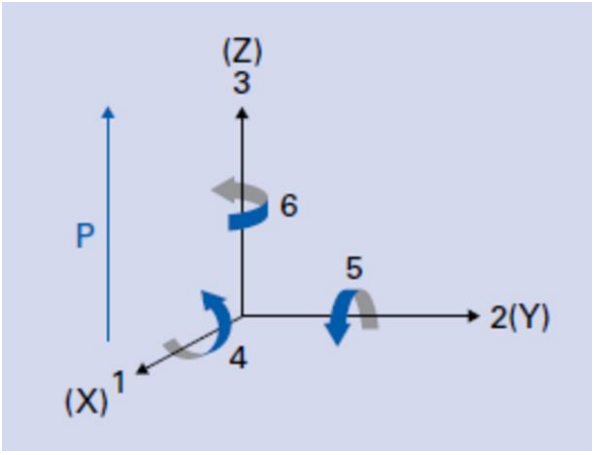

Fig. 2.1 – 1-6 axis coordinates shown with the Cartesian coordinate system [2.2]

Axis 1-3 define the three main axes of the coordinate system; thus, they correspond to XYZ in a cartesian system or RθZ in a cylindrical system. Whilst other coordinate systems are available, these are the most common in piezoelectric analysis. For piezoelectric devices, coordinate systems are orientated with respect to the direction of poling (see section 2.1.3 for poling). The polling direction is typically aligned with the 3rd axis or the Z axis in a cartesian or cylindrical coordinate systems. The direction of the 1st and 2nd axis then depends on the coordinate system. As shown in Fig. 2.1, in a cartesian system it is typical for X to be aligned with the 1st axis and Y to be aligned with the 2nd axis. However, it should be noted that often X and Y can be aligned with the 2nd and 1st axis, respectively without issues noting the symmetry of piezoelectric material (as discussed in [2.1]). In a cylindrical system, the radial axis is aligned with the 1st axis and the theta axis is aligned with the 2nd axis.

Additional to the 1-3 axis, there are 4-6 axis which describe shear motion, which is shown in Fig. 2.1 for a cartesian system. As described in the [2.1], axis 4 corresponds to directions in the plane between the 2nd and 3rd axis (YZ in Cartesian); axis 5 corresponds to directions in the plane between the 1st and 3rd (XZ) axis and axis 6 corresponds to directions in the plane between the 1st and 2nd axis (XY).

Often tensor notation, often referred to as ‘ij’ or ‘kl’ notation (see section 2.1.5 and [2.1]) is used in piezoelectric analysis, which avoids using numbers 4-6 in this coordinate system by using 2 numbers. For example, the 4 axis which is in the plane between the 2nd and 3rd axis, will be descried by ‘23’. Thus, the full conversion between the 1-6 notation and the tensor notion is given in Table 2.1 [2.1].

Table 2.1 – Conversion between different coordinate notation [2.1]

'ij' or 'kl' notation	$'p'$ or 'q' notation
11	1
22	2
33	3
23 or 32	4
31 or 13	5
12 or 21	6

It should be noted that the 'p','q' notation descried above is called compressed matrix notation, as it simplifies the full tensor description by making the assumptions that 'ij' $=$ 'ji'.

Whilst the numerical coordinate systems described here are used throughout piezoelectric analysis, it is common to convert terms to either Cartesian or cylindrical coordinates before analysis.

2.1.2 Piezoelectric effect

The direct piezoelectric effect was defined as 'electric polarisation produced by mechanical strain in crystals belonging to certain classes, the polarization being proportional to the strain and changing sign with it' and was discovered as a subset of pyroelectricity by the Curie brothers, Pierre and Paul-Jacques in 1880 [2.3]. A year later, Lippmann discovered the converse piezoelectric effect, in which an electric field causes a proportional strain in the crystal. These effects mean that when a force is applied to the piezoelectric, an electric field occurs across the device or if an electric field is applied across the device, a deformation of the material will be observed.

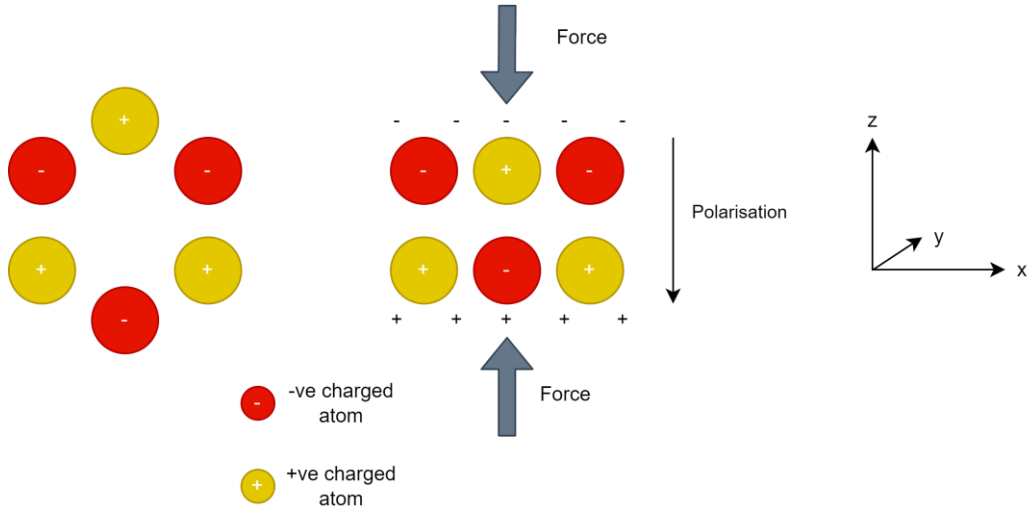

Fig. 2.2 – Non-centrosymmetric material, (left) no external force and thus no net polarisation, (middle) force applied causing polarisation to be induced

Piezoelectricity arises only in materials that can be classed as non-centrosymmetric. A non-centrosymmetric material has no points of inversion symmetry. This means that, given an atom in the unit cell (simplest repeating structure of atoms in a material [2.4]) at a given point, then if that point is inverted through the centre of the unit cell there does not exist another similarly charged atom at this new location. For example, observing Fig. 2.2, in this 2D example if the bottom negatively charged atom was inverted through the central point, then there does not exist another atom of the same charge at this new inverted location, in this case, there is an oppositely charged atom in this position, therefore, this example shows a structure that is non-centrosymmetric.

However, note that in this same diagram that although the structure is non-centrosymmetric, the overall net charge of this unit cell is 0, as the positive and negative charges cancel out. The example in Fig. 2.2 is that of a non-polar piezoelectric, where polar piezoelectrics are those that exhibit a non-zero net charge (i.e they have spontaneous polarisation without an external force) [2.5]. Again, noting the example in Fig. 2.2, if the piezoelectric material becomes deformed, owing to the lack of inversion symmetry, the orientation of the positive and negative charges will change and thus dipoles will be formed (polarisation).

Similarly, if an external electric field is applied to the material, then the charges inside the unit cell will be attracted and repelled by this electric field. This attraction will cause the position of these charged atoms to change, which then causes a deformation of the unit cell and thus a deformation of the overall geometry of the device.

2.1.3 Poling

Piezoelectric materials are often artificially polarised (poled), which aligns the charges inside the material, such that upon deformation in a certain direction, the dipoles which are formed are aligned along a single axis. Thus, during deformation these dipoles occur in the same direction, effectively summing the dipoles, and so the charge occurring on the surface of the material in this certain direction is maximised. Similarly, this ensures maximum deformation upon the application of an electric field in that direction.

Poling a piezoelectric sample is achieved by applying a very high (typically >4kV/mm) electric field across the device in the direction of desired poling, whilst the sample is placed in a silicon oil bath at a raised temperature (typically 120°C) for around 45 minutes [2.6]. It is common for certain non-centrosymmetric materials to require poling before they will exhibit noticeable piezoelectric properties [2.5], as the dipoles which are formed though deformation will effectively cancel each other out (no net charge).

2.1.4 Mechanics and electrostatics

The key property of piezoelectric devices is the electromechanical coupling they exhibit, which is to say the electric field or electric displacement field affects stress and strain acting on the device and vice versa. The following section will discuss these quantities in more detail.

2.1.4.a) Mechanics

For elastic materials, those that once deformed by a force will then return to their original shape once that force is removed, there are two key quantities required for analysing the mechanics of these materials, stress and strain. Stress is defined as the force per unit area and can be thought of as the internal resistance of the material to a mechanical load or the counterforce of a material to the effects of the load [2.7].

Strain is defined as the amount of deformation that occurs as a result of a force acting on the material. It is defined as the ratio of deformation to the initial size of the body being deformed and so it is unitless [2.8]. Stress and strain can be linearly linked for elastic materials using Young's modulus, which is defined as,

$$Y = \frac{T}{S} = \frac{Force/_{Area}}{\Delta length/_{length}} \tag{2.1}$$

where T is the stress ($\mathrm{N/m^2}$) and S is the strain [2.9]. Young's modulus is a property of the material, however, as mentioned previously piezoelectric materials are anisotropic and so the stress and strain and thus by extension the Young's modulus is different in different directions in the material. Therefore, the Young's modulus can be defined by a second rank tensor (see 2.1.5) for anisotropic materials, which allows this property to be defined for multiple directions.

2.1.4.b) Electrostatics

Similarly, for dielectric materials, insulators that can be polarised by an electric field, there also exist two main quantities required for analysis, electric field, and electric displacement. An electric field can be defined as a region where an electrically charged particle would experience a force [2.10]. Therefore, if a charged particle were inside an electric field, depending on the direction of the electric field and the charge of the particle, it would be forced in a certain direction. As electric fields originate from charges, they have units of force per coulomb, however, it is more conventional to use the equivalent SI unit, voltage per meter. For the devices analysed in this work, electric fields are generated by applying a voltage onto electrodes separated by a piece of piezoelectric material, therefore, the electric field occurring in these devices is given by,

$$E = -\frac{V}{d} \tag{2.2}$$

where V is the applied voltage, d is the distance between the electrodes and E is the electric field. Electric displacement is a measure of the displacement of a charge in a dielectric material caused by the application of an electric field and has units of coulomb per square meter [2.11]. It is also often referred to as electric flux density. Similar to stress and strain, these quantities are linked though a property, permittivity, which is defined as

$$\varepsilon = \varepsilon_0 \varepsilon_r = \frac{D}{E} \tag{2.3}$$

where $\varepsilon_0$is the permittivity of air in a vacuum, ε_r is the relativity permittivity of the dielectric material, D is electric displacement and E is electric field. Permittivity has units of Farad per meter. Similar to Young's modulus, owing to the anisotropic materials used here, electric field, electric displacement and thus permittivity is different in differing directions. Therefore, similar to Young's modulus, permittivity is defined as a first rank tensor (see 2.1.5) for anisotropic materials.

It should be noted that polarisation is an additional electrical quantity often seen in the analysis of piezoelectric devices and can be used instead of electric displacement. However, in modern analysis of piezoelectric devices it is common to use electric displacement and so will not be discussed here.

2.1.5 Tensors

Tensors are simply multi-dimensional arrays which are used in the analysis of piezoelectric devices to model the physical properties of an anisotropic material and the mechanical or electrical forces acting on the device [2.12]. Tensors are ranked, with the number of the rank describing the number of dimensions the array exhibits. A tensor of rank 0, is a scalar. Similarly, tensors of rank 1 and 2 describe a 1-dimensional array (vector) and 2-dimentional array (square matrix), respectively.

As the stress and strain are 2nd rank tensors they should be described by a square matrix. Therefore, as [2.13] describes the stress and strain in each direction can be described by 9 components. These 9 components of stress (or strain) can be written in tensor notation for both 'ij' notation and Cartesian coordinates as,

$$T = \begin{bmatrix} T_{11} & T_{12} & T_{31} \\ T_{21} & T_{22} & T_{32} \\ T_{31} & T_{32} & T_{33} \end{bmatrix} = \begin{bmatrix} T_{xx} & T_{xy} & T_{xz} \\ T_{yx} & T_{yy} & T_{yz} \\ T_{zx} & T_{zy} & T_{zz} \end{bmatrix} \tag{2.4}$$

where the tensor notation is described as,

$$T_{ij} \tag{2.5}$$

where i is the direction of the surface normal on which the stress (or strain) acts and j is the direction of the stress (or strain) [2.13]. Similarly, electric field and electric displacement are 1st rank tensors and so they can be described by a vector with 3 components. Therefore, the

electric field (or the electric displacement) can be written in tensor notation for both 'k' notation and Cartesian coordinates as,

$$E = \begin{bmatrix} E_1 \\ E_2 \\ E_3 \end{bmatrix} = \begin{bmatrix} E_x \\ E_y \\ E_z \end{bmatrix} \tag{2.6}$$

where in this case the tensor notation is descried as,

$$E_k \tag{2.7}$$

where k is the direction of the electric field (or electric displacement).

2.1.6 Constitutive equations

As mentioned, the key property of piezoelectric materials is the coupling between the electric and mechanical properties. Therefore, the stress acting on a material is a function of both strain and electric field (or electric displacement). Similarly, the electric displacement of a material is a function of both electric field and stress (or strain). Therefore, additional terms and constants need to be added to equations (2.1) and (2.3) to account for the electromechanical coupling. These resulting equations are called the constitutive equations and are fundamental to the analysis of piezoelectric devices.

Firstly, given the four key properties for analysing piezoelectric devices, stress, strain, electric field and electric displacement, there are 4 different forms of the constitutive equations, these are defined as (S, D), (T, E), (T, D) and (S, E). In this notation, each form is named by the independent variables in the resulting equations. The form of constitutive equations should be carefully chosen based on several factors, including crystal class (see section 2.1.7), the geometry of the device and the assumptions which are to be used in the analysis [2.14]. In the analysis presented in this thesis, the (T, E) form will be exclusively used, as it is convenient for calculating force and current using Gauss's Law. Therefore, stress and electric field will be the independent variables in the resulting equations. The resulting piezoelectric constitutive equations are defined as [2.1], [2.15],

$$S = s^{\mathrm{E}}T + dE \tag{2.8}$$

$$D = dT + \varepsilon^{\mathrm{T}} E \tag{2.9}$$

where S is the 6x1 strain vector, T is the 6x1 stress vector, D is the 3x1 electric field vector and E is the 3x1 electric field vector. Additionally, s^{E} is the 6x6 elastic constant matrix, which is analogous to the Young's modulus, ε^{T} is the 3x3 dielectric constant (relative permittivity) matrix (as discussed in 2.1.4.b), d is a 3x6 piezoelectric constant matrix which is related to the material and accounts for the electromechanical coupling. It should be noted that in s^{E} and ε^{T}, the superscript notation denotes that these quantities are measured at constant electric field and constant stress respectively (subscript T in this case does not denote transpose). Equations (2.8) and (2.9) are notably similar to those defined in (2.1) and (2.3) with additional terms added to account for the piezoelectric coupling. The piezoelectric constant matrix d, is often used to describe how 'piezoelectric' a material, with larger numbers for these constants giving rise to 'greater' piezoelectric coupling.

It should be noted that other forms of the constitutive equations use different definitions for the piezoelectric constants. Therefore, it is common to see several different constants on piezoelectric datasheet, all of which can be transformed to the desired form [2.1]. As discussed, variables and constants in the constitutive equations are matrices to account for the anisotropic properties of piezoelectric materials. Therefore, using Voigt notation, equations (2.8) and (2.9) can be written in matrix form [2.1], [2.15], [2.16],

$$\begin{bmatrix} S_1 \\ S_2 \\ S_3 \\ S_4 \\ S_5 \\ S_6 \end{bmatrix} = \begin{bmatrix} s_{11}^{\mathrm{E}} & s_{12}^{\mathrm{E}} & s_{13}^{\mathrm{E}} & s_{14}^{\mathrm{E}} & s_{15}^{\mathrm{E}} & s_{16}^{\mathrm{E}} \\ s_{21}^{\mathrm{E}} & s_{22}^{\mathrm{E}} & s_{23}^{\mathrm{E}} & s_{24}^{\mathrm{E}} & s_{25}^{\mathrm{E}} & s_{26}^{\mathrm{E}} \\ s_{31}^{\mathrm{E}} & s_{32}^{\mathrm{E}} & s_{33}^{\mathrm{E}} & s_{34}^{\mathrm{E}} & s_{35}^{\mathrm{E}} & s_{36}^{\mathrm{E}} \\ s_{41}^{\mathrm{E}} & s_{42}^{\mathrm{E}} & s_{43}^{\mathrm{E}} & s_{44}^{\mathrm{E}} & s_{45}^{\mathrm{E}} & s_{46}^{\mathrm{E}} \\ s_{51}^{\mathrm{E}} & s_{52}^{\mathrm{E}} & s_{53}^{\mathrm{E}} & s_{54}^{\mathrm{E}} & s_{55}^{\mathrm{E}} & s_{56}^{\mathrm{E}} \\ s_{61}^{\mathrm{E}} & s_{62}^{\mathrm{E}} & s_{63}^{\mathrm{E}} & s_{64}^{\mathrm{E}} & s_{65}^{\mathrm{E}} & s_{66}^{\mathrm{E}} \end{bmatrix} \begin{bmatrix} T_1 \\ T_2 \\ T_3 \\ T_4 \\ T_5 \\ T_6 \end{bmatrix} + \begin{bmatrix} d_{11} & d_{21} & d_{31} \\ d_{12} & d_{22} & d_{32} \\ d_{13} & d_{23} & d_{33} \\ d_{14} & d_{24} & d_{34} \\ d_{15} & d_{25} & d_{35} \\ d_{16} & d_{26} & d_{36} \end{bmatrix} \begin{bmatrix} E_1 \\ E_2 \\ E_3 \end{bmatrix} \tag{2.10}$$

$$\begin{bmatrix} D_1 \\ D_2 \\ D_3 \end{bmatrix} = \begin{bmatrix} d_{11} & d_{12} & d_{13} & d_{14} & d_{15} & d_{16} \\ d_{21} & d_{22} & d_{23} & d_{24} & d_{25} & d_{26} \\ d_{31} & d_{32} & d_{33} & d_{34} & d_{35} & d_{36} \end{bmatrix} \begin{bmatrix} T_1 \\ T_2 \\ T_3 \\ T_4 \\ T_5 \\ T_6 \end{bmatrix} + \varepsilon_0 \begin{bmatrix} \varepsilon_{11}^{\mathrm{T}} & \varepsilon_{21}^{\mathrm{T}} & \varepsilon_{31}^{\mathrm{T}} \\ \varepsilon_{12}^{\mathrm{T}} & \varepsilon_{22}^{\mathrm{T}} & \varepsilon_{32}^{\mathrm{T}} \\ \varepsilon_{13}^{\mathrm{T}} & \varepsilon_{23}^{\mathrm{T}} & \varepsilon_{33}^{\mathrm{T}} \end{bmatrix} \begin{bmatrix} E_1 \\ E_2 \\ E_3 \end{bmatrix} \tag{2.11}$$

where indices 1-6 correspond to the compressed matrix notation discussed in section 2.1.1. Equations (2.10) and (2.11) are the general constitutive equations for piezoelectricity.

2.1.7 Crystal classes

Piezoelectricity occurs in crystalline materials, where a crystal is defined as a solid where there is a single repeating pattern of atoms [2.1]. The smallest repeating group of atoms in a crystal is called a unit cell. There are seven systems for describing the shape of crystals: triclinic, monoclinic, orthorhombic, tetragonal, trigonal, hexagonal, and cubic. Of these 7 systems, they can be split into 32 different classes, where the classes are based on the number of degrees of symmetry the unit cell of the material exhibits. However, 12 of these classes show a high degree of symmetry and so are centrosymmetric, therefore, leaving 20 classes of crystal which could exhibit piezoelectric properties [2.1]. The details of each of the classes is beyond the scope of this work, however, the IEEE standard on piezoelectricity is an excellent resource for more details on this topic [2.1].

For the analysis here, the most important consideration of the materials crystal class, is that owing to the symmetry, the constitutive equations can be simplified. The most important crystal class for the analysis here is the C_{4v} (see [2.1] for more details on this notation) class, which is tetragonal and as such has an axis of four-fold symmetry. Its importance is due to lead zirconium titanate (PZT) and barium titanate, two of the most popular piezoelectric materials, being of this class. These materials exhibit high piezoelectric coefficients, high Q factors, low losses and are versatile, making them ideal for a variety of applications.

Therefore, for this class, the previous constitutive equations can be simplified by observing the Electro-Piezo-Dielectric matrix diagram shown in the IEEE standard on piezoelectricity [2.1], [2.15], and noting the specific symmetries highlighted for this crystal class and thus giving zeros in the following matrices,

$$\begin{bmatrix} S_1 \\ S_2 \\ S_3 \\ S_4 \\ S_5 \\ S_6 \end{bmatrix} = \begin{bmatrix} s_{11}^{\mathrm{E}} & s_{12}^{\mathrm{E}} & s_{13}^{\mathrm{E}} & 0 & 0 & 0 \\ s_{12}^{\mathrm{E}} & s_{11}^{\mathrm{E}} & s_{13}^{\mathrm{E}} & 0 & 0 & 0 \\ s_{13}^{\mathrm{E}} & s_{13}^{\mathrm{E}} & s_{33}^{\mathrm{E}} & 0 & 0 & 0 \\ 0 & 0 & 0 & s_{55}^{\mathrm{E}} & 0 & 0 \\ 0 & 0 & 0 & 0 & s_{55}^{\mathrm{E}} & 0 \\ 0 & 0 & 0 & 0 & 0 & s_{66}^{\mathrm{E}} \end{bmatrix} \begin{bmatrix} T_1 \\ T_2 \\ T_3 \\ T_4 \\ T_5 \\ T_6 \end{bmatrix} + \begin{bmatrix} 0 & 0 & d_{31} \\ 0 & 0 & d_{31} \\ 0 & 0 & d_{33} \\ 0 & d_{15} & 0 \\ d_{15} & 0 & 0 \\ 0 & 0 & 0 \end{bmatrix} \begin{bmatrix} E_1 \\ E_2 \\ E_3 \end{bmatrix} \tag{2.12}$$

$$\begin{bmatrix} D_1 \\ D_2 \\ D_3 \end{bmatrix} = \begin{bmatrix} 0 & 0 & 0 & 0 & d_{15} & 0 \\ 0 & 0 & 0 & d_{15} & 0 & 0 \\ d_{31} & d_{31} & d_{33} & 0 & 0 & 0 \end{bmatrix} \begin{bmatrix} T_1 \\ T_2 \\ T_3 \\ T_4 \\ T_5 \\ T_6 \end{bmatrix} + \varepsilon_0 \begin{bmatrix} \varepsilon_{11}^{\mathrm{T}} & 0 & 0 \\ 0 & \varepsilon_{11}^{\mathrm{T}} & 0 \\ 0 & 0 & \varepsilon_{33}^{\mathrm{T}} \end{bmatrix} \begin{bmatrix} E_1 \\ E_2 \\ E_3 \end{bmatrix} \quad (2.13)$$

These resulting equations can then be used in the analysis of a piezoelectric device made from a material of crystal class C_{4v}, such as PZT.

2.1.8 Constitutive equations in cylindrical coordinates for C_{6v} material

Based on the simplified constitutive equations (2.12) and (2.13) and the discussion of the coordinate systems in 2.1.1, these equations can now be written in cylindrical coordinates. Again, noting that for cylindrical coordinates it is typical for axis 1 to correspond to the radial axis, for axis 2 to correspond to the theta axis, for axis 3 to correspond to the z axis (which is the direction of poling), with axes 4-6, describing the shear directions between the 3 axes. Therefore, for a piezoelectric device made from a material in the C_{4v} crystal class and polled in the z direction, the (T, E) type constitutive equations in cylindrical coordinates are [2.15],

$$S_r = \mathrm{s}_{11}^{\mathrm{E}} T_r + s_{12}^{\mathrm{E}} T_\theta + s_{13}^{\mathrm{E}} T_z + d_{31} E_z \quad (2.14)$$

$$S_\theta = s_{12}^{\mathrm{E}} T_r + s_{11}^{\mathrm{E}} T_\theta + s_{13}^{\mathrm{E}} T_z + d_{31} E_z \quad (2.15)$$

$$S_z = s_{13}^{\mathrm{E}} (T_r + T_\theta) + s_{33}^{\mathrm{E}} T_z + d_{31} E_z \quad (2.16)$$

$$S_{\theta z} = s_{55}^{\mathrm{E}} T_{\theta z} + d_{15} E_\theta \quad (2.17)$$

$$S_{rz} = s_{55}^{\mathrm{E}} T_{rz} + d_{15} E_r \quad (2.18)$$

$$S_{r\theta} = s_{66}^{\mathrm{E}} T_{r\theta} \quad (2.19)$$

$$D_r = d_{15} T_{rz} + \varepsilon_0 \varepsilon_{11}^{\mathrm{T}} E_R \quad (2.20)$$

$$D_\theta = d_{15} T_{\theta z} + + \varepsilon_0 \varepsilon_{11}^{\mathrm{T}} E_\theta \quad (2.21)$$

$$D_Z = d_{31} T_r + d_{31} T_\theta + d_{33} T_z + \varepsilon_0 \varepsilon_{33}^{T} E_z \quad (2.22)$$

These equations will be used throughout the analysis presented in Chapter 5, Chapter 6 and Chapter 8.

2.1.9 Introduction to the analysis of plate vibrations

When analysing piezoelectric devices, it is common to use several assumptions to be able to achieve an analytical solution. Many of these assumptions that are used in the analysis of piezoelectric transformers rely on Plate Theory. A plate is a structural element where its planar dimensions are much larger than its thickness, such as a thin disc [2.17]. Several plate theories have been proposed, simplifying the analysis of plate vibrations, with Kirchhoff providing the most notable contribution to this topic and with Mindlin then extending Kirchhoff's theory to include additional complexity and thus accuracy [2.18]. Ventsel and Krauthammer presented an excellent summary of the many theories and methods for analysing elastic and piezoelectric plates over the past two centuries [2.19].

An understanding of the forces acting on a plate during vibration is critical for analysis, as it allows equilibrium equations and equations of motion to be formed, which is often the starting point when analysing piezoelectric devices. The forces Q, N and moments M acting on a annular plate during vibration are shown in Fig. 2.3.

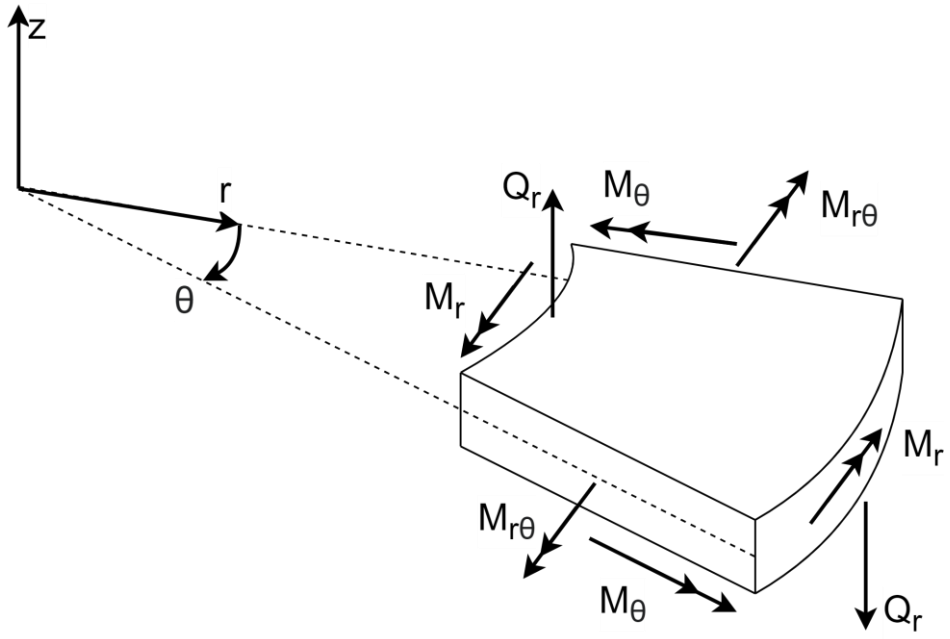

Fig. 2.3 – Forces N, Q and moments M acting on a cross section of an annular plate

Whilst there are several forces and moments acting on a plate at once, depending on the type of vibration mode being analysed, many of these will be negligible and depending on the plate

theory being used, can be ignored. Once the relevant forces are identified, summing forces in each of the coordinate axis directions or using Hamilton's principle allows equilibrium equations to be formed, which can then be extended to equations of motion for the vibration mode of interest. The formulation of the equations of motion are beyond the scope of this review, however, derivation of equations of motion are presented in full by Reddy [2.17] and summarised by Leissa [2.18].

2.1.10 Coupling factor

As discussed in section 2.1.8, piezoelectric constants are key parameters for determining "how piezoelectric" (i.e. how much the electric field affects stress and vice versa) a device is. However, given the large matrix of numbers it is hard to quantify this based on observing the piezoelectric matrix alone. Therefore, it is typical to use coupling factor as a metric to determine how suitable a material is. Coupling factor (k^2) is defined as [2.15],

$$k^2 = \frac{\text{stored mechanical energy}}{\text{supplied electrical energy}}$$
$$k^2 = \frac{\text{stored electrical energy}}{\text{supplied mechanical energy}} \tag{2.23}$$

Therefore, the larger the coupling factor, the greater energy that is converted between the electrical and mechanical domains and therefore, the greater the power handling capability of the device [2.14]. Coupling factor is dependent on the material chosen and the vibration shape (modes) that the device is being operated in. Thus, when choosing a suitable material for a high-power piezoelectric device, such as a transformer, it is important to choose a material with as large a coupling factor for the mode that your device will be operated at.

2.2 Piezoelectric transformers

Piezoelectric transformers (PT) make use of both direct and converse piezoelectric effects to transform energy between electrical and mechanical domains. A PT is made from 1 or more pieces of piezoelectric material that form both an input and an output section. An AC voltage is applied across electrodes on the input section of the PT, forcing it into vibration through the converse piezoelectric effect. The output section of the device is mechanically bonded to the input section, and thus the vibration in the input section is mechanically coupled to the

output section, forcing the output section to vibrate. Finally, the forced vibration of the output section of the PT causes a proportional voltage to occur across the output electrodes, due to the direct piezoelectric effect. Depending on the topology and design of the PT, different turns ratios and electrical characteristics can be achieved. PTs are typically operated at one of their natural resonant frequencies, with each resonant frequency related to a vibration mode (shape). Whilst PTs exhibit several vibration modes, they are typically designed to be operated at a specific vibration mode, which is chosen to optimise the performance of the PT. The additional modes are unwanted (spurious) and can cause performance degradation, therefore, a PT should be carefully designed to avoid such issues [2.39].

Owing to the makeup of PTs, they have several advantageous properties when compared to traditional magnetic transformers. Firstly, as PTs are typically operated at one of their resonant frequencies, from an electrical perspective they can be accurately modelled as having an inherent resonant tank circuit [2.40]. This means that resonant converters made with PTs require few external components, simplifying the converter and leading to high converter power density. Additionally, the inherent resonant tank exhibits extremely high Q factors (>500), leading to low losses, thus high efficiency, and minimal harmonics in the output voltage [2.41]. PTs also offer several other advantages such as being non-magnetic, having a high-power density and are non-flammable [2.41].

There exist many different topologies of PT, each of which are operated at one of the devices natural resonances, with different shapes of PT leading to specific optimal vibration modes (resonances). The Rosen PT was the first and most popular PT topology, developed by Charles A Rosen in 1954 [2.42]. The Rosen PT has a cuboid shape and is normally operated at one of its longitudinal vibration modes. The Rosen PT topology leads to high voltage gains and therefore they are typically used in high voltage/low power step up applications, such as driving CCFL lamps [2.41]. Fig. 2.4 shows a Rosen PT CCFL driver used by Apple in one of their laptops.

Fig. 2.4 – Rosen PT based inverter used in Apple Powerbook laptops [2.20]

In the past 30 years, high-power, step-down PTs have become more prominent in research [2.20]. Whilst many research groups have built and evaluated different high power PTs topologies, the most popular are radial vibrating devices; the radial mode Transoner and ring-dot PTs. These devices make use of the planar coupling factor (k_p^2), which is typically one of the largest coupling factors exhibited by state-of-the-art piezoelectric materials, thus these PTs can exhibit high power densities. The axisymmetric design of these PTs means that, whilst additional vibration modes are still present, there are significantly fewer than square/rectangular devices [2.43].

2.2.1 High-power PT topologies

2.2.1.a) Radial mode Transoner

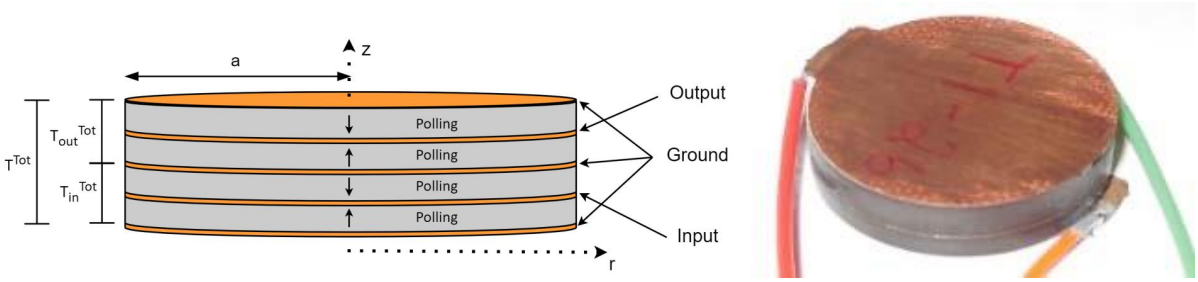

Fig. 2.5 – Radial mode piezoelectric transformer by Face electronics [44], (left) schematic diagram of the Transoner PT, (right) transoner PT [2.20]

The radial mode Transoner was developed by Face electronics in 2003 [2.44]. A typical Transoner design is depicted in Fig. 2.5. The Transoner is simple in construction, with its most basic form being two electroded piezoelectric layers stacked on top of each other, with a common ground electrode in the middle. The input section is driven into vibration in the radial (or planar) direction using the converse piezoelectric effect and induces a similar vibration in the output section which using the direct piezoelectric effect, converts the mechanical vibration back to electrical energy [2.44]. As previously mentioned, the device uses the planar (k_p^2) electromechanical coupling factor and as a result the Transoner PTs have been shown to

exhibit power densities of up to 40W/cm^3 [2.44]. The voltage ratio can be controlled by the number of layers in the input and output sections of the device, allowing this topology to be used for both step-up and step-down applications. Layers of the device are poled alternately and each layer in each section is connected in parallel. Radial mode Transoner PTs have been used in a variety of applications such as MOSFET gate driving [2.45], LED driving [2.46]–[2.48] and as an electronic ballast for fluorescent lamps [2.49]–[2.51].

Characterisation of the Transoner PT was conducted first by Lin [2.52] and then by Horsley [2.14], in which a lumped equivalent circuit model was developed for the PT. Huang and Huang proposed an improved equivalent circuit model [2.53], which unlike the earlier models included the effects caused by the thickness of the PT and so provided a more detailed and accurate model, albeit much more complex.

As with almost all piezoelectric transformers, spurious modes are an issue. Due to the circular shape of the Transoner PT there are a reduced number of spurious modes, owing to the symmetrical shape and thus a constant distance from the centre of the device to the outer edge in the vibrating plane. However, there are several spurious modes that still occur in the fundamental frequency range [2.44].

Some improvements on the Transoner have been presented. Khanna *et al.* improved on the original design by adding additional layers to the device to create a tuneable PT [2.54]. By connecting a capacitor across the new layers effectively changes the value of capacitance in the resonant tank circuit. This can be used to change the voltage gain versus frequency characteristic, providing an additional control method for a PT converter. Valenta *et al.* split the electrode at the top of the device in to two sections, allowing simultaneous power and data transfer using the third radial resonant frequency [2.55]. Experimental tests were successful and they suggest that with further processing the data could be fully extracted.

2.2.1.b) Ring-Dot piezoelectric transformer

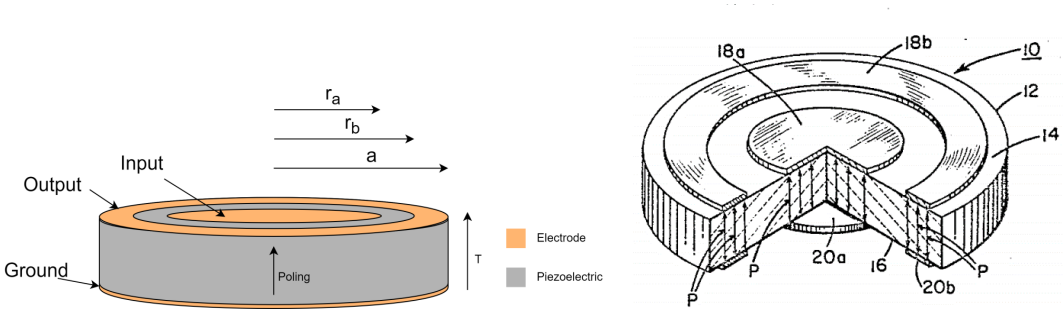

Fig. 2.6 – Ring-dot piezoelectric transformer [2.56]

The ring-dot PT is another radial vibrating topology, patented by Jaffe and Berlincourt [2.56]. This PT is typically made from a single piezoelectric disc polled in the thickness direction. This PT features a dot and a ring electrode on its top face, with the volume under these electrodes forming the input and output sections, respectively, with a common ground electrode on the bottom face. Similar to the Transoner, the ring-dot PT is a radial vibrating device, using the k_p^2 coupling factor and so similar power densities to the Transoner can be achieved. The ring-dot PT has some additional advantages over the radial mode Transoner PT, including an easier manufacturing process and the lack of spurious modes [2.57].

Laoratanakul *et al.* published the first experimental measurements from a practical ring-dot PT [2.58]. The practical PT exhibited a power density of 18.5W/cm^3, 10 times higher than the Rosen PT, but lower than the Transoner PT. Priya *et al.* then improved on this by building a ring-dot device with a 40W/cm^3 power density utilising an improved material and allowing a higher temperature rise [2.59]. Impressively, this is the same value as is often presented for the radial mode Transoner PT [2.20]. Additionally, Priya *et al.* proposed a multi-layer device based on a ring-dot electrode structure; however, this structure meant that heat was harder to remove from the device, thus leading to a lower power density than the single disc variant. Guo *et al.* [2.32], built and tested a lead-free ring-dot PT, showing promising results, but not quite achieving the same performance as lead zirconium titanate (PZT) based devices. Pulpan [2.57] experimentally analysed the effect of different electrode patterns on the key electrical performance characteristics. Whilst some electrode patterns provided improved characteristics in specific quantities, the ring-dot pattern proved to be the more optimal overall electrode shape for this type of device [2.57].

2.2.1.c) Square thickness mode

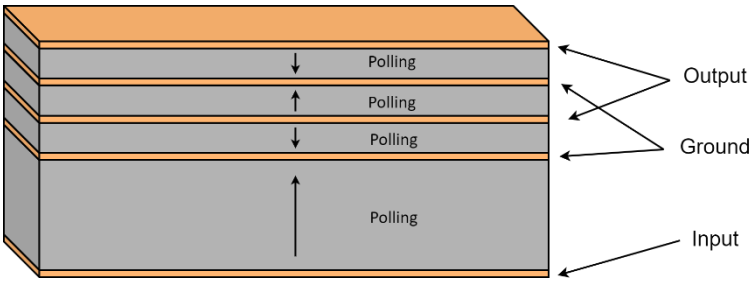

Fig. 2.7 – Square thickness mode piezoelectric transformer

The thickness mode PT was developed by Inoue *et al.* and Zaitsu *et al.* working at NEC in the early 1990's [2.60], [2.61]. The device was polled and driven into vibration in the thickness direction. As a result, this transformer makes use of the thickness electromechanical coupling factor, typically one of the largest in piezoelectric materials and so in theory, should lead to high power densities [2.20], [2.62]. Zaitsu *et al.* then built and tested a thickness mode transformer for use in power supplies [2.63]. However, the resulting PT achieved output powers up to 8W and efficiencies of 80% and above, leading to a power density of 16W/cm^3, with theoretical analysis suggesting that 20W/cm^3 could be achieved. One of the main issues with this device is the influence of spurious vibration modes, which occur in close proximity to the thickness modes, which are known to cause issues for PT performance [2.43]. One application of this topology was for driving low power LEDs, as presented by Kim *et al.* [2.64].

2.2.1.d) Ring

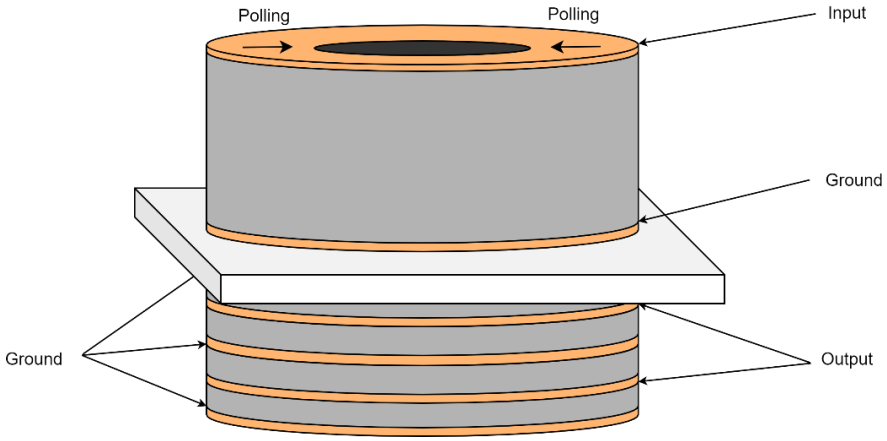

Fig. 2.8 – Ring thickness mode piezoelectric transformer [2.39]

To overcome the limitations of the thickness mode PT, Noliac presented a ring/annular shaped thickness mode PT [2.39]. This transformer had several advantages over the original thickness mode PT. Firstly, through careful design the fundamental spurious mode was at a frequency lower than the thickness mode [2.39]. Additionally, and importantly, due to the ring shape this spurious vibration shows no high order harmonics. Therefore, the higher frequency thickness mode is free of spurious vibration interaction.

This topology of PT achieved power densities above 40W/cm^3 and above 98% efficiency [2.65]. Nava *et al.*, developed a similar design, with additional bevels on the inside of the PT and dead areas to further eliminate spurious modes. Although, the PT presented by Nava *et al.* only achieved a 25W/cm^3 power density, significantly lower than the original presented topology [2.66].

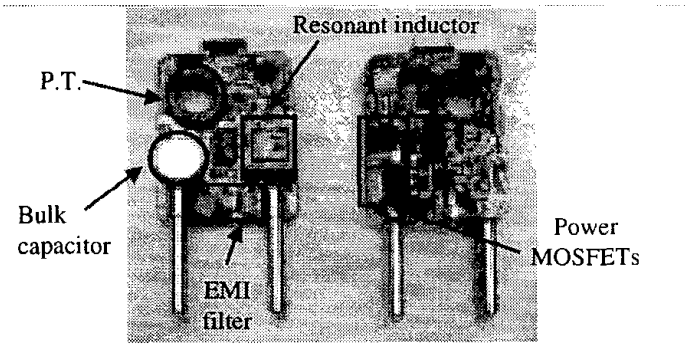

Fig. 2.9 – Small mobile phone charger made with a ring PT [2.66]

Several other authors have presented different forms of ring PT. Hu *et al.* presented a simple high power ring PT with 2 concentric electrodes making up the input (outer ring) and output

(inner ring) sections on top and a single common electrode on the bottom of the PT [2.67], [2.68]. The ring is poled in the thickness direction and the PT is driven in the third symmetric extensional (radial) mode. The electrical connections are made precisely at points of low displacement for reliability. This design gave a power density of 14.3W/cm^3 and up to 90% efficiency. This design was then adapted by Erhart, rather than 1 piece of unipolar piezoelectric, 2 concentric rings of piezoelectric material were used [2.69]. The outer ring is poled in the radial direction with an electrode on the outer side which created the output or secondary section of the PT. The inner (input) ring is poled in the thickness direction with an electrode on the top face of the ring, giving the PT a similar structure to the popular Rosen PT. The resulting optimally designed PT presented by Erhart had a high voltage ratio of 217 and 13.4 under no load and optimum load respectively and an efficiency of 97%. Lin *et al.* performed further analysis on this PT, deriving the equivalent circuit model, investigating the effect of dimensions on the resonant frequency, effective coupling factor, and voltage and power gain [2.70]. The main issue with ring PTs is the difficulty, due to the hole in the centre, of mounting the PT without damping the vibration of the device [2.69].

2.2.1.e) Contour vibration mode

Yoo *et al.* proposed a square, contour mode PT with a ring dot shape in the centre [2.33]. The square input section and the dot output section were polled in the thickness direction, with an isolation gap between the two. In their testing, they found that a PT with the largest dot size gave the highest power density, 12.5W/cm^3 and an efficiency of 97.57%. The same authors also created a similar PT but with a diamond shaped ring and dot. The same process of optimisation was concluded and a 7.4W/cm^3 PT with 98% efficiency was created [2.71]. The ring dot design was further optimised with the assistance of FEA by Seo *et al.* [2.72].

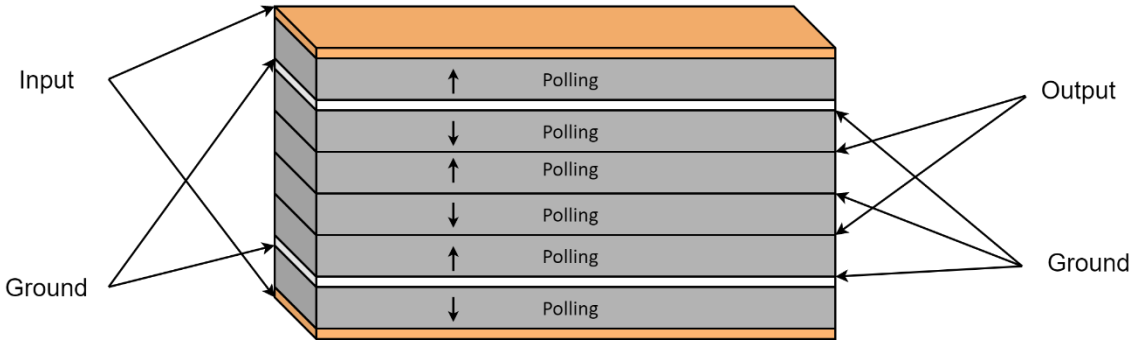

Fig. 2.10 – Square contour mode piezoelectric transformer designed by NEC [2.73], the white section is an insulation layer

A few months later a team at NEC developed a new contour mode PT, seen in Fig. 2.10 [2.73]. This design differed greatly from that presented by Yoo *et al.*, as it was a multilayer structure similar to the Transoner PT, however with circular internal electrodes. Layers of the PT were poled alternately in the thickness direction and the input section was split into two. As the contour vibration mode uses the planar coupling factor (k_p^2), a high-power density should be achieved. However, the device fabricated by this team was only able to produce a power density of 23W/cm^3, although, at an efficiency of 96.3%. As already mentioned, the issue with square shaped PTs is that several spurious modes are present in the device.

2.2.1.f) Thickness-Shear mode

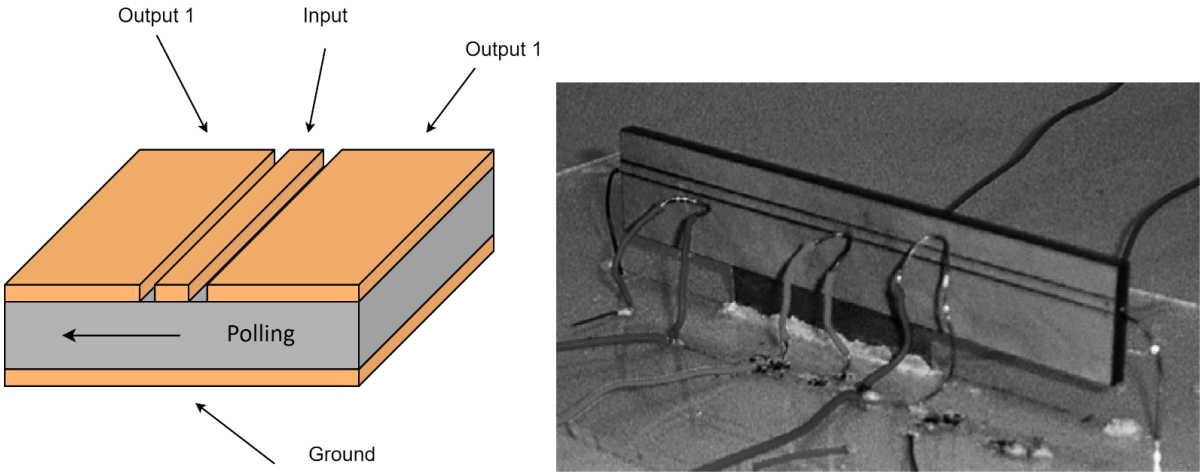

Fig. 2.11 – Thickness-shear vibration mode PT with dual output by Du [2.74]

Du *et al.* produced a thickness-shear vibration mode PT with a combined output of 163.1W, the highest power achieved by a PT published to date [2.74]. The device is a cuboid shape which is poled in the longitudinal direction. Rectangular electrodes were placed on top of the

device with differing sizes which make up the input and output sections, and a single electrode is placed on the bottom of the device as a common ground. The use of the thickness-shear electromechanical coupling (k_{15}^2) factor, which is typically the largest coupling factor in PZT, and designing the PT for good heat dissipation, allows the high-power output to be achieved at efficiencies of up to 95% [2.75]. However, due to the large size of this PT, the power density only equates to 16.9W/cm^3, lower than other topologies. This PT has many advantages over other topologies, most notably having several different outputs, at different voltages in a single PT design. Xu *et al.* performed some theoretical analysis on this topology of transformer, investigating all important electrical parameters [2.76].

2.2.1.g) Other PTs

Huang and Huang presented a circular flexural mode PT with a similar structure to the radial mode Transoner [2.77]. The group that proposed the PT also produced and verified an analytical model, performed parametric analysis to optimise the design [2.78] and derived and verified the equivalent circuit model [2.79], [2.80]. Although the transformer was designed with the purpose of creating a lower resonant frequency PT near to that of mains 50/60Hz, due to the transverse electromechanical coupling involved, the PT will have a lower power density compared to other PTs and the range of frequencies at which high efficiency operation occurs at is very narrow [2.77]. This makes the device difficult to use in a power converter as it would require precise control. A few other topologies have been proposed such as the annular PT by Uchino and Coc [2.81] and the rectangular Lamé mode PT [2.82].

Although in the past few decades progress has been made to improve power PTs, there is still room for significant improvement as the theoretical maximum power density of 300 W/cm^3 is a long way from what has been produced to date [2.83].

2.3 Piezoelectric materials for PTs

Early work on piezoelectric transformers used barium titanate but the introduction of lead zirconate titanate (PZT) gave forth to significant improvements in piezoelectric transformer performance [2.20]–[2.22]. The invention of ‘hard’ PZT materials improved important figures of merit for PTs such as coupling factor and Q factor, this consequently improved the quality of the devices being constructed [2.20]. Over time, the properties of PZT have continued to improve and so it has become the de facto standard. There are several papers presenting

adaptions on PZT using additional elements to improve properties of the piezoelectric specifically for PTs [2.23]–[2.28]. One of the difficulties of using PZT is the high temperature needed to co-fire the material and as such this limits the choice of electrode and insulation material that can be used. Gao investigated using CuO with PZT to reduce the co-firing temperature from 1240 to 930°C [2.29]. This addition, while still producing a PT of similar performance, allowed the use of an Ag/Pb electrode rather than the more expensive platinum electrodes typically used. Chung *et al.* had similar improvements on sintering temperature using $\mathrm{Li_2Co_3}$ and $\mathrm{Bi_2O_3}$ as aids [2.30].

Although PZT is still the most optimal material to make PTs, the dangers of lead are well known and as such lead-free alternatives have become more popular. Due to the requirements of PT materials (high Q factor and coupling factor) only a handful of papers have been published on making PTs out of lead-free piezoelectric. Lin *et al.* proposed the use of potassium sodium niobate (KNN), which is typically a soft piezoelectric, with MnO_2 and KCuTaO as aids in the sintering process in order to achieve a harder material [2.31]. This improved on work performed by the same authors, where a power density of only 6.9W/cm^3 was achieved [2.32]. Notable increases were seen in Q Factor from 215 to 1900, planar coupling factor increasing from 0.36 to 0.4, dissipation factor decreasing from 0.038 to 0.003 were observed over standard KNN material. A contour mode vibration PT (see 2.2.1.e) made using this material, of similar design to that presented by Yoo *et al.* [2.33], had a power density of 10W/cm^3 which, although lower than the PZT based PT of the same topology, was excellent for a lead-free solution.

Yang *et al.* used a $Na_{0.5}K_{0.5}NbO_3$ (NKN) piezoelectric manufactured again using a number of oxide aids to order to harden the piezoelectric properties [2.34]. The resulting material exhibited improved properties compared to Lin *et al*.'s [2.31] work, with an increase of 600 in Q factor, 0.017 in planar coupling factor and a reduction by a factor of 2 in dissipation factor. A ring-dot PT (see 2.2.1.b) made from this material exhibited a power density of 18.3W/cm^3 which is again is an improvement for lead-free PTs but is still much lower than the lead-based PT demonstrated by Yoo *et al.* [2.33]. The main reasons for the lower power densities achieved using lead-free solutions is due to the 30% lower coupling factor, higher resonant impedance (equivalent damping resistance) and significantly lower piezoelectric coefficients these materials exhibit compared to PZT [2.14], [2.34]. Yang *et al.* further proved the

effectiveness of NKN based PTs using a ring-dot PT to drive a 13W lamp, in the process achieving a whole converter efficiency of 82.4% [2.35]. Another possible lead-free material is $LiNbO_3$ and has excellent hard properties. As mentioned by Nakamura and Adachi, the polarization in $LiNbO_3$ is fixed to a particular direction making fabrication of most PT designs very difficult and so only designs requiring very high voltage outputs have used this material [2.36] – [2.38].

2.4 Spurious modes

One of the issues plaguing almost all PT topologies is the occurrence of spurious, unwanted vibration modes, as shown from the impedance spectra of a radial mode Transfer PT in Fig. 2.12. Spurious vibration modes can interfere with the optimum vibration mode of the PT, reducing the lifetime of the device and its energy transfer efficiency [2.39]. Therefore, one of the challenges PT designers must contend with is designing the PT in such a way as to limit the influence of these modes, whilst not affecting optimum mode performance [2.39], [2.84].

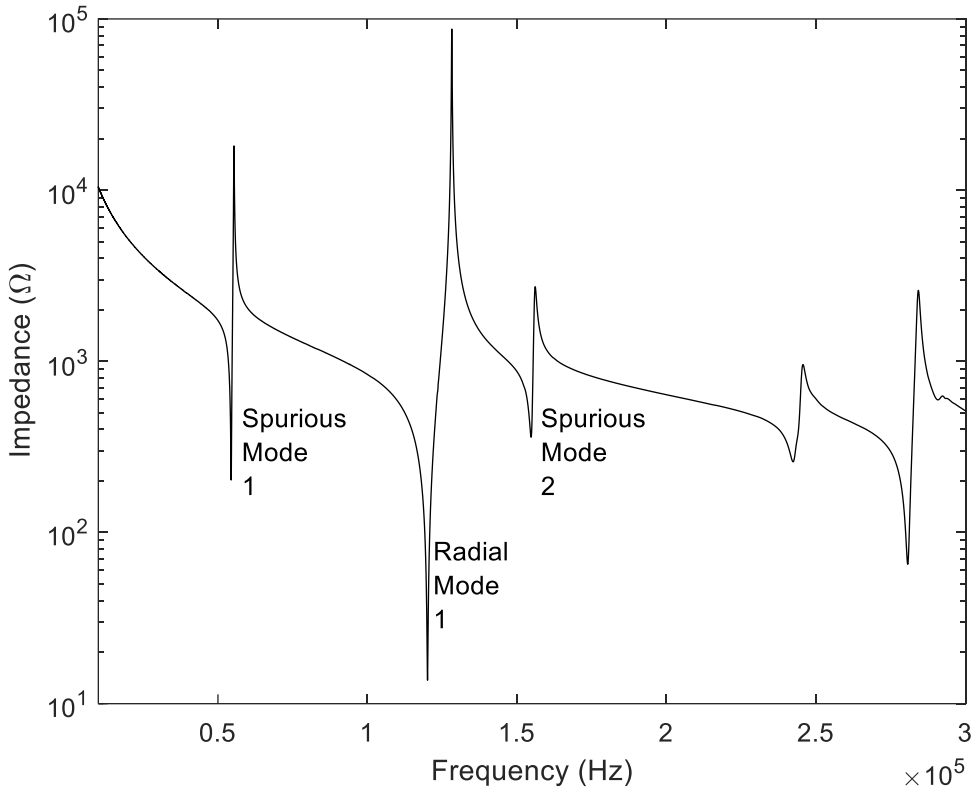

Fig. 2.12 – Input impedance spectra for a radial mode Transoner PT, highlighting the radial (optimum) and spurious modes

Researchers have taken a variety of approaches to avoid these interactions. One of the most popular methods for avoiding interference from spurious modes is by careful selection of the piezoelectric material used. Ohnishi *et al.* [2.43] created a thickness mode PT using lead titanate. A thickness mode PT would typically have to contend with spurious longitudinal vibrations influencing the performance of the PT. One of the key features of lead titanate is that it exhibits a k_t^2 coupling factor much larger than the k_{31}^2 coupling factor. Therefore, in a PT made from this material, spurious longitudinal vibrations (those in the '31' direction in 'ij' coordinates, see section 2.1.1) transfer less energy compared to thickness (t-direction) vibrations. Similarly, Prieto *et al.* [2.85] also proposed using lead titanate for reducing the effect of spurious modes. However, they found that the resulting devices had lower electromechanical coupling in the optimum vibration mode than those made from traditional PZT materials and therefore had reduced power density. To overcome the limitation, Prieto *et al.* proposed altering the shape of the PT, including adding a hole in the centre of the device, to reduce unwanted vibrations for PZT-based devices; however, their method requires careful design and appropriate mounting to avoid damping the vibration. Sanz *et al.* [2.86] used

interleaved electrodes to create a symmetrically designed Rosen PT. Although this method shows some good results, it is only applicable to certain topologies and, even then, reduces the design space for those topologies.

Chapter 4 will analyse spurious modes in greater detail and presents design rules for avoiding interaction between optimum and spurious modes.

2.5 Equivalent circuit characterisation and modelling

Owing to the electromechanical nature of PTs, thus the resonance being a mechanical property, it is not possible to directly measure the component values of the resonant circuit. This becomes a problem, especially for converter design where it is vital to be able to know the component values of the (equivalent) circuit, to determine suitability of the PT for the converter application, determine operating points and the expected performance of the converter. Additionally, component values for the PT also give insight into the quality of the PT and thus the expected losses the PT will exhibit. Therefore, it is common to use an electrical equivalent circuit to model the electrical behaviour of the PT, thus estimating the mechanical resonance as an electrical resonant tank circuit. The equivalent circuit for PTs is called the Mason equivalent circuit, named after its inventor. Whilst the equivalent circuit is known, as discussed it is not possible to directly measure the component values, as is typically done with electrical circuits. Therefore, several methods have been developed which allow the component values to be estimated using a variety of different measurement and algorithms.

Whilst measurement of the equivalent circuit properties of PTs is excellent when building PTs or during finite element analysis, estimation of these equivalent circuit properties at the design stage is vital for effective PT based converter design. Therefore, several authors have modelled the electromechanical properties of specific PT topologies, allowing the lumped equivalent circuit parameters to be estimated from the piezoelectric material properties and the geometry of the device. The equations derived using this modelling can then be used as part of a design algorithm to optimise the design of a PT for a specific application. Each of these topics will be discussed in more detail in the following sections.

2.5.1 Mason equivalent circuit

The Mason equivalent circuit was presented by Warren Mason in the 1940s [2.40]. Mason presented an equivalent circuit for the vibration of a single piezoelectric plate and showed how the impedances in this circuit can be approximated using inductors and capacitors. Mason then extended this analysis by presenting a similar equivalent circuit; however, this time he used two sets of plates, similar to the structure of a piezoelectric transformer. This equivalent circuit is shown in Fig. 2.13.

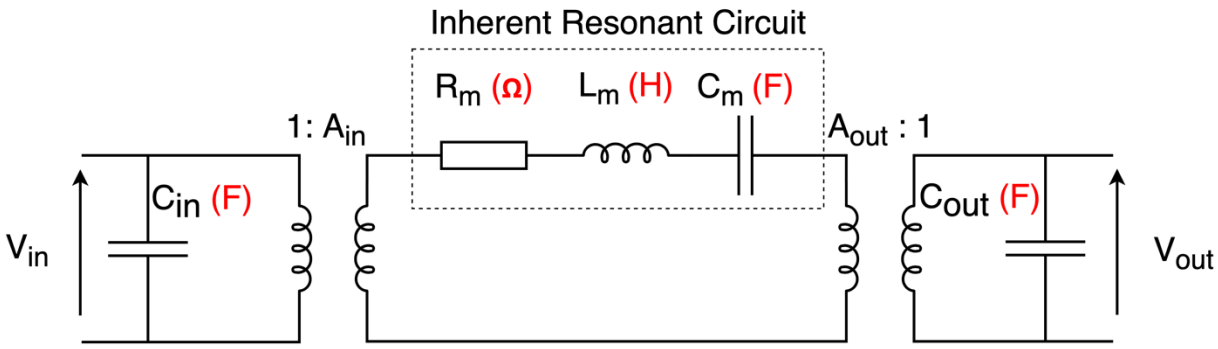

Fig. 2.13 – Two transformer form of the Mason equivalent circuit

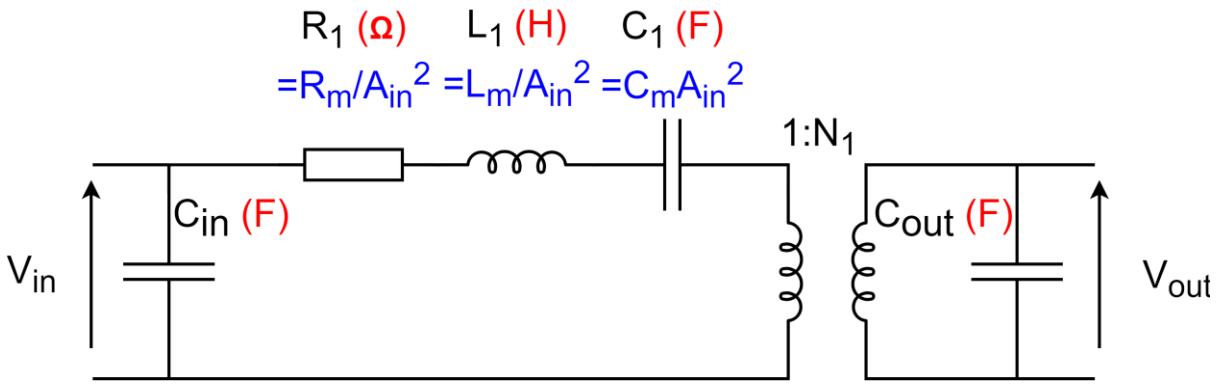

Fig. 2.14 – Single transformer form of the Mason equivalent circuit

The Mason equivalent circuit model can be used to approximate the electrical behaviour of any topology or type of PT when driven at a frequency close to one of its resonances. Importantly, it allows PTs to be analysed using traditional circuit analysis techniques. Fig. 2.13 and Fig. 2.14 show the two common forms of the Mason equivalent circuit. The circuit in Fig. 2.13 is the unsimplifed form of the Mason equivalent circuit, which has the advantage that the resonant current is equal to the vibration velocity of the PT, allowing electrical performance to be related to the mechanical vibration of the PT. This allows heat generation and by extension power density to be analysed. However, in many cases the single transformer form in Fig. 2.14, is more appropriate. The single ideal transformer Mason

equivalent circuit combines the input and output transformers (A_{in} and A_{out}) into a single transformer (N_1), making the circuit easier to analyse and significantly simpler to emulate.

The individual components of the equivalent circuit are linked to the physical properties of the PT. The input and output electrodes of the PT form parallel plate capacitors, giving rise to the input and output capacitances. The input transformer (A_{in}) models the transformation from electrical energy to mechanical energy. Similarly, the output transformer (A_{out}) models the transformation from mechanical energy to electrical energy. The LC components model the resonant behaviour of the PT and, whereas the input and output capacitances exist due to the presence of the input/output electrodes, the LC section is purely mechanical. Finally, the resistance R models the losses in the PT, made up of a combination of dielectric, mechanical and piezoelectric losses [2.87].

Whilst the equivalent circuit models in Fig. 2.13 and Fig. 2.14 allows the PT to be modelled around a single resonance, additional vibration modes can be represented by including additional RLC branches. This allows the performance of a PT to be electrically modelled over a wider frequency range. Lin [2.52] showed that to accurately model additional spurious modes, each RLC branch should have an additional ideal transformer connecting it to the output node. The resulting model for a PT with two vibration modes is presented in Fig. 2.15.

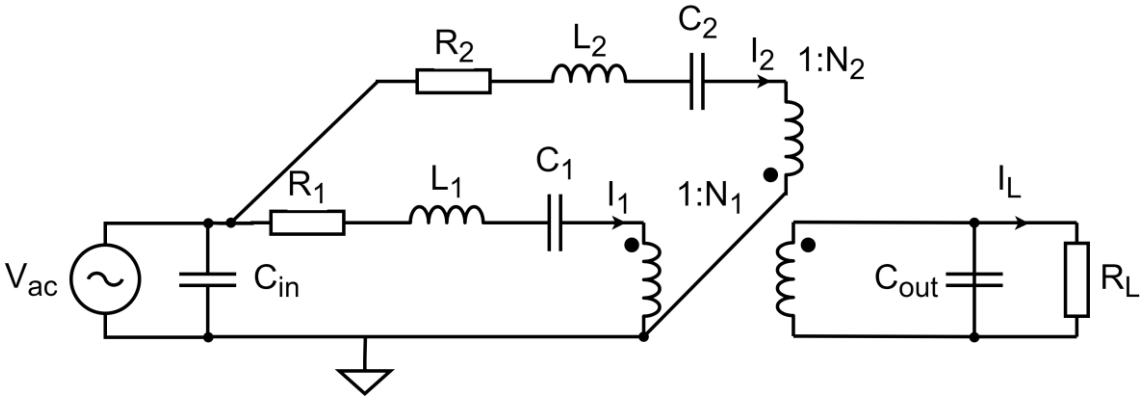

Fig. 2.15 – Extended Mason equivalent circuit, including additional RLC branches for modelling spurious modes

2.5.2 Equivalent circuit component value extraction

Equivalent circuit component value extraction is highly beneficial as it allows the simulation of PTs using traditional circuit analysis techniques and provides insight into the expected

performance of the PT. However, unlike traditional discrete components, these equivalent circuit values cannot be directly measured and, therefore, their values must be estimated.

Several authors have presented techniques for extracting equivalent circuit parameter values. Ivensky *et al.* [2.88] presented a technique, which uses separate input and output capacitance measurements, along with measurements of the Q-factor, conductance, anti-resonant and resonant frequencies to estimate the equivalent circuit component values. Horsely *et al.* used a curve-fitting approach with separate measurements of R and the input and output capacitances, to fit a theoretical gain-frequency curve to the measured curve, thus giving estimated equivalent circuit component values [2.89].

Chapter 3 will detail several new approaches to this topic, two of which improve on the work of Ivensky *et al.* and Horsely *et al.* and a novel technique. Then, building from this work a fourth method will be presented designed specifically for component extraction from high damping modes, such as spurious modes.

2.5.3 Transformation from geometry to equivalent circuit representation

The transformation from geometry to equivalent circuit representation, termed equivalent circuit modelling in this thesis, is an important step in the design process. It allows the electrical characteristics of a PT to be estimated for a given material, geometry and topology of PT. Equivalent circuit modelling is widely used in the study of piezoelectric transformers to allow traditional circuit analysis techniques to be used on PTs, without needing expensive FEA tools [2.90]. The work presented in Chapter 5 - Chapter 8 of this thesis will focus on the modelling efforts for the ring-dot and radial mode Transoner PTs.

2.5.3.a) Radial mode Transoner PT equivalent circuit modelling

Both Horsely and Lin [2.52], [2.91] have presented derivations of a lumped equivalent circuit model of the radial mode of the Transoner PT, providing equations for each of the components in the Mason equivalent circuit. In Horsley's case, this analysis included the effects of insulation and bonding layers on the resulting components values. Huang and Huang then proposed an improved equivalent circuit model [2.53], which, unlike previous models, included the effects caused by the thickness of the PT and so provided a more detailed and accurate model, albeit much more complex. However, whilst this topology has

been analysed when operated at its radial mode, no analysis has been presented analysing the spurious modes of this device.

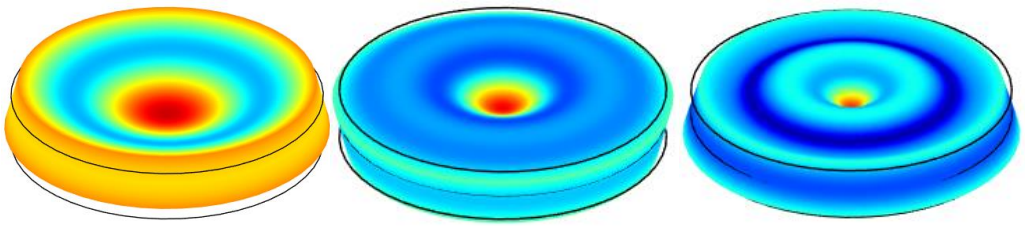

Fig. 2.16 – First 3 flexural modes occuring in the radial mode Transoner PT, colour scheme shows displacement

Forrester *et al.* performed some initial analysis on the spurious modes occurring in the Transoner PT and determined that they are 'Flexural' vibrations [2.92]. Whilst flexural modes have not been analysed in the Transoner PT specifically, they have been widely analysed in elastic and piezoelectric plates/devices over the last century, with Kirchhoff and Mindlin providing key contributions to this topic. Kirchhoff presented a 'thin' plate theory (classic plate theory (CPT)), which makes several assumptions in order to simplify the vibration analysis [2.17]. However, owing to these assumptions, the flexural mode shapes and frequencies derived using this model are only accurate for 'thin' devices (radius >> thickness). Mindlin extended on the CPT, by removing some of these assumptions, adding complexity by accounting for shear deformation, thus improving the accuracy of the estimated mode shapes and frequencies for 'thicker' devices [2.93], [2.94]. Shear deformation of a plate is shown in Fig. 2.17. Leissa [2.18] presented a detailed research paper showing a summary of the solutions for the natural frequencies and mode shapes for a variety of elastic plates, analysed using both Kirchhoff's and Mindlin's plate theories.

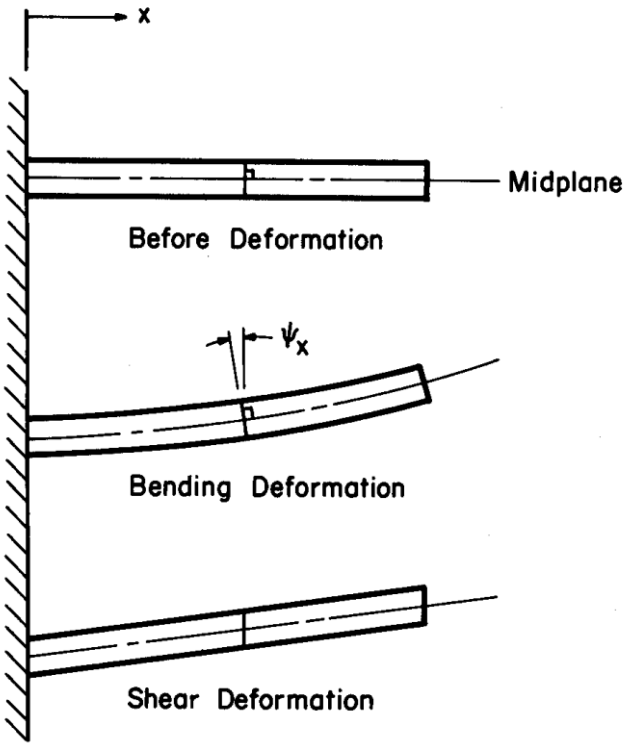

Fig. 2.17 – Diagram showing bending and shear deformation of a 1D plate [2.18]

Flexural modes have been analysed in piezoelectric devices similar to the radial mode PT. Wang *et al*. [2.95] published one of the most important contributions, analysing a device with 2 piezoelectric layers bonded to an elastic host plate, deriving equations for displacement, resonant frequency and electric field shape across the device. Many other authors have analysed the vibration of similar piezoelectric based devices using both Kirchhoff and Mindlin plate theory [2.96]–[2.102].

Whilst most of the work on these types of devices has been based on analysing the resonant frequencies and mode shapes, some authors have extended the analysis to derive lumped equivalent circuit models. Sammoura *et al.* [2.103] analysed a PMUT, a device with a similar structure to the radial mode PT but with a different electrode configuration and on a macroscopic scale. Sammoura *et al.* analysed the mechanical and electrical properties of the PMUT device in a similar way to Horsely and Lin for the radial mode of the Transoner PT, thus, similarly allowing the equivalent circuit components to be estimated. A number of other authors have presented similar derivations for similar devices [2.104]–[2.106]. Yaung [2.77], presented an equivalent circuit derivation for a circular flexural mode PT with a similar structure to the radial mode PT using Hamilton's principal. However, this PT differs from the

radial mode PT as the structure is symmetrical around the thickness mid-point and has exclusively 2 layers in the input and output sections.

Chapter 5 and Chapter 6 will present two lumped equivalent circuit models for the flexural modes occurring in the Transoner PT. These models will be derived using both Kirchhoff and Mindlin plate theories.

2.5.3.b) Ring-dot PT equivalent circuit modelling

Unlike the Transoner, no author has presented the derivation of a full lumped equivalent model for the radial vibration mode of the ring-dot PT. However, authors have analysed certain aspects of the ring-dot topology. Pulpan *et al.* [2.107], [2.108] developed a model of the voltage gain and electrical efficiency of the ring-dot PT. Ho [2.109] modelled the ring-dot PT using Hamilton's principle, allowing them to generate equations for the electrical performance of the PT, including input power, electrical efficiency, gain and equations for each of the equivalent circuit parameters. However, the author does not provide solved equations for the equivalent circuit parameters but leaves them in integral form, meaning it would require significant work from a reader to produce equations for each of the lumped equivalent circuit components in the Mason equivalent circuit. A key issue with the modelling performed by both Pulpan *et al.* and Ho, is the lack of modelling of the 'gap' region (the region between dot and ring electrodes). Additionally, none of the authors of these papers provide simplified, lumped equations for each of the equivalent circuit components in the Mason equivalent circuit.

Chapter 8 details the derivation of a lumped equivalent circuit model for the radial mode of the ring-dot PT.

2.6 Piezoelectric transformer based resonant converters

Resonant converters are a popular application of PTs and, as a result, there is a large amount of literature devoted to this topic. When designing a PT-based power converter, several elements need to be carefully designed these include: choosing a suitable driving topology, designing a suitable PT, choosing a control method and circuitry and if required, appropriate rectification and filtering. Whilst control, rectification and filtering are beyond the scope of this body of work, it is vitally important that converter topolgy is considered when designing

a PTs. Firstly, this is because the converter topology will provide different input voltage amplitudes and waveforms which needed to be factored in to the PT design. Secondly and most importantly, as ZVS is desired in resonant converters, and owing to the difficultly in achieving ZVS with PTs (owing to the relativity large parallel capacitances), different specifications of PT will be required for different topologies.

2.6.1 Inductor based converter topologies

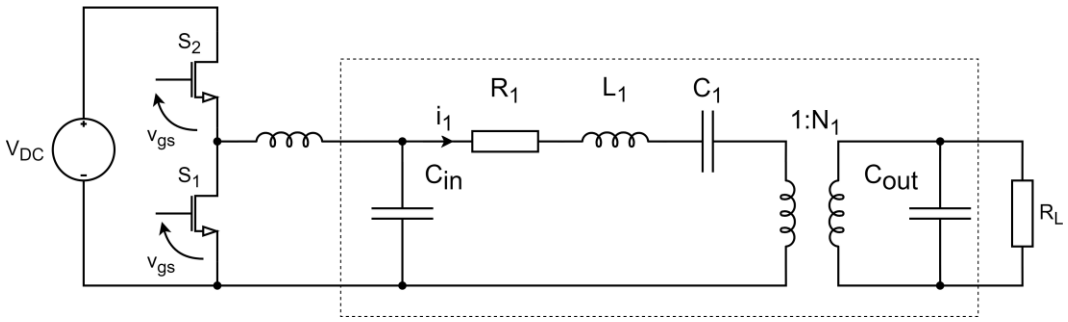

Fig. 2.18 – Half Bridge

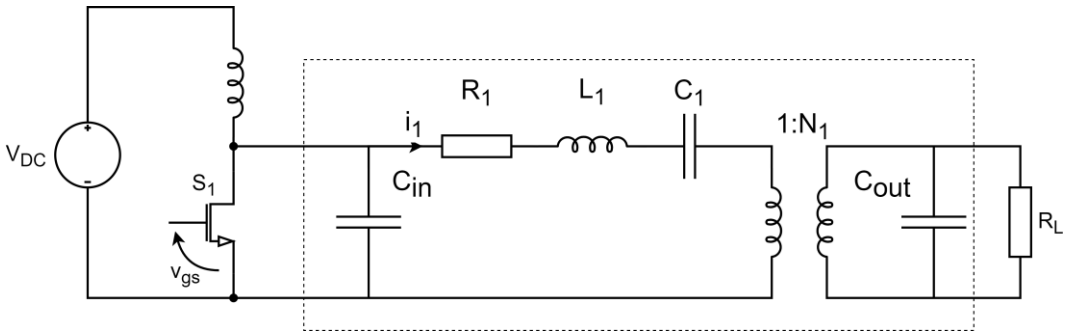

Fig. 2.19 – Class E

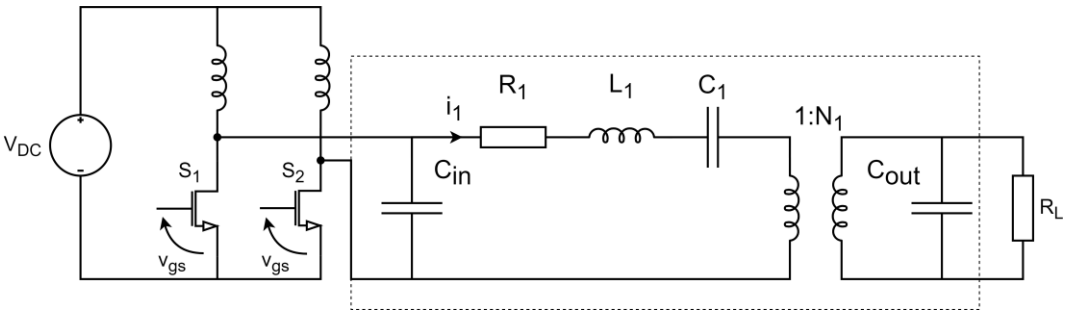

Fig. 2.20 – Push Pull

When deciding on a topology there are 3 popular options for PT based converters, push-pull, half-bridge, and class-E. While the push-pull topology is most suited to step-up applications, the half-bridge and class-E designs are best suited for use in a step-down converter [2.110].

The push-pull circuit has some advantages, including fewer harmonics on the input voltage to the PT due to the filtering [2.111].

Half-bridge and class-E are the most common driving topologies seen in PT based converters. The main difference between the two topologies is that the class-E design uses a single transistor, and the half-bridge requires two transistors, adding to cost and control complexity. Yang *et al.* investigated the two topologies as part of two identical PT converters [2.112]. In their testing they found that the class-E converter has a wider input voltage range and less parameter sensitivity, with the half-bridge operating much more efficiently (almost 30% increase) and requiring a smaller input inductor to achieve ZVS.

2.6.2 Inductorless converter topologies

One of the advantages of PTs is that they have no inherent magnetics and as such can operate in applications where magnetic components cannot. However, the converter topologies discussed in the previous sections have used additional inductors, thus eliminating one of the main advantages of PTs. Whilst the class-E and push-pull topologies require inductors, the half-bridge can be implemented without an inductor, as shown in Fig. 2.21.

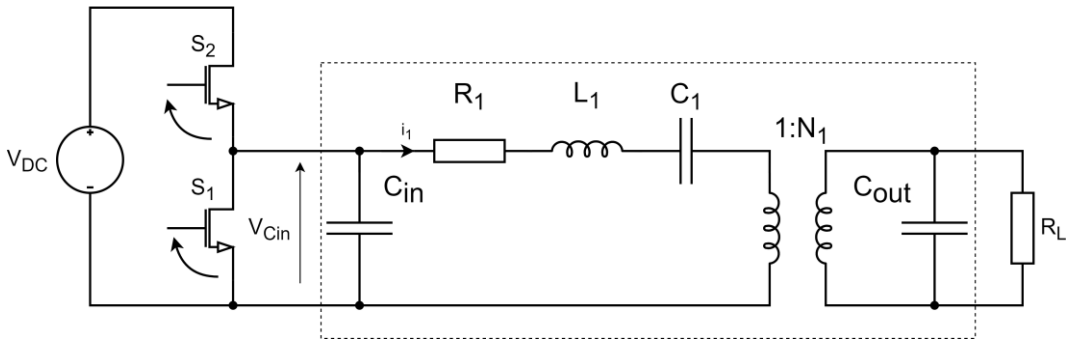

Fig. 2.21 – Inductorless half bridge

One of the challenges of using the half bridge topology without an inductor is that achieving ZVS is significantly more difficult, as the input capacitor is charged/discharged by the resonant current alone, rather than with the assistance of the additional inductor. The circuit is operated by driving the two switches (S_1 and S_2) with 25% duty square waves, in anti-phase. Then, with appropriate PT design, during the deadtime (S_1 and S_2 both off) the resonant current i_1 will charge/discharge the input capacitor allowing the next switching event to occur with 0V across the relevant switch, thus, achieving zero voltage switching (ZVS). The zero-voltage switching behaviour of this topology has been the subject of several analyses [2.49],

[2.113], [2.114]. From these analyses, several models for predicting the ZVS behaviour of PTs have been proposed, with Mayer *et al.* presenting a parametric analysis, and Horsley *et al.* and Foster *et al.* presenting models based on cyclic mode analysis [2.115]–[2.117]. While these models allow the ZVS behaviour of PTs to be predicted, they require significant computation. Authors searched for a simplified expression for ensuring ZVS behaviour in inductor-less designs. Mayer *et al.* derived an equation for the ZVS ability of a PT in terms of only the input and output capacitors, the turns ratio and efficiency [2.115]. While this was simple, it was found to be inaccurate and under predicted the ZVS behaviour [2.118]. Rødgaard *et al.* presented an empirical analysis of the ZVS factor by simulating a sample PT and varying the value of the input capacitor, while using Mayer *et al.*'s equation as a starting point for determining capacitor values [2.118]. This provided an improved but still simple equation, in terms of the same parameters as Mayer *et al.*'s, which agreed with experimental results. Further improving on this, Foster *et al.* presented a purely theoretical analysis using an approximated driving function for $v_{C_{\mathrm{in}}}$. This method further improved on the equation derived by Rødgaard *et al.*, by finding that under certain driving conditions (25% duty cycle, sinusoidal resonant current, negligible losses) and if the input to output capacitance ratio is designed to be less than $2/\pi$, then ZVS could always be achieved irrespective of the load resistance [2.119]. Additionally, as part of this analysis, Foster *et al.* presented equations for K_{ZVS} (proportion of the input DC voltage that the voltage across the input capacitor reaches at the end of the deadtime before the high-side (S_2) MOSFET turns on), allowing the ZVS performance of any PT to be simulated.

As a result of the advantages of the inductorless topology, most of the research on PT based converters published in recent years has been based on the inductorless half bridge.

2.7 Design of PTs for power converter applications

Several authors have previously presented methods for designing PTs for specific applications. Vasic *et al.* [2.120] presented a design method for two-layer thickness mode PTs for use in gate drive circuits. The dimensions of the device are designed by first using the desired operating frequency to determine the total thickness. Then, the area of the PT and the thickness ratio are chosen to ensure the PT is as small as possible, while achieving the desired output power and voltage gain, and ensuring heat (and thus losses) is below a desired

level. Baker *et al.* [2.50] presented a similar method for designing radial mode PTs for use in half-bridge converters. Firstly, the radius is designed based on the desired operating frequency. Then, using this frequency the output capacitance can be matched to the load, by designing the output layer thickness and number of output layers. Finally, the input layer thickness and number of input layers is chosen to ensure ideal gain, efficiency and zero voltage switching performance. This is achieved by varying the number of layers and layer thicknesses in the input section, evaluating each of these electrical quantities and determining the most appropriate design. Huang *et al.* [2.51] again proposed a very similar method, however, they also tried to achieve unity power factor, whilst still trying to optimise gain, efficiency and ZVS. Although this type of approach can lead to optimal designs, by selecting the radius, output layers and thickness at the start, then using only the input layer thickness and number of layers to control three/four key quantities may mean designs often are not possible as the design space is so restricted, as can be seen in Fig. 9 of [2.51]. Additionally, an exhaustive search method such as this, can be slow to execute.

Forrester *et al.* [2.121], presented a simplified, rule-based method for designing multi-layer radial mode PTs for use in half-bridge converters. First, the turns ratio was chosen to achieve the desired output voltage. Then, the input to output thickness ratio was chosen to ensure the critical criterion derived by Foster *et al.* [2.122] was adhered to. Then, the layer thicknesses can be determined based on the desired total device thickness, the thickness ratio, and the number of input/output layers. Although, this method assumes that the PT will be operated at the series resonance (LC resonance) to achieve the correct voltage. However, in most cases ZVS will not be achieved at the series resonance but rather at the total system resonance (resulting from the combination of LC, C_{out} and R_L). Therefore, in some cases, ZVS and desired output voltage cannot be achieved at the same frequency. Additionally, this method does not consider efficiency or vibration velocity and therefore, the chosen design may not be the global optimum device.

Sanchez *et al.* [2.123] presented an approach for designing thickness-mode PT by first using similar analytical methods to Vasic *et al.* and Baker *et al.* to generate an initial design for the material, area, thickness, and number of layers. Then, using a finite element analysis (FEA) method to improve upon this design by choosing the best PT shape (disc, ring, plate) and evaluating additional parameters such as spurious modes and the effect of manufacturing

tolerance on the design. Whilst FEA methods provide good accuracy, they are relatively slow, expensive and require lots of manual interaction from an experienced designer to achieve a good design.

Seo *et al.* [2.72] used a genetic algorithm approach to optimise the design of a contour-mode PTs. The inner-radius, outer-radius and outer length of the PT were variables in this approach, with the algorithm aiming to optimise the output impedance matching to the load and the electro-mechanical coupling. Using FEA methods, each PT is simulated to calculate these output variables. The genetic algorithm then, based on the results, optimises, and improves upon the PT design over multiple generations, finally presenting the device with the most optimal output impedance and electro-mechanical coupling factor. However, the author claims higher coupling factors give PTs a greater chance of achieving ZVS, as pointed out in [2.122] this is not strictly true. Additionally, the author does not explicitly consider output voltage or efficiency, therefore there is no guarantee a device designed by this method will be optimal for a given application. Finally, as mentioned previously, while FEA methods are an excellent tool to use during the design process, they have several downsides and especially in this application, the speed of FEA methods will limit the number of devices analysed and/or the speed of the algorithm.

Authors have applied genetic algorithms to similar applications using equation-based models, rather than FEA, removing the speed limitation and showing excellent results. These applications included motor design [2.124], efficiency optimisation of a wireless power transfer system [2.125], and LCLC and LCC resonant converters [2.126], [2.127].

Chapter 10 will combine the work developed in Chapters 3-8 into an automated genetic algorithm-based PT designer.

2.8 High temperature power conversion

There are several potential applications of high temperature converters. For example, in Oil and geothermal wells for power logging and monitoring tools at temperatures of up to 250°C and 350°C respectively; Electric and conventional vehicles, powering the motors and sensors at up to 300 °C and in the aerospace industry for the control circuitry, for motor and breaking controls and simplifying the electrical design, at temperatures of up to 350°C [2.128], [2.129].

The reliance on silicon devices with a maximum temperature of 150°C meant that high temperature electronics previously was not possible. However, in recent years, the advent of SiC and GaN devices, with their increased temperature capability and performance, has opened the door to high temperature power electronics. Several authors have published results of SiC [2.130]–[2.133] and GaN [2.134]–[2.136] power devices operating at temperatures of >200°C, with minimal degradation of performance compared to room temperature. The issue currently with SiC and GaN MOSFETs is lack of high temperature packaging for the devices [2.137], [2.138].

Authors have built and validated the performance of high temperature converters, combining multiple high temperature elements. Ray *et al.* validated the use of SiC devices as part of a high temperature (up to 200°C) boost converter [2.139]. The SiC MOSFET and diode were heated at temperatures of up to 200°C with minimal effect on converter performance. However, the converter relied on low temperature passive components and drive circuitry to function. Funaki *et al.* built a high temperature buck converter using SiC MOSFETs and diodes, and a high temperature inductor [2.140]. The converter (only MOSFETs, diodes and inductor were heated) was validated from room temperature up to 400°C. It was noted that whilst the converter efficiency dropped with temperature, the converter was still able to output around 20W at an efficiency of greater than 80% at 400°C. Perrin *et al.* built a GaN-based flyback converter with ZVS operation, where all elements including control circuitry and passive components were made from high temperature materials [2.141]. The converter was able to operate at temperatures of up to 200°C, with a 2W output at a maximum efficiency of 75%.

One of the main challenges when building a high-temperature converter is the availability of high-temperature passive components. There are several commercially available high temperature magnetic materials, allowing transformers and inductors to be fabricated with operating temperatures of up to 600°C, however, with inferior properties compared to classical materials. Dubois *et al.* summarised and tested several state-of-the-art high-temperature magnetic materials by building transformers for use in SiC JFET control circuitry [2.142].

Whilst high temperature capacitors are available for operation at up to 250°C, they typically have higher losses, lower capacitance, and lower voltage rating [2.143]. Alberta *et al.* developed a high temperature dielectric which was able to operate at temperatures

exceeding 400°C [2.144]. Colmenares *et al.* built and tested SiC based capacitators and inductors with operating temperatures of up to 300°C and 700°C respectively [2.145]. However, whist both authors present improvements in temperature over traditional devices, the maximum capacitance is still limited.

2.9 High temperature piezoelectric materials

Bismuth-based piezoelectrics are the most popular high temperature piezoelectrics [2.146]. Some popular options are bismuth ferrite and bismuth titanate, and additionally lead metaniobate. However, whilst operation at temperatures greater than 200 ^{o}C is possible with these materials, typical properties of high temperature piezoelectrics are poor for use in PTs [2.146]–[2.149]. A promising option is bismuth scandium lead titanate (BSPT) [2.150]. BSPT offers a high d_{33} constant of 450pm/V and a large planar coupling factor (k_p^2) of 0.56 similar to that of PZT, therefore, providing a potentially good alternative to PZT for use at temperatures up to 350°C [2.150]. Chapter 9 will examine the use of BSPT for making high performance PTs for use in high ambient temperatures.

2.10 Summary

From the findings of this review, PT based power supplies are truly multiphysics and therefore a multidisciplinary approach is required to design them. This thesis aims to simply the design process by developing genetic algorithm-based design optimisation software, that optimises the PT geometry to meet an electrical specification, maximise efficiency and whilst also accounting for spurious modes. The design software is presented in Chapter 10, with Chapter 5, Chapter 6 and Chapter 8 presenting lumped equivalent circuit models that the designer is built on top of, with the analysis in Chapter 4 allowing spurious mode effects to be considered. The equivalent circuit extraction methods presented in Chapter 3, will be used throughout this body of work in the design software and to allow experimental verification of the several model that are developed. Chapter 9 explores the use of PTs in high temperature environments using a specialist high temperature piezoelectric, BSPT.

2.11 References

[2.1] 'IEEE Standard on Piezoelectricity', ANSI/IEEE Std 176-1987, 1988, doi: 10.1109/IEEESTD.1988.79638.

[2.2] P. C. GmbH, 'Fundamentals of Piezo Technology'. https://www.piceramic.com/en/piezo-technology/fundamentals/ (accessed Jun. 30, 2021).

[2.3] W. G. Cady, *Piezoelectricity: an introduction to the theory and applications of electromechanical phenomena in crystals*. New York, NY: McGraw-Hill, 1946.

[2.4] '4.1: Unit Cells', *Chemistry LibreTexts*, Jul. 20, 2018. https://chem.libretexts.org/Courses/Oregon_Institute_of_Technology/OIT%3A_CHE_201_-_General_Chemistry_I_(Anthony_and_Clark)/Unit_4%3A_Quantifying_Chemicals/4.1%3A_Unit_Cells (accessed Jun. 30, 2021).

[2.5] R. S. Dahiya and M. Valle, *Robotic tactile sensing: technologies and system*. Dordrecht ; New York: Springer, 2013.

[2.6] H. Shifeng, C. Jun, L. Futian, L. Lingchao, Y. Zhengmao, and C. Xin, 'Poling process and piezoelectric properties of lead zirconate titanate/sulphoaluminate cement composites', *Journal of Materials Science*, vol. 39, no. 23, pp. 6975–6979, Dec. 2004, doi: 10.1023/B:JMSC.0000047540.71855.3a.

[2.7] 'Stress Equation Defintion - Strength (Mechanics) of Materials - Engineers Edge'. https://www.engineersedge.com/material_science/stress_definition.htm (accessed Jun. 30, 2021).

[2.8] 'Stress and Strain - Definition, Stress-Strain Curve, Hooke's Law, SI Units', *BYJUS*. https://byjus.com/physics/stress-and-strain/ (accessed Jun. 30, 2021).

[2.9] 'Modulus of Elasticity - Definition, Young's Modulus, Formula, Unit, FAQs', *BYJUS*. https://byjus.com/physics/youngs-modulus-elastic-modulus/ (accessed Jun. 30, 2021).

[2.10] M. S. and E. Ph. D., C. B. A., and C. S. B. A., 'What Is an Electric Field?', *ThoughtCo*. https://www.thoughtco.com/electric-field-4174366 (accessed Jun. 30, 2021).

[2.11] 'Electric Displacement- Dielectric Materials, Vacuum Permittivity', *BYJUS*. https://byjus.com/physics/electric-displacement/ (accessed Jun. 30, 2021).

[2.12] 'Tensors, Stress, Strain, Elasticity', *Mineral Physics*. https://serc.carleton.edu/NAGTWorkshops/mineralogy/mineral_physics/tensors.html (accessed Jun. 30, 2021).

[2.13] 'Mechanics of Materials: Stress'. https://www.efunda.com/formulae/solid_mechanics/mat_mechanics/stress.cfm (accessed Jun. 30, 2021).

[2.14] E. Horsley, 'Modelling and Analysis of Radial Mode Piezoelectric Transformers and Inductor-less Resonant Power Converters', University of Sheffield, 2011.

[2.15] T. Ikeda, *Fundamentals of piezoelectricity*. Oxford ; New York: Oxford University Press, 1990.

[2.16] 'Piezoelectric Materials: Understanding the Standards', *COMSOL Multiphysics*. https://uk.comsol.com/blogs/piezoelectric-materials-understanding-standards/ (accessed Feb. 25, 2021).

[2.17] J. N. Reddy, *Theory and analysis of elastic plates*. Philadelphia, PA: Taylor & Francis, 1999.

[2.18] A. W. Leissa, 'Vibration of Plates', OHIO STATE UNIV COLUMBUS, 1969. Accessed: Jan. 08, 2018. [Online]. Available: http://www.dtic.mil/docs/citations/ADA307623

[2.19] E. Ventsel and T. Krauthammer, *Thin plates and shells: theory, analysis, and applications*. New York: Marcel Dekker, 2001.

[2.20] V. Carazo and Alfredo, 'Piezoelectric Transformers: An Historical Review', *Actuators*, vol. 5, no. 2, p. 12, Apr. 2016, doi: 10.3390/act5020012.

[2.21] G. Shirane and K. Suzuki, 'Crystal Structure of Pb(Zr-Ti)O_3', *J. Phys. Soc. Jpn.*, vol. 7, no. 3, pp. 333–333, May 1952, doi: 10.1143/JPSJ.7.333.

[2.22] C.-H. Hong *et al.*, 'Lead-free piezoceramics – Where to move on?', *Journal of Materiomics*, vol. 2, no. 1, Mar. 2016, doi: 10.1016/j.jmat.2015.12.002.

[2.23] J.- Yoo *et al.*, 'Piezoelectric properties of PNW-PMN-PZT ceramics for high power piezoelectric transformer', in *ISAF 2000. Proceedings of the 2000 12th IEEE International Symposium on Applications of Ferroelectrics (IEEE Cat. No.00CH37076)*, Jul. 2000, vol. 1, pp. 495–498 vol. 1. doi: 10.1109/ISAF.2000.941605.

[2.24] S. M. Hwang *et al.*, 'Piezoelectric and dielectric properties of Pb($Ni_1$3$Nb_2$3)O_3-Pb($Mn_1$3$Nb_2$3)O_3-Pb(Zr,Ti)O_3/ ceramics for piezoelectric transformer', in *Proceedings of the 13th IEEE International Symposium on Applications of Ferroelectrics, 2002. ISAF 2002.*, Jun. 2002, pp. 367–370. doi: 10.1109/ISAF.2002.1195945.

[2.25] N.-C. Mun, S.-D. Lee, J.-S. Lee, Y.-H. Jeong, and Y.-S. Kim, 'The electrical properties of piezoelectric transformers using PMS-PZ-PT ceramics [for LCD backlights]', in *Proceedings KORUS 2000. The 4th Korea-Russia International Symposium On Science and Technology*, Jun. 2000, vol. 3, pp. 394–397 vol. 3. doi: 10.1109/KORUS.2000.866120.

[2.26] Y.-D. Hou, M.-K. Zhu, C.-S. Tian, and H. Yan, 'Structure and electrical properties of PMZN–PZT quaternary ceramics for piezoelectric transformers', *Sensors and Actuators A: Physical*, vol. 116, no. 3, pp. 455–460, Oct. 2004, doi: 10.1016/j.sna.2004.05.012.

[2.27] H. Li, Z. Yang, X. Zong, and Y. Chang, 'High electrical properties of W-additive Mn-modified PZT–PMS–PZN ceramics for high power piezoelectric transformers', *Materials Science and Engineering: B*, vol. 130, no. 1, pp. 288–294, Jun. 2006, doi: 10.1016/j.mseb.2006.02.061.

[2.28] L. Kozielski, A. Lisińska-Czekaj, and D. Czekaj, 'Graded PZT ceramics for piezoelectric transformers', *Progress in Solid State Chemistry*, vol. 35, no. 2, pp. 521–530, Jan. 2007, doi: 10.1016/j.progsolidstchem.2007.01.030.

[2.29] X. Gao, Y. Yan, A. V. Carazo, S. Dong, and S. Priya, 'Low-Temperature Co-Fired Unipoled Multilayer Piezoelectric Transformers', *IEEE Transactions on Ultrasonics, Ferroelectrics, and Frequency Control*, vol. 65, no. 3, pp. 513–519, Mar. 2018, doi: 10.1109/TUFFC.2017.2785356.

[2.30] K. H. Chung *et al.*, 'Effects of Li_2CO_3 and Bi_2O_3 additives on sintering temperature and piezoelectric properties of PNIN-PCW-PZT ceramics for multilayer piezoelectric transformer', in *14th IEEE International Symposium on Applications of Ferroelectrics, 2004. ISAF-04. 2004*, Aug. 2004, pp. 262–265. doi: 10.1109/ISAF.2004.1418386.

[2.31] D. Lin, M. S. Guo, K. H. Lam, K. W. Kwok, and H. L. W. Chan, 'Lead-free piezoelectric ceramic $(K_{0.5}Na_{0.5})NbO_3$ with MnO_2 and $K_{5.4}Cu_{1.3}Ta_{10}O_{29}$ doping for piezoelectric transformer application', *Smart Mater. Struct.*, vol. 17, no. 3, 2008, doi: 10.1088/0964-1726/17/3/035002.

[2.32] M. Guo, D. M. Lin, K. H. Lam, S. Wang, H. L. W. Chan, and X. Z. Zhao, 'A lead-free piezoelectric transformer in radial vibration modes', *Review of Scientific Instruments*, vol. 78, no. 3, Mar. 2007, doi: 10.1063/1.2712795.

[2.33] J. Yoo, K. Yoon, S. Hwang, S. Suh, J. Kim, and C. Yoo, 'Electrical characteristics of high power piezoelectric transformer for 28 W fluorescent lamp', *Sensors and Actuators A: Physical*, vol. 90, no. 1, pp. 132–137, May 2001, doi: 10.1016/S0924-4247(01)00454-X.

[2.34] S. Yang, C. Tsai, Y. Liou, C. Hong, B. Li, and S. Chu, 'Effects of improved process for CuO-Doped NKN lead-free ceramics on high-power piezoelectric transformers', *IEEE Transactions on Ultrasonics, Ferroelectrics, and Frequency Control*, vol. 58, no. 12, pp. 2555–2561, Dec. 2011, doi: 10.1109/TUFFC.2011.2118.

[2.35] S. Yang, S. Chen, C. Tsai, C. Hong, and S. Chu, 'Fabrication of high-power piezoelectric transformers using lead-free ceramics for application in electronic ballasts', *IEEE Transactions on Ultrasonics, Ferroelectrics, and Frequency Control*, vol. 60, no. 2, pp. 408–413, Feb. 2013, doi: 10.1109/TUFFC.2013.2577.

[2.36] K. Nakamura and Y. Adachi, 'Piezoelectric transformers using LiNbO3 single crystals', *Electronics and Communications in Japan (Part III: Fundamental Electronic Science)*, vol. 81, no. 7, Jul. 1998, doi: 10.1002/(SICI)1520-6440(199807)81:7<1::AID-ECJC1>3.0.CO;2-O.

[2.37] P. Norgard and S. D. Kovaleski, 'A Lithium Niobate Piezoelectric Transformer Resonant High-Voltage Power Source', *IEEE Transactions on Plasma Science*, vol. 44, no. 5, pp. 808–815, May 2016, doi: 10.1109/TPS.2016.2548427.

[2.38] J. A. VanGordon *et al.*, 'Characterization of high-voltage lithium niobate piezoelectric transformers', in *2014 IEEE International Power Modulator and High Voltage Conference (IPMHVC)*, Jun. 2014, pp. 580–583. doi: 10.1109/IPMHVC.2014.7287342.

[2.39] K. Brebøl, 'Piezoelectric transformer', US6707235B1, Mar. 16, 2004 Accessed: Mar. 19, 2018. [Online]. Available: https://patents.google.com/patent/US6707235B1/en

[2.40] W. P. Mason, *Electromechanical Transducers and Wave Filters*. D. Van Nostrand Company, 1948.

[2.41] E. Wells, 'Comparing magnetic and piezoelectric transformer approaches in CCFL applications', p. 7, 2002.

[2.42] C. A. Rosen, 'Electromechanical transducer', US2974296A, Mar. 07, 1961 Accessed: Sep. 10, 2018. [Online]. Available: https://patents.google.com/patent/US2974296/en

[2.43] O. Ohnishi, H. Kishie, A. Iwamoto, Y. Sasaki, T. Zaitsu, and T. Inoue, 'Piezoelectric ceramic transformer operating in thickness extensional vibration mode for power supply', in *IEEE 1992 Ultrasonics Symposium Proceedings*, Oct. 1992, pp. 483–488 vol.1. doi: 10.1109/ULTSYM.1992.275961.

[2.44] A. V. Carazo, 'Multilayer piezoelectric transformer', US6614144B2, Sep. 02, 2003 Accessed: Jul. 02, 2018. [Online]. Available: https://patents.google.com/patent/US6614144B2/en#nplCitations

[2.45] P. Valenta, V. Koucký, and J. Hammerbauer, 'Piezoelectric transformer for high-side MOSFET driver supplying', in *2017 18th International Scientific Conference on Electric Power Engineering (EPE)*, May 2017, doi: 10.1109/EPE.2017.7967265.

[2.46] L. Le, Y. Yang, and M. Radecker, 'Low profile LED off-line phase-cut dimming ballast with piezoelectric transformer', in *2015 IEEE Industry Applications Society Annual Meeting*, Oct. 2015, doi: 10.1109/IAS.2015.7356873.

[2.47] A. P. Rane and T. N. Date, 'Design and simulation of piezoelectric transformer based LED driver', in *2016 International Conference on Global Trends in Signal Processing, Information Computing and Communication (ICGTSPICC)*, Dec. 2016, pp. 660–662. doi: 10.1109/ICGTSPICC.2016.7955384.

[2.48] F. E. Bisogno, S. Nittayarumphong, M. Radecker, A. V. Carazo, and R. N. do Prado, 'A Line Power-Supply for LED Lighting using Piezoelectric Transformers in Class-E Topology', in *2006 CES/IEEE 5th International Power Electronics and*

Motion Control Conference, Aug. 2006, vol. 2, doi: 10.1109/IPEMC.2006.4778164.

[2.49] R. L. Lin, F. C. Lee, E. M. Baker, and D. Y. Chen, 'Inductor-less piezoelectric transformer electronic ballast for linear fluorescent lamp', in *APEC 2001. Sixteenth Annual IEEE Applied Power Electronics Conference and Exposition (Cat. No.01CH37181)*, Mar. 2001, vol. 2, pp. 664–669 vol.2. doi: 10.1109/APEC.2001.912440.

[2.50] E. M. Baker, W. Huang, D. Y. Chen, and F. C. Lee, 'Radial mode piezoelectric transformer design for fluorescent lamp ballast applications', in *2002 IEEE 33rd Annual IEEE Power Electronics Specialists Conference. Proceedings (Cat. No.02CH37289)*, 2002, vol. 3, pp. 1289–1294 vol.3. doi: 10.1109/PSEC.2002.1022354.

[2.51] W. Huang, D. Chen, E. M. Baker, J. Zhou, H. Hsieh, and F. C. Lee, 'Design of a Power Piezoelectric Transformer for a PFC Electronic Ballast', *IEEE Transactions on Industrial Electronics*, vol. 54, no. 6, pp. 3197–3204, Dec. 2007, doi: 10.1109/TIE.2007.905630.

[2.52] R.-L. Lin, 'Piezoelectric Transformer Characterization and Application of Electronic Ballast', *Ph.D. Dissertation*, Nov. 2001, Accessed: Feb. 15, 2018. [Online]. Available: https://vtechworks.lib.vt.edu/handle/10919/29948

[2.53] Y. Huang and W. Huang, 'An improved equivalent circuit model of radial mode piezoelectric transformer', *IEEE Trans Ultrason Ferroelectr Freq Control*, vol. 58, no. 5, pp. 1069–1076, May 2011, doi: 10.1109/TUFFC.2011.1907.

[2.54] M. Khanna, R. Burgos, Q. Wang, K. D. T. Ngo, and A. V. Carazo, 'New Tunable Piezoelectric Transformers and Their Application in DC-DC Converters', *IEEE Transactions on Power Electronics*, vol. 32, no. 12, pp. 8974–8978, Dec. 2017, doi: 10.1109/TPEL.2017.2702124.

[2.55] P. Valenta, V. Koucký, and J. Hammerbauer, 'Simultaneous power transfer and information transfer via piezoelectric transformer', in *2017 25th Telecommunication Forum (TELFOR)*, Belgrade, Serbia, Nov. 2017, doi: 10.1109/TELFOR.2017.8249412.

[2.56] J. Hans and D. A. Berlincourt, 'Piezoelectric ceramic resonators', US2969512A, Jan. 24, 1961 Accessed: Aug. 25, 2020. [Online]. Available: https://patents.google.com/patent/US2969512/en

[2.57] J. Erhart, P. Pulpán, R. Dolecek, P. Psota, and V. Lédl, 'Disc Piezoelectric Ceramic Transformers', *IEEE Transactions on Ultrasonics, Ferroelectrics, and Frequency Control*, vol. 60, no. 8, pp. 1612–1618, Aug. 2013, doi: 10.1109/TUFFC.2013.2742.

[2.58] P. Laoratanakul, A. Vazquez Carazo, P. Bouchilloux, and K. Uchino, 'Unipoled Disk-type Piezoelectric Transformers', *Japanese Journal of Applied Physics*, vol. 41, pp. 1446–1450, Mar. 2002, doi: 10.1143/JJAP.41.1446.

[2.59] S. Priya, S. Ural, H. W. Kim, K. Uchino, and T. Ezaki, 'Multilayered Unipoled Piezoelectric Transformers', *Jpn. J. Appl. Phys.*, vol. 43, no. 6R, p. 3503, Jun. 2004, doi: 10.1143/JJAP.43.3503.

[2.60] T. Inoue, O. Ohnishi, and N. Ohde, 'Thickness mode vibration piezoelectric transformer', US5118982A, Jun. 02, 1992 Accessed: Sep. 13, 2018. [Online]. Available: https://patents.google.com/patent/US5118982A/en

[2.61] Y. Sasaki, K. Uehara, and T. Inoue, 'Piezoelectric ceramic transformer being driven with thickness extensional vibration', US5241236A, Aug. 31, 1993 Accessed: Sep. 13, 2018. [Online]. Available: https://patents.google.com/patent/US5241236/en

[2.62] 'Ceramic Materials (PZT) - Boston Piezo-Optics Inc.' https://www.bostonpiezooptics.com/ceramic-materials-pzt (accessed Sep. 11, 2018).

[2.63] T. Zaitsu, T. Inoue, O. Ohnishi, and A. Iwamoto, '2 MHz power converter with piezoelectric ceramic transformer', in *[Proceedings] Fourteenth International Telecommunications Energy Conference - INTELEC '92*, 1992, pp. 430–437. doi: 10.1109/INTLEC.1992.268407.

[2.64] H. KIM, E. JANG, D. KIM, L. HWANG, and J. YOO, 'Thickness–Vibration-Mode Multilayer Piezoelectric Transformer for Dc-Dc Converter Application', *Integrated Ferroelectrics*, vol. 107, no. 1, pp. 12–23, Oct. 2009, doi: 10.1080/10584580903324071.

[2.65] T. Bove, W. Wolny, E. Ringgaard, and K. Breboel, 'New type of piezoelectric transformer with very high power density', in *ISAF 2000. Proceedings of the 2000 12th IEEE International Symposium on Applications of Ferroelectrics (IEEE Cat. No.00CH37076)*, 2000, vol. 1, pp. 321–324, doi: 10.1109/ISAF.2000.941564.

[2.66] J. Navas, T. Bove, J. A. Cobos, F. Nuno, and K. Brebol, 'Miniaturised battery charger using piezoelectric transformers', in *APEC 2001. Sixteenth Annual IEEE Applied Power Electronics Conference and Exposition (Cat. No.01CH37181)*, Mar. 2001, vol. 1, pp. 492–496, doi: 10.1109/APEC.2001.911692.

[2.67] J. H. Hu, H. L. Li, H. L. W. Chan, and C. L. Choy, 'A ring-shaped piezoelectric transformer operating in the third symmetric extensional vibration mode', *Sensors and Actuators A: Physical*, vol. 88, no. 1, pp. 79–86, Jan. 2001, doi: 10.1016/S0924-4247(00)00495-7.

[2.68] J.-H. Hu, H.-L. Li, H. L.-W. Chan, and C.-L. Choy, 'Ring-shaped piezoelectric transformer having an inner and outer electrode', US6597084B2, Jul. 22, 2003

Accessed: Sep. 13, 2018. [Online]. Available: https://patents.google.com/patent/US6597084B2/en

[2.69] J. Erhart, 'Parameters and design optimization of the ring piezoelectric ceramic transformer', *Journal of Advanced Dielectrics*, vol. 05, no. 03, p. 1550022, Sep. 2015, doi: 10.1142/S2010135X15500228.

[2.70] S. Lin, J. Xu, and H. Cao, 'Analysis on the Ring-Type Piezoelectric Ceramic Transformer in Radial Vibration', *IEEE Transactions on Power Electronics*, vol. 31, no. 7, pp. 5079–5088, Jul. 2016, doi: 10.1109/TPEL.2015.2482990.

[2.71] J. Yoo, K. Yoon, Y. Lee, S. Suh, J. Kim, and C. Yoo, 'Electrical Characteristics of the Contour-Vibration-Mode Piezoelectric Transformer with Ring/Dot Electrode Area Ratio', *Jpn. J. Appl. Phys.*, vol. 39, no. 5R, p. 2680, May 2000, doi: 10.1143/JJAP.39.2680.

[2.72] J. M. Seo, J. H. Choi, C. W. Moon, and H. G. Sung, 'Optimal design of piezoelectric transformer for high efficiency and high-power density', in *2005 International Conference on Electrical Machines and Systems*, Sep. 2005, vol. 3, pp. 2290-2295, doi: 10.1109/ICEMS.2005.202978.

[2.73] M. Yamamoto, Y. Sasaki, A. Ochi, T. Inoue, and S. Hamamura, 'Step-Down Piezoelectric Transformer for AC-DC Converters', *Jpn. J. Appl. Phys.*, vol. 40, no. 5S, p. 3637, May 2001, doi: 10.1143/JJAP.40.3637.

[2.74] J. Du, J. Hu, and K.-J. Tseng, 'High-power, multioutput piezoelectric transformers operating at the thickness-shear vibration mode', *IEEE Transactions on Ultrasonics, Ferroelectrics, and Frequency Control*, vol. 51, no. 5, pp. 502–509, May 2004, doi: 10.1109/TUFFC.2004.1320823.

[2.75] K. J. Tseng, J. Du, and J. Hu, 'Piezoelectric transformer with high power density and multiple outputs', *Electronics Letters*, vol. 40, no. 12, pp. 786–788, Jun. 2004, doi: 10.1049/el:20040523.

[2.76] L. Xu, Y. Zhang, H. Fan, J. Hu, and J. Yang, 'Theoretical analysis of a ceramic plate thickness-shear mode piezoelectric transformer', *IEEE Transactions on Ultrasonics, Ferroelectrics, and Frequency Control*, vol. 56, no. 3, pp. 613–621, Mar. 2009, doi: 10.1109/TUFFC.2009.1077.

[2.77] Y. Huang and W. Huang, 'Modeling and analysis of circular flexural-vibration-mode piezoelectric transformer', *IEEE Transactions on Ultrasonics, Ferroelectrics, and Frequency Control*, vol. 57, no. 12, pp. 2764–2771, Dec. 2010, doi: 10.1109/TUFFC.2010.1750.

[2.78] Y. Huang, Z. Miao, X. Chen, and W. Huang, 'A verification and parametric analysis of an analytical model of a flexural vibration mode piezoelectric transformer', *IEEE Transactions on Ultrasonics, Ferroelectrics, and Frequency Control*, vol. 59, no. 12, pp. 2731–2741, Dec. 2012, doi: 10.1109/TUFFC.2012.2514.

[2.79] Y. Huang, W. Huang, Q. Wang, and X. Su, 'Research on the equivalent circuit model of a circular flexural-vibration-research on the equivalent circuit model of a circular flexural-vibration-mode piezoelectric transformer with moderate thickness', *IEEE Transactions on Ultrasonics, Ferroelectrics, and Frequency Control*, vol. 60, no. 7, pp. 1538–1543, Jul. 2013, doi: 10.1109/TUFFC.2013.2727.

[2.80] H. Yihua and H. Wenjin, 'Research on the displacement function and equivalent circuit of circular flexural vibration mode piezoelectric ceramic composite transducers', *IEEE Transactions on Ultrasonics, Ferroelectrics, and Frequency Control*, vol. 60, no. 1, pp. 218–234, Jan. 2013, doi: 10.1109/TUFFC.2013.2553.

[2.81] K. Uchino and B. Koc, 'Annular piezoelectric transformer', US5814922A, Sep. 29, 1998 Accessed: Sep. 13, 2018. [Online]. Available: https://patents.google.com/patent/US5814922/en

[2.82] K. Nakamura and K. Kumasaka, 'Lame-mode piezoelectric resonators and transformers using $LiNbO_3$crystals', in *1995 IEEE Ultrasonics Symposium. Proceedings. An International Symposium*, Nov. 1995, vol. 2, pp. 999–1002, doi: 10.1109/ULTSYM.1995.495731.

[2.83] A. M. Flynn and S. R. Sanders, 'Fundamental limits on energy transfer and circuit considerations for piezoelectric transformers', *IEEE Transactions on Power Electronics*, vol. 17, no. 1, pp. 8–14, Jan. 2002, doi: 10.1109/63.988662.

[2.84] J. Forrester, J. N. Davidson, M. P. Foster, and D. A. Stone, 'Influence of Spurious Modes on the Efficiency of Piezoelectric Transformers: a Sensitivity Analysis', *IEEE Transactions on Power Electronics*, 2020, doi: 10.1109/TPEL.2020.3001486.

[2.85] R. Prieto, M. Sanz, J. A. Cobos, P. Alou, O. Garcia, and J. Uceda, 'Design considerations of multi-layer piezoelectric transformers', in *APEC 2001. Sixteenth Annual IEEE Applied Power Electronics Conference and Exposition (Cat. No.01CH37181)*, 2001, vol. 2, pp. 1258–1263 vol.2. doi: 10.1109/APEC.2001.912527.

[2.86] M. Sanz, P. Alou, J. A. Oliver, R. Prieto, J. A. Cobos, and J. Uceda, 'Interleaving of electrodes in piezoelectric transformers', in *2002 IEEE 33rd Annual IEEE Power Electronics Specialists Conference. Proceedings (Cat. No.02CH37289)*, 2002, vol. 2, pp. 567–572, doi: 10.1109/PSEC.2002.1022513.

[2.87] K. Uchino and S. Hirose, 'Loss mechanisms in piezoelectrics: how to measure different losses separately', *IEEE Transactions on Ultrasonics, Ferroelectrics, and Frequency Control*, vol. 48, no. 1, pp. 307–321, Jan. 2001, doi: 10.1109/58.896144.

[2.88] G. Ivensky, I. Zafrany, and S. Ben-Yaakov, 'Generic operational characteristics of piezoelectric transformers', *IEEE Transactions on Power Electronics*, vol. 17, no. 6, pp. 1049–1057, Nov. 2002, doi: 10.1109/TPEL.2002.805602.

[2.89] E. L. Horsley, M. P. Foster, and D. A. Stone, 'A frequency-response-based characterisation methodology for piezoelectric transformers', in *2008 2nd Electronics System-Integration Technology Conference*, London, United Kingdom, Sep. 2008, pp. 959–962. doi: 10.1109/ESTC.2008.4684481.

[2.90] J. Yang, 'Piezoelectric transformer structural modeling - a review', *IEEE Transactions on Ultrasonics, Ferroelectrics, and Frequency Control*, vol. 54, no. 6, pp. 1154–1170, Jun. 2007, doi: 10.1109/TUFFC.2007.369.

[2.91] E. L. Horsley, A. V. Carazo, M. P. Foster, and D. A. Stone, 'A Lumped Equivalent Circuit Model for the Radial Mode Piezoelectric Transformer', in *2009 Twenty-Fourth Annual IEEE Applied Power Electronics Conference and Exposition*, Feb. 2009, pp. 1747–1753. doi: 10.1109/APEC.2009.4802906.

[2.92] J. Forrester, J. Davidson, and M. Foster, 'Effect of Spurious Resonant Modes on the Operation of Radial Mode Piezoelectric Transformers', in *PCIM Europe 2018; International Exhibition and Conference for Power Electronics, Intelligent Motion, Renewable Energy and Energy Management*, Jun. 2018

[2.93] R. D. Mindlin and H. Deresiewicz, 'Thickness-Shear and Flexural Vibrations of a Circular Disk', *Journal of Applied Physics*, vol. 25, no. 10, pp. 1329–1332, Oct. 1954, doi: 10.1063/1.1721554.

[2.94] H. Deresiewicz and R. Mindlin, 'Axially symmetric flexural vibrations of a circular disk', COLUMBIA UNIV NEW YORK, 1953.

[2.95] Q. Wang, S. T. Quek, C. T. Sun, and X. Liu, 'Analysis of piezoelectric coupled circular plate', *Smart Mater. Struct.*, vol. 10, no. 2, p. 229, 2001, doi: 10.1088/0964-1726/10/2/308.

[2.96] A. A. Jandaghian, A. A. Jafari, and O. Rahmani, 'Exact solution for Transient bending of a circular plate integrated with piezoelectric layers', *Applied Mathematical Modelling*, vol. 37, no. 12, pp. 7154–7163, Jul. 2013, doi: 10.1016/j.apm.2013.02.007.

[2.97] G. Mieczkowski, A. Borawski, and D. Szpica, 'Static Electromechanical Characteristic of a Three-Layer Circular Piezoelectric Transducer', *Sensors (Basel)*, vol. 20, no. 1, Dec. 2019, doi: 10.3390/s20010222.

[2.98] Y.-H. Huang, C.-C. Ma, and Z.-Z. Li, 'Investigations on vibration characteristics of two-layered piezoceramic disks', *International Journal of Solids and Structures*, vol. 51, no. 1, pp. 227–251, Jan. 2014, doi: 10.1016/j.ijsolstr.2013.09.026.

[2.99] C.-H. Huang, 'Free vibration analysis of the piezoceramic bimorph with theoretical and experimental investigation', *IEEE Transactions on Ultrasonics, Ferroelectrics, and Frequency Control*, vol. 52, no. 8, pp. 1393–1403, Aug. 2005, doi: 10.1109/TUFFC.2005.1509799.

[2.100] S. Dong, K. Uchino, L. Li, and D. Viehland, 'Analytical solutions for the transverse deflection of a piezoelectric circular axisymmetric unimorph actuator', *IEEE Transactions on Ultrasonics, Ferroelectrics, and Frequency Control*, vol. 54, no. 6, pp. 1240–1249, Jun. 2007, doi: 10.1109/TUFFC.2007.377.

[2.101] M. Brissaud, 'Theoretical modelling of non-symmetric circular piezoelectric bimorphs', *J. Micromech. Microeng.*, vol. 16, no. 5, p. 875, 2006, doi: 10.1088/0960-1317/16/5/001.

[2.102] X. Liu, Q. Wang, and S. T. Quek, 'Analytical solution for free vibration of piezoelectric coupled moderately thick circular plates', *International Journal of Solids and Structures*, vol. 39, no. 8, pp. 2129–2151, Apr. 2002, doi: 10.1016/S0020-7683(02)00081-1.

[2.103] F. Sammoura, K. Smyth, and S. Kim, 'An equivalent network representation of a clamped bimorph piezoelectric micromachined ultrasonic transducer with circular and annular electrodes using matrix manipulation techniques', *IEEE Transactions on Ultrasonics, Ferroelectrics, and Frequency Control*, vol. 60, no. 9, pp. 1989–2003, Sep. 2013, doi: 10.1109/TUFFC.2013.2784.

[2.104] S. K. Ha and Y. H. Kim, 'Analysis of an asymmetrical piezoelectric annular bimorph using impedance and admittance matrices', *The Journal of the Acoustical Society of America*, vol. 110, no. 1, pp. 208–215, Jul. 2001, doi: 10.1121/1.1375139.

[2.105] S. K. Ha and Y. H. Kim, 'Impedance and admittance matrices of symmetric piezoelectric annular bimorphs and their applications', *The Journal of the Acoustical Society of America*, vol. 108, no. 5, pp. 2125–2133, Nov. 2000, doi: 10.1121/1.1312365.

[2.106] S. K. Ha, 'Analysis of the asymmetric triple-layered piezoelectric bimorph using equivalent circuit models', *The Journal of the Acoustical Society of America*, vol. 110, no. 2, pp. 856–864, Aug. 2001, doi: 10.1121/1.1387090.

[2.107] P. Pulpan, J. Erhart, and O. Štípek, 'Analytical Modeling of Piezoelectric Transformers', *Ferroelectrics*, Jun. 2007, doi: 10.1080/00150190701354299.

[2.108] P. Půlpán and J. Erhart, 'Transformation ratio of "ring-dot" planar piezoelectric transformer', *Sensors and Actuators A: Physical*, vol. 140, no. 2, pp. 215–224, Nov. 2007, doi: 10.1016/j.sna.2007.06.011.

[2.109] S. Ho, 'Modeling of a Disk-Type Piezoelectric Transformer', *IEEE Transactions on Ultrasonics, Ferroelectrics, and Frequency Control*, vol. 54, no. 10, pp. 2110–2119, Oct. 2007, doi: 10.1109/TUFFC.2007.506.

[2.110] M. Ekhtiari, Z. Zhang, and M. A. E. Andersen, 'State-of-the-art piezoelectric transformer-based switch mode power supplies', in *IECON 2014 - 40th Annual Conference of the IEEE Industrial Electronics Society*, Oct. 2014, pp. 5072–5078. doi: 10.1109/IECON.2014.7049271.

[2.111] H. Schwarzmann, T. Erlbacher, A. J. Bauer, H. Ryssel, and L. Frey, 'Amplitude Modulated Resonant Push-Pull Driver for Piezoelectric Transformers in Switching Power Applications', p. 5, 2012.

[2.112] Yujia Yang *et al.*, 'Comparison of Inductor-Half-Bridge and Class-E resonant topologies for piezoelectric transformer applications', in *2009 IEEE Energy Conversion Congress and Exposition*, San Jose, CA, Sep. 2009, pp. 776–782. doi: 10.1109/ECCE.2009.5316446.

[2.113] S. Bronstein and S. Ben-Yaakov, 'Design considerations for achieving ZVS in a half bridge inverter that drives a piezoelectric transformer with no series inductor', in *2002 IEEE 33rd Annual IEEE Power Electronics Specialists Conference. Proceedings (Cat. No.02CH37289)*, Cairns, Qld., Australia, 2002, vol. 2, pp. 585–590. doi: 10.1109/PSEC.2002.1022516.

[2.114] E. L. Horsley, N. Nguyen-Quang, M. P. Foster, and D. A. Stone, 'Achieving ZVS in inductor-less half-bridge piezoelectric transformer based resonant converters', in *2009 International Conference on Power Electronics and Drive Systems (PEDS)*, Nov. 2009, pp. 446–451. doi: 10.1109/PEDS.2009.5385842.

[2.115] K. S. Meyer, M. A. E. Andersen, and F. Jensen, 'Parameterized analysis of Zero Voltage Switching in resonant converters for optimal electrode layout of Piezoelectric Transformers', in *2008 IEEE Power Electronics Specialists Conference*, Jun. 2008, pp. 2543–2548. doi: 10.1109/PESC.2008.4592323.

[2.116] E. L. Horsley, A. V. Carazo, N. Nguyen-Quang, M. P. Foster, and D. A. Stone, 'Analysis of Inductorless Zero-Voltage-Switching Piezoelectric Transformer-Based Converters', *IEEE Transactions on Power Electronics*, vol. 27, no. 5, pp. 2471–2483, May 2012, doi: 10.1109/TPEL.2011.2169431.

[2.117] M. P. Foster, E. L. Horsley, and D. A. Stone, 'Predicting the zero-voltage switching profiles of half-bridge driven inductor-less piezoelectric transformer-based inverters', *IET Power Electronics*, vol. 5, no. 7, pp. 1068–1073, Aug. 2012, doi: 10.1049/iet-pel.2011.0344.

[2.118] M. S. Rodgaard, T. Andersen, and M. A. E. Andersen, 'Empiric analysis of zero voltage switching in piezoelectric transformer based resonant converters', in *6th IET International Conference on Power Electronics, Machines and Drives (PEMD 2012)*, Bristol, UK, 2012, pp. A63–A63. doi: 10.1049/cp.2012.0217.

[2.119] M. P. Foster, J. N. Davidson, E. L. Horsley, and D. A. Stone, 'Critical Design Criterion for Achieving Zero Voltage Switching in Inductorless Half-Bridge-Driven Piezoelectric-Transformer-Based Power Supplies', *IEEE Transactions on Power Electronics*, vol. 31, no. 7, pp. 5057–5066, Jul. 2016, doi: 10.1109/TPEL.2015.2481706.

[2.120] D. Vasic, F. Costa, and E. Sarraute, 'A new method to design piezoelectric transformer used in MOSFET and IGBT gate drive circuits', in *IEEE 34th Annual*

Conference on Power Electronics Specialist, 2003. PESC '03., Jun. 2003, vol. 1, pp. 307–312, doi: 10.1109/PESC.2003.1218311.

[2.121] J. Forrester, J. N. Davidson, M. P. Foster, E. L. Horsley, and D. A. Stone, 'Automated design tools for piezoelectric transformer-based power supplies', *The Journal of Engineering*, vol. 2019, no. 17, pp. 4163–4166, 2019, doi: 10.1049/joe.2018.8065.

[2.122] M. P. Foster, J. N. Davidson, E. L. Horsley, and D. A. Stone, 'Critical Design Criterion for Achieving Zero Voltage Switching in Inductorless Half-Bridge-Driven Piezoelectric-Transformer-Based Power Supplies', *IEEE Transactions on Power Electronics*, vol. 31, no. 7, pp. 5057–5066, Jul. 2016, doi: 10.1109/TPEL.2015.2481706.

[2.123] A. M. Sanchez, M. Sanz, R. Prieto, J. A. Oliver, and J. A. Cobos, 'Mixed analytical and numerical design method for piezoelectric transformers', in *Power Electronics Specialist Conference, 2003. PESC '03. 2003 IEEE 34th Annual*, Jun. 2003, vol. 2, pp. 841–846, doi: 10.1109/PESC.2003.1218166.

[2.124] N. Bianchi and S. Bolognani, 'Design optimisation of electric motors by genetic algorithms', *IEE Proceedings - Electric Power Applications*, vol. 145, no. 5, pp. 475–483, Sep. 1998, doi: 10.1049/ip-epa:19982166.

[2.125] R. Pagano, S. Abedinpour, A. Raciti, and S. Musumeci, 'Efficiency optimization of an integrated wireless power transfer system by a genetic algorithm', in *2016 IEEE Applied Power Electronics Conference and Exposition (APEC)*, Mar. 2016, pp. 3669–3676. doi: 10.1109/APEC.2016.7468398.

[2.126] D. R. Williams, M. P. Foster, C. M. Bingham, and D. A. Stone, 'A genetic algorithm for designing LCLC resonant converters', in *2008 4th IET Conference on Power Electronics, Machines and Drives*, Apr. 2008, pp. 732–736. doi: 10.1049/cp:20080618.

[2.127] M. P. Foster, A. J. Gilbert, C. R. Gould, D. A. Stone, and C. M. Bingham, 'Automated design of LCC resonant converters using a genetic algorithm employing a describing function equivalent circuit converter model'.

[2.128] R. Normann, 'First High-Temperature Electronics Products Survey 2005', 2006. doi: 10.2172/889944.

[2.129] J. Watson and G. Castro, 'A review of high-temperature electronics technology and applications', *J Mater Sci: Mater Electron*, vol. 26, no. 12, pp. 9226–9235, Dec. 2015, doi: 10.1007/s10854-015-3459-4.

[2.130] Z. Chen, Y. Yao, D. Boroyevich, K. D. T. Ngo, P. Mattavelli, and K. Rajashekara, 'A 1200-V, 60-A SiC MOSFET Multichip Phase-Leg Module for High-Temperature, High-Frequency Applications', *IEEE Trans. Power Electron.*, vol. 29, no. 5, pp. 2307–2320, May 2014, doi: 10.1109/TPEL.2013.2283245.

[2.131] Z. Wang *et al.*, 'A high temperature silicon carbide mosfet power module with integrated silicon-on-insulator-based gate drive', *IEEE Transactions on Power Electronics*, vol. 30, no. 3, pp. 1432–1445, Mar. 2015, doi: 10.1109/TPEL.2014.2321174.

[2.132] P. Ning *et al.*, 'SiC Wirebond Multichip Phase-Leg Module Packaging Design and Testing for Harsh Environment', *IEEE Transactions on Power Electronics*, vol. 25, no. 1, pp. 16–23, Jan. 2010, doi: 10.1109/TPEL.2009.2027324.

[2.133] F. Xu *et al.*, 'Development of a SiC JFET-Based Six-Pack Power Module for a Fully Integrated Inverter', *IEEE Transactions on Power Electronics*, vol. 28, no. 3, pp. 1464–1478, Mar. 2013, doi: 10.1109/TPEL.2012.2205946.

[2.134] T. Nomura, H. Kambayashi, Y. Niiyama, S. Otomo, and S. Yoshida, 'High-temperature enhancement mode operation of n-channel GaN MOSFETs on sapphire substrates', *Solid-State Electronics*, vol. 52, no. 1, pp. 150–155, Jan. 2008, doi: 10.1016/j.sse.2007.07.035.

[2.135] T. Nomura *et al.*, 'High Temperature Operation AlGaN/GaN HFET with a low on-state resistance, a high breakdown voltage and a fast switching capacity', in *2006 IEEE International Symposium on Power Semiconductor Devices and IC's*, Jun. 2006, pp. 1–4. doi: 10.1109/ISPSD.2006.1666134.

[2.136] Z. Xu, W. Zhang, F. Xu, F. Wang, L. M. Tolbert, and B. J. Blalock, 'Investigation of 600 V GaN HEMTs for high efficiency and high temperature applications', in *2014 IEEE Applied Power Electronics Conference and Exposition - APEC 2014*, Mar. 2014, pp. 131–136. doi: 10.1109/APEC.2014.6803299.

[2.137] B. Grummel, R. McClure, Lei Zhou, A. P. Gordon, L. Chow, and Z. J. Shen, 'Design consideration of high temperature SiC power modules', in *2008 34th Annual Conference of IEEE Industrial Electronics*, Nov. 2008, pp. 2861–2866. doi: 10.1109/IECON.2008.4758413.

[2.138] A. A. Bajwa, Y. Qin, R. Reiner, R. Quay, and J. Wilde, 'Assembly and Packaging Technologies for High-Temperature and High-Power GaN Devices', *IEEE Transactions on Components, Packaging and Manufacturing Technology*, vol. 5, no. 10, pp. 1402–1416, Oct. 2015, doi: 10.1109/TCPMT.2015.2468595.

[2.139] B. Ray, J. D. Scofield, R. L. Spyker, B. Jordan, and Sei-Hyung Ryu, 'High temperature operation of a dc-dc power converter utilizing SiC power devices', in *Twentieth Annual IEEE Applied Power Electronics Conference and Exposition, 2005. APEC 2005.*, Mar. 2005, vol. 1, pp. 315-321, doi: 10.1109/APEC.2005.1452944.

[2.140] T. Funaki *et al.*, 'Power Conversion With SiC Devices at Extremely High Ambient Temperatures', *IEEE Transactions on Power Electronics*, vol. 22, no. 4, pp. 1321–1329, Jul. 2007, doi: 10.1109/TPEL.2007.900561.

[2.141] R. Perrin, N. Quentin, B. Allard, C. Martin, and M. Ali, 'High-Temperature GaN Active-Clamp Flyback Converter With Resonant Operation Mode', *IEEE Journal of Emerging and Selected Topics in Power Electronics*, vol. 4, no. 3, pp. 1077–1085, Sep. 2016, doi: 10.1109/JESTPE.2016.2544346.

[2.142] F. Dubois *et al.*, 'A high temperature ultrafast isolated converter to turn-off normally-on SiC JFETs', in *2012 IEEE Energy Conversion Congress and Exposition (ECCE)*, Sep. 2012, pp. 3581–3588. doi: 10.1109/ECCE.2012.6342486.

[2.143] C. Buttay *et al.*, 'State of the art of High Temperature Power Electronics', in *Microtherm*, Lodz, Poland, Jun. 2009, pp. 8–17. Accessed: May 21, 2020. [Online]. Available: https://hal.archives-ouvertes.fr/hal-00413349

[2.144] E. Alberta, W. Hackenberger, C. Stringer, C. A. Randall, T. Shrout, and G. Schwarze, 'High Temperature Ceramic Capacitors', Jan. 2021.

[2.145] J. Colmenares, S. Kargarrazi, H. Elahipanah, H. Nee, and C. Zetterling, 'High-temperature passive components for extreme environments', in *2016 IEEE 4th Workshop on Wide Bandgap Power Devices and Applications (WiPDA)*, Nov. 2016, pp. 271–274. doi: 10.1109/WiPDA.2016.7799951.

[2.146] T. Stevenson *et al.*, 'Piezoelectric materials for high temperature transducers and actuators', *J Mater Sci: Mater Electron*, vol. 26, no. 12, pp. 9256–9267, Dec. 2015, doi: 10.1007/s10854-015-3629-4.

[2.147] G. Goodman, 'Ferroelectric Properties of Lead Metaniobate', *Journal of the American Ceramic Society*, vol. 36, no. 11, pp. 368–372, 1953, doi: 10.1111/j.1151-2916.1953.tb12820.x.

[2.148] V. V. Shvartsman, W. Kleemann, R. Haumont, and J. Kreisel, 'Large bulk polarization and regular domain structure in ceramic BiFeO3', *Appl. Phys. Lett.*, vol. 90, no. 17, p. 172115, Apr. 2007, doi: 10.1063/1.2731312.

[2.149] H. S. Shulman, M. Testorf, D. Damjanovic, and N. Setter, 'Microstructure, Electrical Conductivity, and Piezoelectric Properties of Bismuth Titanate', *Journal of the American Ceramic Society*, vol. 79, no. 12, pp. 3124–3128, 1996, doi: 10.1111/j.1151-2916.1996.tb08086.x.

[2.150] R. E. Eitel, C. A. Randall, T. R. Shrout, P. W. Rehrig, W. Hackenberger, and S.-E. Park, 'New High Temperature Morphotropic Phase Boundary Piezoelectrics Based on Bi(Me)O3–PbTiO3 Ceramics', *Jpn. J. Appl. Phys.*, vol. 40, no. 10R, p. 5999, Oct. 2001, doi: 10.1143/JJAP.40.5999.

Chapter 3 - Equivalent circuit parameter extraction methods

3.1 Introduction

To facilitate the development and validation of the work presented the later chapters of this thesis, it is important to be able to accurately extract equivalent circuit components from PTs. Therefore, this chapter will detail three new component extraction techniques, two of which are improvements upon previous state of the art techniques, and the third, a novel method.

A fourth method is then developed, combining the previous methods, to better extract components from PTs containing higher losses. All methods are validated with experimental measurements and a detailed noise rejection analysis is additionally performed.

3.2 Equivalent circuit extraction

3.2.1 Mason equivalent circuit

The Mason equivalent circuit is shown in Fig. 3.1.

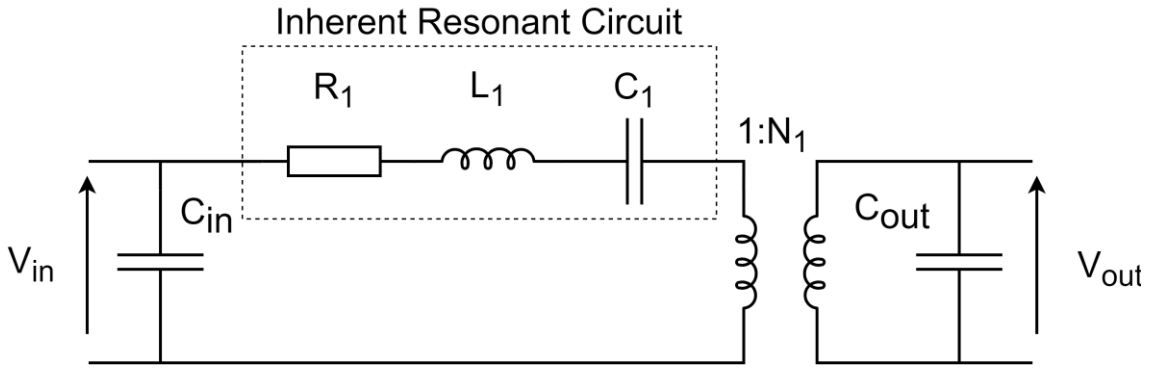

Fig. 3.1 – Mason equivalent circuit

As discussed in Chapter 2, the Mason equivalent circuit models the electrical performance of a PT at frequencies around a single vibration mode. Whilst, the input and output capacitance occur due to the physical layout of the PT, the inherent resonant tank circuit and the ideal transformer are approximations of mechanical properties of the PT. This leads to issues for PT designers, as it is important to be able to control all the components within the PT for

effective converter design, however, it is impossible to measure these components directly. Therefore, to determine the value of these parameters, equivalent circuit estimation techniques are required.

3.2.2 Bode plots

Most equivalent circuit extraction techniques rely on accurate impedance measurements taken from the PT. A sample bode plot from a measurement of the input impedance of a sample radial mode Transoner PT is shown in Fig. 3.2.

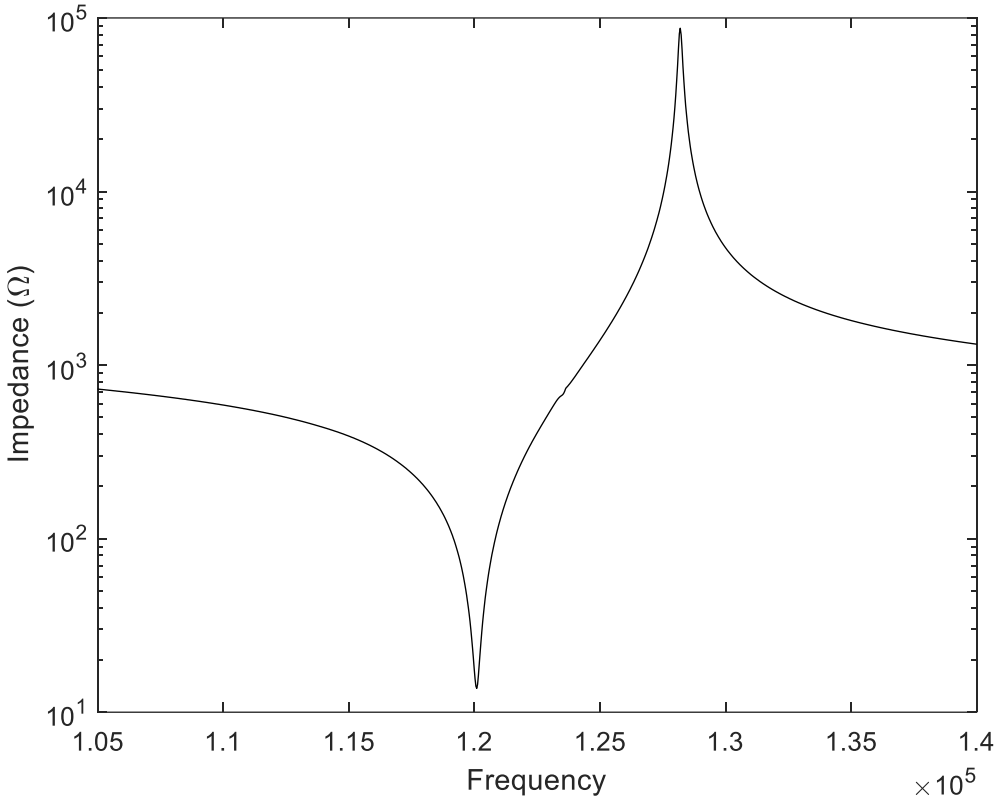

Fig. 3.2 – Input impedance of a radial mode Transoner PT

There are several key elements of the impedance curve that give insight into the equivalent circuit properties. Firstly, as shown in Fig. 3.2, there is a peak and trough in the impedance curve, this occurs due to each vibration mode having two resonances, a series and a parallel resonance. The series resonance occurs when the L and C components in the resonant tank circuit have the same magnitude of impedance, but with opposing sign, therefore, meaning their combined impedance equals 0. The parallel resonance occurs when the impedance of the LC combination and the reactance of the input capacitance C_{in}, have the same magnitude

but with opposing sign. In this case, the combined impedance of these two elements in parallel equals ∞.

Under real-world conditions, there is a damping resistance in series with the LC circuit, therefore, the combined impedance during the series resonance does not reach 0, but however, the combined impedance approximately equals the damping resistance at the series resonance. Similarity, at the parallel resonance the combined impedance does reach ∞, as the damping resistance acts to lower the maximum impedance. Using this information, lots of insight can be gained as to the value of these parameters, as will be discussed in the following sections.

3.3 General purpose parameter extraction methods

Three methods for the extraction of PT equivalent circuit components are presented. Method 1 presents a curve fitting method, fitting a simulated impedances magnitude spectrum curve to an experimentally measured curve. Method 2 uses isolated measurements of the input and output capacitances, along with measurements of the series resonant and parallel resonant frequencies to estimate the equivalent circuit values. Method 3 uses three measurements of the input impedance and then 3 measurements of the output impedance, with an expression for the impedance of the PT to generate simultaneous equations which are then subsequently solved to extract the equivalent circuit values.

3.3.1 Method 1

Method 1 improves upon the technique presented by Horsley *et al.* [3.1]. It employs a curve fitting algorithm to match an impedance spectrum measured from a PT to an appropriate expression for the impedance of the equivalent circuit of the PT. To accomplish this, the Nelder-Mead simplex algorithm [3.2] is used to minimise a cost (loss) function F, where the cost function gives a numerical value which describes the error between the measured and simulated impedance responses, defined in (3.1),

$$F = \sum \left(\frac{|Z_{\text{measured}}(\omega)| - \lceil Z_{\text{expression}}(\omega) \rceil}{|Z_{\text{measured}}(\omega)|} \right)^2 \tag{3.1}$$

The Nelder-Mead algorithm is an optimisation technique, which uses simplexes (n-dimensional triangles) and aims to move the simplex to a more optimum region of the search space, one vertex at a time. Eventually the simplex gets smaller and closes in on the optimum solution. In contrast to Horsely *et al.*, this approach minimises percentage and not absolute, error between measured and simulated responses. If an absolute error approach is used, the Nelder-Mead simplex algorithm will find a solution which is best matched at the anti-resonant frequency, where impedance is at its largest and so error will be at its largest. However, the due to the low current (high impedance) whilst measuring at this frequency, the measurements are highly susceptible to noise and the influence of parasitic components (as discussed in 3.3.4.b). Therefore, by using a percentage error minimisation approach, the Nelder-Mead simplex algorithm will optimise the components to give an excellent match between simulated and measured impedance curves across the whole impedance spectrum (around the resonance of interest).

To simplify the curve fitting process, the number of unknown variables in $Z_{\text{expression}}$ should be minimised where possible. To accomplish this, the input impedance of the PT is measured with the output terminals short-circuited, simplifying the Mason equivalent circuit to that in Fig. 3.3.

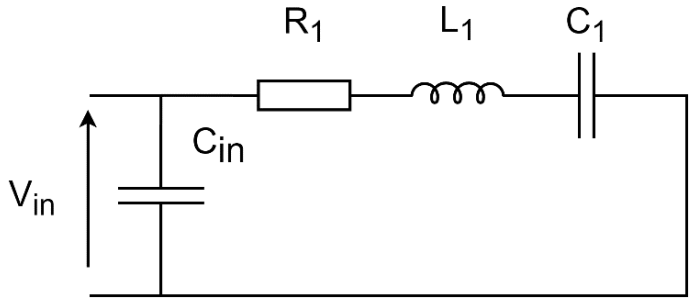

Fig. 3.3 – Simplified Mason equivalent circuit model of a PT with the output terminals short-circuited

This measurement technique reduces the number of unknown component values in the equivalent circuit from six to four. An equation for the input impedance of the circuit in Fig. 3.3 is given by,

$$Z_{\text{in}}(\omega) = \frac{(L_1\omega^2 - jR_1\omega)C_1 - 1}{\omega([j\omega^2 L_1 C_{\text{in}} + R_1\omega C_{\text{in}} - j]C_1 - jC_{\text{in}})} \tag{3.2}$$

Equation (3.2) can be further simplified by defining β as the reactance of both the inductor and the capacitor at the (series) resonant frequency (ω_1),

$$\beta = \frac{1}{\omega_1 C_1} = \omega_1 L_1 \tag{3.3}$$

β is then substituted into (3.2) to create a simplified expression for the input impedance,

$$Z_{\text{in}}(\omega) = \frac{-jR_1\omega\omega_1 + \omega^2\beta - {\omega_1}^2\beta}{\omega(-jC_1\omega_1\beta + [R_1\omega C_{\text{in}} - j]\omega_1 + j\omega^2\beta C_{\text{in}})} \tag{3.4}$$

Equation (3.4) contains four unknowns, two of which can be extracted directly from the impedance spectrum. Firstly, the resonant frequency, ω_1, is assumed to be the frequency at which the magnitude of the PT impedance is at a minimum. Secondly, at resonance, the combined impedance of the resonant inductor and capacitor is equal to 0, therefore, the circuit in Fig. 3.3 is simplified to contain only the input capacitor and the damping resistance in parallel. Then, assuming $1/(\omega_1 C_{\text{in}}) \gg R_1$, the impedance measured at the resonant frequency is approximately equal to the damping resistance R_1. The remaining two unknown parameters in (3.4), β and C_{in}, can be determined using the Nelder-Mead simplex algorithm (FMINSEARCH function in Matlab). Then, using the resonant frequency and β, the resonant inductance L_1 and capacitance C_1 and can be found using (3.3).

To extract the remaining two components in the Mason equivalent circuit, N_1 and C_{out}, the process described for the input impedance is repeated, with similar measurements from the output terminals of the PT with the input shorted and replacing C_{in} with C_{out} in (3.4). It should be noted that the value of β and R_1 extracted from the output terminals will be different from the value of β and R_1 extracted from the input terminals. This is due to the influence of the turn ratio N_1. For the measurements taken from the output terminals, the RLC components are all effectively referred across the ideal transformer, changing their observed value. Therefore, the final unknown parameter N_1 can be found using (3.5).

$$N_1 = \sqrt{\frac{\beta_{\text{out}}}{\beta_{\text{in}}}} \tag{3.5}$$

where β_{out} and β_{in} are the beta values extracted from input and output measurements, respectively.

3.3.1.a) Initial conditions

As Horsely *et al.* found, depending on the initial parameter values passed to the Nelder-Mead algorithm, the resulting component values can be vastly different. Therefore, it is vital that the initial conditions are carefully selected to ensure an accurate extraction and to avoid local minima. To accomplish this, the initial component values are varied, and for each variation the output of the cost function is recorded after minimisation through the Nelder-Mead algorithm. The most accurate solution (lowest cost) is then chosen. Although this increases the solution time, it is necessary to perform this initial step to ensure the global optimum solution is found. During the evaluation of this method, the initial β value was varied between $10\Omega - 100\mathrm{k}\Omega$ and the initial C_{in} (and C_{out}) value was varied between $1\mathrm{fF} - 1\mu\mathrm{F}$. It should be noted that the range of values chosen is extreme. This was done to ensure all conditions are handled. The range of initial conditions could be further restricted if approximate values of C_{in} and β are known.

3.3.2 Method 2

Method 2 is an adaptation of the technique presented by Ivensky *et al.* [3.3]. Firstly, the values of C_{in} and C_{out} are measured directly from the PT. Then, from the simplified Mason equivalent circuit model in Fig. 3.3, equations can be generated for the resonant and anti-resonant frequencies in terms of L_1, C_1 and C_{in}. Solving these equations simultaneously with the measured C_{in} value allows, L_1 and C_1 to be found.

This method improves upon the work of Ivensky *et al.* in two main ways, firstly, a novel C_{in} and C_{out} measurement technique is presented, which removes the influence of the resonant capacitance C_1 from these measurements. Secondly, as part of this technique, the turns ratio N_1 can be directly measured.

3.3.2.a) Capacitance and turns ratio measurements

In the method presented by Ivensky *et al.*, C_{in} and C_{out} are measured at $1\mathrm{kHz}$ using an LCR meter with the output and input, respectively, short-circuited. The main problem with this method is that the impedance of the input or output capacitor is typically only an order of magnitude smaller than the resonant capacitor C_1 in parallel with it. Therefore, the resonant capacitor can cause significant error in the input or output capacitor measurement. To

observe this error, the input impedance of a PT was simulated with a 2nF input capacitor and the parameters in Table 3.1.

Table 3.1 – Equivalent circuit component values used for simulating the impact of C_1 on C_{in} measurement

$R_1(\Omega)$	$L_1(\text{mH})$	$C_{\text{in}}(\text{nF})$	$C_{\text{out}}(\text{nF})$	N_1
10	1	2	2	2

The resonant capacitor value is then varied and the apparent capacitance on the input terminals at 1kHz is measured, allowing the percentage error in the measured capacitance (compared to the known input capacitance of 2nF) to be calculated. The results of this analysis are shown in Fig. 3.4.

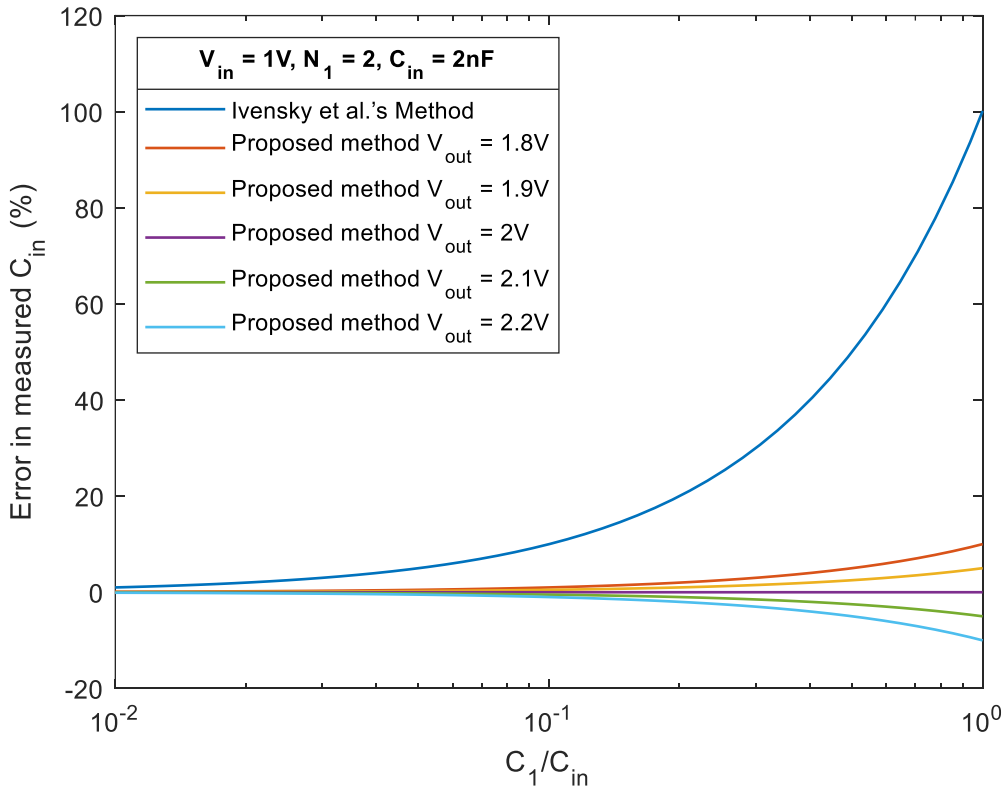

Fig. 3.4 – Error in measured input capacitance with changes in the resonant capacitance (C_1)

Observing Fig. 3.4, for small C_1 values, relative to the input capacitance, minimal error occurs when using Ivensky *et al.* method. Although, at typical resonant capacitor values of around 0.1nF ($C_1/C_{\text{in}} = 0.05$) there is a noticeable error (10%) in the measurement, which increases rapidly with increasing resonant capacitance.

To minimise the influence of the resonant capacitor, the resonant current through the RLC circuit must be reduced. By forcing the voltage across the RLC branch to equal 0, the current through the branch becomes 0 and thus the resonant branch is effectively cancelled out.

To achieve this, a sinusoidal voltage of a known amplitude is applied to the input terminals of the PT. Then, if for example the PT exhibits a 1 turn ratio, then an identical voltage (same frequency and phase) to that which is applied to the input side, is applied to the output terminals of the PT, forcing the voltage across the resonant circuit to equal 0. However, in most cases the turn ratio will not be known a priori. For cases where N_1 is not known, the amplitude of the sinusoidal voltage applied to the output terminals of the PT is varied until the voltage across the RLC circuit is forced equal to 0. The configuration for this technique is shown in Fig. 3.5 below.

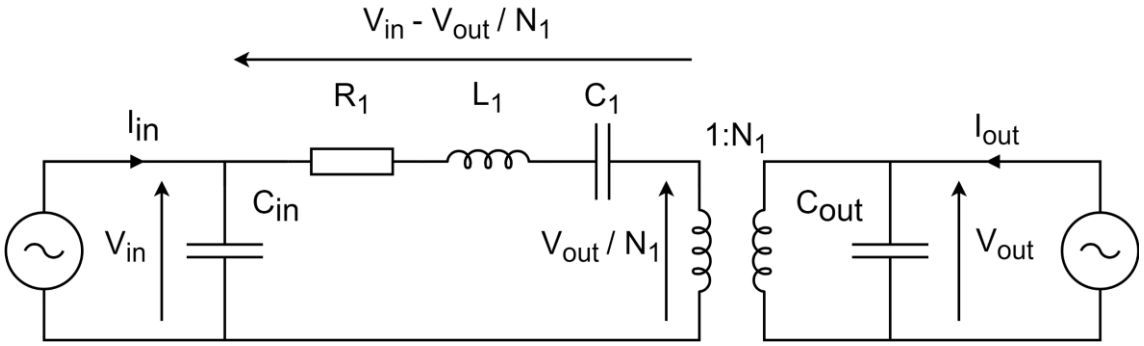

Fig. 3.5 – Hardware setup for the improved input and output capacitance measurement technique

As shown in Fig. 3.5, the voltage on the left-hand side of the RLC circuit is equal to the voltage supplied to the input terminals of the PT. The voltage on the right-hand side of the RLC circuit is equal to the voltage supplied to the output terminals of the PT divided by the turn ratio N_1. Therefore, to make the voltage across the RLC circuit equal to zero, the voltage supplied to the output terminals must have an amplitude 'N_1' times greater than the voltage supplied to the input terminals (3.6). As a result, the turns ratio can be directly determined from the experimental measurements using,

$$V_{\text{in}} - \frac{V_{\text{out}}}{N_1} = 0, V_{\text{out}} = N_1 \text{V}_{\text{in}}, N_1 = \frac{V_{\text{out}}}{V_{\text{in}}} \tag{3.6}$$

However, as the RLC components do not physically exist, it is not possible to directly measure the voltage across the RLC circuit. Therefore, determining if the voltage supplied to the output side of the PT is at the appropriate amplitude, is more difficult. Fortunately, when the

sinusoidal voltage supplied to the output terminals is set to the appropriate amplitude as described by (3.6), the PT should exhibit minimal resonant behaviour. This is visible in the input impedance spectrum, as shown in Fig. 3.6 for varying output voltages.

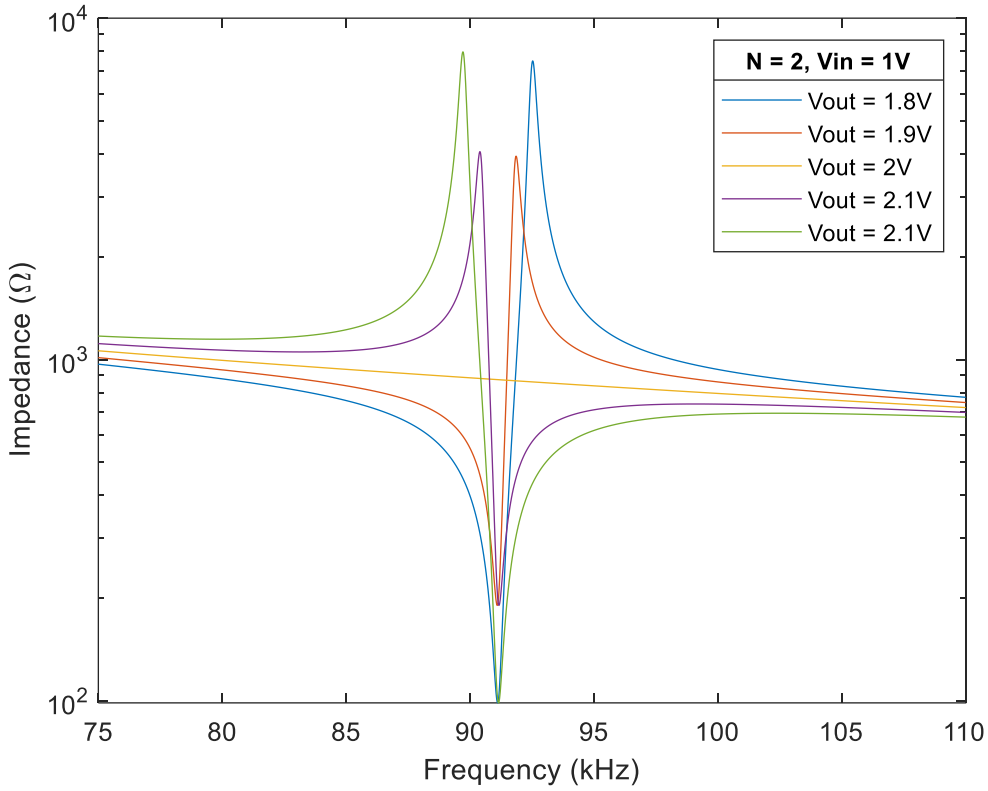

Fig. 3.6 – Simulated input impedance of a PT with changes in the voltage supplied to the output terminals

As expected, the closer V_{out} matches $N_1 V_{\text{in}}$ the smaller the impedance difference between the maximum and minimum points on the curve. In the ideal case, when $V_{\text{out}} = N_1 V_{\text{in}}$, no resonant current flows and therefore any current being supplied to both the input and output terminals is only flowing through the input and output capacitors, respectively. This then allows accurate measurements to be taken of both the input and output capacitors, without the influence of the resonant capacitor.

A comparison between the presented method and the technique presented by Ivensky *et al.* is shown in Fig. 3.4. Observing Fig. 3.4, in the ideal case of $V_{\text{out}} = N_1 V_{\text{in}}$ there is negligible error in the measured capacitance for the presented method. As expected, in the scenarios where $V_{\text{out}} \neq N_1 V_{\text{in}}$there is some error in the measurement. Although, even with 10% error in the voltage matching, with $C_1/C_{\text{in}} = 0.1$, the error in the measured capacitance is significantly (x10) smaller than that exhibited by Ivensky *et al.'s* method.

3.3.2.b) Extracting R_1, L_1 and C_1

The remaining equivalent circuit components are extracted by exploiting the fact that the equivalent circuit model of a PT exhibits two resonant frequencies, a series resonance, and a parallel resonance (anti-resonance). To investigate these resonances in more detail, the circuit in Fig. 3.3 is again used, as is the associated input impedance expression (3.2). If the damping resistance, R_1, is assumed to be 0, then the input impedance of the circuit in Fig. 3.3 is purely imaginary,

$$Z_{\text{in}} = j\frac{1 - L_1 C_1 \omega^2}{\omega(C_1 C_{\text{in}} L_1 \omega^2 - C_1 - C_{\text{in}})} \tag{3.7}$$

Equation (3.7) can then be solved for ω in two scenarios, the first scenario is when considering the series resonant frequency. At this frequency, the impedance is at a minimum, if $R_1 = 0$ is assumed, then $Z_{\text{in}} = 0$. Solving (3.7) for ω where $Z_{\text{in}} = 0$, an equation for the series resonant frequency (f_1) is generated,

$$f_{1_r} = \frac{1}{2\pi\sqrt{L_1 C_1}} = \frac{\omega_1}{2\pi} \tag{3.8}$$

The second scenario is when considering the anti-resonant frequency of the PT. At this frequency, the input impedance is at a maximum. Again assuming $R_1 = 0$, at this frequency $Z_{\text{in}} = \infty$. Solving (3.7) for ω, where $Z_{\text{in}} = \infty$, generates an equation for the anti-resonant frequency (f_{1_a}),

$$f_{1_a} = \frac{\sqrt{C_1 + C_{\text{in}}}}{2\pi\sqrt{C_1 L_1 C_{\text{in}}}} = \frac{\omega_{1_a}}{2\pi} \tag{3.9}$$

Solving both (3.8) and (3.9) as simultaneous equations, allows expressions for both L_1 and C_1 to be derived in terms of f_1, f_{1_a} and C_{in},

$$C_1 = C_{\text{in}}\frac{{f_{1_a}}^2 - {f_1}^2}{{f_1}^2} \tag{3.10}$$

$$L_1 = \frac{1}{\left(4{f_{1_a}}^2\pi^2 - 4{f_1}^2\pi^2\right)C_{\text{in}}} \tag{3.11}$$

Using (3.10) and (3.11), along with experimental measurements of the input capacitance, resonant and anti-resonant frequencies, L_1 and C_1 can be calculated. Finally, by first assuming $1/\omega_1 C_{\text{in}} \gg R_1$, then R_1 is measured as the input impedance of the PT at the series resonant frequency.

3.3.3 Method 3

For method 3, simultaneous equations are created from the expression for the input impedance of the PT, then these equations are solved to find the unknown component values.

Firstly, the impedance of the PT with the output short-circuited is measured at three frequencies. These frequencies include the resonant frequency ω_1 and two other frequencies $\omega_{\alpha,\beta}$ occurring between the series and parallel resonances, $\omega_1 < \omega_{\alpha,\beta} < \omega_{1_\alpha}$. In this implementation, the anti-resonant frequency, and the frequency exactly between the resonant and anti-resonant frequencies are chosen. Similar to the previous two methods, assuming that $1/\omega_1 C_{\text{in}} \gg R_1$, R_1 is found as the impedance measured at the series resonant frequency.

Then, using the three impedance measurements, with the equation for the input impedance of a PT with the output short-circuited (3.4), two simultaneous equations can be generated:

$$Z_2 = \mathrm{Z_{in}}(\omega_\alpha) = \frac{\left(\omega_\alpha - \frac{{\omega_1}^2}{\omega_\alpha}\right)\beta - \mathrm{j}R\omega_1}{R\mathrm{C_{in}}\omega_\alpha\omega_1 + \mathrm{j}\left((\omega_\alpha^2 - {\omega_1}^2)\beta\mathrm{C_{in}} - \omega_1\right)} \tag{3.12}$$

$$Z_3 = Z_{\text{in}}(\omega_\beta) = \frac{\left(\omega_\alpha - \frac{{\omega_1}^2}{\omega_\beta}\right)\beta - \mathrm{j}R\omega_1}{R\mathrm{C_{in}}\omega_\beta\omega_1 + \mathrm{j}\left(\left(\omega_\beta^2 - {\omega_1}^2\right)\beta\mathrm{C_{in}} - \omega_1\right)} \tag{3.13}$$

where Z_1, Z_2 and Z_3 are the impedance of the PT at frequencies ω_1, ω_α and ω_β (rad/s) respectively in the complex form $(a + \mathrm{j}b)$. Equations (3.12) and (3.13) are both rearranged to make C_{in} the subject giving,

$$C_{\text{in}} = \frac{\mathrm{j}Z_1\omega_1\omega_\alpha - \mathrm{j}Z_2\omega_1\omega_\alpha + \beta{\omega_1}^2 - \beta{\omega_\alpha}^2}{Z_2\omega_\alpha(\mathrm{j}\beta{\omega_1}^2 - \mathrm{j}{\omega_\alpha}^2\beta - Z_1\omega_1\omega_\alpha)} \tag{3.14}$$

$$C_{\text{in}} = \frac{\mathrm{j}Z_1\omega_1\omega_\beta - \mathrm{j}Z_3\omega_1\omega_\beta + \beta{\omega_1}^2 - \beta{\omega_\beta}^2}{Z_3\omega_\beta\left(\mathrm{j}\beta{\omega_1}^2 - \mathrm{j}{\omega_\beta}^2\beta - Z_1\omega_1\omega_\beta\right)} \tag{3.15}$$

The resulting equations for C_{in} contain only a single unknown β. Equating (3.14) and (3.15) then rearranging yields a polynomial containing β. After excluding trivial solutions, a quadratic equation remains and is in the form, $a\beta^2 + b\beta + c = 0$. When solved, there are two solutions for β in the form $d \pm \sqrt{e}$, only one of which is valid. These solutions have been omitted due to length. Since both d and e are complex, which solution is valid is affected by the location of the complex number branch points and changes dynamically with ω_0.

Therefore, we will initially consider β to have two potentially valid solutions, $\hat{\beta} \in \{\beta_{<1>}, \beta_{<2>}\}$. Using (3.14) now provides $\hat{C}_{\text{in}} \in \{C_{\text{in}<1>}, C_{\text{in}<2>}\}$. Due to measurement error in Z_1, Z_2 and Z_3, C_{in} and/or β may contain an imaginary part; however, only the real part should be used for solutions. To determine the correct solution set, the two possibilities are evaluated using the cost function F (3.1), with the solution giving the lost cost being selected. Once the most appropriate solutions for C_{in} and β have been found, L_1 and C_1 can then be found using (3.3) and the measured resonant frequency ω_1. Then, as discussed R_1 found as the impedance measured at the series resonant frequency.

To find the final two unknowns C_{out} and N_1, a similar process is performed. Three impedance measurements are again taken at 3 frequencies, but this time from the output terminals of the PT with the input terminals shorted and C_{out} replaces C_{in} in the relevant equations. Finally, N_1 is calculated using (3.5), as was done in method 1.

3.3.3.a) Validity check

In some scenarios, particularly with noisy data, the incorrect set of solutions for C_{in} and β can be chosen. This is due to the correct solution having significant cost, owing to the noisy data, and so a very inaccurate impedance curve can falsely achieve a lower cost. This affect can be mitigated by using a validity check to ensure the resulting components are realistic for PTs. In our implementation, the Q-factor of both solutions sets was calculated using (3.16), in most cases, the invalid solution set gave Q factors < 1, which is too low for typical PT materials.

$$Q_1 = \frac{1}{R_1}\sqrt{\frac{L_1}{C_1}} \tag{3.16}$$

In our testing, by only accepting solutions for C_{in} and β which give a Q factor greater than 1 (typical of a piezoelectric system), negates these issues and greatly increases the noise resilience of the algorithm.

3.3.4 Comparison of methods

A comparison of the implementation complexity of each of the three methods is shown in Table 3.2.

Table 3.2 – A comparison of the ease of implantation of all three methods

	Method 1	Method 2	Method 3
Number of measurements required	Whole frequency sweep around resonance from both input and output terminals. The more impedance measurements recorded, the more accurate the extraction should be	2 capacitance measurements (after varying the output voltage), 2 measurements to find the resonant and anti-resonant frequencies and 1 measurement to find the impedance at the resonant frequency	3 impedance measurements required from both input and output terminals, 1 at the resonant frequency, and two others at frequencies close to resonance
Type of measurement equipment required	Can be performed with a signal generator and an oscilloscope, although a high-quality impedance analyser would	Can be performed with a signal generator and an oscilloscope or an LCR meter, although requires circuitry to ensure the voltage on	Could be performed with a signal generator and an oscilloscope, although a high-quality impedance analyser is required

	increase the accuracy of the measurement	the output terminals is at the correct amplitude and in-phase	to ensure high accuracy in both impedance magnitude and phase measurements
Suitable for all PT topologies	Yes	Yes	Yes
A priori knowledge of PT geometry	No	No (Although it is useful to estimate the turns ratio to accelerate the voltage matching process)	No
Approximate computation time (MATLAB implementation)	>1 min, however, depends on the amount of data	<1 sec	<1 sec

As Table 3.2 shows, each of the three methods are applicable to different situations, depending on the experimental equipment or the time required for each extraction.

3.3.4.a) Experimental results

In most cases, implementation challenges or slow execution time can be overlooked if the method in question provides noticeable accuracy improvement. Analysing the accuracy of each method is difficult, as it is impossible to know the precisely correct equivalent circuit values of the PT under test. Therefore, the accuracy of the extracted parameters can only be determined by first extracting the equivalent circuit parameters of the PTs using each method, substituting these parameters into (3.2), simulating the impedance of the PT across a range of frequencies $\left(Z_{\text{expression}}\right)$ and then observing how well the simulated impedance spectra matches the measured impedance spectra (Z_{measured}).

To begin, the relevant impedance measurements are taken from a radial mode Transoner PT using an OMICRON Bode 100 vector network analyser. Each of the three algorithms are then used with the relevant measurement data to extract the equivalent circuit components. The resulting extracted component values are shown in Table 3.3.

Table 3.3 – Extracted equivalent circuit component values

	$R_1(\Omega)$	$L_1(\mathrm{mH})$	$C_1(\mathrm{pF})$	$C_{\mathrm{in}}(\mathrm{nF})$	$C_{\mathrm{out}}(\mathrm{nF})$	N_1
Method 1	14.98	8.486	178.8	2.170	1.124	0.92
Method 2	14.98	8.549	177.5	2.155	1.431	1
Method 3	14.98	9.397	161.5	1.962	1.145	0.98

Using the results in Table 3.3, with the equation for the input impedance of a PT with the output short-circuited (3.2), the input impedance spectrum is simulated. The three simulated input impedance spectra are shown in Fig. 3.7, along with the measured input impedance spectrum for comparison.

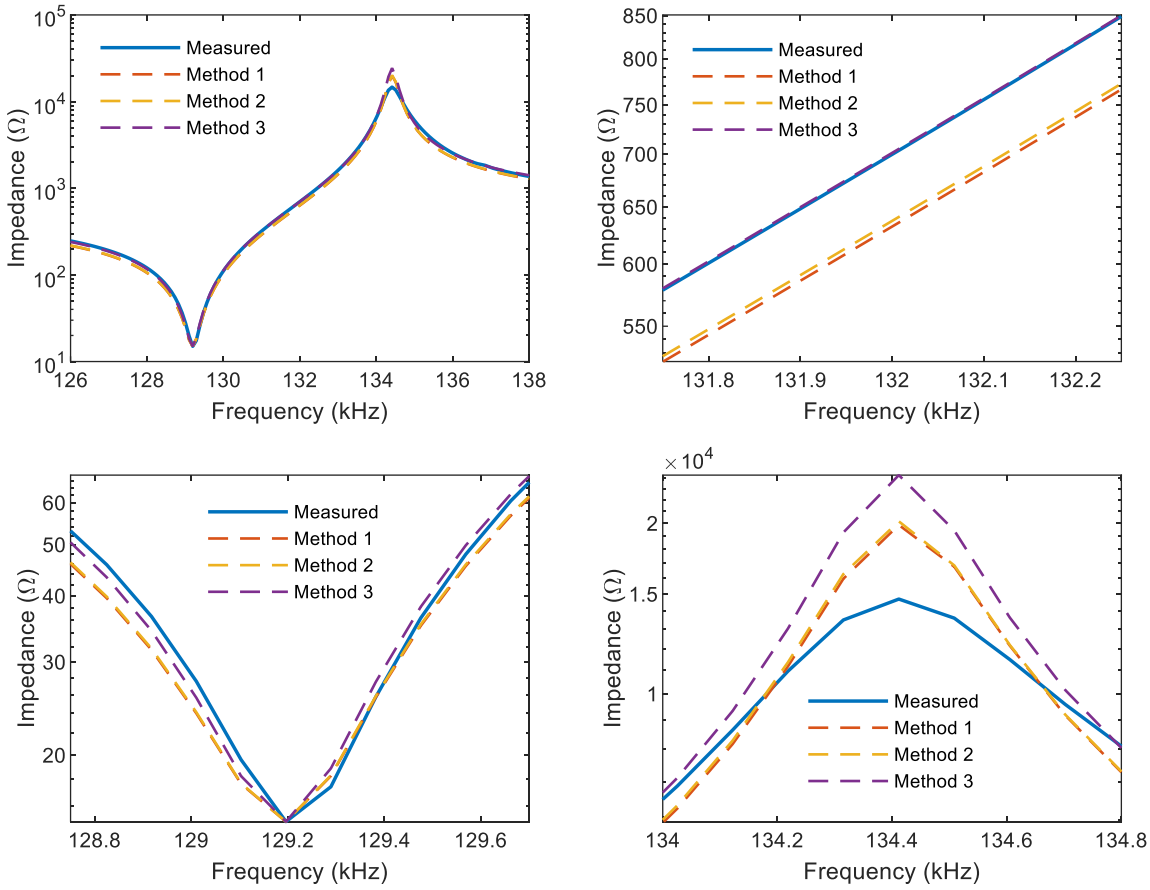

Fig. 3.7 – Measured input impedance of the PT with the estimated input impedance from each of the 3 methods

Observing Fig. 3.7, each of the three methods produces a similar impedance spectrum to that which was measured. The resulting impedance curves from all three methods exhibit the same resonant and anti-resonant frequencies. Observing the impedance curves at 132kHz, method 3 matches closely to the measured response, whereas methods 1 and 2 produce impedance spectra that have some error. Conversely, at 134.4kHz (anti-resonant frequency), all methods exhibit a large error, however, methods 1 and 2 have significantly less error than method 3.

Although it is not possible to determine which of the 3 methods provides the most accurate extraction, due to not knowing the exact equivalent circuit values, overall, each of the three methods produced a simulated impedance which provided an acceptable match to the measured impedance. Method 2 had the lowest root-mean-square error (RMSE) (3.17) between the measured and simulated impedance spectra, 521Ω, 544Ω and 948Ω for method 1 ,2 and 3, respectively. Although, this is mainly due to its closer match to the measured impedance at the anti-resonance compared to method 3. Method 3 had the lowest

percentage error (3.18) between the measured and simulated response, 8.5%, 7.9% and 4.6% error for methods 1, 2 and 3, respectively.

$$RMSE = \sqrt{\sum (|Z_{\text{measured}}(\omega)| - \lceil Z_{\text{simulated}}(\omega) \rceil)^2} \tag{3.17}$$

$$\%\ \text{error} = \frac{\sum \left| \frac{|Z_{\text{measured}}(\omega)| - \lceil Z_{\text{simulated}}(\omega) \rceil}{|Z_{\text{measured}}(\omega)|} \times 100 \right|}{\text{no. of datapoints}} \tag{3.18}$$

3.3.4.b) Noise resilience

To perform accurate component extraction, accurate impedance measurements are required. However, measurement systems are not noise-free. In an ideal case, the impedance would be measured many times and then averaged to remove the influence of noise. However, this is often not practical and so in most scenarios only a single measurement will be performed. Therefore, it is important that the extraction methods can still provide accurate component extractions even when the impedance measurements contain noise.

Table 3.4 – Equivalent circuit component values used in the noise simulation

$R_1(\Omega)$	$L_1(\mathbf{mH})$	$C_1(\mathbf{pF})$	$C_{\text{in}}(\mathbf{nF})$	$C_{\text{out}}(\mathbf{nF})$	N_1
10	4	500	1	2	2

The equivalent circuit model of a PT was simulated, using the component values in Table 3.4. The relevant voltage and current measurements required for each extraction method are recorded at frequencies near the resonant frequency. For this analysis, the noise will be attributed exclusively to measurement noise. Firstly, assuming the measurement device has an analogue-to-digital converter (ADC) which will read a voltage between 0-1V, the current will be converted to a voltage for the ADC to read, and it is assumed that the maximum current to be measured is 10 times smaller in magnitude than the maximum voltage. If the maximum amplitude of the voltage signal is 1V (to fully utilise the ADC), then the current should be amplified by a factor of 10 to similarly use the full range of the ADC. Therefore, if the noise introduced during the measurement process is the same magnitude for both the voltage and current measurements, when the current is reduced by a factor of 10 after analogue to digital conversion, the current noise will also be reduced by this factor. This means the voltage noise

will be an order of magnitude larger than the current noise. To simulate the noise, white Gaussian noise of a known amplitude is then added to both the voltage and current measurements and from this, the impedance is then simulated. An example of the noisy impedance is shown in Fig. 3.8.

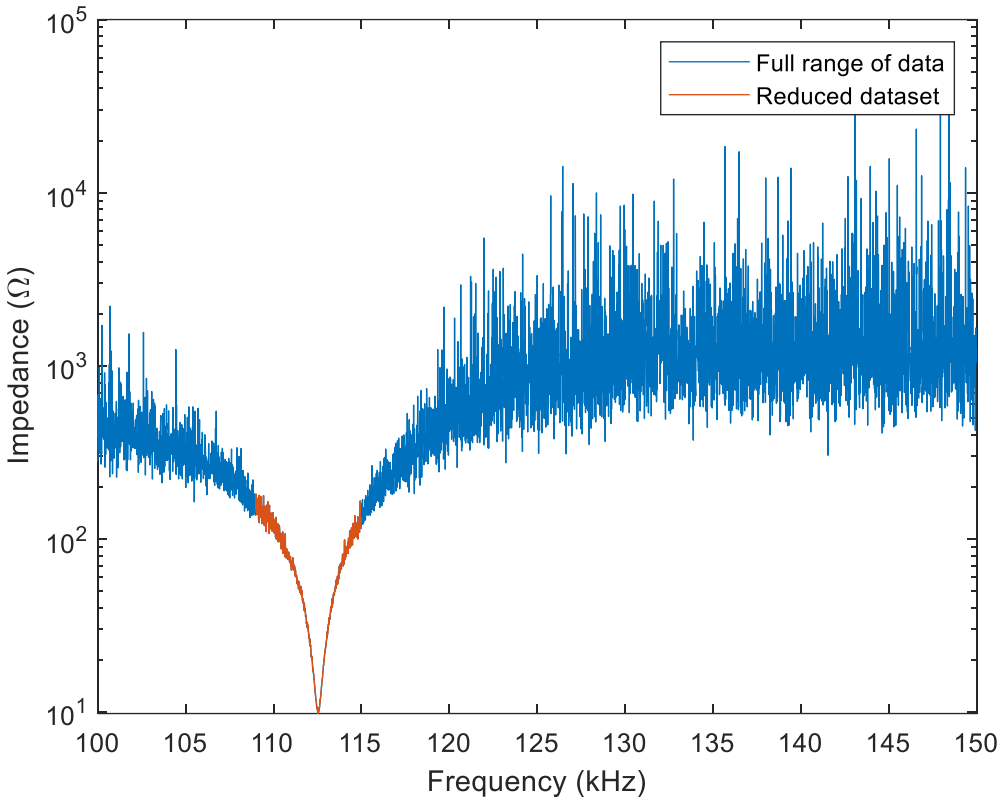

Fig. 3.8 – Example impedance with -40dB of voltage noise and -60dB of current noise

Using the noisy data, each of the three methods are used to extract the equivalent circuit component values of the simulated PT. Methods 1 and 3 are additionally repeated a second time but only extracting the components from a smaller dataset containing only the low impedance section of the response. At the frequencies where the PT exhibits low impedance, the input current is therefore large and as the measurement noise is constant in this case, where the current is large, the signal to noise ratio (SNR) is consequently large. Therefore, in theory, using only data that has a high SNR should lead to increased accuracy in the extracted components. Unfortunately, due to method 2 requiring the anti-resonant frequency to derive some of the components, it is not possible to use the reduced dataset with this method. This process of adding noise to the measurements and component extraction is then repeated 100 times to simulate different noise conditions. The average percentage error and the standard

deviation in this error for the extracted L_1 and C_{in} values are found across the 100 measurements. The results of this analysis are shown in Fig. 3.9 and Fig. 3.10.

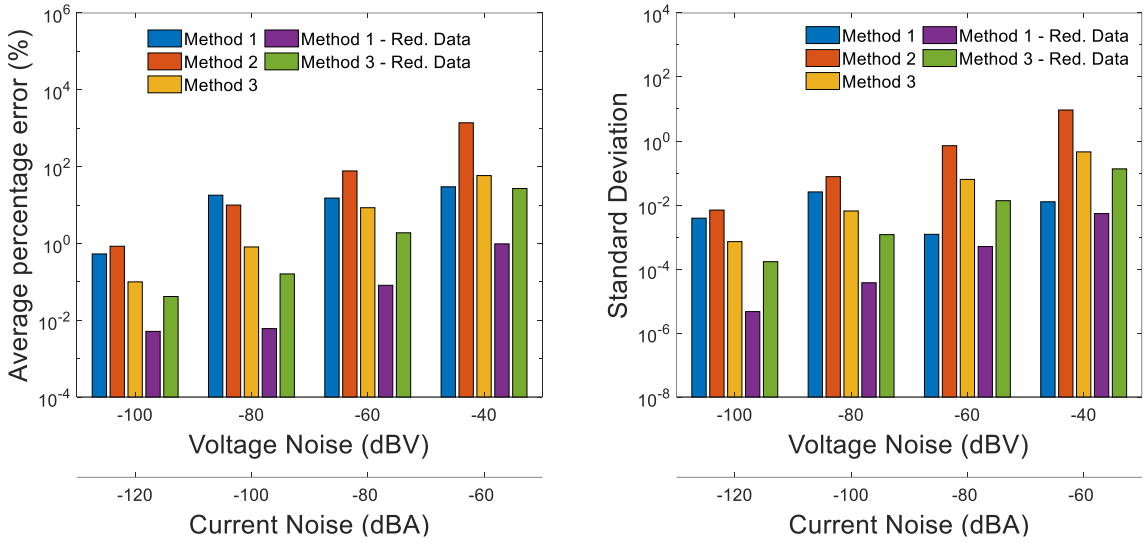

Fig. 3.9 – Average percentage error and standard deviation in the percentage error in the extraction of the inductance (L_1) from impedance data containing various levels of noise

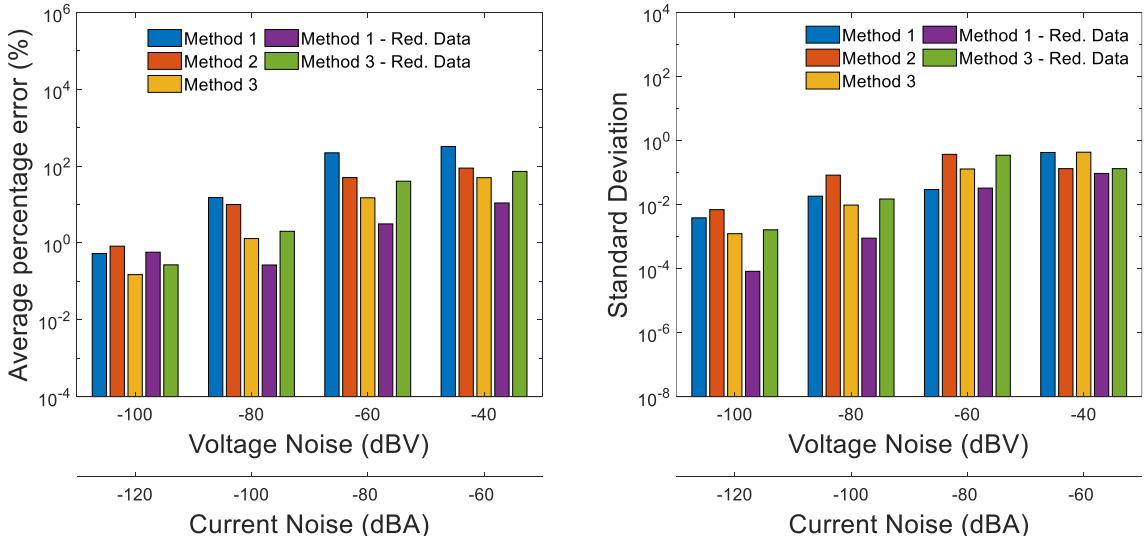

Fig. 3.10 – Average percentage error and standard deviation in the percentage error in the extraction of the input capacitance (C_{in}) from impedance data containing various levels of noise

In general, the results show that the greater the noise level, the more error and the greater the standard deviation in the resulting extracted components. Comparing the three methods using the full range of data, method 3 is the most optimum method, exhibiting the lowest mean error and lowest standard deviation of each of the three methods. Method 1 is slightly more accurate at very high (-40 dBV voltage and -60 dBA current) noise in the L_1 extraction but was worst of the three methods during the C_{in} extraction. Method 2 provides the least accurate extractions of the three methods, only producing slightly better C_{in} extractions than

method 1. The results show that overall, method 1 and 2 are more sensitive to noise than method 3.

Method 1 with the reduced dataset proves to be the most optimum method for combatting noise in the data. The resulting component extractions exhibited the lowest error and standard deviation across all noise powers tested. Using method 3 with a reduced dataset has mixed results, with improvements over method 3 using the full range of data in the inductance extraction but more error in the C_{in} extraction. This can be attributed to the spot measurements and any noise in these measurements having dramatic effect on the results. Therefore, when the impedance measurements contain significant noise, using method 1 to perform the extraction with only the section of the impedance data that has a high SNR is the most optimal, due to the estimation technique method 1 employs.

3.4 Low capacitance/ high damping Extraction Method

Whist the methods presented in section 3.3 perform excellently on standard, high Q factor PTs, they become inaccurate for higher damping, non-ideal PTs. Therefore, a technique is presented, which is suitable for measuring non-ideal PTs or the non-dominant and/or spurious modes.

3.4.1 Limitations of previous approaches

When the output terminals of the PT are short circuited, and the PT is driven at the resonant frequency (ω_1), the input impedance is equal to the input capacitance and the damping resistance in parallel,

$$Z_1 = \left.\frac{R_1 Z_{C_{\mathrm{in}}}}{R_1 + Z_{C_{\mathrm{in}}}}\right|_{\omega=\omega_1} \tag{3.19}$$

where Z_1 is the input impedance of the PT at resonance and $\mathrm{Z}_{C_{\mathrm{in}}}$, a function of ω, is the impedance of the input capacitor given by,

$$Z_{C_{\mathrm{in}}} = \frac{-\mathrm{j}}{\omega C_{\mathrm{in}}} \tag{3.20}$$

If $1/(\omega_1 C_{\mathrm{in}}) \gg R_1$ is a valid assumption, Z_1 is dominated by the damping resistance and so R_1 is approximately equal to the magnitude of the input impedance and the resonant frequency

can be taken as the frequency at which the input impedance at a minimum. However, when $1/(\omega_1 C_{\text{in}}) \gg R_1$ is invalid, R_1 does not dominate the input impedance and, as a result, estimation of R_1 using existing approaches is prone to error. Additionally, and as a consequence, the minimum impedance frequency is no longer the resonant frequency of the PT.

This limitation can be illustrated by simulating the input impedance of a PT with the output shorted (Fig. 3.3). The damping resistance is varied through a range of values, and the apparent resonant frequency and damping resistance are extracted using any of the general-purpose methods presented previously. The results of the analysis are shown in Table 3.5.

Table 3.5 – Error in extracted damping resistance and resonant frequency with changes in true damping resistance relative to input capacitance (L_1=10mH, C_1=50pF, C_{in}=5nF, V_{out} short circuited)

$R_1/\lvert Z_{C_{\text{in}}}\rvert$		0.1	0.2	1	2	10
Error in R_1	%	0.99	3.7	38	61	90
	Ω	0.14	1.05	54	172	1275
Error in ω_1	%	<0.01	0.019	0.31	0.75	2.3
	Hz	11	43	687	1681	5099

The results in Table 3.5 confirm that when $1 / (\omega_1 C_{\text{in}}) \gg R_1$, the error in the extracted components is negligible. However, for high R_1 or small $Z_{C_{\text{in}}}$, the extracted values show significant error.

3.4.2 Proposed method

The proposed extraction method uses, as its foundation, method 3 as described previously. The proposed method has two elements—component value extraction and ω_1 estimation—both of which are executed simultaneously. In our proposal, we initially assume ω_1 is known before optimising the extracted component values to find the correct solution for ω_1.

3.4.2.a) Component extraction

The input impedance (output shorted) of the PT is measured at two arbitrarily chosen frequencies in the vicinity of the resonant frequency. An expression for the impedance at these two arbitrarily chosen frequencies, ω_α and ω_β, is given by (3.12) and (3.13).

It is difficult to measure R_1 accurately independent of our approach, therefore it is beneficial to initially remove it from (3.12) and (3.13). At resonance (ω_1), the RLC reduces to just R_1, therefore, the input impedance (output shorted) is equal to the input capacitance and damping resistance in parallel [see (3.19)]. Substituting (3.20) into (3.19) and rearranging for R_1 yields,

$$R_1 = \frac{Z_1}{1 - \mathrm{j}C_{\mathrm{in}}Z_1\omega_1} \tag{3.21}$$

Equation (3.21) is then substituted into (3.12) and (3.13).

$$Z_2 = \frac{\left(\omega_2 - \frac{{\omega_1}^2}{\omega_2}\right)\beta - \mathrm{j}\frac{Z_1}{1 - \mathrm{j}C_{\mathrm{in}}Z_1\omega_1}\omega_1}{\frac{Z_1 C_{\mathrm{in}}\omega_2\omega_1}{1 - \mathrm{j}C_{\mathrm{in}}Z_1\omega_1} + \mathrm{j}\left((\omega_2^2 - {\omega_1}^2)\beta C_{\mathrm{in}} - \omega_1\right)} \tag{3.22}$$

$$Z_3 = \frac{\left(\omega_3 - \frac{{\omega_1}^2}{\omega_3}\right)\beta - \mathrm{j}\frac{Z_1}{1 - \mathrm{j}C_{\mathrm{in}}Z_1\omega_1}\omega_1}{\frac{Z_1 C_{\mathrm{in}}\omega_3\omega_1}{1 - \mathrm{j}C_{\mathrm{in}}Z_1\omega_1} + \mathrm{j}\left((\omega_3^2 - {\omega_1}^2)\beta C_{\mathrm{in}} - \omega_1\right)} \tag{3.23}$$

Equations (3.22) and (3.23) are no longer a function of R_1 but, rather, are a function of Z_1, which is directly measurable. Equations (3.22) and (3.23) can be rearranged for β,

$$\beta = \frac{\left(C_{\mathrm{in}}(\omega_2 - \omega_1)Z_2Z_1 + \mathrm{j}(Z_1 - Z_2)\right)\omega_1\omega_2}{\left(1 - C_{\mathrm{in}}^2 Z_1Z_2\omega_1\omega_2 - \mathrm{j}C_{\mathrm{in}}(Z_1\omega_1 + Z_2\omega_2)\right)(\omega_2^2 - \omega_1^2)} \tag{3.24}$$

$$\beta = \frac{\left(C_{\mathrm{in}}(\omega_3 - \omega_1)Z_3Z_1 + \mathrm{j}(Z_1 - Z_3)\right)\omega_1\omega_3}{\left(1 - C_{\mathrm{in}}^2 Z_1Z_3\omega_1\omega_3 - \mathrm{j}C_{\mathrm{in}}(Z_1\omega_1 + Z_3\omega_3)\right)(\omega_3^2 - \omega_1^2)} \tag{3.25}$$

Equating (3.24) and (3.25) then rearranging yields a polynomial containing C_{in}. After excluding trivial solutions, a quadratic equation remains and is in the form, $aC_{\mathrm{in}}^2 + bC_{\mathrm{in}} + c = 0$. When solved, there are two solutions for C_{in} in the form $d \pm \sqrt{e}$, only one of which is valid. These solutions have been omitted due to length. Since both d and e are complex, which solution is valid is affected by the location of the complex number branch points and changes dynamically with ω_1.

Therefore, we will initially consider C_{in} to have two potentially valid solutions, $\widehat{C}_{\text{in}} \in \{C_{\text{in}<1>}, C_{\text{in}<2>}\}$. Given experimental input impedance measurements at the resonant frequency and two neighbouring frequencies (Z_1, Z_2 and Z_3 respectively), using $\widehat{C}_{\text{in}}$ leads to two solutions for R_1 from (3.21), thus $\widehat{R_1} \in \{R_{1<1>}, R_{1<2>}\}$. Using (3.24) then provides $\hat{\beta} \in \{\beta_{<1>}, \beta_{<2>}\}$. Due to measurement error in Z_1, Z_2 and Z_3, any of C_{in}, β or R_1 may contain an imaginary part; however, only the real part should be used for solutions. To determine the correct solution set, the two possibilities are evaluated using an adapted version of the cost function F (3.1), $J(\omega_1)$, which has dependency on the unknown resonant frequency ω_1,

$$\min_{\omega_1, x} J = \int_{\omega_1-\Delta\omega}^{\omega_1+\Delta\omega} \left(\frac{|Z_{\text{measured}}(\omega)| - |Z_{\text{in}}(\omega, \omega_1, x)|}{|Z_{\text{measured}}(\omega)|} \right)^2 \mathrm{d}\omega \tag{3.26}$$

where $x \in \{\hat{C}_{\text{in}}, \widehat{R_1}, \hat{\beta}\}$ and Z_{measured} is the measured input impedance of the PT, with the output shorted, at a range of frequencies in the vicinity of the expected resonance ($\Delta\omega$ is typically around 15% of ω_1). Using (3.26) and (3.2) with both possible solution sets for β, C_{in} and R_1, and experimental measurements of the input impedance over the range of frequencies, yields J. The set of parameters with the lowest cost, yields the best model parameters for a particular value of ω_1.

3.4.2.b) Determination of ω_1

In the methods presented in the previous section and by Ivensky *et al.* [3.3] and Horsley *et al.* [3.1], the resonant frequency (ω_1) is taken as the frequency at which input impedance is minimised. This is inaccurate if R_1 is large. However, without prior knowledge of L_1 and C_1, it is not possible to precisely calculate the resonant frequency and therefore its value must be estimated.

Here, the minimum impedance frequency is a first approximation for ω_1. The value of ω_1 is then optimised using (3.26). The ω_1 value, which leads to the overall minimum cost, will give the best approximation to β, C_{in}, R_1 and ω_1. The values of L_1 and C_1 can then be calculated using (3.3).

The range of possible values for ω_1 is constrained since ω_1 must lie between the minimum and maximum impedances for the mode of interest. Many methods may be used to minimise J; in our implementation, an exhaustive search was used. An example of the typical output of

J, for both sets of x, across the range of ω_1 values examined, is shown in Fig. 3.11. The overall minimum point on Fig. 3.11 corresponds to the most accurate model parameters.

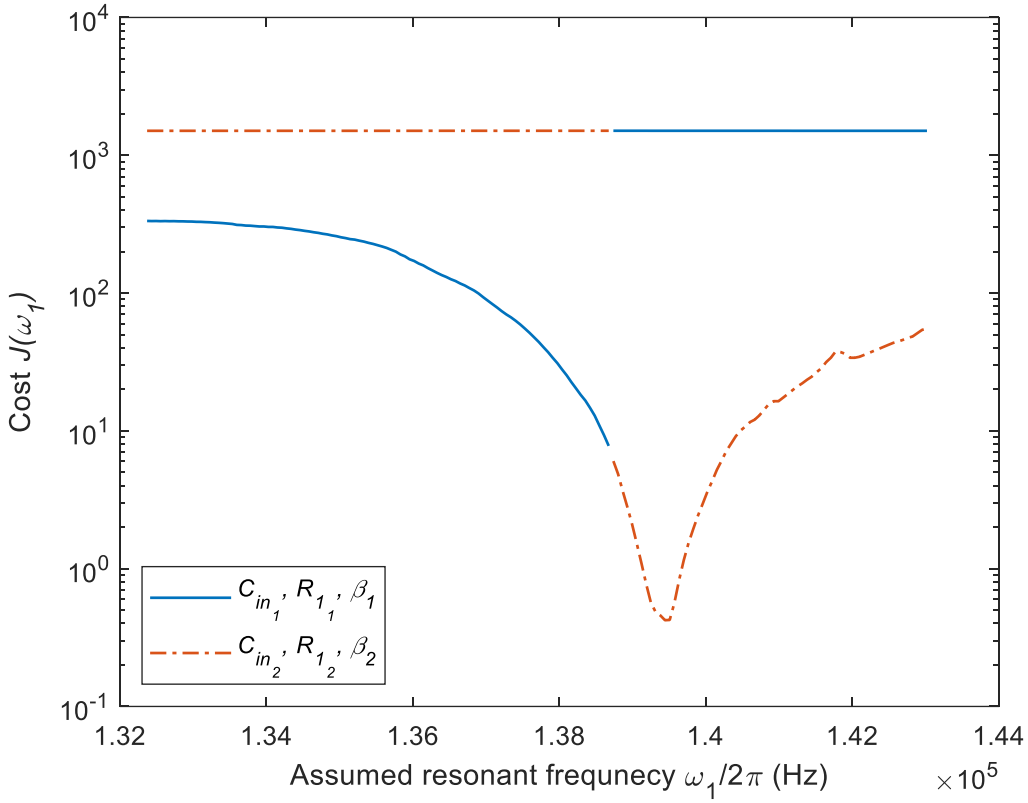

Fig. 3.11 – Typical output of the cost function J for both solution sets (x) across the range of ω_1 tested. This is the output from the parameter extraction of the BSPT PT discussed in experimental results and shown in Fig. 3.16. Discontinuity in the solution is due to the branch point selection in the principal solution for complex square roots

3.4.2.b.i) Additional methods of determining $\boldsymbol{\omega_1}$

Whilst the method described previously works in the majority of situation, in some cases the measured impedance is highly non-ideal, as is often the case for high temperatures PTs where, owing to need for specific materials, the damping is very high and the difference between the maximum and minimum impedance is small. In these situations, incorrect parameters can give the lowest cost, as they give a better fitting curve to the measured impedance. In some cases, the resulting impedance curve is highly incorrect and gives rise to very unrealistic resulting parameters.

To avoid this, an alternative method of determining the correct ω_1 can be used. One alternative is to choose an ω_1 which leads to the most accurate maximum and minimum impedance frequencies. Therefore, a second cost function can be derived,

$$\min_{\omega_1, x} J = \left|\omega(\min(Z_{\text{measured}})) - \omega\left(\min\left(Z_{\text{in}}(\omega_1, x)\right)\right)\right| + \left|\omega(\max(Z_{\text{measured}})) - \omega\left(\max\left(Z_{\text{in}}(\omega_1, x)\right)\right)\right| \quad (3.27)$$

As with the previous method, the combination of parameters that leads to the lowest cost, gives the best estimate for the parameters of the PT.

3.4.2.c) Determination of C_{out} and N_1

The remaining equivalent circuit parameters, C_{out} and N_1 can be found by repeating the same extraction process but with experimental measurements from the output terminals (input shorted) and with C_{out} replacing C_{in} in all relevant equations. Finally, N_1 can be determined by recognising that

$$N_1 = \sqrt{\frac{\beta_{\text{out}}}{\beta_{\text{in}}}} \quad (3.28)$$

β_{in} and β_{out} are the β values found from parameter extraction using input and output impedance measurements, respectively.

3.4.2.d) Validity check

As was done for method 3 presented previously, a validity check will be used to reduce the likelihood of choosing the incorrect solution set. Again, Q factor was calculated for both solution sets using (3.16), and only solutions which lead to a Q factor greater than 1 are accepted. However, unlike low damping PTs, PTs with higher damping typically exhibit lower Q-factors, therefore, this value should be set carefully as in some cases, modes may correctly exhibit Q-factors less than 1.

3.4.3 Comparison with general purpose methods

3.4.3.a) Simulated data

The performance of this method is compared to the general-purpose methods presented in the previous section. A PT, with parameters given in Table 3.4, is simulated with the damping resistance R_1 varied in the range $100\Omega - 1\text{k}\Omega$. At each variation, the proposed method, and the previous method(s) (all 3 methods use the same damping resistance extraction method) described in section 3.3 will be used to extract the damping resistance. The results of this simulation are shown in Fig. 3.12.

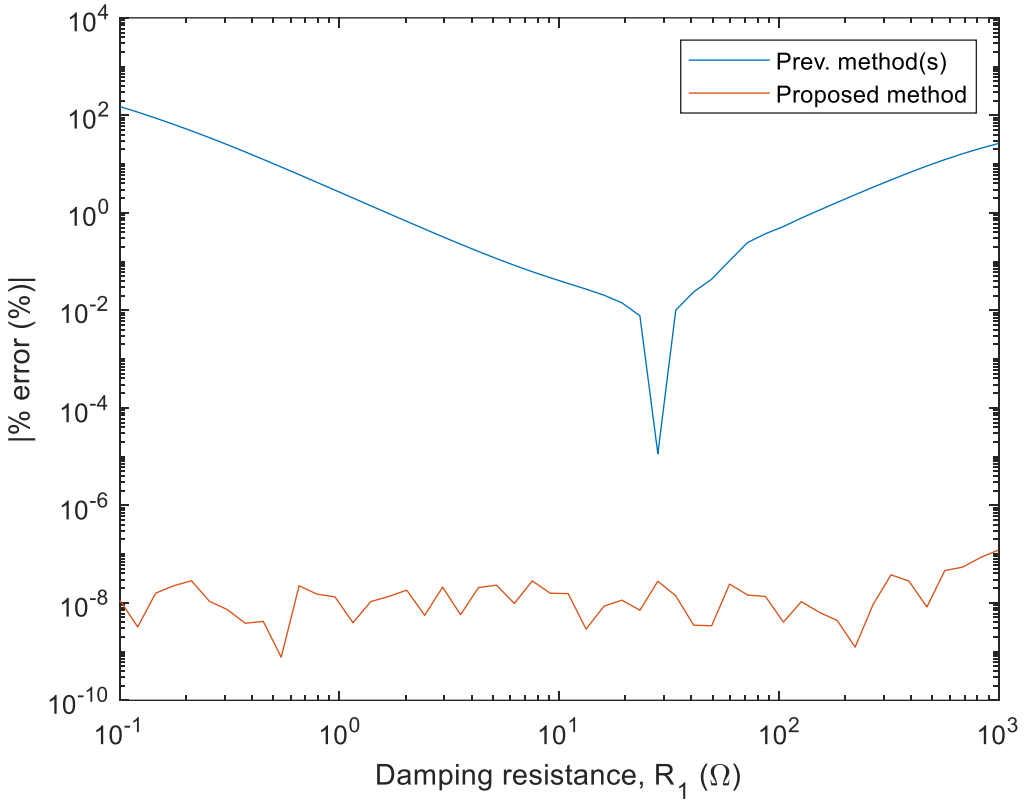

Fig. 3.12 – Percentage error in R_1 extraction with damping resistance R_1, for the three general-purpose methods and the proposed method

Observing Fig. 3.12, the proposed method shows significant performance improvements over previous approaches. The proposed method shows an average error of $8.37x10^{-9}\%$, whilst the previous method has an average error of 9.02%. The previous method gives poor results at both high and low values of damping resistance. Whilst the error at high damping has been discussed previously, the error at low damping is due to poor frequency resolution in the impedance measurement, therefore, by not having an impedance measurement at exactly the minimum impedance frequency the extracted damping value is in accurate. Therefore, this error can be reduced with increased frequency resolution. The proposed method showed consistent and excellent performance across the range of damping values tested.

As described earlier, some of the general-purpose methods use the damping resistance to then subsequently calculate the remaining equivalent circuit components. Therefore, when large errors are observed in the damping resistance, large errors in the other components can be expected. To evaluate this, a similar simulation will be performed as was done in Fig. 3.12. Each of the three previous methods and the proposed method will be used to extract L_1 and C_1 from the simulated input impedance, with an increasing value of damping resistance. The

percentage error of the extracted inductance L_1 and capacitance C_1 are plotted in Fig. 3.13 and Fig. 3.14 respectively.

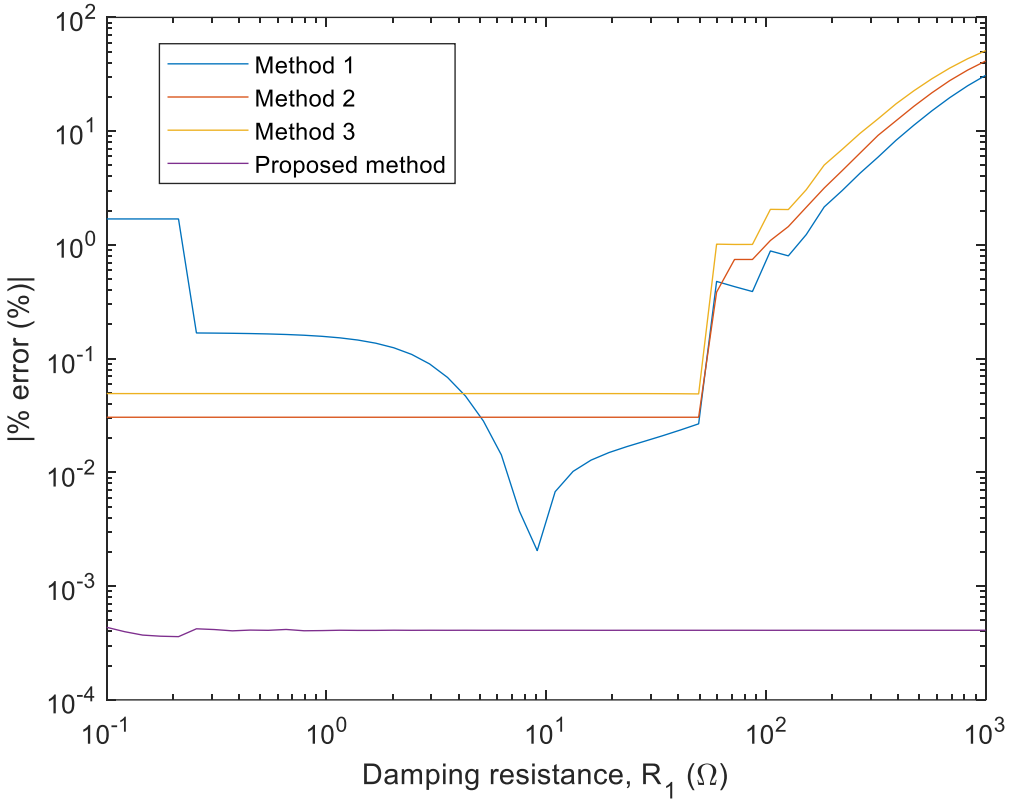

Fig. 3.13 – Percentage error in L_1 extraction with damping resistance R_1, for the three general-purpose methods and the proposed method

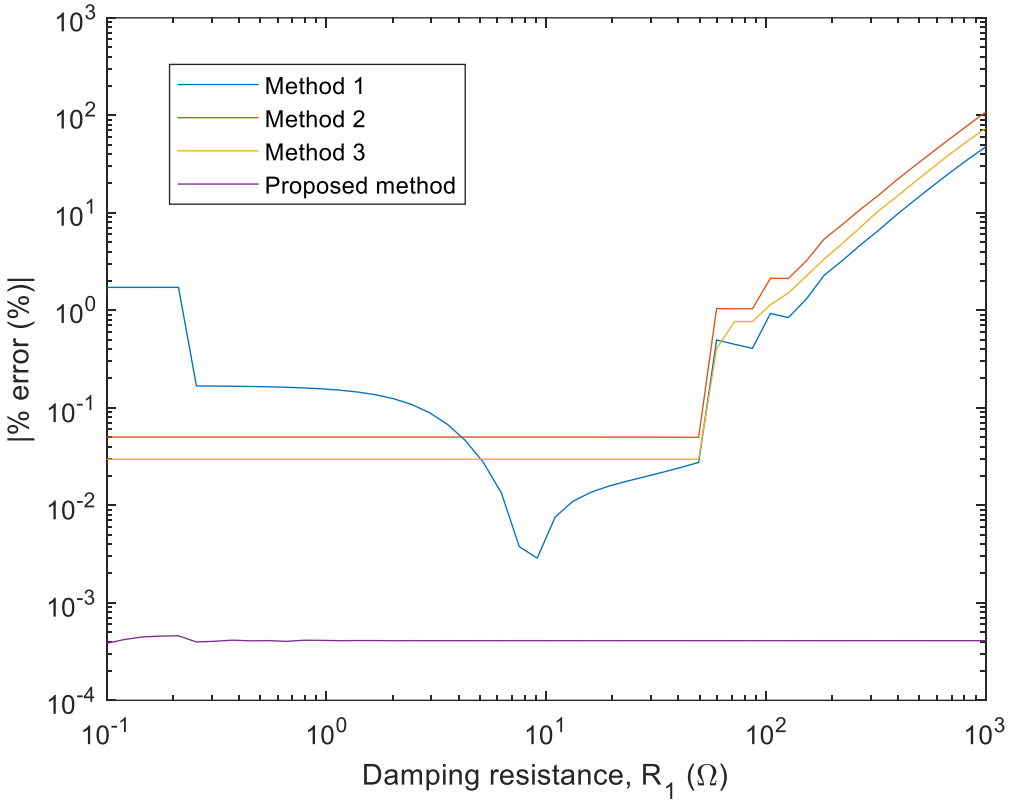

Fig. 3.14 – Percentage error in C_1 extraction with damping resistance R_1, for the three general-purpose methods and the proposed method

Observing Fig. 3.13, as expected, all three of the previous methods show increasing error with increasing damping resistance for damping resistances greater than 50Ω. Methods 2 and 3 show consistent and accurate results at lower damping values, whereas method 1 exhibits large error at very high and very low damping values. However, method 1 has a lower average error (3.6%) than both method 2 (5.3%) and method 3 (7.8%). This lower error in method 1 is due to its significantly lower percentage error when damping is between $5\Omega - 50\Omega$. However, the proposed method shows significantly lower average error than all other methods ($4.1x10^{-4}\%$) and unlike previous approaches is very consistent across the range of damping values tested. Fig. 3.14 shows very similar results to Fig. 3.13, with the three previous methods showing increasing error with larger damping resistances. Again, the proposed method shows significantly lower error overall and is consistent across the range of damping resistances evaluated.

Based on the results in Fig. 3.13 and Fig. 3.14, the proposed method provides significant improvement over the methods described previously, even when extracting low damping PTs.

Therefore, the proposed method is the most optimal method to use when analysing all PTs when the input impedance data is ideal.

3.4.3.b) Experimental results

The equivalent circuit parameters of two sample PTs are extracted to verify the accuracy of the proposed method. Method 3 is also included for comparison, as this method had the lowest percentage error of the three general purpose methods when extracting from an experimental PT, as shown in Fig. 3.7. The accuracy of each method is quantified by calculating RMSE (3.17) and percentage error (3.18) between the theoretical impedance spectrum of the parameterised model and the experimentally measured impedance spectrum. Error is calculated using both linear frequency and impedance.

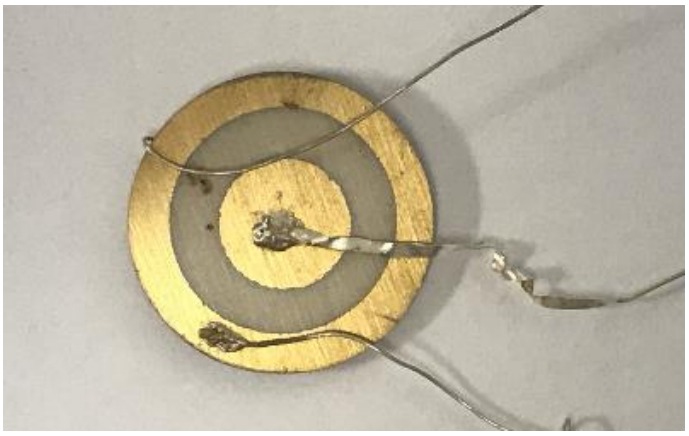

Fig. 3.15 – BSPT ring-dot PT used in experimental measurements

The first PT under test is a ring-dot PT made from $BiScO_3$–$PbTiO_3$ (BSPT), shown in Fig. 3.15. The PT has a dot radius of 3mm, an inner ring radius of 5mm, an outer radius of 8mm and a thickness of 1mm. The output electrode (outer ring) of the PT is shorted to ground, and the input impedance of the PT is measured between the input (dot) and ground (bottom face) electrodes using an Omicron Bode 100 vector network analyser. The measured and theoretical output impedance spectra (input shorted) produced from both extraction methods are shown in Fig. 3.16.

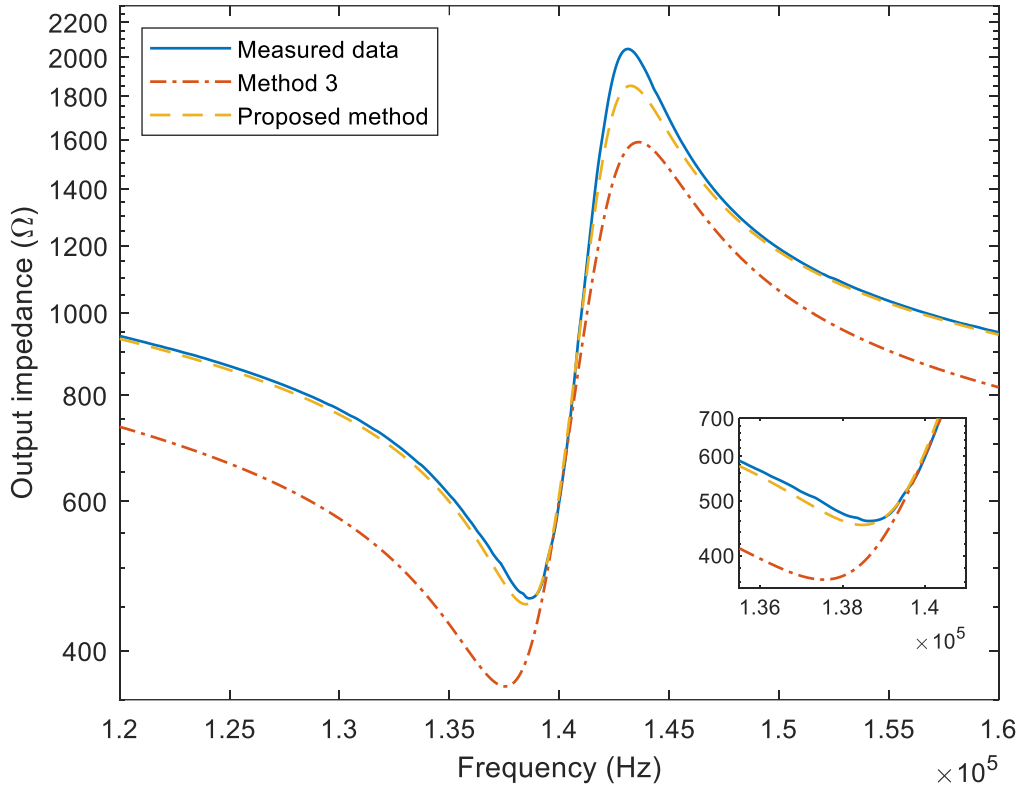

Fig. 3.16 – Measured and simulated output impedance spectra from the BSPT PT

From the results in Fig. 3.16, it is clear the proposed method produces a fitted impedance, which is a closer match to the measured response than method 3. Whilst method 3 exhibits 180.7Ω RMSE and 17.8% error, the proposed method only exhibits 29.3Ω RMSE and 1.4% error between simulated and measured impedance spectra. It should be noted there is a noticeable error at the anti-resonant frequency between the proposed method and the measured response. This is likely due to unmodelled parasitic elements, such as inductance in the measurement leads.

A second PT is also tested. This time, extraction is performed on a spurious resonant mode. The PT under test (TI-PP0361) is a radial mode Transoner PT made from APC841, with dimensions as shown in Fig. 7b of [3.4]. Extraction is performed on the lowest-frequency-resonance exhibited by the PT (36 kHz). The resulting measured and simulated input impedance spectra are shown in Fig. 3.17.

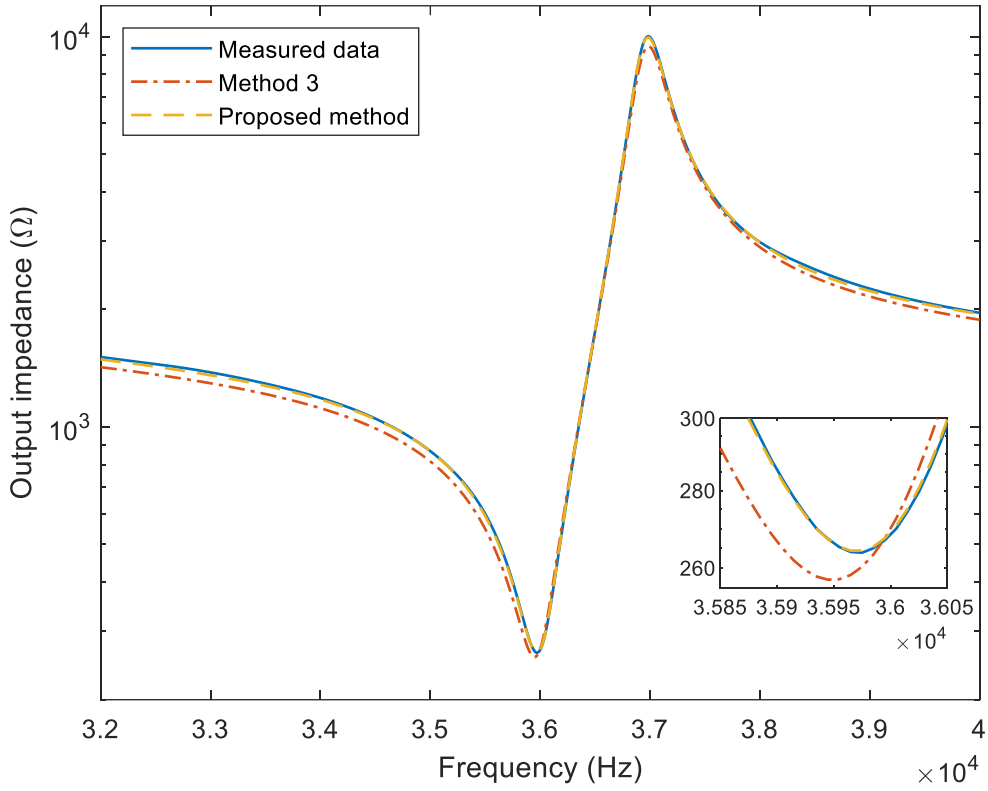

Fig. 3.17 – Measured and simulated input impedance spectra from the TI-PP0361 PT

Again, the proposed method produces a more accurate extraction, with the fitted impedance spectra produced by previous and proposed methods having 114.6Ω and 22.2Ω RMSE compared to the measured spectra, respectively. Additionally, whilst method 3 had a percentage error of 4.2%, the proposed method exhibited only 0.5% error.

3.4.3.c) Noise resilience

As was discussed previously for the general-purpose methods, impedance data can often be noisy, therefore, equivalent circuit extraction methods are required to be accurate even with high levels of noise in the impedance data. A similar noise analysis is performed to that in section 3.3.4.b). For comparison, the noise results for method 3 and method 1 with reduced data were included, as these were the best performing methods in the previous section. The results are shown in Fig. 3.18 and Fig. 3.19.

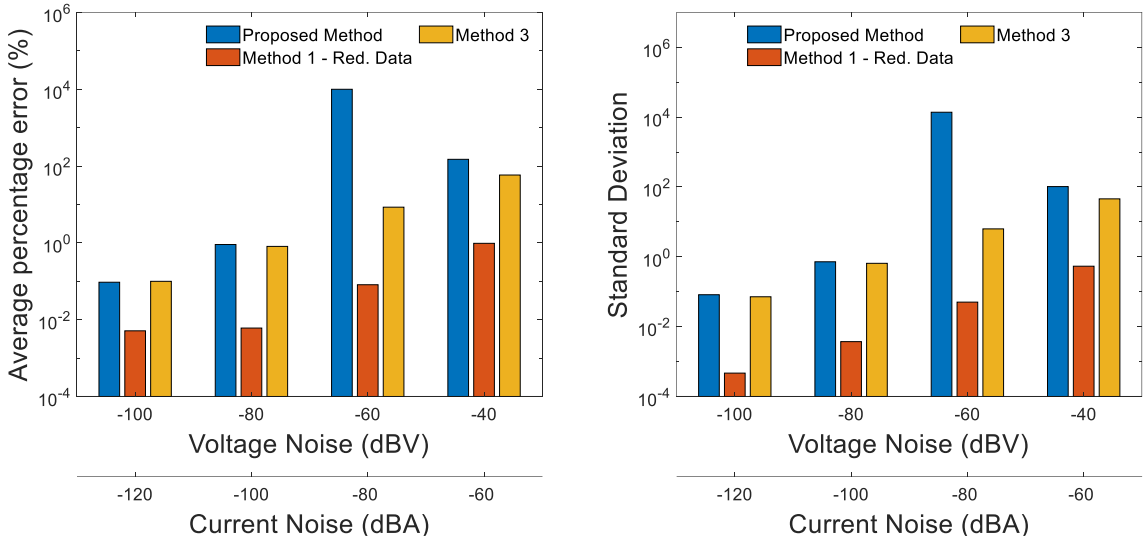

Fig. 3.18 – Average percentage error and standard deviation of the estimated L_1 values against noise

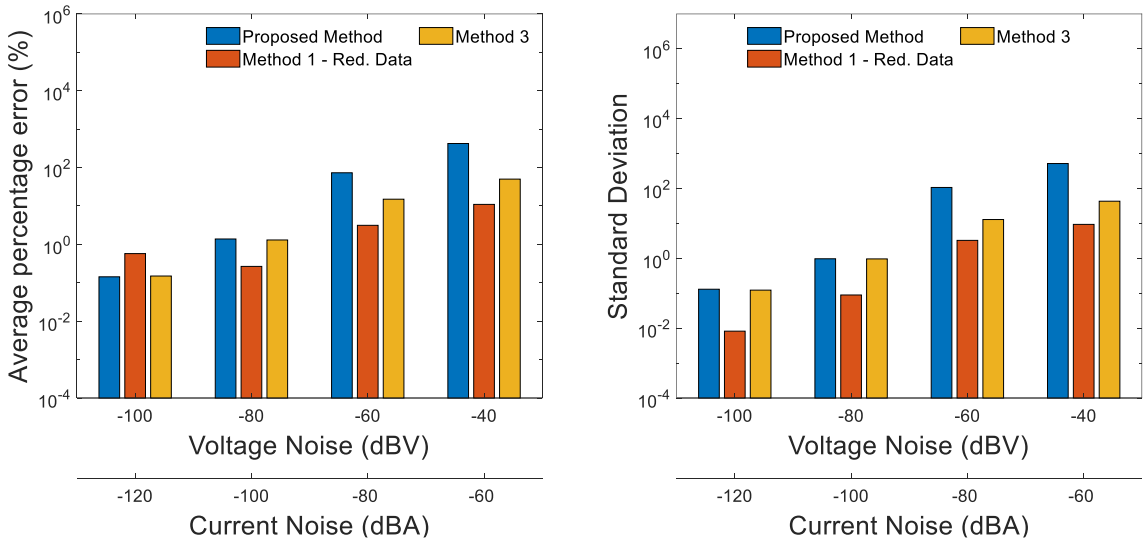

Fig. 3.19 – Average percentage error and standard deviation of the estimated C_{in} values against noise

Observing the results in Fig. 3.18 and Fig. 3.19, we can see that the proposed method performs similarly to method 3 at low noise powers, which is to be expected as the algorithms are similar. At the lowest noise power, both the proposed method and method 3 outperform method 1 with reduced data in the C_{in} extraction, however, method 1 with the reduced dataset outperforms both method 3 and the proposed method in all other tests. At higher levels of noise, the proposed method has greater error and standard deviation than both other methods, owing to the added complexity of estimating ω_1 which, with noisy data, can cause increased error.

Therefore, care should be taken when performing impedance measurements, as large levels of noise could cause significant errors in extraction accuracy with the proposed high damping method.

3.5 Summary

In this chapter, several equivalent circuit extraction methods have been presented, three being general purpose and a fourth being optimised for high damping/low capacitance PTs, such as high temperature PTs. These methods will be used throughout following chapters in the verification of equivalent circuit models, providing data for analysis and as part of a automated PT design algorithm.

3.6 References

[3.1] E. L. Horsley, M. P. Foster, and D. A. Stone, 'A frequency-response-based characterisation methodology for piezoelectric transformers', in *2008 2nd Electronics System-Integration Technology Conference*, London, United Kingdom, Sep. 2008, pp. 959–962. doi: 10.1109/ESTC.2008.4684481.

[3.2] J. A. Nelder and R. Mead, 'A Simplex Method for Function Minimization', The Computer Journal, vol. 7, no. 4, pp. 308–313, Jan. 1965, doi: 10.1093/comjnl/7.4.308.

[3.3] G. Ivensky, I. Zafrany, and S. Ben-Yaakov, 'Generic operational characteristics of piezoelectric transformers', *IEEE Transactions on Power Electronics*, vol. 17, no. 6, pp. 1049–1057, Nov. 2002, doi: 10.1109/TPEL.2002.805602.

[3.4] M. P. Foster, J. N. Davidson, E. L. Horsley, and D. A. Stone, 'Critical Design Criterion for Achieving Zero Voltage Switching in Inductorless Half-Bridge-Driven Piezoelectric-Transformer-Based Power Supplies', *IEEE Transactions on Power Electronics*, vol. 31, no. 7, pp. 5057–5066, Jul. 2016, doi: 10.1109/TPEL.2015.2481706.

Chapter 4 - Influence of spurious modes on PT efficiency

4.1 Introduction

One area often overlooked when designing PTs is the impact of spurious modes on the performance of the PT. Spurious modes occur in almost all PT topologies and so should be carefully managed when designing PTs. The techniques presented in the previous chapter allow the equivalent circuit component values of these unwanted modes to be extracted; however, minimal work has been done on understanding how the equivalent circuit values for the spurious mode affect the performance of a PT when operated at its optimal mode.

This work is part one of a study on spurious modes. In this chapter the PT will be treated purely as an electrical circuit, to then ascertain which components of that circuit affect the performance of the PT as a result of the spurious mode. Using the equivalent circuit, ensures the results of this analysis are applicable to all PT topologies. The second part of the study (Chapters 5-7) will focus on deriving a model to take a physical design for a Transoner PT and determine the equivalent circuit component values for the spurious modes occurring in the PT. Thus, combining the two elements allows Transoner PTs to be designed in a way which reduces the likelihood of performance degradation at as a result of spurious modes.

In this chapter a mathematical model for efficiency loss arising from spurious mode interaction is derived and subsequently used in several analyses to be able to determine which equivalent components are critical for avoiding such loss.

4.2 Optimum and spurious vibration modes

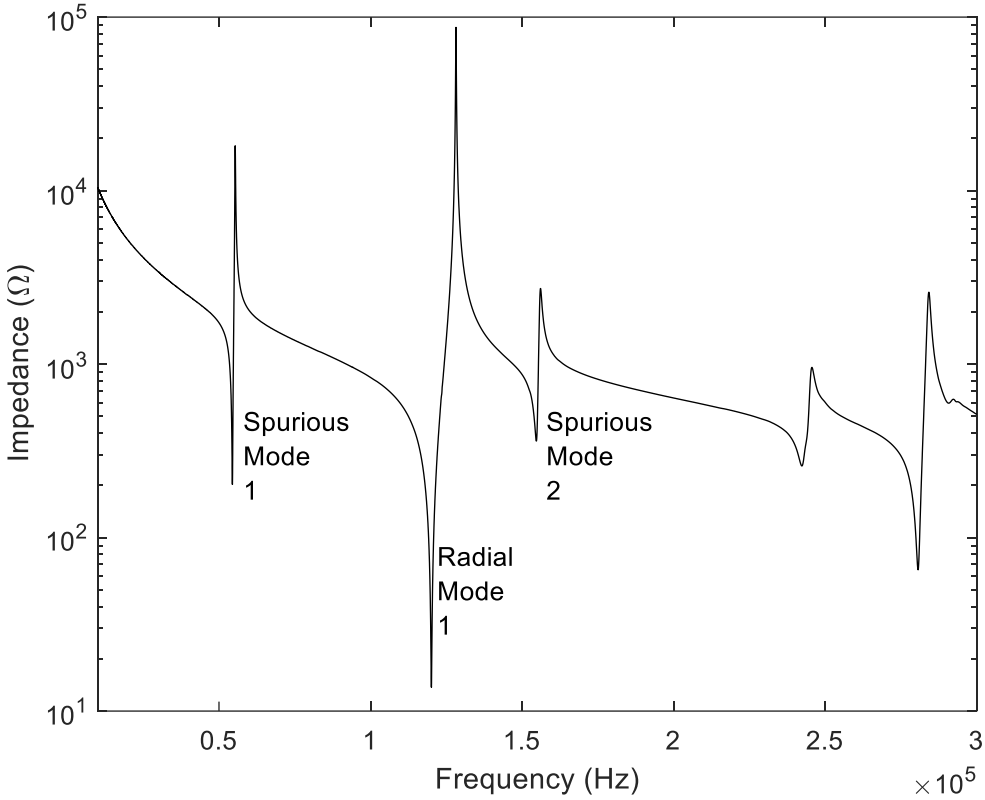

Fig. 4.1 – Input impedance spectra for a radial mode Transoner PT, highlighting the radial (optimum) and spurious modes

PTs and other piezoelectric devices exhibit several vibration modes, where a mode is a shape or direction of vibration. However, owing to the orientation of the electrodes, the poling in the device and the material being used (due to coupling factor), there will be a dominant mode where the device is able to transfer energy between electrical and mechanical domains most effectively (lowest losses, higher power). In this work we will term this mode the optimum mode. For example, in the Transoner PT, this mode is the radial mode (see Fig. 4.1). Spurious modes can be classed as all modes other than the optimum mode and will be numbered starting at the lowest frequency mode (see Fig. 4.1). For best performance (highest output power and efficiency), a PT should be typically operated at the optimum mode.

4.3 Impact of PT design on efficiency loss from spurious modes

In this section, each of the parameters that influence the efficiency degradation occurring from spurious modes are extracted and are then analysed to determine methods for minimising the efficiency degradation. First, increased frequency separation between

optimum and spurious modes will be analysed for its impact on efficiency, using a COMSOL simulation. Then, analysis will be performed using AC circuit analysis techniques on simplified and extended Mason equivalent circuit models. Using the mathematical models generated for efficiency, an expression for the efficiency degradation from spurious modes can be found, allowing sensitivity analyses to be performed, highlighting key parameters for minimising efficiency degradation.

4.3.1 Spurious mode proximity to optimum mode

Maximising the frequency separation between optimum and spurious modes is the most obvious method for minimizing interaction between modes. Spurious mode frequencies are generally influenced by changing the dimensions of a device; for example, controlling the radius/thickness ratio of a radial mode Transoner PT controls the spurious mode resonant frequencies. Intuitively, and correctly, the greater the separation in the frequency of the optimum and the spurious modes, the lesser the effect the spurious mode has on efficiency.

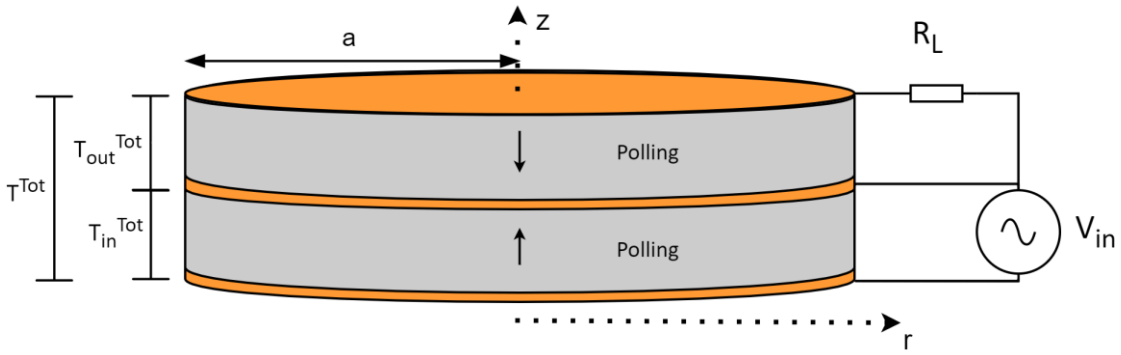

Fig. 4.2 – Two-layer radial mode Transoner PT

A COMSOL simulation was used to validate this assumption. A 2D axisymmetric, two-layer radial mode Transoner PT (Fig. 4.2) model is created in COMSOL. The radius of the PT (a) is varied from 5mm - 15mm and the thickness of the PT (T^{Tot}) is varied from 1mm - 5mm. The two layers are equal in thickness ($T_{\mathrm{in}}^{\mathrm{Tot}} = T_{\mathrm{out}}^{\mathrm{Tot}}$), the PTs are made from PZT-4 and the Q-factor of the optimum mode is fixed at 150. Both piezoelectric layers were setup with piezoelectric coupling between solid mechanics and electrostatics physics within COMSOL. A free vibration boundary condition was used on the outer edges of the device. A 10 V amplitude sinusoidal voltage source and a resistive load are used within COMSOL. This is done by using the electrical circuits physics which allows the FEA model to form part of a SPICE simulation. For

each PT studied, the efficiency is determined at the optimum mode resonant frequency and with a matched load.

To determine the matched load, a frequency domain simulation was performed on each PT to find both the optimum mode resonant frequency and the output capacitance, thus allowing the matched load to be calculated. The resonant frequency of the closest spurious mode is also extracted. For example, observing Fig. 4.1, in this case the resonant frequency of spurious mode 2 would have been extracted, as it is the mode which occurs at a frequency closest to the optimum (radial in this case) mode. The resulting efficiencies are plotted against the percentage difference in frequency between the optimum and spurious modes. The results of this are shown in Fig. 4.3.

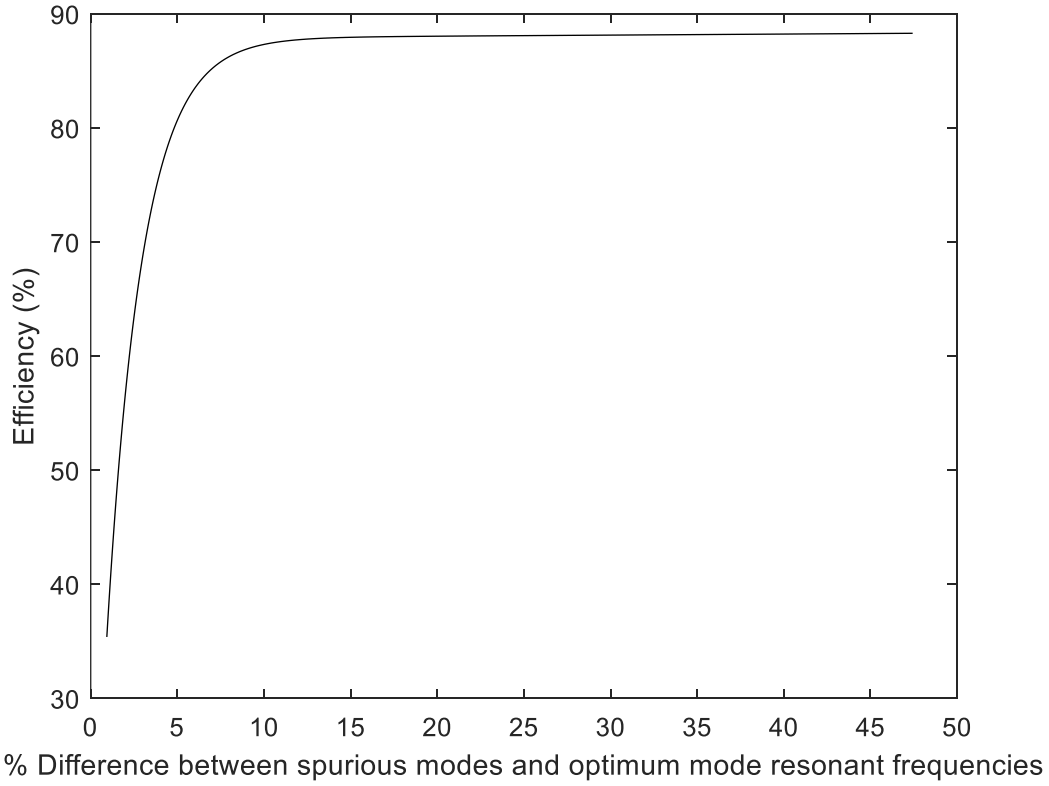

Fig. 4.3 – Exponential line of best fit for the simulated efficiency of multiple PT models from COMSOL against percentage difference between optimum and nearest spurious mode resonant frequencies

With increased frequency difference, higher efficiencies tend to be achieved (but there are exceptions). However, achieving a large frequency difference between optimum and spurious modes requires careful control of the PT dimensions and therefore limits the PT design space.

Since PTs can exhibit multiple spurious modes, as the frequency difference between the optimum and an adjacent spurious mode increase, the optimum mode might move to a frequency closer to that of another spurious mode. Therefore, designing the PT to exhibit very large frequency difference between the optimum and only one of the several spurious modes is unlikely to result in an optimised design.

It is also likely that the values of the other equivalent circuit components will affect the frequency difference required to achieve a desired level of efficiency. Therefore, these other elements will now be analysed.

4.3.2 Efficiency modelling

First, the single branch Mason equivalent circuit model will be used to analyse the efficiency of an idealised single-mode PT (η_1)—this is an idealised PT with all spurious modes deleted. The Mason model will then be extended to include multiple resonant branches, allowing both operating and spurious modes to be modelled together. This allows the efficiency of a PT, driven at the optimum mode resonant frequency and including the effects of a spurious mode, to be analysed (η_2). Finally, a metric describing the loss in efficiency originating from the spurious mode ($\Delta\eta$) will be found.

4.3.2.a) Efficiency in the single branch model ($\boldsymbol{\eta_1}$)

It is well-known that PTs can achieve high efficiency due to the high Q-factor exhibited by the hard-piezoelectric materials employed in their construction. The efficiency ratio, η_1, of a device is defined in (4.1).

$$\eta_1(\omega) = \frac{P_{\text{out}}(\omega)}{P_{\text{in}}(\omega)} \tag{4.1}$$

By generating equations for the voltage and currents in the device, equations for the input and output power can be found. The input and output currents can be written, in the frequency domain, as

$$I_{\text{in}}(\omega) = \frac{V_{\text{in}} - \frac{V_{\text{out}}(\omega)}{N_1}}{R_1 + \text{j}X_1} + \text{j}\omega C_{\text{in}} V_{\text{in}} \tag{4.2}$$

$$I_{\mathrm{out}}(\omega) = \frac{V_{\mathrm{out}}(\omega)}{R_{\mathrm{L}}} \tag{4.3}$$

where X_1 is the reactance of the LC branch,

$$X_1 = \omega L_1 - \frac{1}{\omega C_1} \tag{4.4}$$

This allows V_{out} to be calculated as,

$$V_{\mathrm{out}}(\omega) = \frac{N_1 V_{\mathrm{in}}}{1 + (R_1 + \mathrm{j}X_1)N_1^2\left(\frac{1}{R_{\mathrm{L}}} - \frac{\mathrm{j}}{X_{\mathrm{out}}}\right)} \tag{4.5}$$

where X_{out} is the reactance of capacitor C_{out}. Power in and out can then be calculated. Note that the input capacitor dissipates no power. Together with the output power, an expression for efficiency can be derived. Producing the full solution is trivial with computer algebra packages such as Maple but excessively long to present and is therefore omitted.

$$P_{\mathrm{in}}(\omega) = \Re(V_{\mathrm{in}}(\omega)I_{\mathrm{in}}(\omega)^*) = \Re\left(V_{\mathrm{in}}R_1\frac{\mathrm{V_{in}} - \frac{V_{\mathrm{out}}(\omega)}{N_1}}{R_1^2 + X_1^2}\right) \tag{4.6}$$

$$P_{\mathrm{out}}(\omega) = \frac{|V_{\mathrm{out}}(\omega)|^2}{R_L} \tag{4.7}$$

where $*$ means the complex conjugate. By combining all these equations, it can be shown that

$$\eta_1(\omega) = \frac{R_L}{R_1\left(\omega^2 {C_{\mathrm{out}}}^2 {R_L}^2 + 1\right)N_1^2 + R_L} \tag{4.8}$$

Equation (4.8) suggests there are several equivalent circuit elements that ought to be carefully selected to achieve high efficiency. The damping resistance (R_1) has a significant effect on efficiency (from heat dissipation modelled as I^2R losses). However, R_1 is multiplied by $\omega^2 {C_{\mathrm{out}}}^2 {R_L}^2$ and N_1^2, therefore higher efficiency operation is achieved for low values of all these parameters. However, C_{out} should be carefully designed to ensure zero-voltage switching (ZVS) can be achieved, as shown by Foster *et al.* and N_1 will be chosen depending

on the required application of the PT [4.1]. Due to the implications of not being able to minimise C_{out} and N_1 due to the application requirements, it is advantageous to ensure R_1 is minimised as this has no detrimental effects.

To ensure optimal efficiency, the load is often matched to the output capacitance as shown in (4.9) [4.2].

$$R_{\text{L}} = \frac{1}{\omega C_{\text{out}}} \tag{4.9}$$

And hence (4.8) can be simplified to

$$\eta_1(\omega) = \frac{1}{2N_1^2 \omega C_{\text{out}} R_1 + 1} \tag{4.10}$$

To analyse the effect of using an unmatched load on the efficiency of the PT, the efficiency of the single branch model can be simulated under various load conditions. Equation (4.8) was used with the equivalent circuit parameters for the optimum (radial) mode of the T1-13 Transoner PT defined in Table 4.1, and assuming the PT was driven at the series resonant frequency (ω_1). The resulting efficiency against load curve is shown in Fig. 4.4.

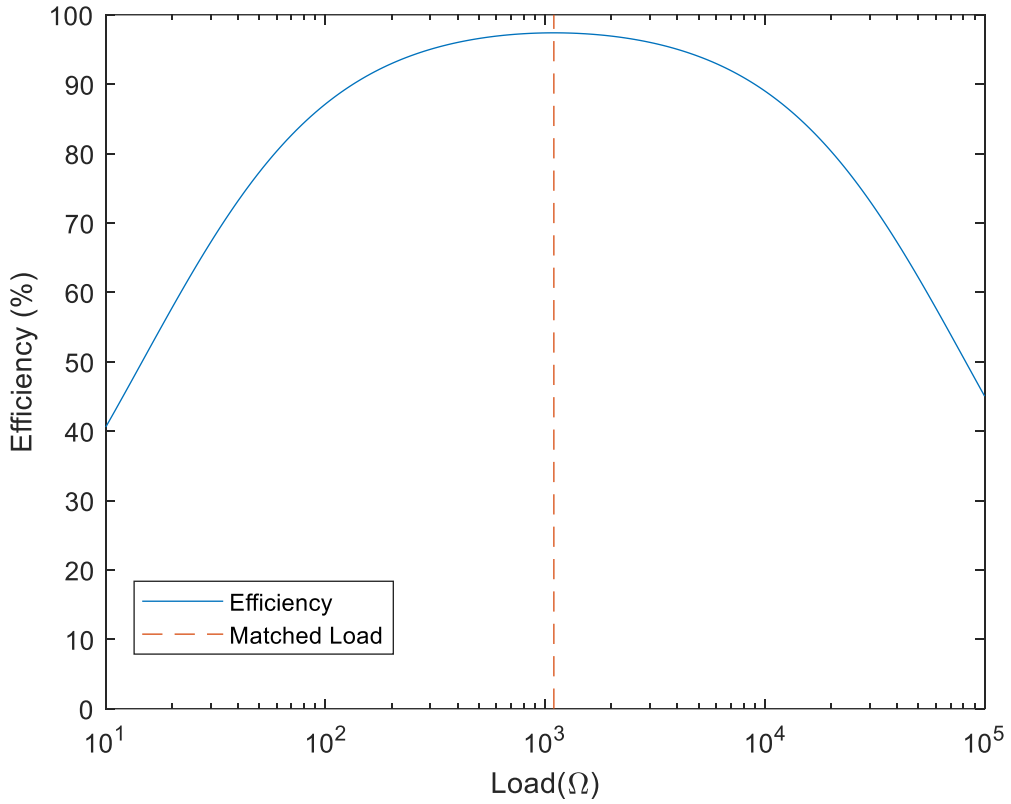

Fig. 4.4 – Efficiency of the single branch equivalent circuit model of the T1-13 radial mode PT against load resistance

Table 4.1 – T1-13 Radial mode PT equivalent circuit parameters, including optimal and closest occurring spurious mode

R_1 (Ω)	R_2 (Ω)	L_1 (mH)	L_2 (mH)	C_1(pF)
18.9	233.7	12.7	95.2	138.7
C_2(pF)	N_1	N_2	C_{in}(nF)	C_{out}(nF)
89.8	0.88	1.32	1.90	1.21

As can be seen in Fig. 4.4, η_1 peaks when the load is equal to the matched load. Very small or very large loads should be avoided as this gives low efficiency. When R_L is small, the output voltage is low and therefore the voltage across the resonant circuit is maximised, increasing I^2R losses. When R_L is large, the output current is much lower than the current through the resonant circuit, again lowering the efficiency. Also, from (4.10), the matched load is

dependent on frequency, which adds to the complexity of designing and controlling PT-based power converters.

4.3.2.b) Multiple branch model

The equivalent circuit shown in Fig. 2.14 is a simplification of the full equivalent circuit for a PT and, as a result, is only applicable when the PT is driven at the resonant frequency of the optimum mode and when all other vibration modes have negligible effect. The full equivalent circuit model of a PT contains many RLC branches which model each of the different vibration modes. Lin [4.3] showed that each of these RLC branches should be connected to the output node of the PT through an ideal inverting transformer to correctly model the impedance and performance of a PT, as shown in Fig. 4.5. Although the PT contains many vibration modes, most of these have high impedance at the operating frequency and pass negligible current, and thus have negligible influence on the performance of the PT. They can therefore be omitted from the model. However, even when considering a small number of spurious modes, the analysis of the efficiency of the PT is difficult. As a result, the investigation in this chapter will consider only two modes interacting: the optimum mode and a single spurious mode.

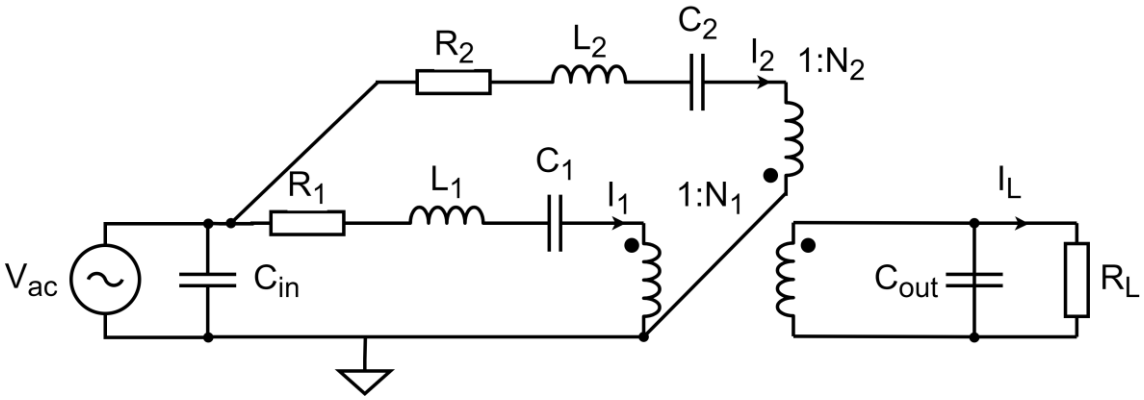

Fig. 4.5 – Extended Mason equivalent circuit model of a PT

It should be noted that a subscript $'2'$ is used when discussing the equivalent circuit parameters of the spurious mode in the following analysis, however, this notation does not necessarily mean that spurious mode being analysed is the 2nd mode occurring in the PT (i.e. first spurious mode). In this chapter, the parameters being referred to with a subscript 2 are those of the spurious mode of interest and therefore could be referring to any of the spurious modes.

4.3.2.b.i) Efficiency in the multiple branch model ($\boldsymbol{\eta_2}$)

An understanding of the efficiency loss mechanism in the multiple branch model is required before analysing the impact of a spurious mode on efficiency. To begin, a frequency domain analysis was performed in LTSpice using the equivalent circuit model in Fig. 4.5 and the equivalent circuit parameters of a T1-13 radial mode Transoner PT (Table 4.1). The efficiency suggested by the model was examined and shown in Fig. 4.6.

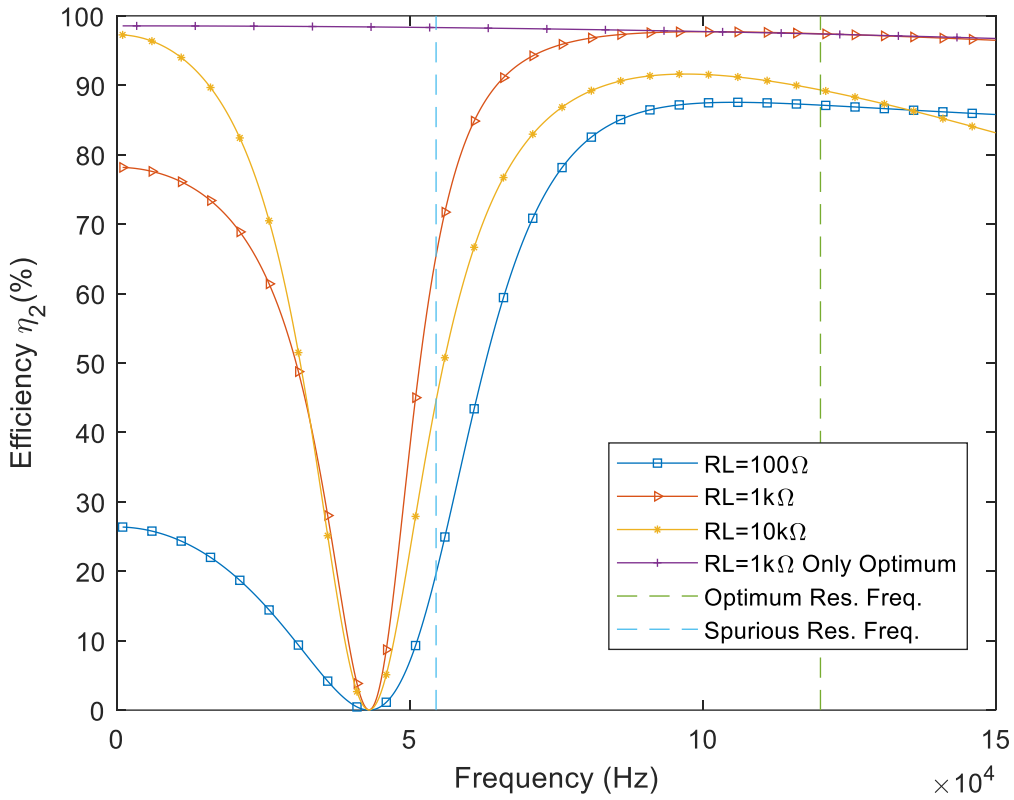

Fig. 4.6 – Efficiency of a two-branch equivalent circuit model of the T1-13 PT against operating frequency under various load conditions, single branch efficiency included for 1kΩ load for comparison

As can be observed in Fig. 4.6, while the efficiency is usually high around the optimum mode, there is a region of significant inefficiency near the spurious mode resonant frequency. This effect is due to the interaction between the two resonant modes. To understand the reason for this interaction, the current through the resonant branches, when the PT is operated at the minimum efficiency frequency (~43kHz in Fig. 4.6), is analysed and is shown in Fig. 4.7, where I_1, I_2 and I_L are the currents through the optimum mode branch, spurious mode branch and the load respectively.

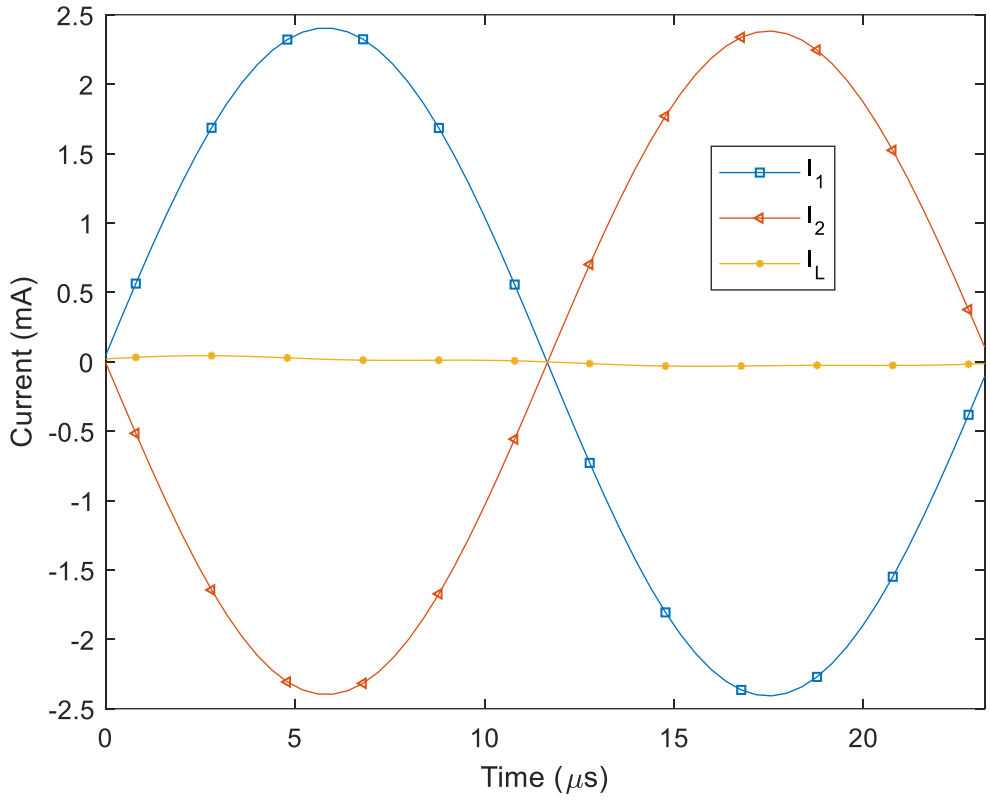

Fig. 4.7 – Current flowing through the optimum mode, spurious mode and load at 43kHz

The resonant branch currents are near-equal in magnitude and in antiphase and when combined through the transformer, this results in negligible output current. Energy loss is incurred through damping: there is still notable input power. There is a large region of frequencies where this interaction occurs and degrades the efficiency. In this region, the currents suffer destructive interference. It should be noted that other factors, such as the load, have an impact on the range of frequencies that are affected by the efficiency loss as demonstrated by the different curve shapes shown in Fig. 4.6.

To minimise the effect of spurious modes on the efficiency of a PT, the condition where there is significant interference should be avoided or should occur at frequencies away from the optimum mode, where the power transfer is already negligible. As shown in Fig. 4.3, increasing the frequency difference between modes helps to ensure high efficiency because the minimum efficiency frequency would then occur away from the optimum mode. Also, the range of frequencies at which destructive interference occurs should be minimised.

4.3.2.b.ii) Efficiency modelling for two modes

To determine the best method of minimising spurious mode influence on efficiency, it is first necessary to derive an expression of the efficiency of a PT containing an ideal and a spurious vibration mode.

To determine the efficiency of the circuit in Fig. 4.5, when operated at the optimum mode resonant frequency, an equation for the input and output power is derived in terms of the equivalent circuit component values. The power and efficiency can be derived by considering the current in each resonant branch and the output current in terms of input and output voltages.

$$I_1(\omega) = \frac{V_{\text{in}} - \frac{V_{\text{out}}(\omega)}{N_1}}{R_1 + \text{j}X_1} \tag{4.11}$$

$$I_2(\omega) = \frac{V_{\text{in}} + \frac{V_{\text{out}}(\omega)}{N_2}}{R_2 + \text{j}X_2} \tag{4.12}$$

$$I_{\text{in}}(\omega) = I_1 + I_2 + j\omega C_{\text{in}} V_{\text{in}} \tag{4.13}$$

$$I_{\text{out}}(\omega) = \frac{V_{\text{out}}(\omega)}{R_{\text{L}}} \tag{4.14}$$

where X_1 and X_2 are the reactance of the LC combinations of branch 1 and 2, respectively. That is to say,

$$X_n = \omega L_n - \frac{1}{\omega C_n} \tag{4.15}$$

Assuming only these two branches are significant, (4.11), (4.12), (4.14) can be re-arranged to give an expression for V_{out}

$$V_{\text{out}}(\omega) = \frac{\frac{V_{\text{in}}}{(R_1 + \text{j}X_1)N_1} + \frac{V_{\text{in}}}{(R_2 + \text{j}X_2)N_2}}{\frac{1}{N_1^2(R_1 + \text{j}X_1)} + \frac{1}{N_2^2(R_2 + \text{j}\text{X}_2)} + \frac{1}{R_L} - \frac{\text{j}}{X_{\text{out}}}} \tag{4.16}$$

$$P_{\text{out}}(\omega) = \frac{|V_{\text{out}}(\omega)|^2}{R_L} \tag{4.17}$$

$$\eta_2(\omega) = \frac{P_{\text{out}}(\omega)}{P_{\text{in}}(\omega)} = \frac{P_{\text{out}}(\omega)}{\Re(V_{\text{in}}(\omega) I_{\text{in}}(\omega)^*)} \tag{4.18}$$

A closed-form expression for η_2 can be easily derived by solving (4.11), (4.12), (4.13), (4.16), (4.17), (4.18), but it is too long to print here. Instead, we will write η_2 in function format.

$$\eta_2 = f(L_1, L_2, C_1, C_2, R_1, R_2, N_1, N_2, C_{\text{out}}, \omega, R_L) \tag{4.19}$$

4.3.2.c) Efficiency degradation ($\Delta\eta$)

It is helpful to introduce the concept of efficiency degradation, $\Delta\eta$. This parameter describes the proportional loss in efficiency due to a proximate spurious mode. It neglects the reduction of efficiency that can occur from losses in the optimum resonant mode regardless of spurious-mode interactions. We define it thus

$$\Delta\eta = 1 - \frac{\eta_2}{\eta_1} \tag{4.20}$$

where η_1 is the efficiency calculated from the single-branch model, and η_2 is the efficiency calculated from the two-branch model. Zero degradation, $\Delta\eta = 0$ corresponds to $\eta_2 = \eta_1$, thus the spurious modes have no effect on device efficiency. It is worth noting that $\Delta\eta$, like η_2, is a function of L_1, L_2, C_1, C_2, R_1, R_2, N_1, N_2, C_{out}, ω and R_L. It is useful to perform a series of substitutions so that efficiency is written in terms of resonant frequencies.

$$\omega = \omega_1;\ \omega_1 = \frac{1}{\sqrt{L_1 C_1}};\ \omega_2 = \frac{1}{\sqrt{L_2 C_2}};$$
$$\zeta_1 = \sqrt{\frac{L_1}{C_1}};\ \zeta_2 = \sqrt{\frac{L_2}{C_2}} \tag{4.21}$$

where ω_1 and ω_2 are the resonant frequencies of the optimum and spurious mode, respectively; and ζ_1 and ζ_2 are the magnitude of the reactance of L_1 and L_2 (or C_1 and C_2), respectively, at the relevant resonant frequency. ζ_1 and ζ_2 could also be termed the characteristic impedances of each branch. These substitutions eliminate L_1, L_2, C_1 and C_2 from (4.20) and eliminates, ζ_1, therefore simplifying the (still long) expression.

4.3.3 Sensitivity analysis

Owing to the complexity of the efficiency degradation mechanism in a PT, it is not easy to determine which equivalent circuit parameters have a significant effect. We therefore perform a sensitivity analysis to isolate the relevant parameters.

4.3.3.a) One factor at a time

The 'one-factor-at-a-time' is the simplest type of sensitivity analysis to perform and to understand. The results of this analysis will help to show the general trends that each of the circuit parameters have on efficiency degradation. Whilst the results of this analysis are focused around one specific PT (T1-13 in this case), similar results would be achieved for other PT topologies, noting the similarity between equivalent parameters.

Table 4.2 – Equivalent circuit parameters for the T1-13 PT and the adjusted T1-13 PT, termed the T1*

	R_1 (Ω)	R_2 (Ω)	$\omega_1/2\pi$ (kHz)	$\omega_2/2\pi$ (kHz)	ζ_1(Ω)	ζ_2(Ω)	N_1	N_2	C_{in} (nF)	C_{out} (nF)
T1-13	18.9	233.7	120.1	54.4	9556.3	32568	0.88	1.32	1.90	1.21
T1*	18.9	233.7	120.1	108.3	9556.3	32568	0.88	1.32	1.90	1.2

The analysis is performed with the exemplar PT parameter set in Table 4.2. However, the T1-13 PT has low efficiency degradation owing to the significant frequency difference between its optimum (radial) mode and any spurious mode. However, as described in [4.4], spurious modes are typically not considered in the design process and therefore, an optimised frequency difference is not likely to be true of initial designs. Subsequent sensitivity analyses will therefore be performed on a modified set of parameters, based on the T1-13, which brings ω_2 closer to ω_1 whist maintaining all other parameters. This PT model, which is will termed T1*, has the parameters given in Table 4.2. The new design improves the viewability of the sensitivity analysis and represents a realistic early PT design. At matched load and optimum resonant frequency, this modification increases the efficiency degradation from -0.04% to 1.46% (with a single-branch efficiency, η_1, of 97.4%).

To perform the sensitivity analysis, a range of parameters to study is required. Each of the parameters will be varied through the range $x_{\text{n}}/100 \leq x \leq 100x_{\text{n}}$ where x is the parameter and x_{n} is its nominal value from Table 4.2. This allows the analysis to cover a wide range of

potential devices. The only exception is the turn ratios (N_1, N_2) which will only be varied in the range $N_n/10 \leq N \leq 10N_n$ because the turn ratio typically correlates linearly to the geometry, which is physically constrained. The analysis will be performed at a frequency equal to the optimum mode resonant frequency, ω_1.

4.3.3.a.i) Initial study on exemplar PT, T1-13

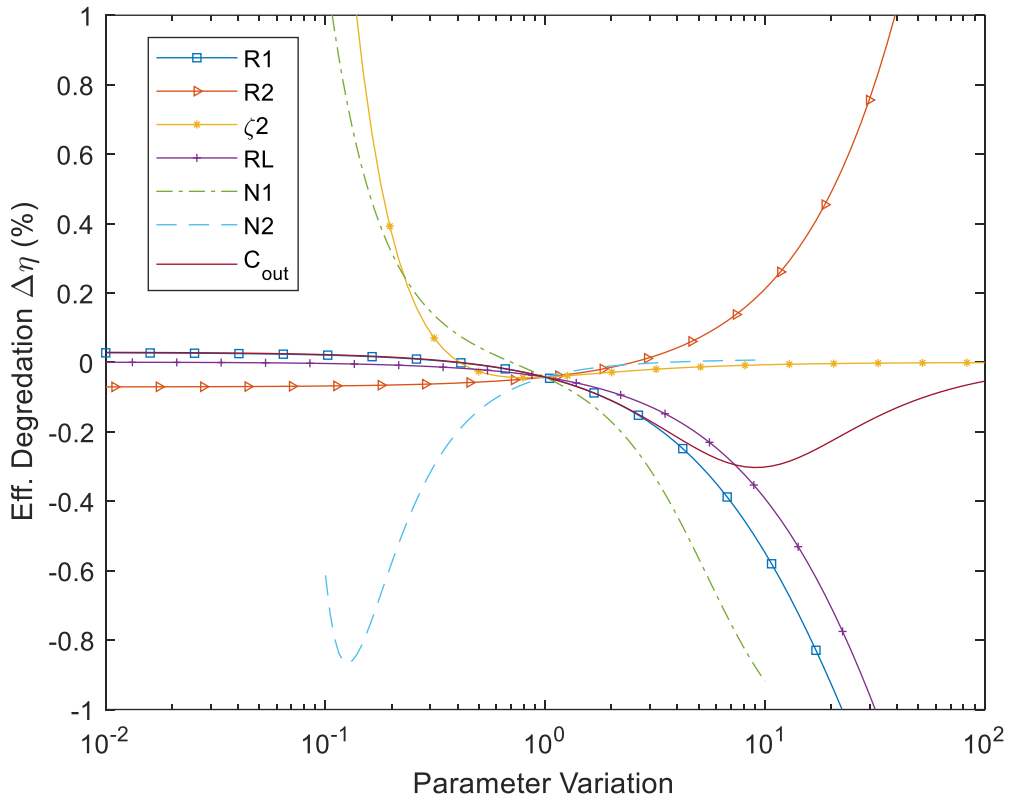

Fig. 4.8 – Sensitivity analysis on the influence of parameter value on the efficiency degradation of a nominal T1-13 PT

Each curve in Fig. 4.8 demonstrates the effect of varying a single parameter while keeping the other parameters at their nominal value. As shown in Fig. 4.8, ζ_2 has the greatest effect on efficiency degradation. As ζ_2 decreases from its nominal value, the efficiency degradation rapidly increases. Each of the other parameters have minimal effect on the efficiency degradation across its full range of variation. However, as discussed above, the overall low efficiency degradation is unrealistic for early designs (such as those generated using [4.4]), due to the large frequency difference between modes. Nevertheless, from the initial analysis, we can see that ζ_2 is a vital design parameter in ensuring low efficiency degradation.

4.3.3.a.ii) Study on modified PT, T1*

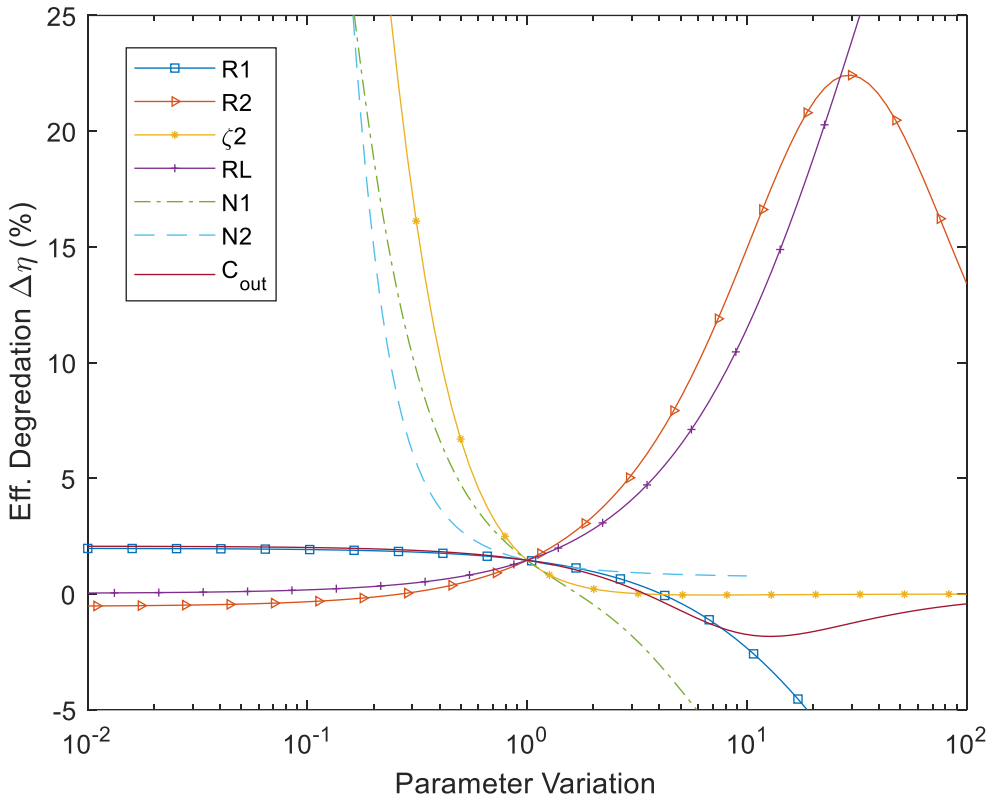

Fig. 4.9 – Sensitivity analysis on the influence of parameter value on the efficiency degradation of the T1* PT

Fig. 4.9 shows the same analysis performed on the modified model, T1*. Comparing Fig. 4.9 to Fig. 4.8 shows that each of the parameters has an increased effect on the efficiency degradation when the spurious mode is closer to the optimum mode. ζ_2 remains the parameter with the largest effect on efficiency degradation, again highlighting its importance in design. N_2, R_L N_1 and R_2 all have significant effects on the efficiency degradation, with proximity of the modes determining how impactful the parameter is. For this case study, R_1 and C_{out} have negligible effect on efficiency degradation compared to the other parameters. It should be noted that negative efficiency degradation, means an efficiency increase caused by the spurious mode. However, using (4.8) it can be concluded that increasing these parameters decreases optimum mode efficiency and so should typically be avoided.

The effect R_2 has on the efficiency degradation is interesting. Initially, as one would expect, increasing R_2 increases the efficiency degradation due to higher I^2R losses. However, beyond a certain value (30 times nominal), the efficiency degradation peaks, thereafter falling with

increased R_2. This effect is due to reduced power flow in the spurious mode, therefore, if $R_2 = \infty$, there is no power through the spurious mode and so no efficiency degradation. However, as damping in PTs is largely due to mechanical losses, common to all modes, higher damping in the spurious mode typically results in higher damping in the optimum mode [4.5]. Therefore, while increasing the damping (i.e. R_2) in the PT may minimise efficiency degradation, it will typically cause a decrease in the optimum mode efficiency of the PT (due to increases in R_1) and thus degrade performance. However, if a designer could increase the damping in a specific mode without affecting the optimum mode, this would be a good option for improving the efficiency degradation in the device.

4.3.3.b) Parametric Sweep

While studying variations of a single parameter gives useful insight into how the efficiency degradation of a specific PT is affected by each parameter in isolation, the results of a 'one-factor-at-a-time' analysis are dependent on the device studied. To study multiple parameters simultaneously, a parametric sweep-based sensitivity analysis is performed. For this analysis, all parameters are varied in a 7-dimentional space with each dimension having the same range of variation as the previous analysis, which was derived from the T1-13 PT (Table 4.2).

To visualise the results, each parameter (dimension) is varied in turn and the 6-dimensional space extracted. A good device is then defined as one which achieves an efficiency degradation of less than 5%. The proportion of good devices in this space is calculated. Graphical plots are then produced showing the trend in proportion of good devices with the parameter at hand.

To further describe this type of analysis, a simplified scenario is shown with only 2 input variables, ζ_2 and R_2. The efficiency degradation will be analysed for each variation of both parameters. The T1* PT will be used for the remaining parameters, as given in Table 4.2. Firstly, this data can be visualised on a 3D graph, as only 2 parameters are considered. This is shown in Fig. 4.10.

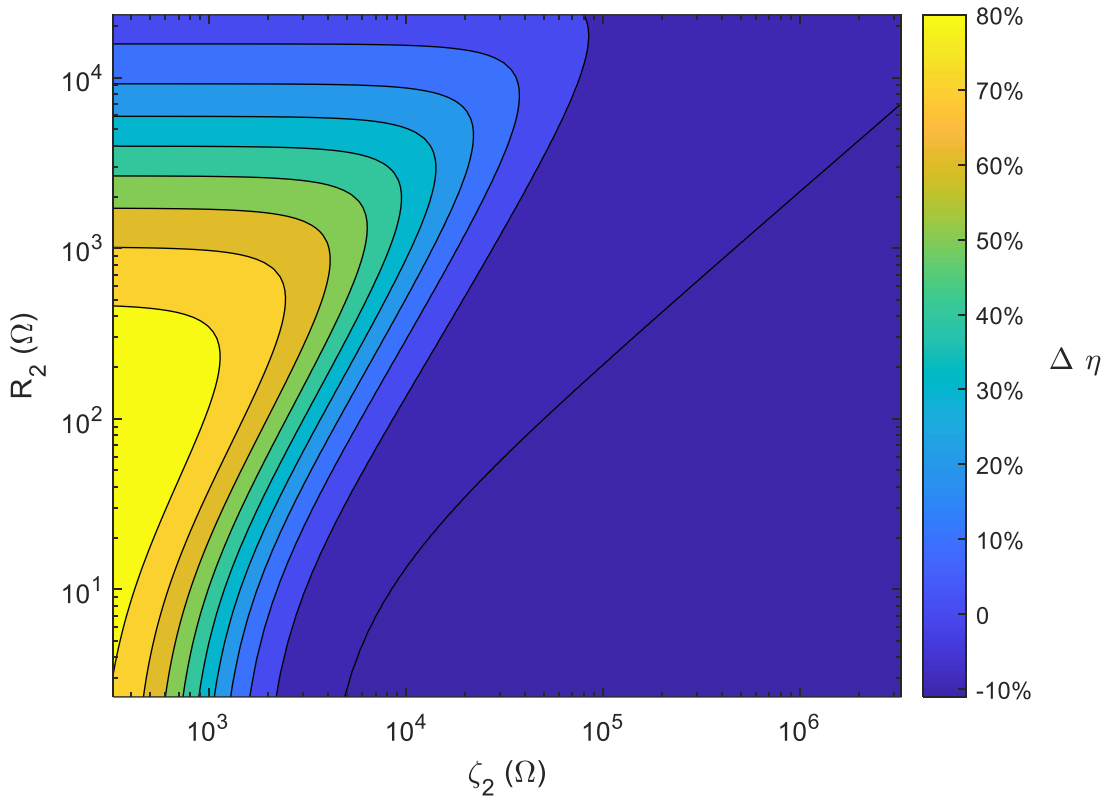

Fig. 4.10 – Contour plot of efficiency degradation with changes in ζ_2 and R_2

Although, with greater than 2 input variables, such as in our analysis, it is impractical to visualise the data on a single graph. To overcome this, first, for each variation of a parameter's value a probability density plot can be produced, showing the likelihood of achieving various levels of efficiency degradation. An example plot is shown for $R_2 = 5.4\Omega$.

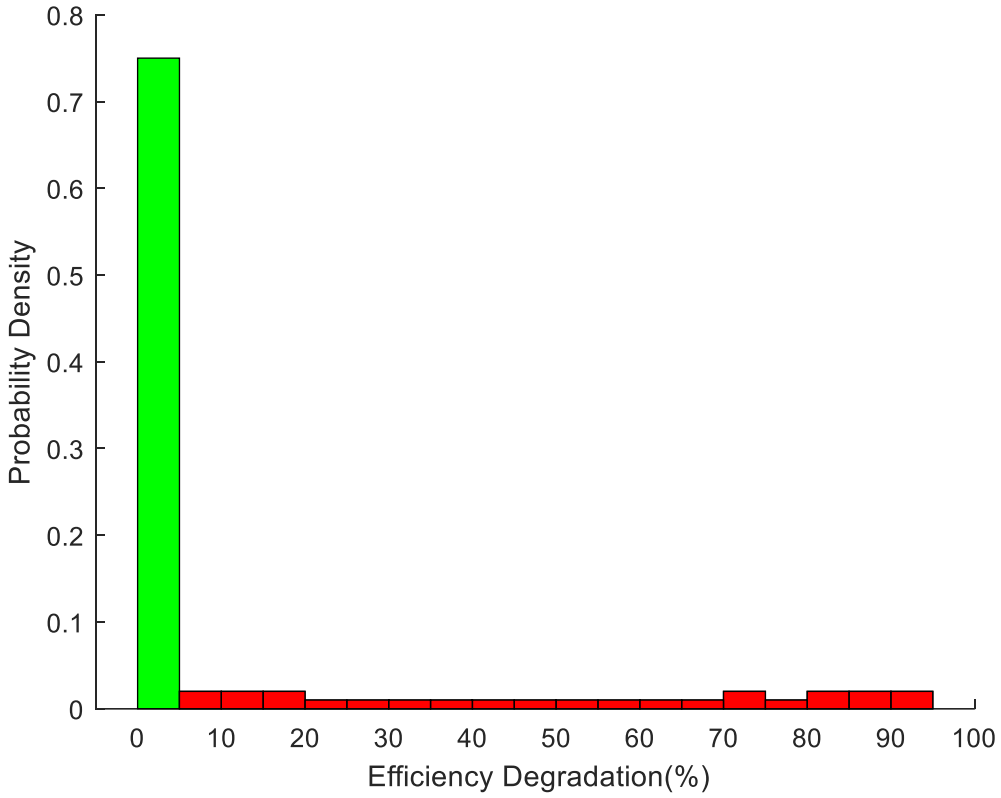

Fig. 4.11 – Probability density plot for R_2 = 5.4Ω, the green bar highlighting the desired (<5% $\Delta\eta$) specification

From Fig. 4.11, we calculate that 75% of devices are within the specification (<5% $\Delta\eta$) when $\mathrm{R}_2 = 5.4\Omega$. This process is then repeated for all values of said parameter, and a graph of the percentage of devices in specification against the variation in the parameter value can be produced, as shown in Fig. 4.12. This process is then repeated for the remaining parameter(s), as also shown in Fig. 4.12.

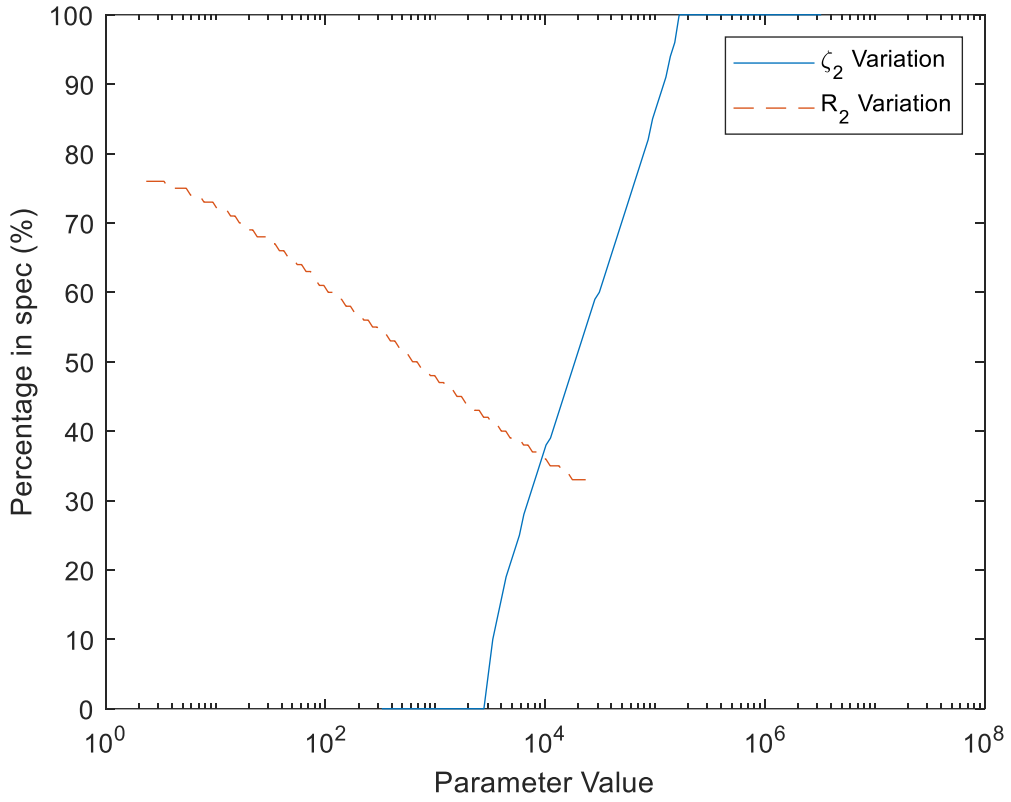

Fig. 4.12 – Percentage of datapoints in specification against variation in each parameter's values

From Fig. 4.12, we can see a similar general trend as was visable in the contour plot in Fig. 4.10, with a positive and a negative correlation observed for ζ_2 and R_2 respectively. It should be noted that more subtle trends are lost in this analysis, such as $\Delta\eta$ improving with very large R_2 values.

To perform this analysis on a PT, several changes need to be made from the 'one-factor-at-a-time' analysis, although, the range of parameter variation will be kept the same. Firstly, as there is no longer a nominal device, it is important that all results are indepedent of the chosen optimum mode resonant frequency. Therefore, C_{out} will be considered as an impedance $\left(X_{C_{\text{out}}} = -1/\omega C_{\text{out}}\right)$, to ensure matched load conditions don't affect the results. In this case, $X_{C_{\text{out}}}$ will be varied from 13.2 Ω to 132 kΩ. Secondly, the spurious mode resonant frequency is set as $\omega_2 = 0.9\omega_1$ and $\omega_2 = 1.1\omega_1$. The close proximity of the modes to the optimum mode, will accentuate the affect each parameter has and, using multiple spurious resonant frequencies, highlights the differences between modes occurring at frequencies either side of the optimum mode resonance. The results of the parametric sweep sensitivity analysis are presented in Fig. 4.13.

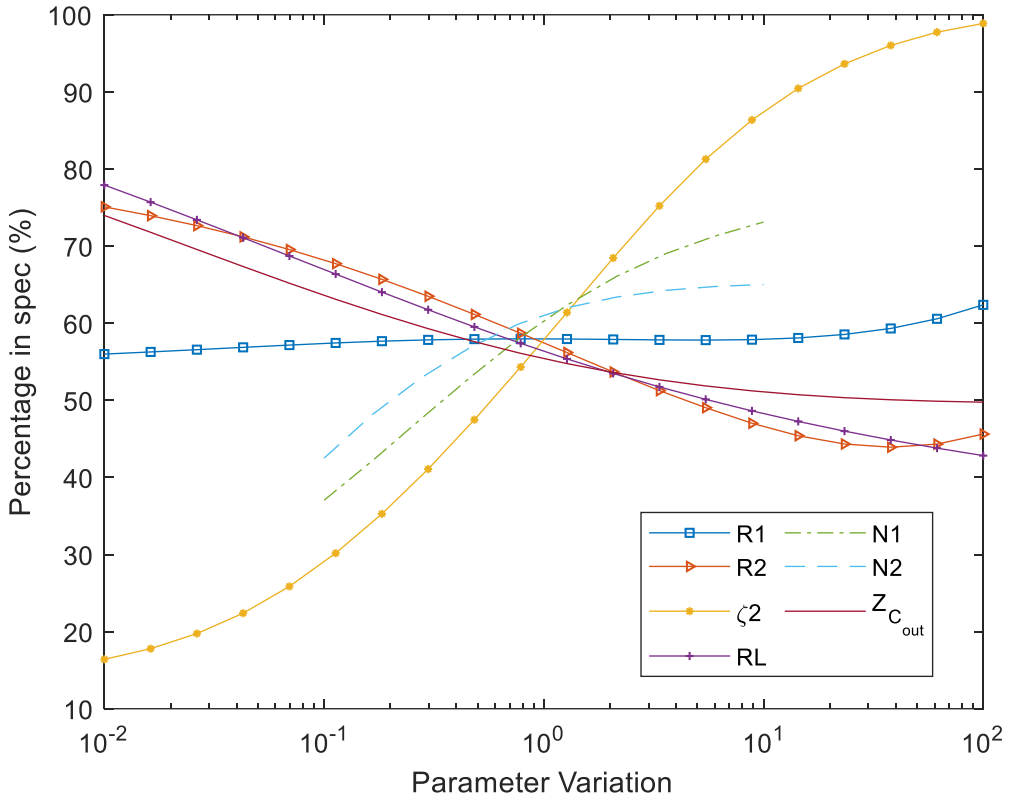
Percentage in spec (%)
Parameter Variation
100
90
80
70
60
50
40
30
20
10
10^{-2}
10^{-1}
10^{0}
10^{1}
10^{2}
R1
R2
ζ2
RL
N1
N2
$Z_{C_{out}}$

a)

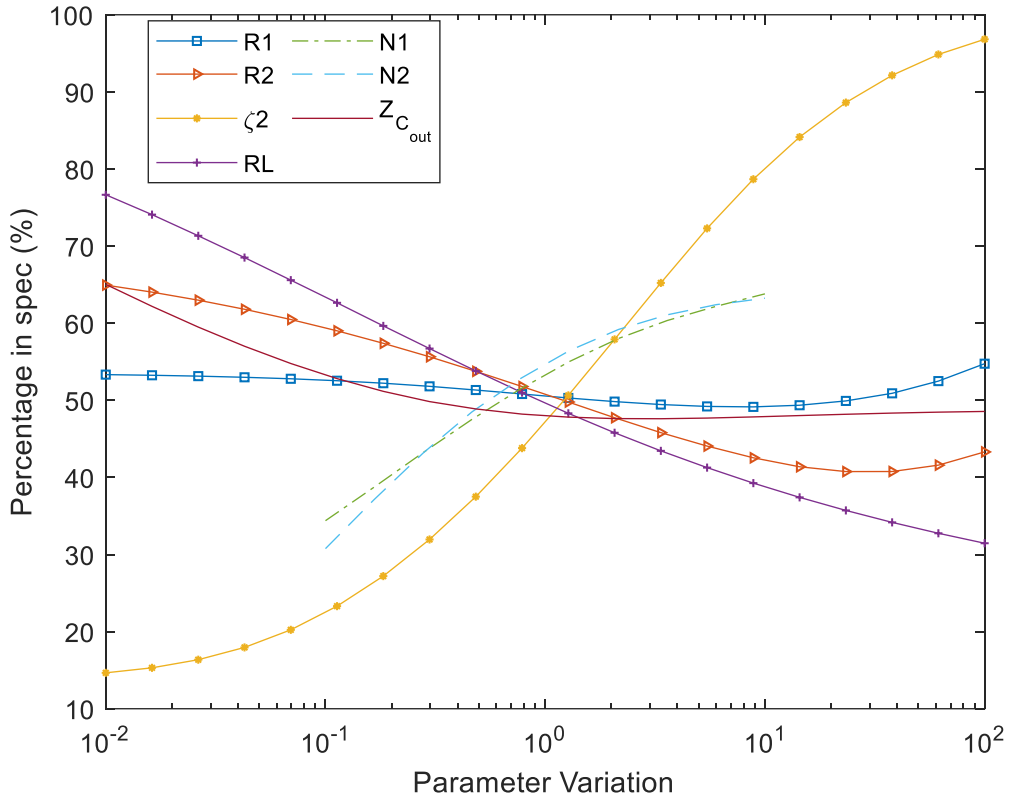

b)

Fig. 4.13 – Parametric sweep-based sensitivity analysis. (a)$\omega_2 = 0.9\omega_1$ (b) $\omega_2 = 1.1\omega_1$

Fig. 4.13 shows that all parameters have some influence on the proportion of good devices and hence the efficiency degradation. However, ζ_2 has the greatest effect on the number of good devices, with a change of up to 82.5 percentage points (from worst to best case ζ_2 value) in the percentage of devices exhibiting <5% efficiency degradation. This analysis also highlights the impact the load resistor, R_L, has on the proportion of acceptable devices. A change of up to 45.2 percentage points is observed across the parameter range.

In a similar way to R_L, increases in R_2 and $Z_{C_{\text{out}}}$ cause a decrease in the proportion of good devices. Conversely, N_1 and N_2 have a similar impact on the proportion of good devices, each with an increase of up to 36 percentage points across the parameter range. R_1 has a negligible effect when compared to the other parameters.

4.4 PT design for minimal efficiency degradation

From the previous analyses, a few parameters have been highlighted as vital for low efficiency degradation. Most notably these include frequency difference and ζ_2. Previous analyses have

also shown that both variables have a negative correlation with efficiency degradation. From the parametric sweep sensitivity analysis, it was also found that for ζ_2 values greater than ~18MΩ, all PTs have minimal efficiency degradation, irrespective of the other parameter values (given they are in the range used for this analysis). This is useful from a design perspective, as efficiency loss from spurious modes can be negated by careful design of only a single parameter (assuming $\omega_1 \neq \omega_2$), especially as ζ_2 has no impact on optimum mode performance. However, the critical value of ζ_2 (that required 100% of devices tested to exhibit <5% $\Delta\eta$) from the parametric sweep sensitivity analysis is at least two orders of magnitude greater than that exhibited by the T1-13 PT, and such a large value may be unachievable.

4.5 Typical ζ_2 values achieved by PTs

The following section will analyse the typical ζ_2 values that are typically achieved in various PTs topologies. This will help to give some context to ζ_2 values that are required to avoid minimal spurious mode interaction for all PTs.

Table 4.3 – Key dimensions of various PT topologies in [4.6] - [4.11]

PT	Length/Diameter (mm)	Total Thickness (mm)	Width (mm)
[4.6]	24.00	0.80	6.00
[4.7]	19.05	3.81	-
[4.8]	42.86	1.26	10.00
[4.9]	30.00	3.54	-
[4.10]	120.00	4.00	20.00
[4.11]	27.5	2.5	27.5

To determine typically achievable values of ζ_2, a COMSOL simulation study was performed on various PT topologies [4.6] - [4.11]. The shape and dimensions of each topology (Table 4.3) were modelled according to the description given in each paper; however, PZT-4 material was used for each PT (other than where otherwise mentioned). For each PT examined, an eigenfrequency study was performed, allowing the resonant frequencies to be extracted. The impedance of each PT at frequencies surrounding the two nearest spurious modes to the

optimum mode were simulated, and ζ_2 extracted using method 3 presented in Chapter 3.3.3. The results of this analysis are presented in Fig. 4.14.

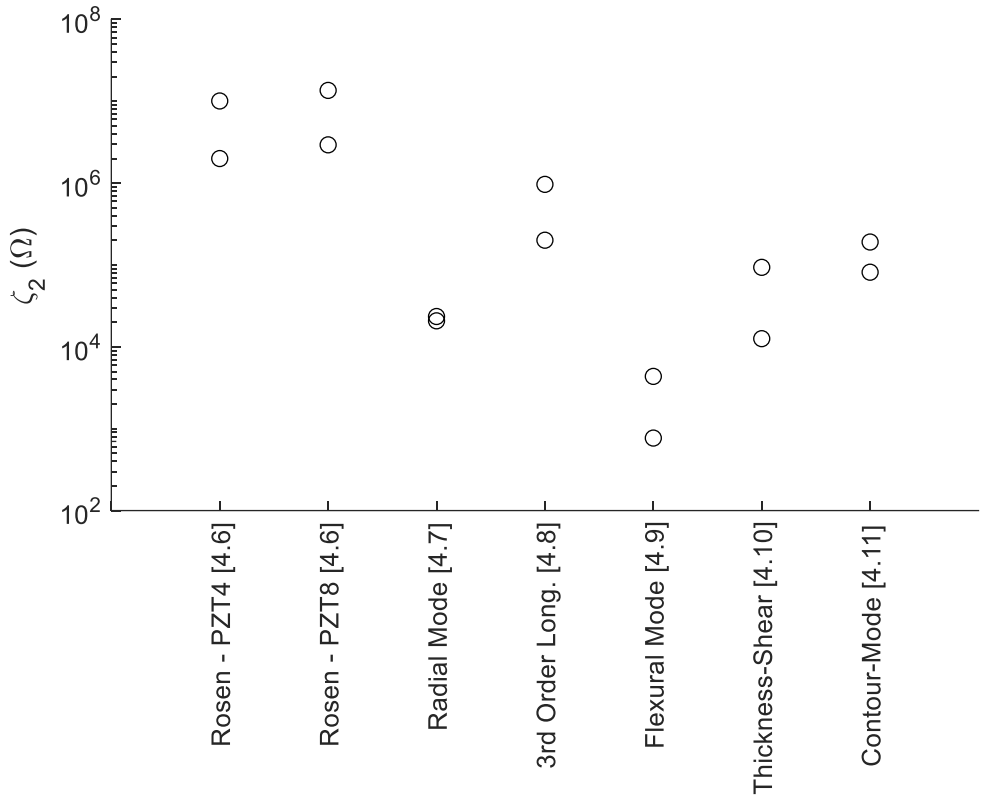

Fig. 4.14 – Typical ζ_2 values exhibited by several different PT topologies

As shown in Fig. 4.14, there is significant variation in ζ_2 exhibited across the range of PT topologies. The bar shaped PTs (Rosen and 3rd order longitudinal) exhibit very large ζ_2, so large that these PTs will typically have minimal efficiency degradation irrespective of the other equivalent parameters. However, the other PT topologies exhibit significantly smaller ζ_2 values. Fig. 4.14 also shows that using a harder PZT, such as PZT8, leads to larger ζ_2 values than the softer PZT4. Importantly, this analysis has also shown that most PTs, even if made from PZT8, will not achieve a ζ_2 greater than the ∼18MΩ figure found in the sensitivity analysis, that is required to ensure minimal $\Delta\eta$ without considering other parameters.

Returning to Fig. 4.12 it can be seen that the percentage of devices meeting the 5% specification threshold is strongly influenced by the proximity of the spurious mode to the optimum mode. This is further confirmed by the 'one-factor-at-a-time' analyses, as for the same ζ_2 value, different levels of efficiency degradation were achieved at different $\Delta\omega$ values.

Therefore, the critical value of ζ_2, at which all PTs analysed had <5% efficiency degradation, will change with proximity of the spurious mode to the optimum mode. Furthermore, with greater frequency difference, the critical value of ζ_2 will be smaller and more achievable.

4.6 Analysing the influence of frequency separation and ζ_2 On the percentage of good devices

Previous analyses have proven that mode proximity and a large ζ_2 value are key factors in ensuring low efficiency degradation. Therefore, the following analysis will focus on analysing the combined impact these two parameters have on the efficiency degradation. This will be extended by analysing various scenarios which constrain the other equivalent parameters. This will provide insight into the optimum frequency separation for a given ζ_2, informing PT design decisions.

The relationship between frequency separation ($\Delta\omega = (\omega_2 - \omega_1)/\omega_1$), ζ_2 and the percentage of devices within the <5% efficiency degradation threshold will be analysed. Similar to the parametric sweep sensitivity analysis, all parameters will be independently varied in a 7-dimentional space. However, in this analysis, the spurious mode resonant frequency will also be included in the variation, with load being matched to the output capacitance, and therefore not independently varied. The PT will be driven at the optimum mode resonant frequency ω_1 and all other parameters varied in the same way as the previous parametric sweep analysis. The percentage of good devices ($\Delta\eta$ <5%) for variations in ζ_2 and $\Delta\omega$ will be extracted and plotted, using the same method as used in the parametric sweep analysis. The range of variation for all parameters is kept the same as in previous sensitivity analyses, with $\Delta\omega$ varied between $-0.75 < \Delta\omega < 0.75$ by changing ω_2, with ω_1 fixed at 100kHz (although, choice has no impact on the results). A contour plot of $\Delta\omega$, ζ_2 and percentage of good (exhibiting <5% $\Delta\eta$) devices is shown in Fig. 4.15 below.

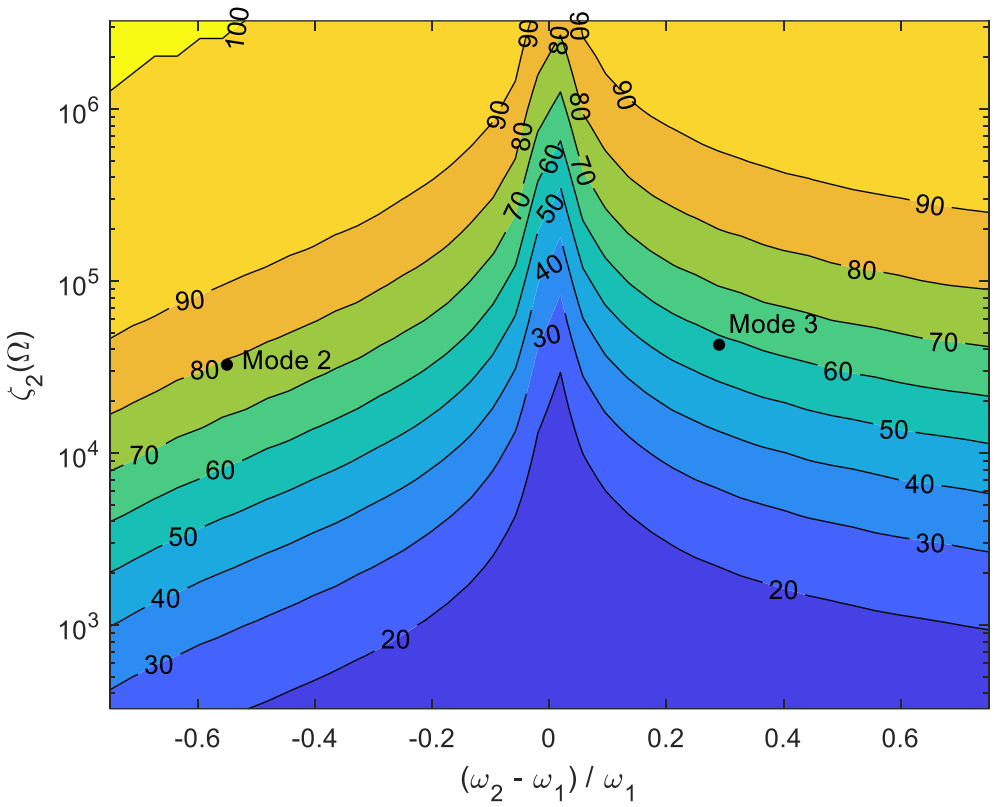

Fig. 4.15 – Contour plot of the percentage of good devices, against ζ_2 and $\Delta\omega$. Modes 2 and 3, corresponding to the 1st and 2nd spurious modes respectively, of the T1-13 PT.

As theorised, the results in Fig. 4.15 show that the values of ζ_2 required to ensure all devices have <5% $\Delta\eta$ decreases with spurious mode proximity to the optimum mode. However, even with a frequency difference of -0.75, ζ_2 values in excess of 1MΩ are required for 100% of devices to be classed as good, with only 1.25% of combinations (of ζ_2 and $\Delta\omega$) leading to 100% of devices being good. The asymmetry in the results should also be noted. As a result, for the same value of ζ_2, a spurious resonance will require a greater frequency difference if it occurs at a frequency greater than the optimum mode, compared to a mode occurring below ω_1.

4.7 Parameter range effect on required ζ_2 and $\Delta\omega$

Several different stipulations will be applied to the range of parameter variation in order to provide insight into realistic requirements for ζ_2 and $\Delta\omega$.

4.7.1 Reducing parameter range

The wide range of parameter variation used throughout the previous analyses, ensures that most potential PT designs are included. However, typically PT designs will have parameters similar to the T1-13 PT. Therefore, removing some of the more extreme parameter variations will give results that are more relevant to typical PT designs. A similar analysis to that in Fig. 4.15 will be performed, however, the range of parameter variation will be $x_n/10 \leq x \leq 10x_n$ where x is the parameter and x_n is its nominal value from Table 4.2 and $N_n/5 \leq N \leq 5N_n$ for the turn ratios (N_1 and N_2). Again, $\Delta\omega$ is varied, by changing ω_2, between $-0.75 < \Delta\omega < 0.75$, ω_1 is again assumed to be 100kHz. The results of this analysis are shown in Fig. 4.16.

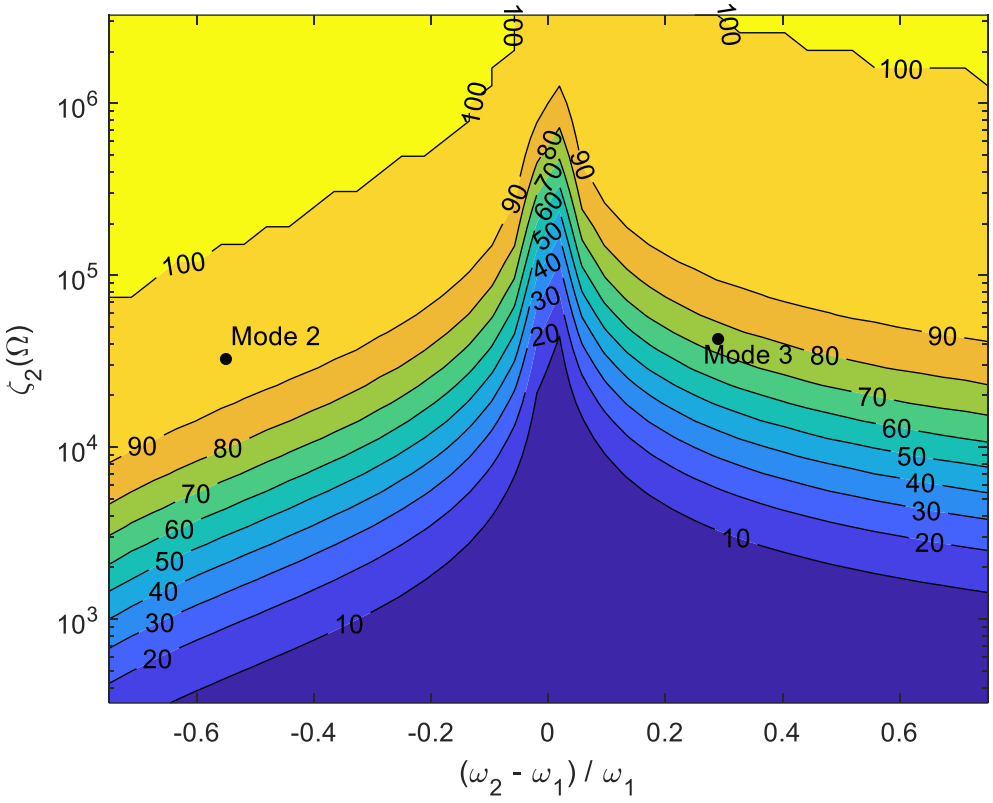

Fig. 4.16 – Contour plot of the percentage of good devices against ζ_2 and $\Delta\omega$, with the parameter space of the other parameters reduced. Modes 2 and 3, corresponding to the 1st and 2nd spurious modes respectively, of the T1-13 PT

Fig. 4.16 shows that reducing the range of parameter variation greatly reduces the required ζ_2 values for 100% of devices to exhibit $\Delta\eta$ <5%, with 16.3% of combinations (of ζ_2 and $\Delta\omega$) leading to 100% of devices meeting the <5% criterion. However, this graph also shows that for small $|\Delta\omega|$ and ζ_2 values, a smaller percentage of devices have $\Delta\eta$ <5%. This highlights that while the extreme parameter variations in some cases greatly increase $\Delta\eta$, in other cases

these extreme variations can allow a PT to have $\Delta\eta$ <5%, even when exhibiting small $\Delta\omega$ and ζ_2. However, $\Delta\omega$ and ζ_2 values required for 80%+ of devices to be good, has greatly reduced.

4.7.2 Lower damping

Typically, a PT will be designed for high optimum mode efficiency. As described earlier (4.3.2.a), minimising R_1 is vital for high optimum mode efficiency. R_1 values of <50Ω are typical in PZT based devices and as a result, 90%+ efficiency can be easily achieved irrespective of the other equivalent circuit parameters, when operated at the matched load. Also discussed previously, spurious mode damping is linked to optimum mode damping and so, if a PT is designed for high optimum mode efficiency (low R_1), then R_2 is also typically, relatively small. Again, these stipulations will be analysed. The range of parameter variation will be the same as in Fig. 4.15. However, devices exhibiting $R_1 > 50\Omega$ and/or $R_2 > 500\Omega$ will be excluded from the analysis. It should be noted that 50Ω was chosen by assuming 95% or better efficiency is desired in the optimum mode (if it is assumed $C_{\text{out}} = 0$, R_L = 1kΩ and $N_1 = 1$) and 500Ω was chosen noting the ratio of R_1/R_2 in the T1-13 PT. It should be noted that $X_{C_{\text{out}}}$, R_L and N_1 are all still varied through the same range as was used in Fig. 4.15, the assumptions above were used exclusively to determine the desired range of R_1 and R_2. The results of this analysis are shown in Fig. 4.17.

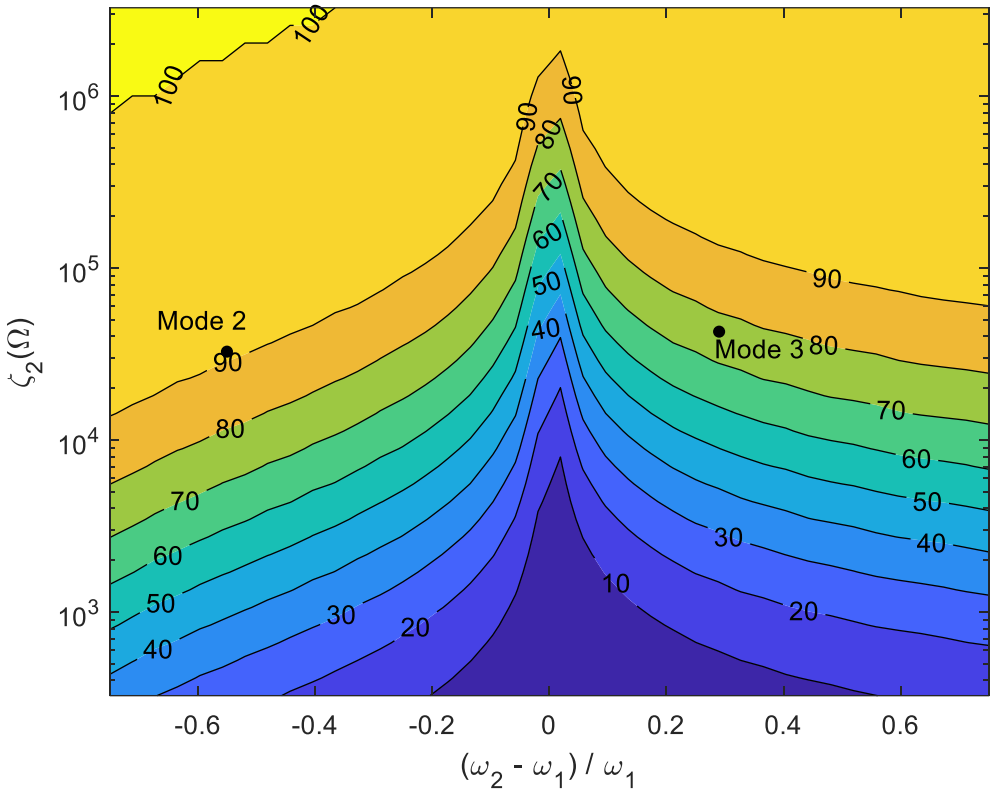

Fig. 4.17 – Contour plot of the percentage of good devices against ζ_2 and $\Delta\omega$, with the damping resistances, R_1 and R_2, less than 50Ω and 500Ω respectively. Modes 2 and 3, corresponding to the 1st and 2nd spurious modes respectively, of the T1-13 PT

The results in Fig. 4.17 are similar those in Fig. 4.16, with higher ζ_2 values leading to a higher percentage of devices achieving <5% $\Delta\eta$ for the same $\Delta\omega$, compared to Fig. 4.15. However, again for small $|\Delta\omega|$ and small ζ_2 values, a slightly lower percentage of good devices is achieved, compared to Fig. 4.15. Fig. 4.17 shows that reducing R_1 and R_2 makes achieving <5% $\Delta\eta$ easier.

4.7.3 Design case study – 5V, 1W output

A potential application for PTs is in low power, resonant converters, such as those used for charging mobile phones, tablets or laptops. In these applications typically a 5V output is required, providing 1W to the load, leading to a load resistance of 25Ω. Ideally, the transformer should have high efficiency, as losses across the switching and rectification elements will also reduce the overall system efficiency, which is beyond the scope of this analysis. Therefore, in this analysis, the PT will be designed to achieve an optimum mode

efficiency greater than 80%. Given these stipulations, an analysis can be performed to determine desired ζ_2 and $\Delta\omega$ values for minimal $\Delta\eta$.

For this analysis, all parameters will be varied through the same range as in Fig. 4.15 with the load fixed at 25Ω. All combinations of parameters which lead to an optimum mode efficiency of <80% will be removed from the analysis. Noting the ratio of R_1/R_2 in the T1-13 PT, devices exhibiting R_2 values > $15R_1$ were also removed from the analysis. It should be noted that, as the input voltage is not given in this scenario, the desired value of N_1 to achieve 5V output is unknown. Its value is therefore varied through the full range as was used in Fig. 4.15. The results of this analysis are presented in Fig. 4.18.

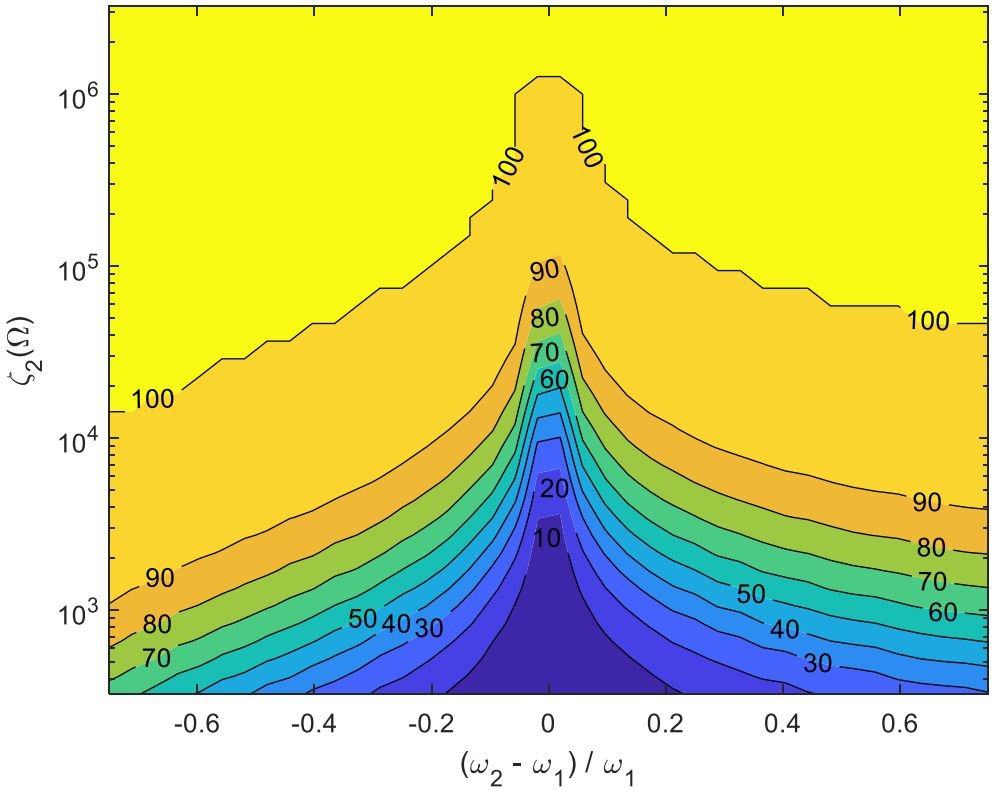

Fig. 4.18 – Contour plot of the percentage of good devices against ζ_2 and $\Delta\omega$, with optimum mode efficiency η_1 greater than 80%, load fixed at 25Ω and the damping resistance, R_2, no larger than $15R_1$

As is shown in Fig. 4.18, the required ζ_2 value to achieve <5% $\Delta\eta$ in 100% of devices for a given $\Delta\omega$ is greatly reduced in this scenario. As in previous figures, for small ζ_2 and $|\Delta\omega|$ values, fewer devices achieve <5% $\Delta\eta$, than in Fig. 4.15. However, observing the ζ_2 values presented in Fig. 4.14, in most cases a frequency difference of -0.37> $\Delta\omega$ and/or $\Delta\omega$ > 0.56 will ensure

that, so long as the other equivalent circuit values are within the relevant ranges, the PT should exhibit minimal efficiency degradation.

However, as with all the results published here, if a PT exbibits ζ_2 and $\Delta\omega$ values which lead to <100% of devices achieving <5% $\Delta\eta$, then it is still possible that a specific PT will have minimal $\Delta\eta$. Therefore, the results presented should be used as a guideline for design and if accurate estimations of the efficiency degradation in the PT are required, then they can be generated using the equations presented earlier.

4.8 Experimental validation

To validate the findings, the T1-13 PT will have its efficiency measured at its optimum mode frequency. The input impedance spectrum for this device is shown in Fig. 4.1. The efficiency is compared to predictions made using the equivalent circuit parameters presented in Table 4.2 and the various contour plots (Fig. 4.15-Fig. 4.17). It is important to note that it is not possible to directly measure efficiency degradation (as the modes are inseparable). The single-branch efficiency (η_1) was therefore estimated from the equivalent circuit parameters. A sinusoidal voltage was supplied to the PT and the input power, output power and efficiency were measured using a Yokogawa PX-8000 power oscilloscope. Using the estimated single-branch efficiency and measured efficiency, an estimate of efficiency degradation can be made. For this analysis, a load of 1kΩ (approx. matched) was used. Also, in this PT there are two offending spurious modes, these will be analysed separately.

First the equivalent circuit parameters of the third most significant mode (second spurious mode in Fig. 1), are extracted and shown in Table 4.4. Efficiency degradation from this mode can be found by using R_3, ω_3, ζ_3 and N_3 in place of R_2, ω_2, ζ_2 and N_2.

Table 4.4 – Equivalent circuit components for mode occurring at a frequency above the optimum in the T1-13 PT

	R_3	$\omega_3/2\pi$	ζ_3	N_3
T1-13	234.9 Ω	154.7 kHz	42,637 Ω	1.31

The ζ and $\Delta\omega$ values for the 1st and 2nd spurious modes (Fig. 4.1) are shown in Table 4.5 below.

Table 4.5 – ζ and $\Delta\omega$ values for the two spurious modes occurring closest (in terms of frequency) to the optimum mode

	Mode 2	**Mode 3**
ζ	32.6 kΩ	42.6 kΩ
$\Delta\omega$	-0.55	0.29

In the contour plots (Fig. 4.15-Fig. 4.17), the percentage of good devices (<5% $\Delta\eta$) with the ζ_2 and $\Delta\omega$ values from Table 4.5, can be found. They are labelled on each figure and summarised in Table 4.6.

Table 4.6 – Estimated percentage chance of achieving <5% $\Delta\eta$ for both modes from the contour plots previously presented in the respective figures

	Mode 2	Mode 3
Fig. 4.15	80.8 %	59.4 %
Fig. 4.16	97.9 %	77.0 %
Fig. 4.17	92.2 %	77.8 %

As Table 4.6 shows, both modes exhibit high percentage chances of achieving <5% $\Delta\eta$, with a maximum of 97.9% and 77.8% for 1st and 2nd spurious modes respectively. This suggests that both 1st and 2nd spurious modes may influence the PTs performance during operation at the optimum mode. However, with these modes achieving a high percentage chance of <5% $\Delta\eta$ in Fig. 4.15 - Fig. 4.17, it is highly likely they would have no influence on optimum mode performance, especially considering they exhibit a high turns ratio and low damping compared to the maximum 500Ω used in the analysis shown in Fig. 4.17.

For validation, the efficiency degradation of the PT is measured. The optimum mode efficiency was estimated using the equivalent circuit values in Table 4.2 and using equation (4.8). Using this value and the experimentally measured efficiency, the efficiency degradation is found.

For this PT and a 1kΩ load, the optimum mode efficiency is calculated at 97.3%. The efficiency is then experimentally measured as 96.9%. Using (4.20), the efficiency degradation is 0.4%.

Therefore, confirming the PT does exhibit <5% efficiency degradation from both spurious modes, as suggested by the analysis presented.

4.9 Discussion

The work presented here has highlighted the importance of optimising certain parameters at the design stage. As a result, designing a PT to exhibit large ζ_2 is vital, as this is the most influential parameter for minimising efficiency degradation, whilst having negligible effect on optimum mode performance. Secondly, decreasing damping in both the optimal and spurious modes is important for high efficiency. Both are typically determined by the piezoelectric material chosen, the electrode material chosen and the construction of the PT. Finally, increasing the spurious mode turn ratio also has a beneficial effect on $\Delta\eta$, whilst not affecting optimum mode performance. However, designing this parameter is difficult, as it requires knowledge of the type of spurious mode and how geometry or material changes affects its parameters. This will be analysed for the radial mode Transoner PT in the following chapters.

Efficiency loss from spurious modes can be minimised though careful design of the spurious mode resonant frequencies and ζ_2. It has also been shown that the required ζ_2 can be reduced through careful design of the other equivalent circuit values. Therefore, the analysis in this chapter provides designers with a method of appraising designs and, if required, provides information regarding potential design improvements.

It should also be noted that, while the analysis here looks at the required components and design to achieve less than 5% efficiency degradation, it does not analyse how far below or above 5% efficiency degradation represents a good or bad design. Additionally, this analysis does not consider whether $\Delta\eta < 5\%$ is in fact a good performance indicator. Readers will be able to reproduce the graphs for any desired efficiency degradation or nominal PT parameters using the presented equations.

The presence of spurious modes also causes an unwanted reduction in the output voltage. Therefore, even with appropriate optimum mode design, a PT may not supply the intended output voltage. However, improvements to efficiency degradation by adjusting spurious mode parameters (ω_2, R_2, N_2 and ζ_2), minimises the output voltage reduction, further demonstrating the importance of appropriate design for these parameters. R_1 and C_{out} have

a complicated relationship with voltage degradation and so decreasing their value (to decrease $\Delta\eta$) can increase or decrease voltage degradation depending on other parameters. Increasing the optimum mode turns ratio (N_1) to decrease $\Delta\eta$, causes voltage degradation to increase and therefore should be avoided. However, in T1-13 PT the voltage degradation was <1%, and so in most cases, voltage degradation is unlikely to be an issue.

Due to the number of variables that influence the efficiency degradation and the wide range of potential variation in these parameters, there will be cases where a parameter is outside the presented range of variation. The results of this analysis should be used as a guideline for appropriate design with a view to producing an exact specification following circuit and finite element analysis. The parameters of a PT design should be carefully analysed using the equations presented in this chapter to calculate the efficiency degradation and the required ζ_2.

Spurious modes will typically occur at frequencies both above and below the optimum mode frequency. However, the analysis in this paper has primarily considered interaction with a single spurious mode. It can be assumed that each spurious mode can be considered and analysed separately, which is likely in practice.

4.10 Summary

In this chapter, the impact of spurious modes on the efficiency of PTs has been analysed. This analysis has included the development of several efficiency models and performing multiple sensitivity analyses to determine key factors in ensuring minimal efficiency loss from PTs. The results of this analysis will be used with the models developed in the next three chapters as part of the automated design algorithm.

4.11 References

[4.1] M. P. Foster, J. N. Davidson, E. L. Horsley, and D. A. Stone, 'Critical Design Criterion for Achieving Zero Voltage Switching in Inductorless Half-Bridge-Driven Piezoelectric-Transformer-Based Power Supplies', *IEEE Transactions on Power Electronics*, vol. 31, no. 7, pp. 5057–5066, Jul. 2016, doi: 10.1109/TPEL.2015.2481706.

[4.2] G. Ivensky, I. Zafrany, and S. Ben-Yaakov, 'Generic operational characteristics of piezoelectric transformers', *IEEE Transactions on Power Electronics*, vol. 17, no. 6, pp. 1049–1057, Nov. 2002, doi: 10.1109/TPEL.2002.805602.

[4.3] R.-L. Lin, 'Piezoelectric Transformer Characterization and Application of Electronic Ballast', *Ph.D. Dissertation*, Nov. 2001, Accessed: Feb. 15, 2018. [Online]. Available: https://vtechworks.lib.vt.edu/handle/10919/29948

[4.4] J. Forrester, J. N. Davidson, M. P. Foster, E. L. Horsley, and D. A. Stone, 'Automated design tools for piezoelectric transformer-based power supplies', *The Journal of Engineering*, vol. 2019, no. 17, pp. 4163–4166, 2019, doi: 10.1049/joe.2018.8065.

[4.5] V. Loyau, Y. P. Liu, and F. Costa, 'Analyses of the Heat Dissipated by Losses in a Piezoelectric Transformer', *IEEE Transactions on Ultrasonics, Ferroelectrics, and Frequency Control*, vol. 56, no. 8, pp. 1745–1752, Aug. 2009, doi: 10.1109/TUFFC.2009.1239.

[4.6] MEGACERA INC, 'PT291C3 Specification Sheet'. MEGACERA INC, Oct. 15, 2001. [Online]. Available: http://mmech.com/images/stories/Standard_Products/Transformers/High_Voltage/PT291C3_Specification_Sheet.pdf

[4.7] Micromechatronics Inc., 'Transoner® Data Sheet'. Micromechatronics Inc., May 24, 2005. [Online]. Available: http://mmech.com/images/stories/Standard_Products/Transformers/Step_Down/Datasheet_of_T1-noniso-6_-_MMech.pdf

[4.8] S. Kawashima *et al.*, 'Third order longitudinal mode piezoelectric ceramic transformer and its application to high-voltage power inverter', in *1994 Proceedings of IEEE Ultrasonics Symposium*, Oct. 1994, vol. 1, pp. 525–530, doi: 10.1109/ULTSYM.1994.401643.

[4.9] Y. Huang, Z. Miao, X. Chen, and W. Huang, 'A verification and parametric analysis of an analytical model of a flexural vibration mode piezoelectric transformer', *IEEE Transactions on Ultrasonics, Ferroelectrics, and Frequency Control*, vol. 59, no. 12, pp. 2731–2741, Dec. 2012, doi: 10.1109/TUFFC.2012.2514.

[4.10] J. Du, J. Hu, and K.-J. Tseng, 'High-power, multioutput piezoelectric transformers operating at the thickness-shear vibration mode', *IEEE Transactions on Ultrasonics, Ferroelectrics, and Frequency Control*, vol. 51, no. 5, pp. 502–509, May 2004, doi: 10.1109/TUFFC.2004.1320823.

[4.11] J. Yoo, K. Yoon, Y. Lee, S. Suh, J. Kim, and C. Yoo, 'Electrical Characteristics of the Contour-Vibration-Mode Piezoelectric Transformer with Ring/Dot Electrode Area Ratio', *Jpn. J. Appl. Phys.*, vol. 39, no. 5R, p. 2680, May 2000, doi: 10.1143/JJAP.39.2680.

Chapter 5 - Derivation of a lumped equivalent circuit model of the spurious modes of the radial mode Transoner PTs using Kirchhoff plate theory (CPT)

5.1 Introduction

In the previous chapter, the effect of spurious modes on the efficiency of a PT was analysed, based on the extended multiresonant branch Mason equivalent circuit model of a PT. However, to be able to apply the previous analysis to PT design methodology, a method of estimating the spurious mode equivalent circuit parameters is required. For a physical PT, these parameters can easily be extracted from impedance measurements, using one of the methods presented in Chapter 3; however, it is beneficial to be able to estimate these values at the design stage. Whilst lumped equivalent modelling is often performed on the optimal mode of a PT (i.e. the radial mode in the ring-dot PT or the radial mode Transoner), it is rarely performed for spurious modes.

Parameterisation of these modes has been typically achieved using FEA approaches, however, it is time consuming to simulate a large variety of devices to determine an optimum solution based on trial and error. Additionally, there are often large costs associated with FEA tools and they require expert knowledge to achieve useful results. In this chapter a model is presented which allows the Mason equivalent circuit model of the flexural modes of the Transoner PT to be parameterised. This allows a PT designer to achieve a near optimal PT design based on these theoretical values, before using FEA tools and prototyping to finalise the design, reducing costs, and increasing design speed.

As discussed in Chapter 2, there are several plate theories which can be used to analyse the vibration of PTs. Two of the most common are Kirchhoff plate theory (CPT) and Mindlin plate

theory (MPT). These models use several assumptions to simplify the constitutive equations for piezoelectrics and allow devices to be analysed without approximation.

In the following two chapters lumped equivalent circuit models for the flexural, spurious modes occurring in the radial mode Transoner PT are developed using both plate theories. Then in Chapter 7 both models are verified against COMSOL simulation and experimental data. In this chapter, an electromechanical model is derived using the Kirchhoff plate theory (CPT). Firstly, the relevant assumptions are presented. Then, a full derivation of the model is presented. Finally, the full equivalent circuit model is simplified using several circuit transformations to the Mason equivalent circuit form.

5.2 Scope of model and assumptions

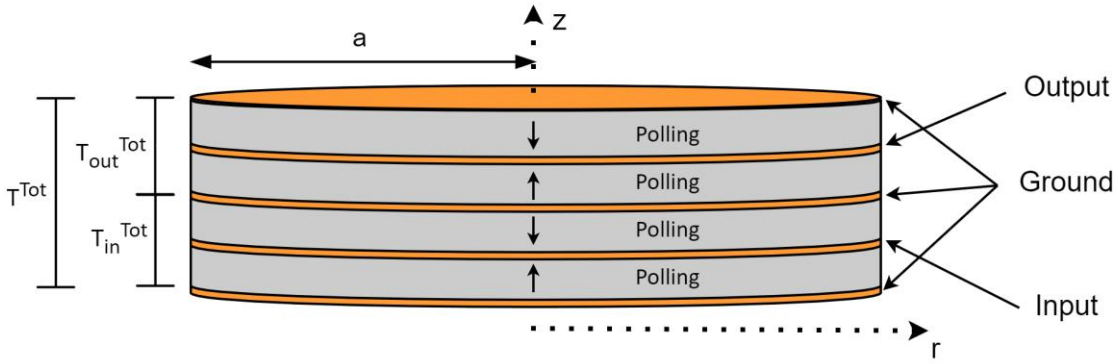

Fig. 5.1 – Radial mode PT

The model derived here will be based on a 1D analysis of a radial-mode Transoner device, operating exclusively with flexural motion. The PT has an input and an output section, with each section split into several layers (N_{in} and N_{out}). Each of the layers have the same radius (a), and all layers in a section (either input or output) have the same thickness, although the sections can have differing thicknesses ($T_{\mathrm{in}}^{\mathrm{tot}}$ and $T_{\mathrm{out}}^{\mathrm{tot}}$). In this analysis, all additional layers (electrode, insulation, adhesive) will be assumed to have negligible effect. Each of the piezoelectric layers are polled in opposing directions. The electrode between input and output sections is a common ground, with adjacent electrodes alternating between terminal (either input or output) and ground, as shown in Fig. 5.1. Therefore, layers in each section are connected in parallel. Fig. 5.1 also shows the cylindrical coordinate system with the radius a in the r-axis and the thickness in the z-axis.

5.2.1 Classic plate theory assumptions

The Kirchhoff/classic plate theory (CPT) requires several assumptions to be made. These assumptions are [5.1],

- T_z is negligible ($T_z = 0$)
- Vibration is axisymmetric, $u_\theta = 0$ (displacement in θ direction)
- Transverse displacement (w) is independent of z coordinate
- Straight lines perpendicular to the mid-surface before deformation, remain straight after deformation (i.e. no shear deformation)
- The transverse normal do not experience elongation, $S_{zz} = 0$
- The transverse normals rotate such that they remain perpendicular to the mid-surface after deformation, $S_{rz} = S_{\theta z} = 0$
- For these assumptions to be valid, the PT will need to have a radius much greater than its total thickness.

5.3 Derivation

As discussed in Chapter 2, analysis of piezoelectric devices often starts with the constitutive equations. These equations link the mechanical and electrical properties of the piezoelectric device. In this derivation, we will assume the use a material of class C_{6v} (see 2.1.7 for more details) and so we can use the simplified constitutive equations as given by equations (2.12) and (2.13). As the Transoner PT uses discs which are polled in the 'z' direction, the constitutive equations in polar coordinates are given by [5.2],

$$T_r = \frac{S_r + \sigma S_\theta}{(s_{11}^{\mathrm{E}}(1-\sigma^2))} - \frac{d_{31}E_z}{s_{11}^{\mathrm{E}}(1-\sigma)} \tag{5.1}$$

$$T_\theta = \frac{S_\theta + \sigma S_r}{(s_{11}^{\mathrm{E}}(1-\sigma^2))} - \frac{d_{31}E_z}{s_{11}^{\mathrm{E}}(1-\sigma)} \tag{5.2}$$

$$T_{rz} = \frac{S_{rz} - d_{15}E_r}{s_{55}^{\mathrm{E}}} = \frac{S_{rz}}{s_{55}^{\mathrm{E}}} \tag{5.3}$$

$$D_z = d_{31}T_r + d_{31}T_\theta + \varepsilon_{33}^{\mathrm{T}}E_z \tag{5.4}$$

where d_{31} is the piezoelectric strain constant, s_{11}^{E} and s_{55}^{E} are the elastic compliance, $\varepsilon_{33}^{\mathrm{T}}$ is the dielectric constant and σ is Poisson's ratio given by

$$\sigma = -\frac{s_{12}^{\mathrm{E}}}{s_{11}^{\mathrm{E}}} \tag{5.5}$$

Wang *et al.* [5.3] found that for piezoelectric bimorphs (with a similar structure to a PT) the electric potential in the thickness direction, has a quadratic variation during flexural vibration. Additionally, Wang *et al.* also discussed the use of a sinusoidal model of the electric potential in the thickness direction when analysing devices with only piezoelectric layers. Sammoura *et al.* [5.4] used a linear model for the electric potential across the layer thicknesses. A linear model meaning in each layer the potential increases linearly from the ground terminal adjacent to each layer to the input or output terminal adjacent to each layer, in the direction of polling. Whilst Wang *et al.* found that a linear model is mathematically invalid for this device (disagrees with Gauss's law), Sammoura *et al.* achieved excellent results using a linear model, whilst greatly simplifying the analysis compared to that presented by Wang *et al*. Therefore, in this analysis, a linear model for the electric potential through each layer will be used. Based on this, the electric field $E_{z_{\mathrm{in,out}}}$ in each layer of the input and output sections are given by,

$$E_{z_{\mathrm{in}}} = {V_{\mathrm{in}}}\Big/{\left(\frac{T_{\mathrm{in}}^{\mathrm{tot}}}{N_{\mathrm{in}}}\right)} \tag{5.6}$$

$$E_{z_{\mathrm{out}}} = {V_{\mathrm{out}}}\Big/{\left(\frac{T_{\mathrm{out}}^{\mathrm{tot}}}{N_{\mathrm{out}}}\right)} \tag{5.7}$$

where N_{in} is the number of input layers, N_{out} is the number of output layers, $T_{\mathrm{in}}^{\mathrm{tot}}$ and $T_{\mathrm{out}}^{\mathrm{tot}}$ are the input and output section total thicknesses, and V_{in} and V_{out} are the magnitude of the voltages on the input and output terminals, respectively.

Observing equations (5.1)-(5.4) only the radial and azimuth strains are of interest (shear strain is negligible for the CPT), owing to the thin plate assumptions discussed in section 5.2 and the assumed perfect axisymmetric motion of the device. Based on the CPT, these strains can be written in terms of the transverse displacement of the device, where the transverse displacement describes the displacement of the device in the 'z' direction. The radial S_r and azimuth S_θ strains can be shown to be given by [5.2],

$$S_r = z\frac{\partial^2 w}{\partial r^2} \tag{5.8}$$

$$S_\theta = \frac{z}{r}\frac{\partial w}{\partial r} \tag{5.9}$$

where w is transverse displacement of the PT.

5.3.1 Forces, moments, and equation of motion

Reddy [5.1] and Leissa [5.5] both present descriptions of the forces and moments acting each direction on a plate during vibration. These forces and moments are shown in Fig. 2.3 in cartesian coordinates. In cylindrical coordinates the transverse shearing force Q_r, in the radial direction is given by [5.5],

$$Q_r = -\frac{\partial M_r}{\partial r} - \frac{M_r - M_\theta}{r} \tag{5.10}$$

Similarly, the flexural moments $M_{r,\theta}$ can also be shown to be given by [5.5],

$$M_r = \int_{H_1}^{H_2} T_{r_{\text{in}}} z\, dz + \int_{H_3}^{H_4} T_{r_{\text{out}}} z\, dz \tag{5.11}$$

$$M_\theta = \int_{H_1}^{H_2} T_{\theta_{\text{in}}} z\, dz + \int_{H_3}^{H_4} T_{\theta_{\text{out}}} z\, dz \tag{5.12}$$

where constants $H_{1,2,34}$ are defined with respect to the neutral plane [5.5], which is assumed to be at $T_{\text{tot}}/2$, and are given by,

$$H_1 = \frac{T_{\text{tot}}}{2} - T_{\text{in}}^{\text{tot}} \tag{5.13}$$

$$H_2 = \frac{T_{\text{tot}}}{2} \tag{5.14}$$

$$H_3 = -\frac{T_{\text{tot}}}{2} \tag{5.15}$$

$$H_4 = T_{\text{out}}^{\text{tot}} - \frac{T_{\text{tot}}}{2} \tag{5.16}$$

Then, by summing the forces in the 'z' direction in Leissa's case and using the principal of virtual work done (See [5.1] for more details), a general equation of flexural motion can be derived. In the case of axisymmetric modes (transverse shear force $Q_\theta = 0$), with the CPT assumptions discussed in section 5.2, this equation of motion can be written as [5.5],

$$\frac{\partial(rQ_r)}{\partial r} = -\bar{\rho}\omega^2 rw \tag{5.17}$$

where $\bar{\rho}$ is the mass per unit area of the PT. This is the equation of motion for flexural vibration of an axisymmetric thin disc.

5.3.2 Displacement

In sections 5.3.3 and 5.3.4, equations for the forces acting on the PT and the currents flowing into the PT will be derived in terms of the displacement of the PT. Therefore, to be able to later solve these equations, an expression for the displacement of the PT is required. This equation will be derived from the equation of motion (5.17).

First, substituting M_r (5.11) and M_θ (5.12) into the equation for Q_r (5.10), then, substituting the result into (5.17) gives a differential equation in terms of the transverse displacement of the PT,

$$\mathrm{D}\nabla^4 w = \bar{\rho}\omega^2 w \tag{5.18}$$

where ∇^4 is the fourth order differential operator, D is the flexural rigidity given by

$$D = \frac{(T_{\text{tot}})^3}{12 s_{11}^{\mathrm{E}}(1 - \sigma^2)} \tag{5.19}$$

where T_{tot} is the total device thickness ($T_{\text{tot}} = T_{\text{out}}^{\text{tot}} + T_{\text{in}}^{\text{tot}}$). Then, by introducing the lambda parameter [5.5],

$$\lambda^4 = \frac{\rho T_{\text{tot}}\omega^2}{D} \tag{5.20}$$

allows (5.18) to be written as,

$$\nabla^4 w = \lambda^4 w \tag{5.21}$$

All mechanical and electrical responses will be assumed to be harmonically excited. Therefore, the time varying transverse displacement is given by,

$$W(r,t) = w(r)e^{\mathrm{j}\omega t} \tag{5.22}$$

Finally, substituting (5.21) into (5.22) and solving for W gives,

$$W(r,t) = A_1 \mathrm{I}_0(\lambda r) + A_2 \mathrm{J}_0(\lambda r) + A_3 \mathrm{K}_0(\lambda r) + A_4 \mathrm{Y}_0(\lambda r)\mathrm{e}^{\mathrm{j}\omega t} \tag{5.23}$$

where J_0 and I_0 are the Bessel function and modified Bessel function, respectively, of the first kind and zeroth order. Y_0 and K_0 are the Bessel function and modified Bessel function of the second kind and zeroth order, respectively. $A_{1,2,3,4}$ are constants to be found from the application of boundary conditions and the capitalised W indicates the transverse displacement is now a function of time due to harmonic excitation.

5.3.2.a) Application of boundary conditions

In order to derive an equation for the transverse displacement of the PT, constants $A_{1,2,3,4}$ in (5.23) must first be found by applying the free vibration boundary condition. Firstly, (5.23) can be simplified by noting that at $r = 0$ the displacement of the PT must be finite. Therefore, substituting $r = 0$ in (5.23), we observe that $\mathrm{Y}_0(0) = \mathrm{K}_0(0) = \infty$. Therefore A_3 and A_4 must both equal 0 and as a result (5.23) can be simplified to,

$$W(r,t) = A_1 \mathrm{I}_0(\lambda r) + A_2 \mathrm{J}_0(\lambda r)\, e^{\mathrm{j}\omega t} \tag{5.24}$$

During flexural vibration the PT has two main forces acting upon it, F_1 and F_2, which are as a result of the flexural moment and shear force, respectively, these are shown in Fig. 5.2.

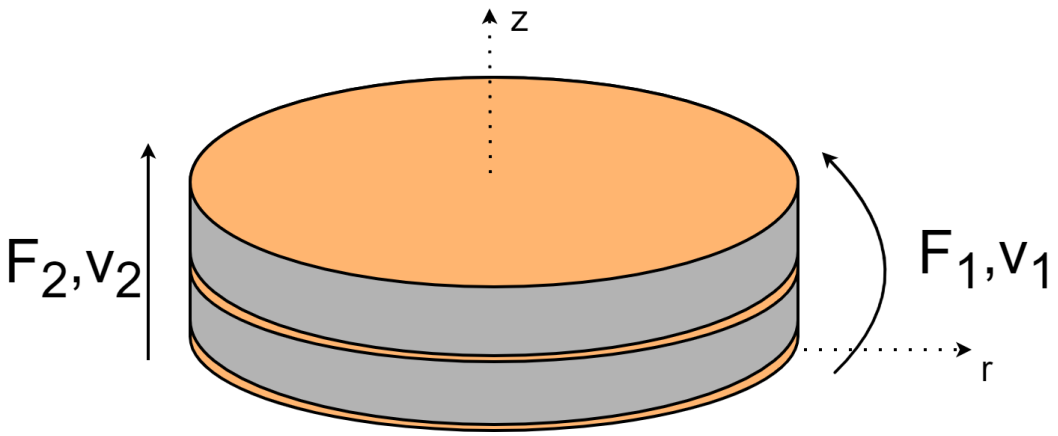

Fig. 5.2 – Forces and velocities acting on the radial mode PT during flexural vibration

Each force causes a vibration and thus has a velocity associated with that movement, defined as v_1 and v_2. Constants A_1 and A_2 will be found in terms of these vibration velocities. The vibration velocities are calculated by differentiating the angle of rotation $(\partial w/\partial r)$ and transverse displacement (w) (5.24) at the outer edge of the PT $(r = a)$ with respect to time [5.6],

$$v_1(t) = \frac{\partial\left(\frac{\partial W}{\partial r}\right)}{\partial t} = \mathrm{j}\omega\frac{\partial W}{\partial r} = \mathrm{j}\omega\lambda\left(A_1\mathrm{I}_1(\lambda a) - A_2\mathrm{J}_1(\lambda a)\right)e^{\mathrm{j}\omega t} \tag{5.25}$$

$$v_2(t) = \frac{\partial W}{\partial t} = \mathrm{j}\omega W = \mathrm{j}\omega\left(A_1\mathrm{I}_0(\lambda a) + A_2\mathrm{J}_0(\lambda a)\right)e^{\mathrm{j}\omega t} \tag{5.26}$$

Equations (5.25) and (5.26) can then be solved simultaneously. Firstly, solving (5.25) and (5.26) for A_1 gives,

$$A_1 = \frac{-\mathrm{j}v_1(t)e^{-\mathrm{j}\omega t} + \omega A_2\mathrm{J}_1(\lambda a)\lambda}{\mathrm{I}_1(\lambda a)\lambda\omega} \tag{5.27}$$

$$A_1 = \frac{-\mathrm{j}v_2(t)e^{-\mathrm{j}\omega t} - A_2\mathrm{J}_0(\lambda a)\omega}{\mathrm{I}_0(\lambda a)\omega} \tag{5.28}$$

Equating (5.27) and (5.28), and solving for A_2 gives

$$A_2 = \frac{-\mathrm{j}(-\mathrm{I}_1(\lambda a)v_2(t)\lambda + \mathrm{I}_0(\lambda a)v_1(t))e^{-\mathrm{j}\omega t}}{\lambda\omega\left(\mathrm{I}_1(\lambda a)\mathrm{J}_0(\lambda a) + \mathrm{I}_0(\lambda a)\mathrm{J}_1(\lambda a)\right)} \tag{5.29}$$

A_1 is then found by substituting (5.29) into either (5.27) or (5.28) and simplifying, giving

$$A_1 = \frac{-\mathrm{j}\big(\mathrm{J}_1(\lambda a)v_2(t)\lambda + \mathrm{J}_0(\lambda a)v_1(t)\big)e^{-\mathrm{j}\omega t}}{\big(\mathrm{I}_1(\lambda a)\mathrm{J}_0(\lambda a) + \mathrm{I}_0(\lambda a)\mathrm{J}_1(\lambda a)\big)\lambda\omega} \tag{5.30}$$

Finally, substituting (5.29) and (5.30) into (5.24) gives an equation for the transverse displacement of a particle in the PT,

$$W(r,t) = \frac{\mathrm{j}\begin{pmatrix} (v_1(t)\mathrm{I}_0(\lambda a) - \mathrm{I}_1(\lambda a)v_2(t)\lambda)\mathrm{J}_0(\lambda r) \\ -\big(\mathrm{J}_1(\lambda a)v_2(t)\lambda + \mathrm{J}_0(\lambda a)v_1(t)\big)\mathrm{I}_0(\lambda r)\end{pmatrix}}{\big(\mathrm{I}_0(\lambda a)\mathrm{J}_1(\lambda a) + \mathrm{I}_1(\lambda a)\mathrm{J}_0(\lambda a)\big)\lambda\omega} \tag{5.31}$$

Whilst this equation could be used to determine the displacement of the PT at a certain radius, this would require explicit expressions for the vibration velocities which are cumbersome to derive. However, in the following sections this equation will be used to generate equations for the forces and currents acting on and flowing into the PT, in terms of vibration velocities, which will allow equivalent circuits to be formulated.

5.3.3 Electrical equations

In this section, equations for the current into the input and output section will be derived in terms of vibration velocities, and input and output voltages. Firstly, the charge into and out of the PT, Q_{in} and Q_{out}, is given by Gauss's law,

$$Q_{\mathrm{in}} = \frac{2\pi}{T_{\mathrm{in}}^{\mathrm{tot}}}\int_{H_1}^{H_2}\int_0^a rD_{z_{\mathrm{in}}}\,dr\,dz \tag{5.32}$$

$$Q_{\mathrm{out}} = \frac{2\pi}{T_{\mathrm{out}}^{\mathrm{tot}}}\int_{H_3}^{H_4}\int_0^a rD_{z_{\mathrm{out}}}\,dr\,dz \tag{5.33}$$

where $H_{1,2,3,4}$ are given by (5.13)-(5.16). Substituting D_z (5.4) into (5.32) and (5.33), gives

$$Q_{\mathrm{in}} = \frac{2\pi}{T_{\mathrm{in}}^{\mathrm{tot}}}\int_{H_1}^{H_2}\int_0^a \big(d_{31}T_{r_{\mathrm{in}}} + d_{31}T_{\theta_{\mathrm{in}}} + \varepsilon_{33}^{\mathrm{T}}E_{z_{\mathrm{in}}}\big)r\,dr\,dz \tag{5.34}$$

$$Q_{\mathrm{out}} = \frac{2\pi}{T_{\mathrm{out}}^{\mathrm{tot}}}\int_{H_3}^{H_4}\int_0^a \big(d_{31}T_{r_{\mathrm{out}}} + d_{31}T_{\theta_{\mathrm{out}}} + \varepsilon_{33}^{\mathrm{T}}E_{z_{\mathrm{out}}}\big)r\,dr\,dz \tag{5.35}$$

Then, substituting equations for $T_{r_{\mathrm{in,out}}}$ (5.1) and $T_{\theta_{\mathrm{in,out}}}$ (5.2) into (5.34) and (5.35) with S_r (5.8) and S_θ (5.9), gives

$$Q_{\mathrm{in}} = \frac{2\pi}{s_{11}^{\mathrm{E}}(\sigma-1)T_{\mathrm{in}}^{\mathrm{tot}}} \int_{H_1}^{H_2} \int_0^a \left(\left(\frac{\partial^2 w}{\partial r^2} r + \frac{\partial^2 w}{\partial r^2} \right) d_{31} z + \left(2d_{31}^2 + \varepsilon_{33}^{\mathrm{T}} s_{11}^{\mathrm{E}} (\sigma-1) \right) E_{z_{\mathrm{in}}} r \right) dr\, dz \tag{5.36}$$

$$Q_{\mathrm{out}} = \frac{2\pi}{s_{11}^{\mathrm{E}}(\sigma-1)T_{\mathrm{out}}^{\mathrm{tot}}} \int_{H_3}^{H_4} \int_0^a \left(\left(\frac{\partial^2 w}{\partial r^2} r + \frac{\partial^2 w}{\partial r^2} \right) d_{31} z + \left(2d_{31}^2 + \varepsilon_{33}^{\mathrm{T}} s_{11}^{\mathrm{E}} (\sigma-1) \right) E_{z_{\mathrm{out}}} r \right) dr\, dz \tag{5.37}$$

As previously mentioned, we assume the voltage applied to the PT is sinusoidally varying as $e^{\mathrm{j}\omega t}$, therefore, the charge on the input and output electrodes will also vary with time,

$$q_{\mathrm{in}}(t) = Q_{\mathrm{in}} e^{\mathrm{j}\omega t} \tag{5.38}$$

$$q_{\mathrm{out}}(t) = Q_{\mathrm{out}} e^{\mathrm{j}\omega t} \tag{5.39}$$

The current into the input and output layers can then be found by

$$\mathrm{I}_{\mathrm{in}}^{\mathrm{Lay}} = \frac{\partial q_{\mathrm{in}}}{\partial t} = \mathrm{j}\omega Q_{\mathrm{in}} e^{\mathrm{j}\omega t} \tag{5.40}$$

$$\mathrm{I}_{\mathrm{out}}^{\mathrm{Lay}} = \frac{\partial q_{\mathrm{out}}}{\partial t} = \mathrm{j}\omega Q_{\mathrm{out}} e^{\mathrm{j}\omega t} \tag{5.41}$$

The magnitude of the total input current into the input and output sections is given by

$$I_{\mathrm{in}}^{\mathrm{Tot}} = N_{\mathrm{in}} \mathrm{I}_{\mathrm{in}}^{\mathrm{Lay}} \tag{5.42}$$

$$I_{\mathrm{out}}^{\mathrm{Tot}} = N_{\mathrm{out}} \mathrm{I}_{\mathrm{out}}^{\mathrm{Lay}} \tag{5.43}$$

Substituting w(5.31), electric fields $E_{z_{\mathrm{in}}}$ (5.6) and $E_{z_{\mathrm{out}}}$ (5.7) into Q_{in} (5.36) and Q_{out} (5.37), then into $\mathrm{I}_{\mathrm{in}}^{\mathrm{Lay}}$ (5.40) and $\mathrm{I}_{\mathrm{out}}^{\mathrm{Lay}}$ (5.41), and finally into (5.42) and (5.43) gives equations for the current $I_{\mathrm{in}}^{\mathrm{Tot}}$ and $I_{\mathrm{out}}^{\mathrm{Tot}}$ into the input and output section,

$$I_{\mathrm{in}}^{\mathrm{Tot}} = \frac{\mathrm{j}\omega N_{\mathrm{in}}^2 a^2 \pi \left(2d_{31}^2 + \varepsilon_{33}^{\mathrm{T}} s_{11}^{\mathrm{E}}(\sigma-1)\right)}{T_{\mathrm{in}}^{\mathrm{tot}} s_{11}^{\mathrm{E}}(\sigma-1)} V_{\mathrm{in}} - \frac{(N_{\mathrm{in}} a d_{31} T_{\mathrm{out}}^{\mathrm{tot}} \pi)}{s_{11}^{\mathrm{E}}(\sigma-1)} v_1 \tag{5.44}$$

$$I_{\mathrm{out}}^{\mathrm{Tot}} = \frac{\mathrm{j}\omega N_{\mathrm{out}}^2 a^2 \pi \left(2d_{31}^2 + \varepsilon_{33}^{\mathrm{T}} s_{11}^{\mathrm{E}}(\sigma-1)\right)}{T_{\mathrm{out}}^{\mathrm{tot}} s_{11}^{\mathrm{E}}(\sigma-1)} V_{\mathrm{out}} + \frac{(N_{\mathrm{out}} a d_{31} T_{\mathrm{in}}^{\mathrm{tot}} \pi)}{s_{11}^{\mathrm{E}}(\sigma-1)} v_1 \tag{5.45}$$

Then, as was done in [5.7] force factors, $A_{\mathrm{in}}$and A_{out} are introduced. Force factors describe the conversion factor from electrical to mechanical energy in the input section and from mechanical to electrical energy in the output section. The A_{in} and A_{out} force factors are defined in this case as,

$$A_{\mathrm{in}} = -\frac{(N_{\mathrm{in}} a d_{31} T_{\mathrm{out}}^{\mathrm{tot}} \pi)}{s_{11}^{\mathrm{E}}(\sigma-1)} \tag{5.46}$$

$$A_{\mathrm{out}} = \frac{(N_{\mathrm{out}} a d_{31} T_{\mathrm{in}}^{\mathrm{tot}} \pi)}{s_{11}^{\mathrm{E}}(\sigma-1)} \tag{5.47}$$

Using A_{in} (5.46) and A_{out} (5.47) allows (5.44) and (5.45) to be written as

$$I_{\mathrm{in}}^{\mathrm{Tot}} = \mathrm{j}\omega C_{\mathrm{in}} V_{\mathrm{in}} + A_{\mathrm{in}} v_1 \tag{5.48}$$

$$I_{\mathrm{out}}^{\mathrm{Tot}} = \mathrm{j}\omega C_{\mathrm{out}} V_{\mathrm{out}} + A_{\mathrm{out}} v_1 \tag{5.49}$$

where input and output capacitances are given by

$$C_{\mathrm{in}} = \frac{\pi a^2 \varepsilon_{33}^{\mathrm{T}} N_{\mathrm{in}}^2}{T_{\mathrm{in}}^{\mathrm{tot}}} + \frac{\pi a^2 2d_{31}^2 N_{\mathrm{in}}^2}{T_{\mathrm{in}}^{\mathrm{tot}} s_{11}^{\mathrm{E}}(\sigma-1)} \tag{5.50}$$

$$C_{\mathrm{out}} = \frac{\pi a^2 \varepsilon_{33}^{\mathrm{T}} N_{\mathrm{out}}^2}{T_{\mathrm{out}}^{\mathrm{tot}}} + \frac{\pi a^2 2d_{31}^2 N_{\mathrm{out}}^2}{T_{\mathrm{out}}^{\mathrm{tot}} s_{11}^{\mathrm{E}}(\sigma-1)} \tag{5.51}$$

5.3.4 Mechanical equations

In this section, equations will be generated for the forces F_1 and F_2, as shown in Fig. 5.2. Forces F_1 and F_2 can be written as [5.6],

$$F_1 = 2\pi a M_r(a) \tag{5.52}$$

$$F_2 = 2\pi a Q_r(a) \tag{5.53}$$

Substituting M_R (5.11) and Q_r (5.10) into F_1 (5.52) and F_2 (5.53), with T_r (5.1) and T_θ (5.2), and $E_{z_{\text{in}}}$ (5.6) and $E_{z_{\text{out}}}$ (5.7) gives,

$$\begin{aligned} F_1 = &-\frac{a\pi(T_{\text{in}}^{\text{tot}} + T_{\text{out}}^{\text{tot}})^3\left(\left(\frac{\partial W(a)}{\partial r}\right)\sigma + r\left(\frac{\partial^2 W(a)}{\partial r^2}\right)\right)}{6s_{11}^{\text{E}}(\sigma^2-1)r} \\ &+ \frac{a\pi d_{31}(1+\sigma)T_{\text{out}}^{\text{tot}}N_{\text{in}}}{s_{11}^{\text{E}}(\sigma^2-1)}V_{\text{in}} - \frac{a\pi d_{31}(1+\sigma)T_{\text{in}}^{\text{tot}}N_{\text{out}}}{s_{11}^{\text{E}}(\sigma^2-1)}V_{\text{out}} \end{aligned} \tag{5.54}$$

$$F_2 = \frac{a\pi(T_{\text{in}}^{\text{tot}} + T_{\text{out}}^{\text{tot}})^3\left(\left(\frac{\partial^3 W(a)}{\partial r^3}\right) + \frac{1}{r}\left(\frac{\partial^2 W(a)}{\partial r^2}\right) - \frac{1}{r^2}\left(\frac{\partial W(a)}{\partial r}\right)\right)}{(6s_{11}^{\text{E}}\sigma^2 - 6s_{11}^{\text{E}})} \tag{5.55}$$

Then, substituting W (5.31) into (5.54) and (5.55), and using A_{in} and A_{out} force factors gives,

$$F_1 = Z_1 v_1 + Z_2 v_2 - A_{\text{in}}V_{\text{in}} - A_{\text{out}}V_{\text{out}} \tag{5.56}$$

$$F_2 = Z_2 v_1 + Z_3 v_2 \tag{5.57}$$

where impedances $Z_{1,2,3}$ are given by

$$Z_1 = -\frac{4j\pi D\left(\begin{array}{c}\left(\lambda a \mathrm{J}_0(\lambda a) + \frac{1}{2}(\sigma-1)\mathrm{J}_1(\lambda a)\right)\mathrm{I}_0(\lambda a) \\ +\frac{1}{2}\mathrm{I}_1(\lambda a)(\sigma-1)\mathrm{J}_0(\lambda a)\end{array}\right)}{\omega\left(\mathrm{I}_1(\lambda a)\mathrm{J}_0(\lambda a) + \mathrm{I}_0(\lambda a)\mathrm{J}_1(\lambda a)\right)} \tag{5.58}$$

$$Z_2 = -\frac{2j\pi\left(-\mathrm{I}_1(\lambda a)\mathrm{J}_0(\lambda a) + \mathrm{I}_0(\lambda a)\mathrm{J}_1(\lambda a)\right)\lambda^2 aD}{\omega\left(\mathrm{I}_1(\lambda a)\mathrm{J}_0(\lambda a) + \mathrm{I}_0(\lambda a)\mathrm{J}_1(\lambda a)\right)} \tag{5.59}$$

$$Z_3 = \frac{4\mathrm{j}\pi a\lambda^3 D\left(\mathrm{J}_1(\lambda a)\mathrm{I}_1(\lambda a)\right)}{\omega\left(\mathrm{I}_1(\lambda a)\mathrm{J}_0(\lambda a) + \mathrm{I}_0(\lambda a)\mathrm{J}_1(\lambda a)\right)} \tag{5.60}$$

Equations (5.56) and (5.57) could then be used to determine the forces acting on the PT and by applying correct boundary conditions, it would also allow the resonant frequencies to be solved for, as will be shown in section 5.3.5.a). Additionally, by treating force as an equivalent to voltage and vibration velocity as an equivalent to current, an equivalent circuit can be formulated based on these equations as is shown in the following section.

5.3.5 Equivalent circuit

Based on equations (5.48), (5.49), (5.56) and (5.57), and treating force in an analogous way to voltage and velocity in an analogous way to current, an equivalent circuit can be generated. Horsely *et al.* [5.8], showed that A_{in} and A_{out} can be modelled as ideal transformers. Fig. 5.3 shows the full equivalent circuit for the spurious flexural modes of the radial mode PT.

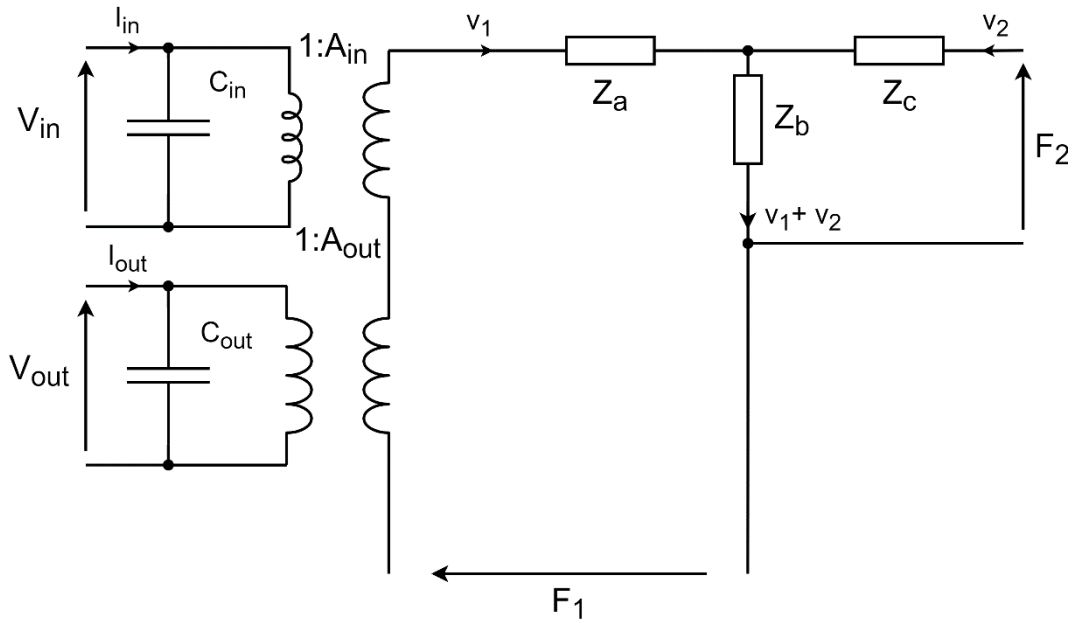

Fig. 5.3 – Equivalent circuit for the flexural spurious modes of a radial mode Transoner PT, under CPT assumptions

where impedances $Z_{a,b,c}$ are given by

$$Z_a = Z_1 - Z_2 \tag{5.61}$$

$$Z_b = Z_2 \tag{5.62}$$

$$Z_c = Z_3 - Z_2 \tag{5.63}$$

Then, after substituting in impedances $Z_{1,2,3}$ (5.58)-(5.60) into $Z_{a,b,c}$ (5.61)-(5.63), $Z_{a,b,c}$ are given by,

$$Z_a = \frac{2\mathrm{j}\pi a\lambda^2 D\left(2\mathrm{J}_1(\lambda a)\mathrm{I}_1(\lambda a)\lambda + \mathrm{I}_0(\lambda a)J_1(\lambda a) - \mathrm{I}_1(\lambda a)\mathrm{J}_0(\lambda a)\right)}{\omega\left(\mathrm{I}_1(\lambda a)\mathrm{J}_0(\lambda a) + \mathrm{I}_0(\lambda a)\mathrm{J}_1(\lambda a)\right)} \tag{5.64}$$

$$Z_b = -\frac{2\mathrm{j}\pi a\lambda^2 D\left(-\mathrm{I}_1(\lambda a)J_0(\lambda a) + \mathrm{I}_0(\lambda a)\mathrm{J}_1(\lambda a)\right)}{\omega\left(\mathrm{I}_1(\lambda a)\mathrm{J}_0(\lambda a) + \mathrm{I}_0(\lambda a)\mathrm{J}_1(\lambda a)\right)} \tag{5.65}$$

$$Z_c = \frac{2\mathrm{j}\pi D\begin{pmatrix}\left(-2\lambda a\mathrm{J}_0(\lambda a) + \mathrm{J}_1(\lambda a)(\lambda^2 a - \sigma + 1)\right)\mathrm{I}_0(\lambda a)\\ -\mathrm{J}_0(\lambda a)\mathrm{I}_1(\lambda a)(\lambda^2 a + \sigma - 1)\end{pmatrix}}{\omega\left(\mathrm{I}_1(\lambda a)\mathrm{J}_0(\lambda a) + \mathrm{I}_0(\lambda a)\mathrm{J}_1(\lambda a)\right)} \tag{5.66}$$

The circuit in Fig. 5.3 can then be simplified by the application of boundary conditions. As the outer radius of the PT is free to vibrate, forces, F_1 and F_2 as a result are equal to 0. Therefore, the circuit in Fig. 5.3 can be rearranged to that shown in Fig. 5.4.

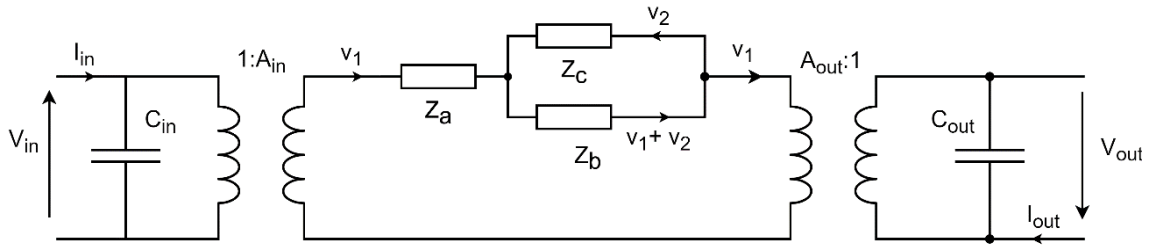

Fig. 5.4 – Equivalent circuit for the spurious flexural modes of a radial mode Transoner PT with forces $F_1 = 0$ and $F_2 = 0$

Then, the circuit in Fig. 5.4 can be simplified by combining impedances Z_a, Z_b and Z_c into a single impedance. The resulting circuit is shown in Fig. 5.5,

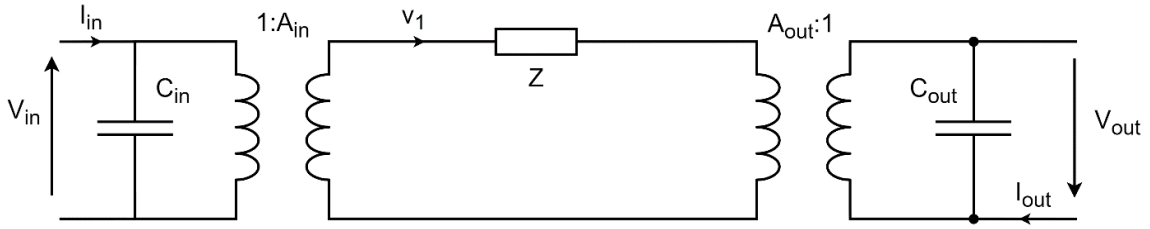

Fig. 5.5 – Simplified equivalent circuit for the spurious flexural modes of a radial mode Transoner PT

where the mechanical impedance Z is given by

$$Z = Z_a + \frac{Z_b Z_c}{Z_b + Z_c} \tag{5.67}$$

Finally, substituting $Z_{a,b,c}$ (5.64)-(5.66) into Z (5.67) gives

$$Z = \frac{-\mathrm{j}\pi\left(\left((2\sigma - 2)\mathrm{J}_1(\lambda a) + \lambda a \mathrm{J}_0(\lambda a)\right)\mathrm{I}_1(\lambda a) + \mathrm{I}_0(\lambda a)\mathrm{J}_1(\lambda a)\lambda a\right) D}{\mathrm{I}_1(\lambda a)\mathrm{J}_1(\lambda a)\omega} \tag{5.68}$$

5.3.5.a) Resonant frequencies

As described in Chapter 4, controlling the frequency separation between optimum and spurious mode is critical for ensuring minimal efficiency loss. Therefore, this requires close control of spurious mode resonant frequencies. At resonance, the impedance Z will be 0 (initially assuming PT is lossless). Therefore, firstly, solving (5.68) with $Z = 0$ gives,

$$\sigma + \frac{\left(\mathrm{I}_0(\lambda a)\mathrm{J}_1(\lambda a)\lambda a + \mathrm{J}_0(\lambda a)\mathrm{I}_1(\lambda a)\lambda a - 2\mathrm{J}_1(\lambda a)\mathrm{I}_1(\lambda a)\right)}{2\mathrm{J}_1(\lambda a)\mathrm{I}_1(\lambda a)} \tag{5.69}$$

Then, solving (5.69) for λa, defining positive solutions (roots) as R_{s_n}, n is the root index with $n = 2$ referring to the first solution (as $n = 1$ is for the radial mode occurring in this PT). Solutions for (5.69) must be found using numerical methods, as it is transcendental. Finally, substituting R_{s_n} into (5.70) allows resonant frequencies for the spurious modes to be calculated,

$$\omega_n = \frac{R_{s_n}^2 \sqrt{\rho(T^{\mathrm{tot}})D}}{a^2 \rho(T^{\mathrm{tot}})} \tag{5.70}$$

where T^{tot} is the total thickness of the PT ($T^{\mathrm{tot}} = T_{\mathrm{in}}^{\mathrm{tot}} + T_{\mathrm{out}}^{\mathrm{tot}}$) and ω_n denotes the n$^{\mathrm{th}}$ spurious resonant mode (with the first spurious mode $n = 2$, as the radial mode $n = 1$). Therefore, based on equations (5.69) and (5.70), the spurious resonant frequencies can be easily calculated for any Transoner PT.

5.4 Derivation of lumped equivalent circuit

Whilst the circuit in Fig. 5.5 can be mathematically analysed, owing to the form of the mechanical impedance Z, circuit analysis software such as SPICE is unable to simulate such a circuit. To rectify this, the mechanical impedance, Z, is modelled as a lumped equivalent

circuit around a single resonant frequency. First, a Taylor series expansion of the mechanical impedance (Z) will be taken about each flexural (spurious) resonant frequency. The first two elements in the Taylor series are,

$$Z_T = 0 + \frac{\mathrm{j}T^{\mathrm{tot}}\rho\pi a^4 \begin{pmatrix} (2\sigma^2 - 2\sigma)\mathrm{I}_1(R_{s_n})^2 \\ +2R\mathrm{I}_0(R_{s_n})(\sigma - 1)\mathrm{I}_1(R_{s_n}) \\ +{R_{s_n}}^2\mathrm{I}_0(R_{s_n})^2 \end{pmatrix}}{{R_{s_n}}^4\mathrm{I}_1(R_{s_n})^2}(\omega - \omega_n) \tag{5.71}$$

where subscript T means the Taylor series. A series LC circuit (Z_{LC_n}) is then introduced to model this impedance. The combined impedance of the LC circuit is given by,

$$Z_{LC_{\mathrm{n}}} = \mathrm{j}\left(\omega L_{m_n} - \frac{1}{\omega C_{m_n}}\right) \tag{5.72}$$

A Taylor series expansion of the impedance of the LC series circuit is then taken around its resonant frequency giving,

$$Z_{LC_{\mathrm{n_T}}} = 0 + 2\mathrm{j}L_{m_n}(\omega - \omega_{LC_{\mathrm{n}}}) \tag{5.73}$$

where the resonant frequency $\omega_{LC_{\mathrm{n}}}$ of the LC circuit is given by,

$$\omega_{LC_{\mathrm{n}}} = \frac{1}{\sqrt{L_{m_n}C_{m_n}}} \tag{5.74}$$

In this case subscript m denotes that the parameters are related to a mechanical quantity. Then, equating Z_T (5.71) and $Z_{LC_{\mathrm{n_T}}}$ (5.73) and solving for L_{m_n}gives

$$L_{m_n} = \frac{T^{\mathrm{tot}}\rho\pi a^4 \begin{pmatrix} (2\sigma^2 - 2\sigma)\mathrm{I}_1(R_{s_n})^2 \\ +2R_{s_n}\mathrm{I}_0(R_{s_n})(\sigma - 1)\mathrm{I}_1(R_{s_n}) + {R_{s_n}}^2\mathrm{I}_0(R_{s_n})^2 \end{pmatrix}}{2{R_{s_n}}^4\mathrm{I}_1(R_{s_n})^2} \tag{5.75}$$

We can then find C_{m_n} using the resonant frequency of the LC equivalent circuit (5.74). Substituting L_{m_n} (5.75) into $\omega_{LC_{\mathrm{n}}}$(5.74) and solving for C_{m_n} gives,

$$C_{m_n} = \frac{2{R_{s_n}}^4 \mathrm{I}_1\left(R_{s_n}\right)^2}{\omega_n^2 T^{\mathrm{tot}} \rho \pi a^4 \begin{pmatrix} (2\sigma^2 - 2\sigma)\mathrm{I}_1\left(R_{s_n}\right)^2 + 2R_{s_n}\mathrm{I}_0\left(R_{s_n}\right)(\sigma - 1)\mathrm{I}_1\left(R_{s_n}\right) \\ +{R_s}^2 \mathrm{I}_0\left(R_{s_n}\right)^2 \end{pmatrix}} \tag{5.76}$$

Then, finally substituting the equation for the resonant frequencies of the spurious modes (5.70) into (5.76) gives,

$$C_{m_n} = \frac{2\mathrm{I}_1\left(R_{s_n}\right)^2}{D\pi \begin{pmatrix} (2\sigma^2 - 2\sigma)\mathrm{I}_1\left(R_{s_n}\right)^2 \\ +2R_{s_n}\mathrm{I}_0\left(R_{s_n}\right)(\sigma - 1)\mathrm{I}_1\left(R_{s_n}\right) + {R_{s_n}}^2 \mathrm{I}_0\left(R_{s_n}\right)^2 \end{pmatrix}} \tag{5.77}$$

5.4.1.a) Mechanical Loss

As Chapter 4 describes, spurious mode damping (loss) is an important factor in determining the efficiency loss from spurious modes in a PT. Whilst efforts have been made to analyse this quantity, estimating this parameter is difficult as it depends on a wide variety of factors, including material choice, bonding material, use of additional layers, quality of construction and temperature. Therefore, the best estimate of this quantity is typically made by estimating its value based on knowledge of previous PT designs of similar devices. This loss will be included as a resistance in series with the LC circuit, as is typical in the Mason equivalent circuit (see Fig. 2.13). It is common to introduce this loss in terms of Q factor. The Q factor the spurious resonant branch is given by,

$$Q_s = \frac{1}{R_{m_n}} \sqrt{\frac{L_{m_n}}{C_{m_n}}} \tag{5.78}$$

where R_{m_n} is the equivalent damping resistance for the n$^{\mathrm{th}}$ mode. It is worth noting that Q_s is the Q factor of the spurious modes in a PT, this Q factor is typically much lower than the radial mode Q factor. Substituting, L_{m_n} (5.75) and C_{m_n} (5.77) into Q_s (5.78) and solving for R_{m_n} gives,

$$R_{m_n} = \frac{\sqrt{\rho}a^2\sqrt{D}\sqrt{T_{\text{tot}}}\pi\begin{pmatrix}(2\sigma^2 - 2\sigma)\mathrm{I}_1\left(R_{s_n}\right)^2 + 2R_{s_n}\mathrm{I}_0\left(R_{s_n}\right)(\sigma - 1)\mathrm{I}_1\left(R_{s_n}\right) \\ +{R_{s_n}}^2\mathrm{I}_0\left(R_{s_n}\right)^2\end{pmatrix}}{Q_s 2{R_{s_n}}^2\mathrm{I}_1\left(R_{s_n}\right)^2} \quad (5.79)$$

5.4.1.b) Formulation as Mason equivalent circuit

The final simplified lumped equivalent circuit model of a single spurious mode is shown in Fig. 5.6.

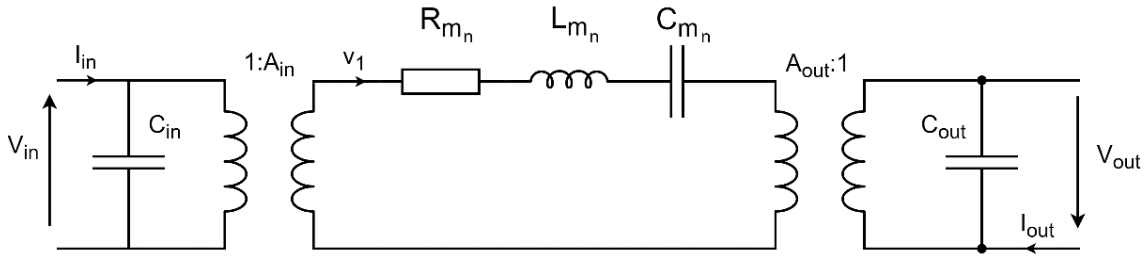

Fig. 5.6 – Final simplified equivalent circuit model of the spurious modes of a radial mode Transoner PT,

The circuit in Fig. 5.6 allows a single spurious mode of the Transoner PT to be modelled around its resonance. As there are infinite solutions to (5.69), then in theory, there will be infinite spurious modes and as a result, this will require an infinite number of RLC branches and ideal transformers [5.9] in parallel to model these modes. However, as discussed in Chapter 4 many of these modes have negligible influence on optimum mode performance and so can be ignored. If multiple modes are required, these can be added as additional RLC circuits with the values calculated using equations (5.75), (5.77) and (5.79), and the relevant solution to (5.69).

In this model the current through the RLC branch is equal to the vibration velocity, v_1 of the PT when operated around the relevant resonance. However, in many cases, it is beneficial to combine A_{in} and A_{out} transformers into a single transformer, making analysis and simulation easier. To achieve this, we refer the RLC circuit across the A_{in} transformer and combine A_{in} and A_{out} into a single transformer N_n. Therefore, producing the equivalent circuit model shown in Fig. 5.7.

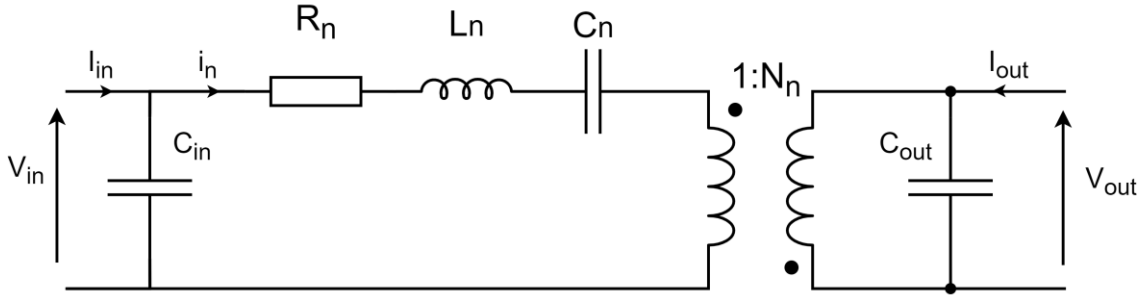

Fig. 5.7 – Single transformer equivalent circuit model of the spurious modes of a radial mode Transoner PT

The equivalent parameters R_n, L_n, C_n and N_n are defined as,

$$R_n = \frac{R_{m_n}}{A_{\text{in}}^2} \tag{5.80}$$

$$L_n = \frac{L_{m_n}}{A_{\text{in}}^2} \tag{5.81}$$

$$C_n = C_{m_n} A_{\text{in}}^2 \tag{5.82}$$

$$N_n = -\frac{A_{\text{in}}}{A_{\text{out}}} = -\frac{\left(-\frac{\pi d_{31} T_{\text{out}}^{\text{tot}} N_{\text{in}} a}{s_{11}^{\text{E}}(\sigma-1)}\right)}{\left(\frac{\pi d_{31} T_{\text{in}}^{\text{tot}} N_{\text{out}} a}{s_{11}^{\text{E}}(\sigma-1)}\right)} = \frac{T_{\text{out}}^{\text{tot}} N_{\text{in}}}{T_{\text{in}}^{\text{tot}} N_{\text{out}}} \tag{5.83}$$

It should be noted that the phase of the N_n transformers was changed to correctly orient the output voltage. In this form of the equivalent circuit, the vibration velocity, v_n, of the PT is no longer equal to the current through the RLC branch, however they are still proportional to each other,

$$v_{\text{n}} \propto i_n \;\; v_n = \frac{i_n}{A_{\text{in}}} \tag{5.84}$$

Therefore, if direct consideration of the vibration velocity is required, then the form in Fig. 5.6 is required. However, the model presented in Fig. 5.7 has a reduced component count and therefore, is often more suitable for simulation and emulation.

5.5 Summary

In this chapter an equivalent circuit model has been presented for the spurious modes occurring in the Transoner PT using the Kirchhoff plate theory. Chapter 7 will validate this model and the Mindlin plate theory-based model derived in the following chapter, against both COMSOL simulations and experimental data.

5.6 References

[5.1] J. N. Reddy, *Theory and analysis of elastic plates*. Philadelphia, PA: Taylor & Francis, 1999.

[5.2] T. Ikeda, *Fundamentals of piezoelectricity*. Oxford ; New York: Oxford University Press, 1990.

[5.3] Q. Wang, S. T. Quek, C. T. Sun, and X. Liu, 'Analysis of piezoelectric coupled circular plate', *Smart Mater. Struct.*, vol. 10, no. 2, p. 229, 2001, doi: 10.1088/0964-1726/10/2/308.

[5.4] F. Sammoura, K. Smyth, and S. Kim, 'An equivalent network representation of a clamped bimorph piezoelectric micromachined ultrasonic transducer with circular and annular electrodes using matrix manipulation techniques', *IEEE Transactions on Ultrasonics, Ferroelectrics, and Frequency Control*, vol. 60, no. 9, pp. 1989–2003, Sep. 2013, doi: 10.1109/TUFFC.2013.2784.

[5.5] A. W. Leissa, 'Vibration of Plates', OHIO STATE UNIV COLUMBUS, 1969. Accessed: Jan. 08, 2018. [Online]. Available: http://www.dtic.mil/docs/citations/ADA307623

[5.6] S. K. Ha and Y. H. Kim, 'Impedance and admittance matrices of symmetric piezoelectric annular bimorphs and their applications', *The Journal of the Acoustical Society of America*, vol. 108, no. 5, pp. 2125–2133, Nov. 2000, doi: 10.1121/1.1312365.

[5.7] E. Horsley, 'Modelling and Analysis of Radial Mode Piezoelectric Transformers and Inductor-less Resonant Power Converters', University of Sheffield, 2011.

[5.8] E. L. Horsley, A. V. Carazo, M. P. Foster, and D. A. Stone, 'A Lumped Equivalent Circuit Model for the Radial Mode Piezoelectric Transformer', in *2009 Twenty-Fourth Annual IEEE Applied Power Electronics Conference and Exposition*, Feb. 2009, pp. 1747–1753. doi: 10.1109/APEC.2009.4802906.

[5.9] R.-L. Lin, 'Piezoelectric Transformer Characterization and Application of Electronic Ballast', *Ph.D. Dissertation*, Nov. 2001, Accessed: Feb. 15, 2018. [Online]. Available: https://vtechworks.lib.vt.edu/handle/10919/29948

Chapter 6 - Derivation of a lumped equivalent circuit model of the spurious modes of the radial mode Transoner PTs using Mindlin plate theory (MPT)

6.1 Introduction

This chapter follows on from the previous chapter and presents a second lumped equivalent circuit model for the spurious flexural modes occurring in the Transoner PT based on the Mindlin plate theory (MPT).

6.2 Mindlin plate theory assumptions

Mindlin plate theory (MPT) extends the CPT by accounting for shear deformation (see Fig. 2.17) and rotary inertia. For the MPT a reduced set of assumptions are made [6.1], [6.2]:

- T_z is negligible ($T_z = 0$)
- Vibration is axisymmetric, $u_\theta = 0$ (displacement in θ direction)
- Transverse displacement (w) is independent of z coordinate, $S_{zz} = 0$
- Radial displacement (u_r) is proportional to z coordinate

6.3 Derivation

It is widely acknowledged that the CPT is inaccurate for 'thick' devices and/or for higher order modes, as it ignores shear deformation and rotary inertia, leading to overestimated resonant frequencies [6.3]. The MPT improves upon the CPT by including the effects of shear deformation and rotary inertia, using a first order shear deformation model [6.3]. Therefore, assuming perfect axisymmetric motion and based on the assumptions described previously (section 6.2), the strain on the device in each direction, in terms of displacements are given by [6.2],

$$S_r = z\frac{\partial \psi_r(r,z)}{\partial r} \tag{6.1}$$

$$S_\theta = z\frac{\psi_r(r,z)}{r} \tag{6.2}$$

$$S_{rz} = z\frac{\partial \psi_r(r,z)}{\partial z} + \frac{\partial w(r,z)}{\partial r} \tag{6.3}$$

$$S_{rz}, S_{\theta z}, S_z = 0 \tag{6.4}$$

where $w(r,z)$ is the displacement function in the transverse direction and $\psi_r(r,z)$ is the displacement function in the radial direction. As discussed previously for the CPT model, equations of motions are generated by summing the forces and moment in each direction of the device. The radial and transverse equations of motion of the flexural mode of the Transoner PT under MPT assumptions are given by [6.1],

$$\frac{\partial M_r}{\partial r} + \frac{(M_r - M_\theta)}{r} - Q_r = -\frac{\left(\left(T_{\text{in}}^{\text{tot}^3} + T_{\text{out}}^{\text{tot}^3}\right)\rho\psi_r\omega^2\right)}{3} \tag{6.5}$$

$$\frac{\partial Q_r}{\partial r} + \frac{Q_r}{r} = -(T_{\text{in}}^{\text{tot}} + T_{\text{out}}^{\text{tot}})w\rho\omega^2 \tag{6.6}$$

where M_r, M_θ and Q_r are the flexural moments and shear stresses of the PT given by,

$$M_r = \int_{H_1}^{H_2} T_{r_{\text{in}}} z\, dz + \int_{H_3}^{H_4} T_{r_{\text{out}}} z\, dz \tag{6.7}$$

$$M_\theta = \int_{H_1}^{H_2} T_{\theta_{\text{in}}} z\, dz + \int_{H_3}^{H_4} T_{\theta_{\text{out}}} z\, dz \tag{6.8}$$

$$Q_r = k^2\left(\int_{H_1}^{H_2} T_{rz_{\text{in}}} z\, dz + \int_{H_3}^{H_4} T_{rz_{\text{out}}} z\, dz\right) \tag{6.9}$$

where $H_{1,2,3,4}$ are given in (5.13) - (5.16) and k^2 is the shear correction factor. In this analysis, the shear correction factor $k^2 = \pi^2/12$ is used, as presented by Deresiewicz and Mindlin [6.1].

6.3.1 Displacement

In the thin plate model (CPT), the radial displacement can be directly found from the transverse displacement and so upon solving for the transverse displacement, radial displacement can be calculated. However, in the thick plate model, the radial displacement is not simply a function of transverse displacement. Therefore, equations for both w and ψ_r need to be found.

This will be achieved by solving (6.5) and (6.6) as simultaneous equations. Firstly, substituting $H_{1,2,34}$ (5.13) - (5.16) into M_r, M_θ, Q_r (6.7)-(6.9) and then the resulting equations into (6.5) and (6.6) gives,

$$\frac{\partial^2 \psi_r}{\partial r^2} r^2 + \frac{\frac{\partial \psi_r}{\partial r}}{r} - \frac{\partial w}{\partial r} - \psi_r \left(\frac{1}{S} + \frac{1}{r}\right) + \delta^4 \psi_r R = 0 \tag{6.10}$$

$$\frac{\partial \psi_r}{\partial r} + \frac{\partial^2 w}{\partial r^2} + \frac{\psi_r}{r} + \frac{\frac{\partial w}{\partial r}}{r} + Sw\delta^4 = 0 \tag{6.11}$$

where S is the shear deformation coefficient, R is the rotary inertia coefficient and δ is the non-dimensional frequency given by [6.1],

$$S = \frac{s_{55}^E D}{(T_{\text{in}}^{\text{tot}} + T_{\text{out}}^{\text{tot}})k^2} \tag{6.12}$$

$$R = \frac{T_{\text{in}}^{\text{tot}^2} - h_1 T_{\text{out}}^{\text{tot}} + T_{\text{out}}^{tot^2}}{3} \tag{6.13}$$

$$\delta^4 = \frac{(T_{\text{in}}^{\text{tot}} + T_{\text{out}}^{\text{tot}})\rho\omega^2}{D} \tag{6.14}$$

where

$$D = \frac{(T_{\text{in}}^{\text{tot}} + T_{\text{out}}^{\text{tot}})^3}{12(1-\sigma^2)s_{11}^E} \tag{6.15}$$

Then, as discussed in [6.1], (6.11) is differentiated with respect to r, giving

$$\frac{\partial^3 w}{\partial r^3}+\frac{\partial^2 \psi_r}{\partial r^2}+\frac{\frac{\partial \psi_r}{\partial r}}{r}+\frac{\frac{\partial^2 w}{\partial r^2}}{r}-\frac{\psi_r}{r^2}-\frac{\frac{\partial w}{\partial r}}{r^2}+S\frac{\partial w}{\partial r}\delta^4 = 0 \tag{6.16}$$

Subtracting (6.10) from (6.16) gives,

$$\frac{\partial^3 w}{\partial r^3}+\frac{\partial^2 w}{\partial r^2}\frac{1}{r}-\frac{\partial w}{\partial r}\frac{1}{r^2}+\frac{\partial w}{\partial r}S\delta^4+\frac{\psi_r}{S}+\frac{\partial w}{\partial r}\frac{1}{S}-\delta^4\,\psi_r R=0 \tag{6.17}$$

Then, equation (6.17) can be solved for ψ_r, giving

$$\psi_r = \frac{\frac{\partial^3 w}{\partial r^3}+\frac{\partial^2 w}{\partial r^2}\frac{1}{r}+\frac{\partial w}{\partial r}\left(S\delta^4+\frac{1}{S}-\frac{1}{r^2}\right)}{R\delta^4-\frac{1}{S}} \tag{6.18}$$

Next an equation for w can then be found by first substituting (6.18) into (6.11) and simplifying, thus resulting in an equation in terms of only w,

$$\frac{\begin{pmatrix}\frac{\partial^4 w}{\partial r^4}r^3+2\frac{\partial^3 w}{\partial r^3}r^2+\left((\delta_1^2+\delta_2^2)r^3-r\right)\frac{\partial^2 w}{\partial r^2}\\ +(1+(\delta_1^2+\delta_2^2)r^2)\frac{\partial w}{\partial r}+w\delta_1^2\delta_2^2 r^3\end{pmatrix}}{r^3} = 0 \tag{6.19}$$

where δ_1^2 and δ_2^2 are given by

$$\delta_1^2,\delta_2^2 = \left(\frac{1}{2}\right)\delta^4\left(R+S\pm\sqrt{(R-S)^2+\frac{4}{\delta^4}}\right) \tag{6.20}$$

Finally, equation (6.19) is solved for w giving,

$$w(r) = A_1\mathrm{J}_0(\delta_1 r)+A_2\mathrm{J}_0(\delta_2 r)+A_3\mathrm{Y}_0(\delta_1 r)+A_4\mathrm{Y}_0(\delta_2 r) \tag{6.21}$$

At this point, similar to the CPT model, (6.21) can be simplified by again noting that at the centre of the disk the transverse displacement must be finite, and $Y_0(0)=\infty$ and therefore, $A_3=A_4=0$. Therefore, equation (6.21) becomes,

$$w(r) = A_1\mathrm{J}_0(\delta_1 r)+A_2\mathrm{J}_0(\delta_2 r) \tag{6.22}$$

Then, as with the CPT model, we assume all mechanical and electrical responses are harmonically excited. Therefore, using (5.22), (6.22) can be written as

$$W(r,t) = A_1 \mathrm{J}_0(\delta_1 r) + A_2 \mathrm{J}_0(\delta_2 r) e^{\mathrm{j}\omega t} \tag{6.23}$$

where the capitalised W indicates the transverse displacement is a function of time due to harmonic excitation. Then, substituting (6.22) into (6.18) gives an equation for ψ_r

$$\Psi_r(r,t) = -A_1(B-\sigma_1)\delta_1 \mathrm{J}_1(\delta_1 r) - A_2(B-\sigma_2)\delta_2 \mathrm{J}_1(\delta_2 r) e^{\mathrm{j}\omega t} \tag{6.24}$$

where [6.1],

$$\Psi_r(r,t) = \psi_r e^{j\omega t} \tag{6.25}$$

$$\sigma_1 = \frac{S\delta_1^2}{\delta^4 RS - 1} \tag{6.26}$$

$$\sigma_2 = \frac{S\delta_2^2}{\delta^4 RS - 1} \tag{6.27}$$

$$B = \frac{S^2\delta^4 + 1}{\delta^4 RS - 1} \tag{6.28}$$

Therefore, giving equations for the transverse and radial displacement of the PT during flexural vibration. However, to be able to solve for the resonant frequencies, mode shapes or in the case of this analysis use these equations to generate equivalent circuits, the constants A_1 and A_2 must first be found.

6.3.1.a) Application of boundary conditions

Similar to the CPT model, the remaining constants $A_1$and A_2 can be found using the vibration velocities v_1 and v_2 as described by Fig. 5.2. Velocities v_1 and v_2 can be found by differentiating the transverse displacement W and radial displacement Ψ_r at the outer edge of the PT ($r = a$) with respect to time,

$$v_1(t) = \frac{\partial \Psi_r(a,t)}{\partial t} = \mathrm{j}\omega\big(-A_1(B-\sigma_1)\delta_1 \mathrm{J}_1(\delta_1 a) - A_2(B-\sigma_2)\delta_2 \mathrm{J}_1(\delta_2 a)\big) e^{\mathrm{j}\omega t} \tag{6.29}$$

$$v_2(t) = \frac{\partial W(a,t)}{\partial t} = \mathrm{j}\omega\big(A_1\mathrm{J}_0(\delta_1 a) + A_2\mathrm{J}_0(\delta_2 a)\big)e^{\mathrm{j}\omega t} \tag{6.30}$$

Then, solving both (6.29) and (6.30) for A_1 gives,

$$A_1 = \frac{\mathrm{j}v_1 e^{-\mathrm{j}\omega t} - (B-\sigma_2)A_2\omega\delta_2\mathrm{J}_1(\delta_2 a)}{(B-\sigma_1)\delta_1\mathrm{J}_1(\delta_1 a)\omega} \tag{6.31}$$

$$A_1 = \frac{-\mathrm{j}v_2 e^{-\mathrm{j}\omega t} - A_2\mathrm{J}_0(\delta_2 a)\omega}{\omega\mathrm{J}_0(\delta_1 a)} \tag{6.32}$$

Substituting (6.31) into (6.32) and solving for A_2 gives

$$A_2 = \frac{(\mathrm{j}v_2(B-\sigma_1)\delta_1\mathrm{J}_1(\delta_1 a) + \mathrm{j}\mathrm{J}_0(\delta_1 a)v_1)e^{-\mathrm{j}\omega t}}{\big(-\mathrm{J}_0(\delta_2 a)\delta_1(B-\sigma_1)\mathrm{J}_1(\delta_1 a) + \mathrm{J}_0(\delta_1 a)\mathrm{J}_1(\delta_2 a)\delta_2(B-\sigma_2)\big)\omega} \tag{6.33}$$

A_1 is then found by substituting (6.33) into either (6.31) or (6.32) and simplifying, giving

$$A_1 = \frac{(-\mathrm{j}v_2(B-\sigma_2)\delta_2\mathrm{J}_1(\delta_2 a) - \mathrm{j}\mathrm{J}_0(\delta_2 a)v_1)e^{-\mathrm{j}\omega t}}{\big(-\mathrm{J}_0(\delta_2 a)\delta_1(B-\sigma_1)\mathrm{J}_1(\delta_1 a) + \mathrm{J}_0(\delta_1 a)\mathrm{J}_1(\delta_2 a)\delta_2(B-\sigma_2)\big)\omega} \tag{6.34}$$

Finally, substituting A_2 (6.33) and A_1 (6.34) into equations for transverse and radial displacement, W (6.21) and Ψ_r (6.24) gives,

$$W(r,t) = \frac{\begin{pmatrix}\mathrm{j}(B-\sigma_1)v_2\delta_1\mathrm{J}_0(\delta_2 r)\mathrm{J}_1(\delta_1 a) - \mathrm{j}(B-\sigma_2)\delta_2 v_2\mathrm{J}_0(\delta_1 r)\mathrm{J}_1(\delta_2 a)\\ +\mathrm{j}v_1\big(\mathrm{J}_0(\delta_1 a)\mathrm{J}_0(\delta_2 r) - \mathrm{J}_0(\delta_1 r)\mathrm{J}_0(\delta_2 a)\big)\end{pmatrix}}{\big(-\mathrm{J}_0(\delta_2 a)\delta_1(B-\sigma_1)\mathrm{J}_1(\delta_1 a) + \mathrm{J}_0(\delta_1 a)\mathrm{J}_1(\delta_2 a)\delta_2(B-\sigma_2)\big)\omega} \tag{6.35}$$

$$\Psi_r(r,t) = -\frac{\begin{pmatrix}\mathrm{j}\mathrm{J}_1(\delta_2 r)(B-\sigma_2)(B-\sigma_1)\delta_2 v_2\delta_1\mathrm{J}_1(\delta_1 a)\\ +\mathrm{j}(B-\sigma_1)(v_2(B-\sigma_2)\delta_2\mathrm{J}_1(\delta_2 a) + \mathrm{J}_0(\delta_2 a)v_1)\delta_1\mathrm{J}_1(\delta_1 r)\\ -\mathrm{j}\mathrm{J}_1(\delta_2 r)v_1(B-\sigma_2)\delta_2\mathrm{J}_0(\delta_1 a)\end{pmatrix}}{\big(-\mathrm{J}_0(\delta_2 a)\delta_1(B-\sigma_1)\mathrm{J}_1(\delta_1 a) + \mathrm{J}_0(\delta_1 a)\mathrm{J}_1(\delta_2 a)\delta_2(B-\sigma_2)\big)\omega} \tag{6.36}$$

Equations (6.35) and (6.36) will now be used in the following sections to generate equations for the current and forces acting on the PT. Then, similar to the CPT model derived in the previous chapter, an equivalent circuit will be generated by treating vibration velocity analogously to current and force analogously to voltage.

6.3.2 Electrical equations

Similar to the CPT model, equations for the current into the input and output electrodes will now be derived in terms of vibration velocities, and input and output voltages. Substituting T_r(5.1) and T_θ (5.2) into S_r, $S_\theta$and $S_{r\theta}$ (6.1)-(6.4) and then the result into Q_{in} (5.34) and Q_{out} (5.35) gives,

$$Q_{\text{in}} = \frac{2\pi}{s_{11}^{\text{E}}(\sigma-1)T_{\text{in}}^{\text{tot}}} \int_{H_1}^{H_2}\int_0^a \left[\left(-\left(\frac{\partial \psi_r}{\partial r}r + \psi_r\right)d_{31}z + \left(2d_{31}^2 + \varepsilon_{33}^{\text{T}} s_{11}^{\text{E}}(\sigma-1)\right)E_{z_{\text{in}}} r\right)\right] dr\, dz \tag{6.37}$$

$$Q_{\text{out}} = \frac{2\pi}{s_{11}^{\text{E}}(\sigma-1)T_{\text{out}}^{\text{tot}}} \int_{H_3}^{H_4}\int_0^a \left[\left(-\left(\frac{\partial \psi_r}{\partial r}r + \psi_r\right)d_{31}z + \left(2d_{31}^2 + \varepsilon_{33}^{\text{T}} s_{11}^{\text{E}}(\sigma-1)\right)E_{z_{\text{out}}} r\right)\right] dr\, dz \tag{6.38}$$

The total input current into the input and output sections is given by equations (5.42) and (5.43). Substituting ψ_r (6.36), electric fields $E_{z_{\text{in}}}$ (5.6) and $E_{z_{\text{out}}}$ (5.7) into Q_{in} (6.37) and Q_{out} (6.38), and then into I_{in_L} (5.40) and I_{out_L} (5.41), then finally into I_{in_T} (5.42) and I_{out_T} (5.43) gives equations for the magnitudes of these currents,

$$I_{\text{in}_T} = \frac{\text{j}N_{\text{in}}^2 a^2 \omega\left(2d_{31}^2 + \varepsilon_{33}^{\text{T}} s_{11}^{\text{E}}(\sigma-1)\right)\pi}{T_{\text{in}}^{\text{tot}} s_{11}^{\text{E}}(\sigma-1)} V_{\text{in}} - \frac{(N_{\text{in}} a d_{31} T_{\text{out}}^{\text{tot}}\pi)}{s_{11}^{E}(\sigma-1)} v_1 \tag{6.39}$$

$$I_{\text{out}_T} = \frac{\text{j}N_{\text{out}}^2 a^2 \omega\left(2d_{31}^2 + \varepsilon_{33}^{\text{T}} s_{11}^{E}(\sigma-1)\right)\pi}{T_{\text{out}}^{\text{tot}} s_{11}^{\text{E}}(\sigma-1)} V_{\text{out}} + \frac{(N_{\text{out}} a d_{31} T_{\text{in}}^{\text{tot}}\pi)}{s_{11}^{\text{E}}(\sigma-1)} v_1 \tag{6.40}$$

Again if $A_{\text{in}}$and A_{out} force factors are used. Equations (6.39) and (6.40) can be written as

$$I_{\text{in}_T} = \text{j}\omega C_{\text{in}} V_{\text{in}} + A_{\text{in}} v_1 \tag{6.41}$$

$$I_{\text{out}_T} = \text{j}\omega C_{\text{out}} V_{\text{out}} + A_{\text{out}} v_1 \tag{6.42}$$

where input C_{in} and output C_{out} capacitances are given by

$$C_{\text{in}} = \frac{\pi a^2 \varepsilon_{33}^{\text{T}} N_{\text{in}}^2}{T_{\text{in}}^{\text{tot}}} + \frac{\pi a^2 2 d_{31}^2 N_{\text{in}}^2}{T_{\text{in}}^{\text{tot}} s_{11}^{\text{E}} (\sigma - 1)} \tag{6.43}$$

$$C_{\text{out}} = \frac{\pi a^2 \varepsilon_{33}^{\text{T}} N_{\text{out}}^2}{T_{\text{out}}^{\text{tot}}} + \frac{\pi a^2 2 d_{31}^2 N_{\text{out}}^2}{T_{\text{out}}^{\text{tot}} s_{11}^{\text{E}} (\sigma - 1)} \tag{6.44}$$

It is worth noting that the electrical equations generated using the MPT are identical to the CPT model, thus both models exhibit the same input and output capacitances and force factors.

6.3.3 Mechanical equations

The two forces, F_1 and F_2 in Fig. 5.2, are given by [6.4],

$$F_1 = 2\pi a M_r(a) \tag{6.45}$$

$$F_2 = 2\pi a Q_r(a) \tag{6.46}$$

Substituting M_r (6.7) and Q_r (6.9) into F_1 (6.45) and F_2 (6.46), with T_r (5.1) and T_θ (5.2), $E_{z_{\text{in}}}$ (5.6) and $E_{z_{\text{out}}}$ (5.7) gives,

$$F_1 = -\frac{\pi (T_{\text{in}}^{\text{tot}} + T_{\text{out}}^{\text{tot}})^3 \left(a \left[\frac{\partial \psi_r(a)}{\partial a} \right] + \sigma \psi_r(a) \right)}{6 s_{11}^{\text{E}} \sigma^2 - 6 s_{11}^{\text{E}}} + \frac{a\pi d_{31}(1+\sigma) T_{\text{out}}^{\text{tot}} N_{\text{in}}}{s_{11}^{\text{E}}(\sigma^2 - 1)} V_{\text{in}} - \frac{a\pi d_{31}(1+\sigma) T_{\text{in}}^{\text{tot}} N_{\text{out}}}{s_{11}^{\text{E}}(\sigma^2 - 1)} V_{\text{out}} \tag{6.47}$$

$$F_2 = \frac{2\pi a k^2 \left(\psi_r(a) + \frac{\partial w(a)}{\partial a} \right) (T_{\text{in}}^{\text{tot}} + T_{\text{out}}^{\text{tot}})}{s_{55}^{\text{E}}} \tag{6.48}$$

Then, substituting in W (6.35)(5.22) and Ψ_r (6.36)(6.25) into F_1 (6.47) and F_2 (6.48), and again using A_{in} (5.46) and A_{out} (5.47) force factors gives,

$$F_1 = Z_1 v_1 + Z_2 v_2 - A_{\text{in}} V_{\text{in}} - A_{\text{out}} V_{\text{out}} \tag{6.49}$$

$$F_2 = Z_3 v_1 + Z_4 v_2 \tag{6.50}$$

where mechanical impedances $Z_{1,2,3,4}$ are given by

$$Z_1 = \frac{\mathrm{j}2\pi D\begin{pmatrix}\left\{\begin{matrix}[(B-\sigma_1)\delta_1^2-\delta_2^2(B-\sigma_2)]a\mathrm{J}_0(\delta_2 a)\\ -\mathrm{J}_1(\delta_2 a)\delta_2(\sigma-1)(B-\sigma_2)\end{matrix}\right\}\mathrm{J}_0(\delta_1 a)\\ +\delta_1\mathrm{J}_0(\delta_2 a)(\sigma-1)(B-\sigma_1)\mathrm{J}_1(\delta_1 a)\end{pmatrix}}{\omega\left(-\mathrm{J}_0(\delta_2 a)\delta_1(B-\sigma_1)\mathrm{J}_1(\delta_1 a)+\mathrm{J}_0(\delta_1 a)\mathrm{J}_1(\delta_2 a)\delta_2(B-\sigma_2)\right)} \tag{6.51}$$

$$Z_2 = \frac{\mathrm{j}2\pi\delta_1\delta_2 Da(B-\sigma_2)(B-\sigma_1)(\mathrm{J}_1(\delta_2 a)\delta_1\mathrm{J}_0(\delta_1 a)-\mathrm{J}_0(\delta_2 a)\mathrm{J}_1(\delta_1 a)\delta_2)}{\left(-\mathrm{J}_0(\delta_2 a)\delta_1(B-\sigma_1)\mathrm{J}_1(\delta_1 a)+\mathrm{J}_0(\delta_1 a)\mathrm{J}_1(\delta_2 a)\delta_2(B-\sigma_2)\right)\omega} \tag{6.52}$$

$$Z_3 = -\frac{2\pi\mathrm{j}aD\begin{pmatrix}-\mathrm{J}_0(\delta_2 a)(B-\sigma_1+1)\delta_1\mathrm{J}_1(\delta_1 a)\\ +\mathrm{J}_0(\delta_1 a)\mathrm{J}_1(\delta_2 a)\delta_2(B-\sigma_2+1)\end{pmatrix}}{\left(-\mathrm{J}_0(\delta_2 a)\delta_1(B-\sigma_1)\mathrm{J}_1(\delta_1 a)+\mathrm{J}_0(\delta_1 a)\mathrm{J}_1(\delta_2 a)\delta_2(B-\sigma_2)\right)\omega S} \tag{6.53}$$

$$Z_4 = \frac{2\pi\mathrm{j}a\delta_2 D(\sigma_1-\sigma_2)\mathrm{J}_1(\delta_2 a)\delta_1\mathrm{J}_1(\delta_1 a)}{\left(-\mathrm{J}_0(\delta_2 a)\delta_1(B-\sigma_1)\mathrm{J}_1(\delta_1 a)+\mathrm{J}_0(\delta_1 a)\mathrm{J}_1(\delta_2 a)\delta_2(B-\sigma_2)\right)\omega S} \tag{6.54}$$

As with the CPT model derived in the previous chapter equations (6.49) and (6.50) will be used to generate an equivalent circuit for the PT in the following section.

6.3.4 Equivalent circuit

Based on the equations for force (6.49) - (6.50) and currents (6.41) - (6.42) an equivalent circuit model can be created. However, unlike the CPT model, F_1 and F_2 in the MPT do not have a common impedance (Z_2 in (5.56) and (5.57)). Therefore, it is not possible to create a single circuit which satisfies both F_1 and F_2 definitions directly. However, by first applying the free vibration boundary conditions to F_2, therefore $F_2 = 0$, (6.50) can be solved for v_2 giving

$$v_2 = -\frac{Z_3}{Z_4}v_1 \tag{6.55}$$

Then, using this definition of v_2, F_1 (6.49) can then be simplified to,

$$F_1 = \frac{(Z_1Z_4 - Z_2Z_3)}{Z_4}v_1 - V_{\mathrm{in}}A_{\mathrm{in}} - V_{\mathrm{out}}A_{\mathrm{out}} = Zv_1 - V_{\mathrm{in}}A_{\mathrm{in}} - V_{\mathrm{out}}A_{\mathrm{out}} \tag{6.56}$$

Where mechanical impedance Z is defined as,

$$Z = \frac{2j\pi D\left(\left(\begin{matrix}-(\sigma-1)(\sigma_1-\sigma_2)\mathrm{J}_1(\delta_2 a)\\ -\mathrm{J}_0(\delta_2 a)a\delta_2(B-\sigma_2)(B-\sigma_1+1)\end{matrix}\right)\mathrm{J}_1(\delta_1 a)\right)}{\mathrm{J}_1(\delta_1 a)\mathrm{J}_1(\delta_2 a)(\sigma_1-\sigma_2)\omega} \quad (6.57)$$

Using this definition of F_1 an equivalent circuit can now be easily drawn, by again treating force analogous to voltage and vibration velocity analogous to current. The resulting circuit is shown in Fig. 6.1.

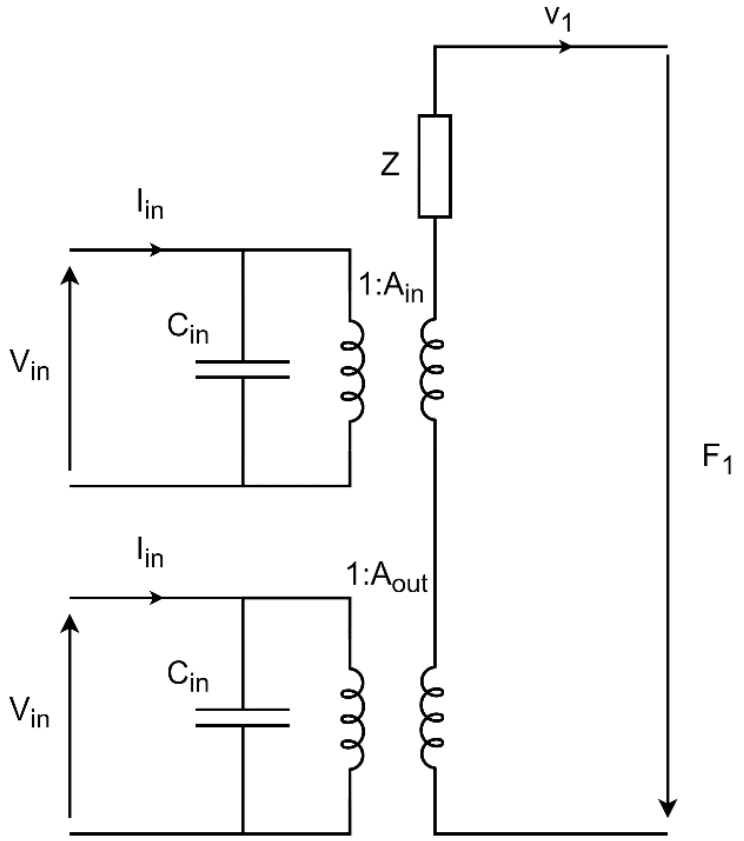

Fig. 6.1 – Full equivalent circuit model for the MPT model of the flexural mode in the radial mode PT

As with the CPT, force factors A_{in} and A_{out} are modelled as ideal transformers. Then, applying the free vibration boundary condition $(F_1 = 0)$ to the circuit in Fig. 6.1, the circuit can be simplified to that shown in Fig. 6.2.

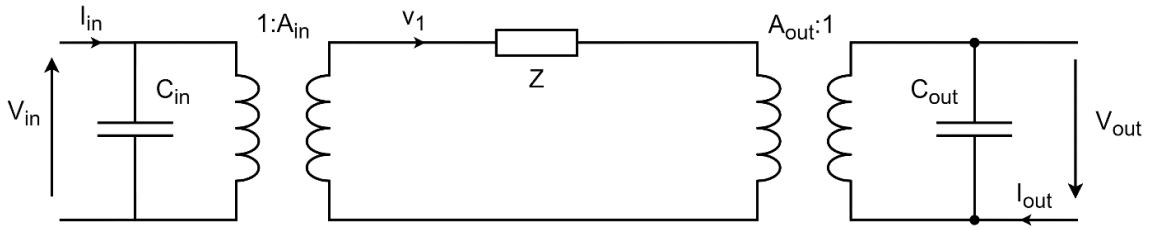

Fig. 6.2 – Two-transformer equivalent circuit model of the spurious modes of a radial mode Transoner PT

Finally, as with the CPT model, if desired, the circuit in Fig. 6.2 can then be further simplified by combining A_{in} and A_{out} force factors into a single turn ratio N_n,

$$N_n = -\frac{A_{\text{in}}}{A_{\text{out}}} = -\frac{\left(-\frac{\pi d_{31} T_{\text{out}}^{\text{tot}} N_{\text{in}} a}{s_{11}^{\text{E}}(\sigma-1)}\right)}{\left(\frac{\pi d_{31} T_{\text{in}}^{\text{tot}} N_{\text{out}} a}{s_{11}^{\text{E}}(\sigma-1)}\right)} = \frac{T_{\text{out}}^{\text{tot}} N_{\text{in}}}{T_{\text{in}}^{\text{tot}} N_{\text{out}}} \tag{6.58}$$

Thus, allowing the circuit in Fig. 6.2 to be simplified to that in Fig. 6.3.

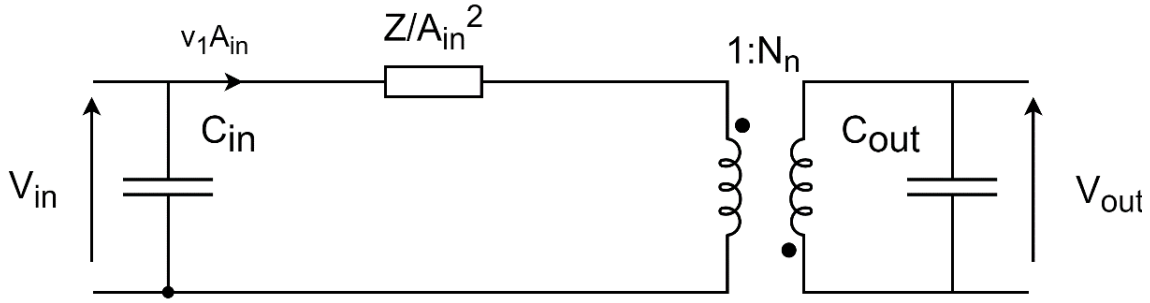

Fig. 6.3 – Single transformer equivalent circuit model of the spurious modes of a radial mode Transoner PT

Again, it should be noted that the phase of the N_n transformer was changed to correctly orient the output voltage.

6.3.5 Lumped equivalent circuit

As mentioned in the CPT model derivation in the previous chapter, it is often convenient to convert the impedance Z to an RLC circuit, so that it is possible to SPICE simulate or emulate the circuit. However, this process is more complicated for the MPT model as its more difficult than the CPT model to extract the resonant frequencies.

In the more complex MPT model, there are several terms in the impedance equation (6.57) that are a function of frequency, therefore, the resonant frequencies of the PT cannot be

found as simply as in the CPT model. Therefore, in the MPT model, equations for L_n and C_n cannot be approximated using the same technique that was used for the CPT model.

One method of determining L_n and C_n for the MPT model is to first simulate the input impedance of the PT across a range of frequencies. Then, the values of L_n and C_n can be found using an equivalent circuit extraction method such as that presented in Chapter 3.

To achieve this, first an equation for the input impedance of the PT at frequencies around the spurious mode(s) should be derived. Observing Fig. 6.3, if the output terminal is shorted, the input impedance is given by,

$$Z_{\text{in}} = \frac{Z_{C_{\text{in}}} \dfrac{Z}{A_{\text{in}}^2}}{Z_{C_{\text{in}}} + \dfrac{Z}{A_{\text{in}}^2}} \tag{6.59}$$

where $Z_{C_{\text{in}}}$ is given by,

$$Z_{C_{\text{in}}} = \frac{1}{\text{j}\omega C_{\text{in}}} \tag{6.60}$$

Then, applying an equivalent circuit extraction method, such as those presented in Chapter 3, the inductance and capacitance can be extracted. Finally, similar to the CPT model, the damping resistance can be found from the spurious Q factor (Q_s),

$$R_n = \frac{1}{Q_s}\sqrt{\frac{L_n}{C_n}} \tag{6.61}$$

The resulting equivalent components can then be converted back to two-transformer equivalent circuit component form (Fig. 6.2) using,

$$R_{m_n} = R_n A_{\text{in}}^2 \tag{6.62}$$

$$L_{m_n} = L_n A_{\text{in}}^2 \tag{6.63}$$

$$C_{m_n} = \frac{C_n}{A_{\text{in}}^2} \tag{6.64}$$

6.4 Summary

Following on from the previous chapter, an equivalent circuit model has been presented for the spurious modes occurring in the Transoner PT using the Mindlin plate theory. The next chapter will present a validation of the two equivalent circuit model using both simulated COMSOL data and experimental data.

6.5 References

[6.1] H. Deresiewicz and R. Mindlin, 'Axially symmetric flexural vibrations of a circular disk', COLUMBIA UNIV NEW YORK, 1953.

[6.2] H. Yihua and H. Wenjin, 'Research on the displacement function and equivalent circuit of circular flexural vibration mode piezoelectric ceramic composite transducers', *IEEE Transactions on Ultrasonics, Ferroelectrics, and Frequency Control*, vol. 60, no. 1, pp. 218–234, Jan. 2013, doi: 10.1109/TUFFC.2013.2553.

[6.3] J. N. Reddy, *Theory and analysis of elastic plates*. Philadelphia, PA: Taylor & Francis, 1999.

[6.4] S. K. Ha and Y. H. Kim, 'Impedance and admittance matrices of symmetric piezoelectric annular bimorphs and their applications', *The Journal of the Acoustical Society of America*, vol. 108, no. 5, pp. 2125–2133, Nov. 2000, doi: 10.1121/1.1312365.

Chapter 7 - Validation of Kirchhoff and Mindlin based equivalent circuit models for flexural modes of the Transoner PT

7.1 Introduction

In the previous two chapters, two equivalent circuit models have been developed for the flexural vibration modes of the Transoner PT. One uses the Kirchhoff plate theory (CPT), using several simplifications and the second uses Mindlin plate theory (MPT), which extends CPT by including the effects of shear deformation and rotary inertia. Both models allow the Mason equivalent circuit parameters for the flexural vibration modes to be estimated based on the physical geometry of the PT and the material properties.

The following analysis will evaluate the effectiveness of both presented models when estimating equivalent circuit component values of thin and thick PTs in a variety of scenarios. Both CPT and MPT based models will be validated against simulated single layer and multilayer PTs in COMSOL with varying radius/thickness ratios. Finally, the two models will be validated against experimental PT measurements.

7.2 Simulation setup

In this section, several devices are to be simulated in COMSOL, the equivalent circuit values are to be extracted from this data and then compared to those estimated using the models derived in the previous 2 chapters.

7.2.1 COMSOL model and setup

A 2D axisymmetric model of the Transoner PT was built within COMSOL. The radius of the simulated model was varied between $5\text{mm} < a < 20\text{mm}$, the total thickness varied between $1\text{mm} < T^{\text{tot}} < 5\text{mm}$ and with the ratio of input total thickness to device total thickness varied between $0.2 < T_{\text{in}}^{\text{Tot}}/T^{\text{Tot}} < 0.5$ (ratios above 0.5 are not required, as the device is

effectively symmetrical in the thickness direction, i.e. 0.2==0.8 [7.1]). The number of layers in both the input and output sections will be fixed at 1. Each of the PTs simulated are made from PZT-4 material with material properties given in Table 7.1.

Table 7.1 – PZT 4 material properties

$s_{11}^{\mathrm{E}}\left(\mathrm{m}^2/\mathrm{N}\right)$	$s_{55}^{\mathrm{E}}\left(\mathrm{m}^2/\mathrm{N}\right)$	$\varepsilon_{33}^{\mathrm{T}}$	$d_{31}(\mathrm{m}/\mathrm{V})$	σ	$\rho\left(\mathrm{Kg}/\mathrm{m}^3\right)$
$1.23\mathrm{x}10^{-11}$	$3.9\mathrm{x}10^{-11}$	1300	$-1.23\mathrm{x}10^{-10}$	0.329	7500

The input impedance spectra for the first 3 flexural modes are simulated for each device variation. However, first an eigenfrequency study was performed to extract the resonant frequencies for the first 3 flexural modes (3 lowest frequency flexural modes) and the radial mode, thus allowing the frequency domain simulation to be focused on these frequencies. Then, frequency domain simulations are performed at frequencies, $\omega_n - 5\mathrm{kHz} < \omega < \omega_n + 10\mathrm{kHz}$, with $2 < n < 4$ ($n = 1$ is the radial mode and $n = 2$ being the lowest frequency spurious mode, $n = 3$ the next highest frequency spurious mode and so on). Thus, only the modes of interest are captured in the simulation range. This process allows a high frequency resolution to be used but by only simulating at frequencies close to the resonant frequencies increases execution speed.

7.2.2 Component value extraction

For each frequency domain simulation performed, an input impedance spectrum is extracted. An example of this spectra is shown in Fig. 7.1.

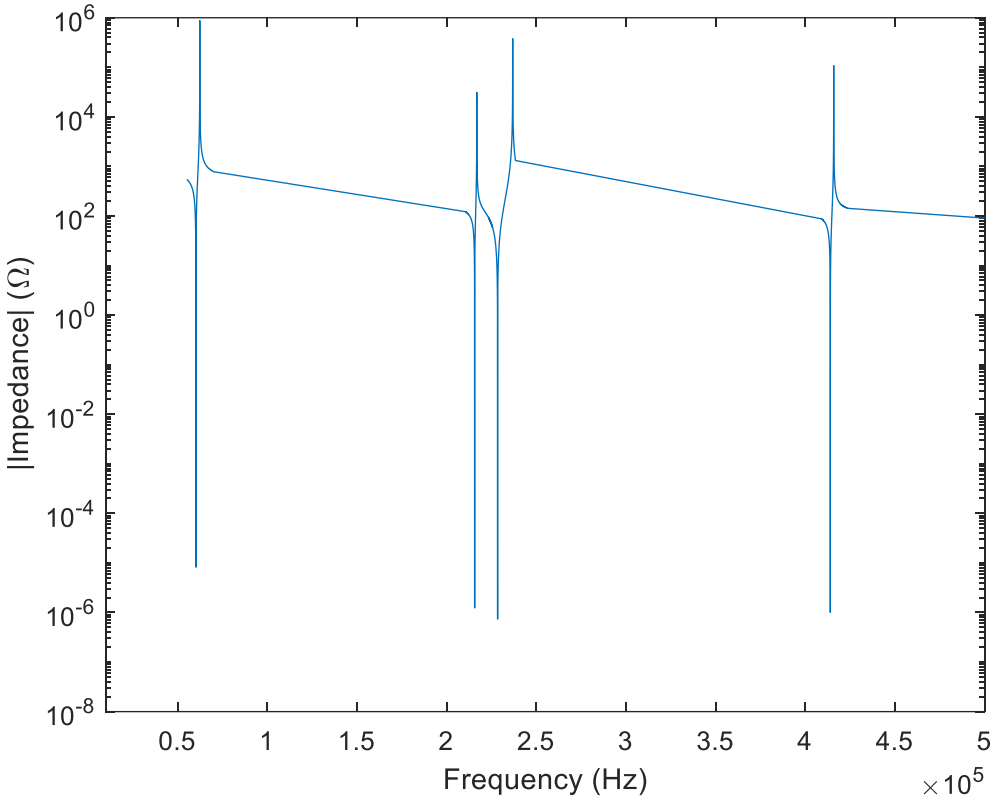

***Fig. 7.1 – Impedance spectra for the first 4 modes of a device with a* $= 5mm$, $T^{Tot} = 1mm$ *and* $T_{in}{}^{Tot}/\,T^{Tot} = 0.2$**

For each of the simulated flexural modes (not radial modes), the impedance spectra around that mode are extracted and then method 3 presented in section 3.3 is used to extract L_n, C_n and ω_n. From this, ζ_n is calculated using,

$$\zeta_n = \sqrt{\frac{L_n}{C_n}} \tag{7.1}$$

Then, these equivalent components are estimated using the two equivalent models presented in the previous two chapters and the percentage error is calculated using

$$X_n\%\ \text{error} = \frac{X_{n_{COMSOL}} - X_{n_{Model}}}{X_{n_{COMSOL}}}\% \tag{7.2}$$

where X_n is the relevant parameter of the nth spurious mode. The resulting data is plotted against the ratio of radius to total device thickness (a/T^{tot}).

7.3 Simulation results

7.3.1 Single input and output layer

Fig. 7.2, Fig. 7.3, Fig. 7.4 and Fig. 7.5 show the average percentage error in L_n, C_n, ω_n and ζ_n respectively across all devices and all three modes, against the ratio of radius to total device thickness.

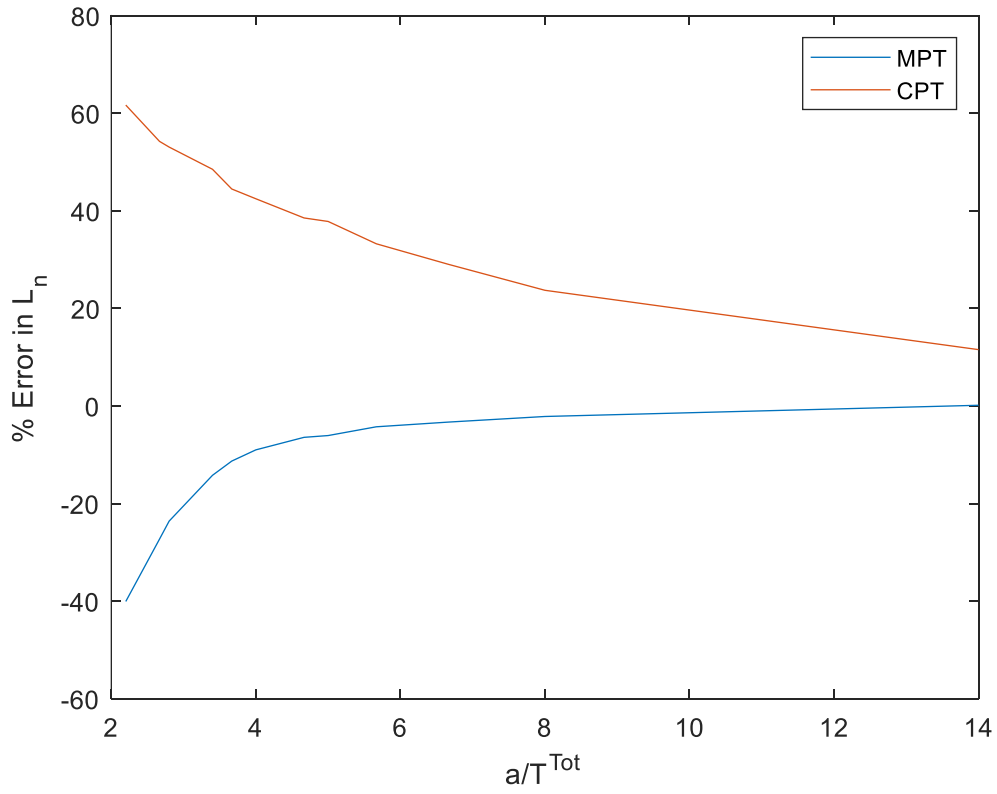

Fig. 7.2 – Average percentage error in the extracted inductance L_n across the first three flexural modes, against the radius to thickness ratio, for both CPT and MPT based models

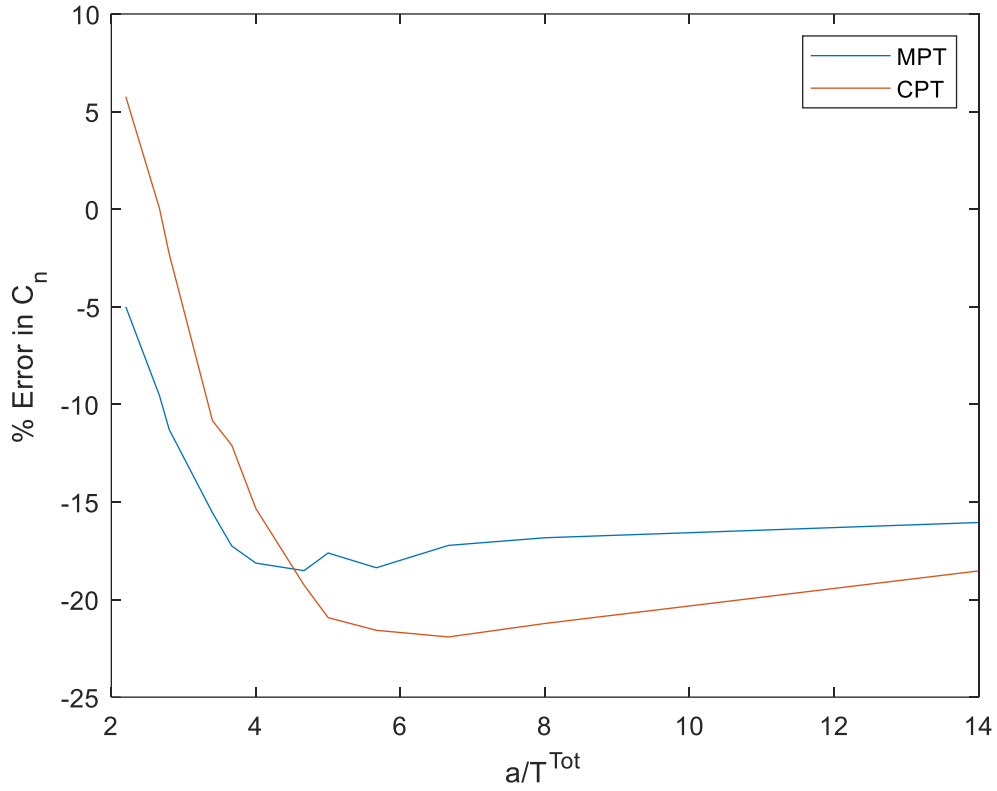

Fig. 7.3 – Average percentage error in the extracted capacitance C_n cross the first three flexural modes, against the radius to thickness ratio, for both CPT and MPT based models

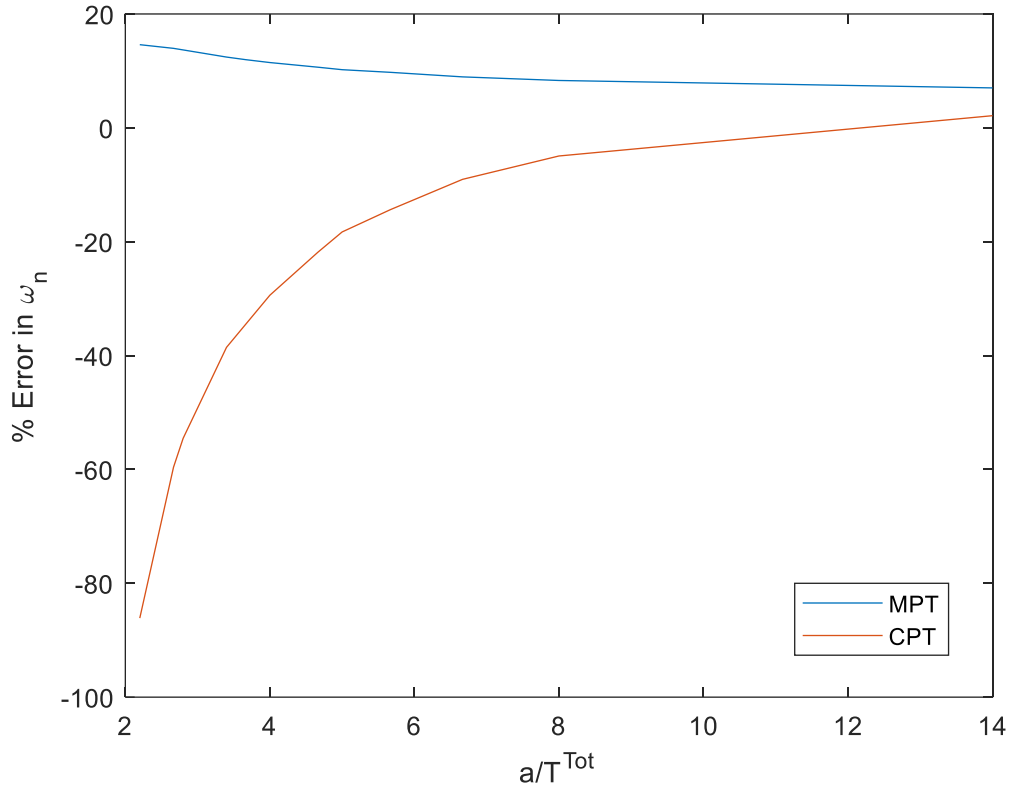

Fig. 7.4 – Average percentage error in the extracted resonant frequency ω_n across the first three flexural modes, against the radius to thickness ratio, for both CPT and MPT based models

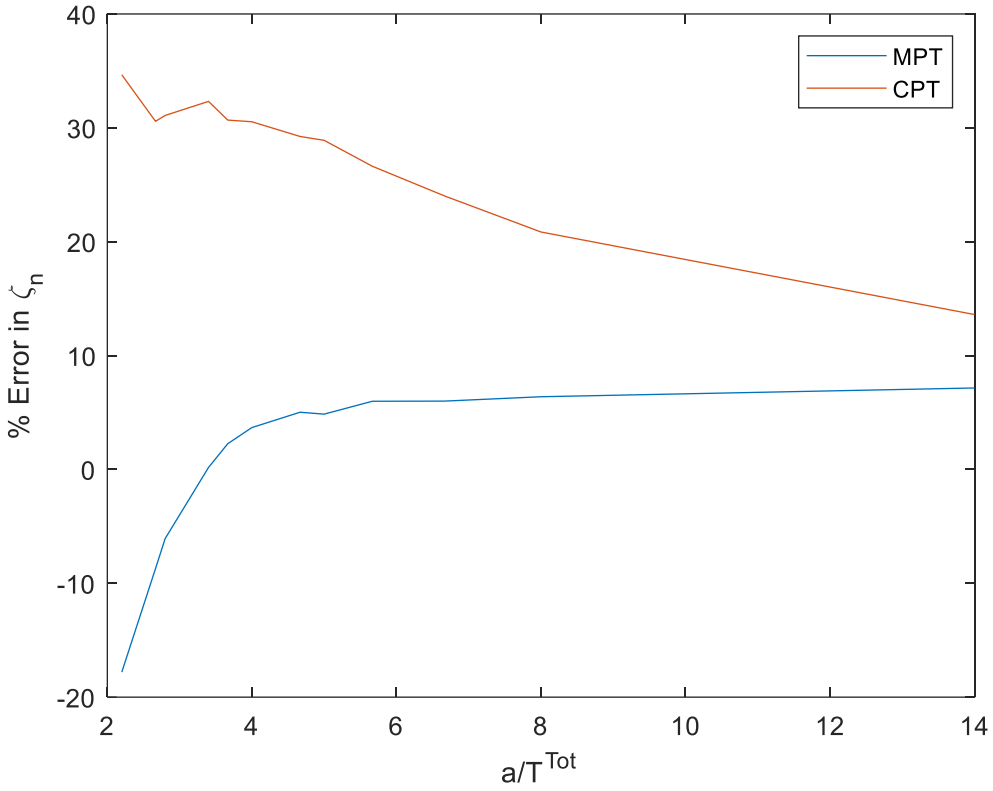

Fig. 7.5 – Average percentage error in the extracted ζ_n across the first three flexural modes, against the radius to thickness ratio, for both CPT and MPT based models

Firstly, results in Fig. 7.2 show that across the whole range of a/T^{Tot} values simulated, the inductance measured using the Mindlin model is significantly more accurate than the CPT model, with an average of 27.1% less error. Similarly, Fig. 7.3 shows that for most a/T^{Tot} values the Mindlin model is more accurate, however, owing to the increased accuracy of the thin model at lower radii to thickness ratios, the MPT based model only has an average of 4.8% less error across all devices. Owing to the lower error in both capacitance and inductance, the Mindlin model is also more accurate when estimating the resonant frequency as shown in Fig. 7.4, with on average 21.0% less error across all devices tested. Finally, for ζ_n, the MPT based model has 18.9% less error on average than the CPT based model.

Overall, both models show a similar trend of percentage error with radius to thickness ratio, both being more accurate at for thinner devices and showing less accuracy for thicker devices as expected based on the assumptions made. As expected, error rapidly increases at very low radii to thickness ratios.

The error in the equivalent values for each mode individually at each a/T^{Tot} ratio can also be analysed. Fig. 7.6, Fig. 7.7, Fig. 7.8 and Fig. 7.9 show the percentage error in L_n, C_n, ω_n and ζ_n for each of the first 3 spurious modes, for both CPT and MPT models. From this point on 1st, 2nd and 3rd modes will refer to the 1st, 2nd and 3rd spurious modes occurring in the transoner PT (lowest 3 spurious mode resonant frequencies).

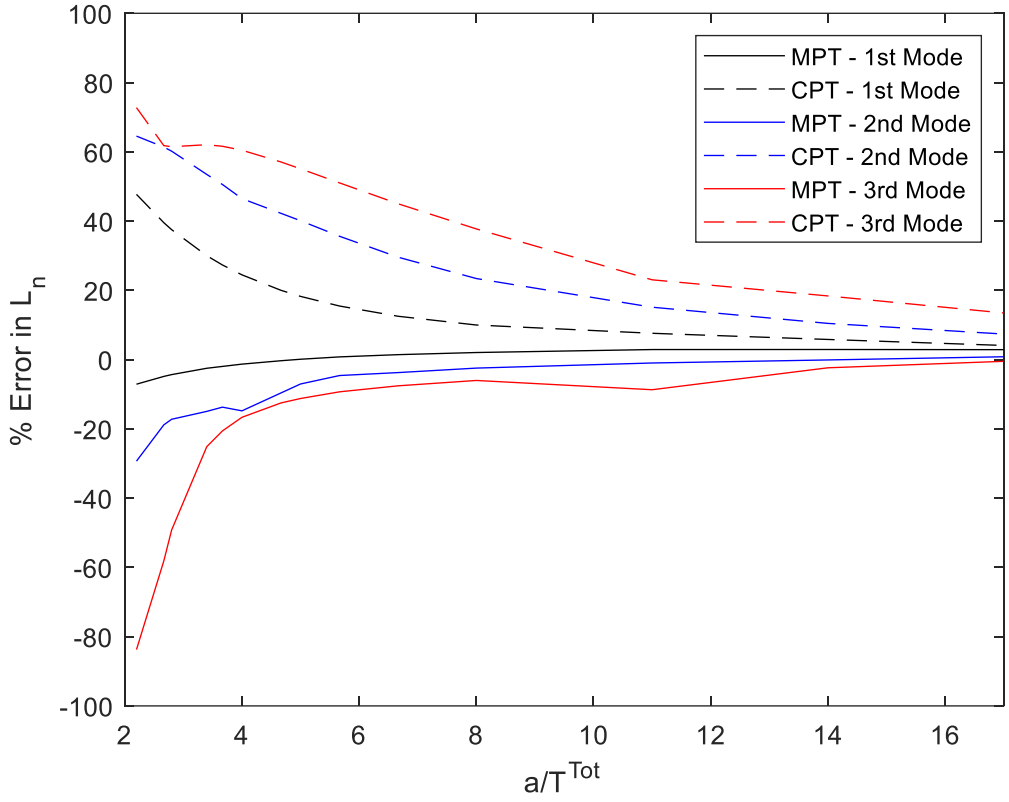

Fig. 7.6 – Percentage error in inductance L_n for each of the first 3 flexural mode for both CPT and MPT plate models

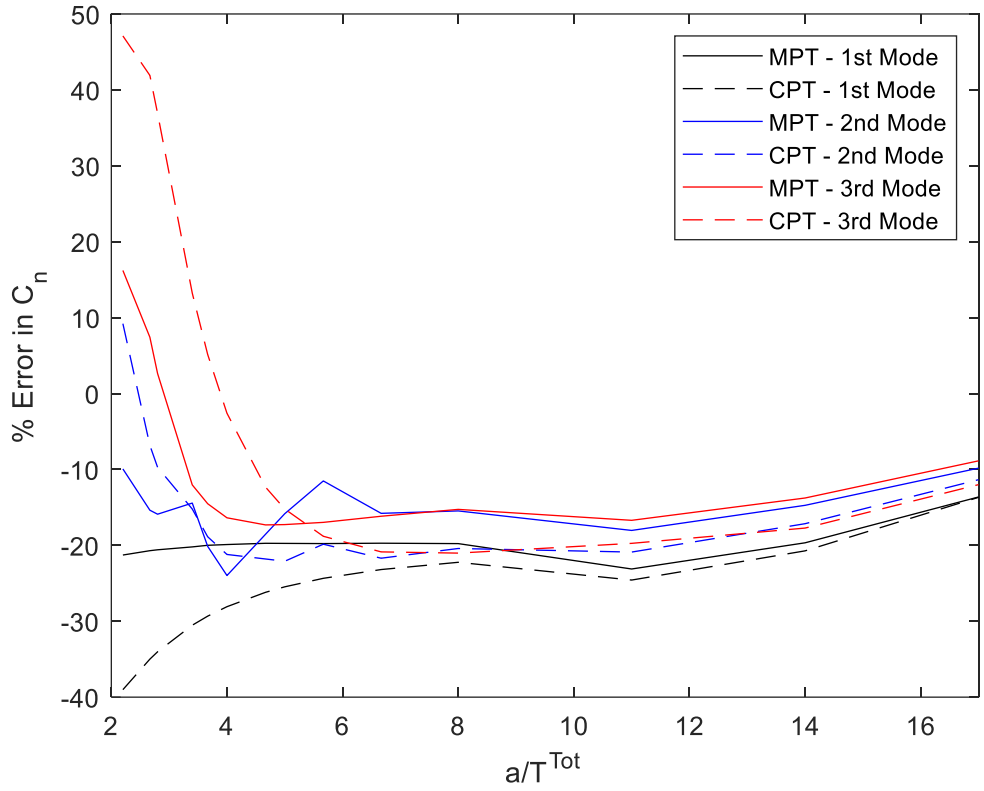

Fig. 7.7 – Percentage error in capacitance C_n for each of the first 3 flexural mode for both CPT and MPT plate models

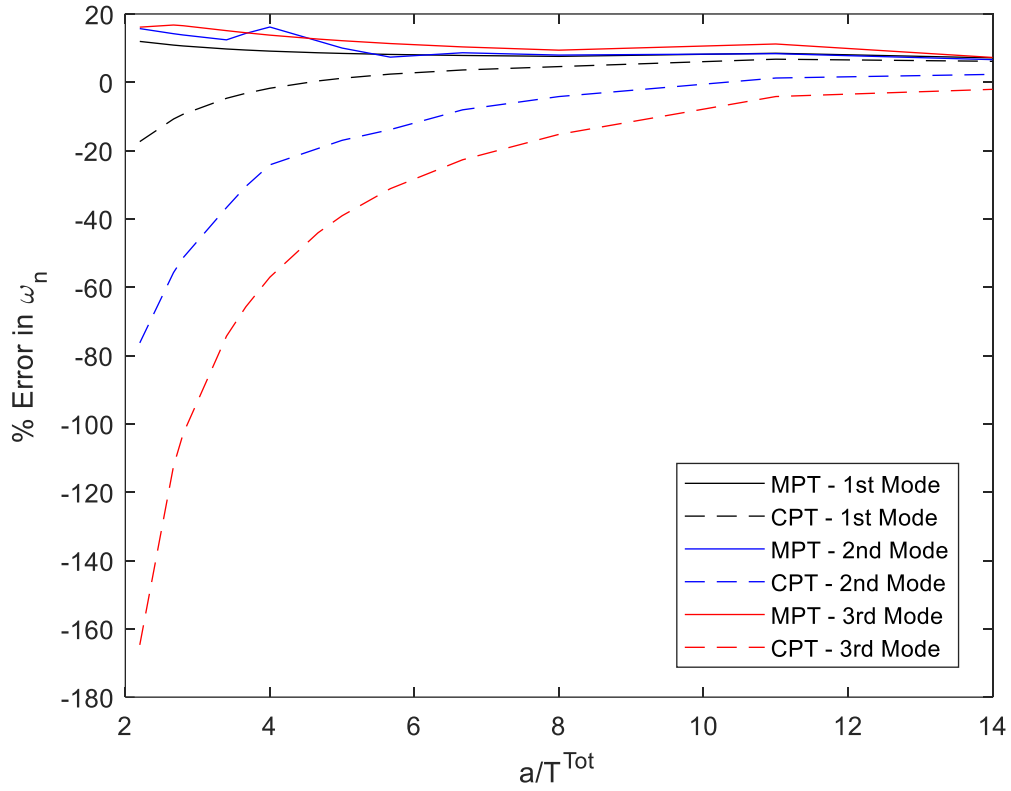

Fig. 7.8 – Percentage error in resonant frequency ω_n for each of the first 3 flexural mode for both CPT and MPT plate models

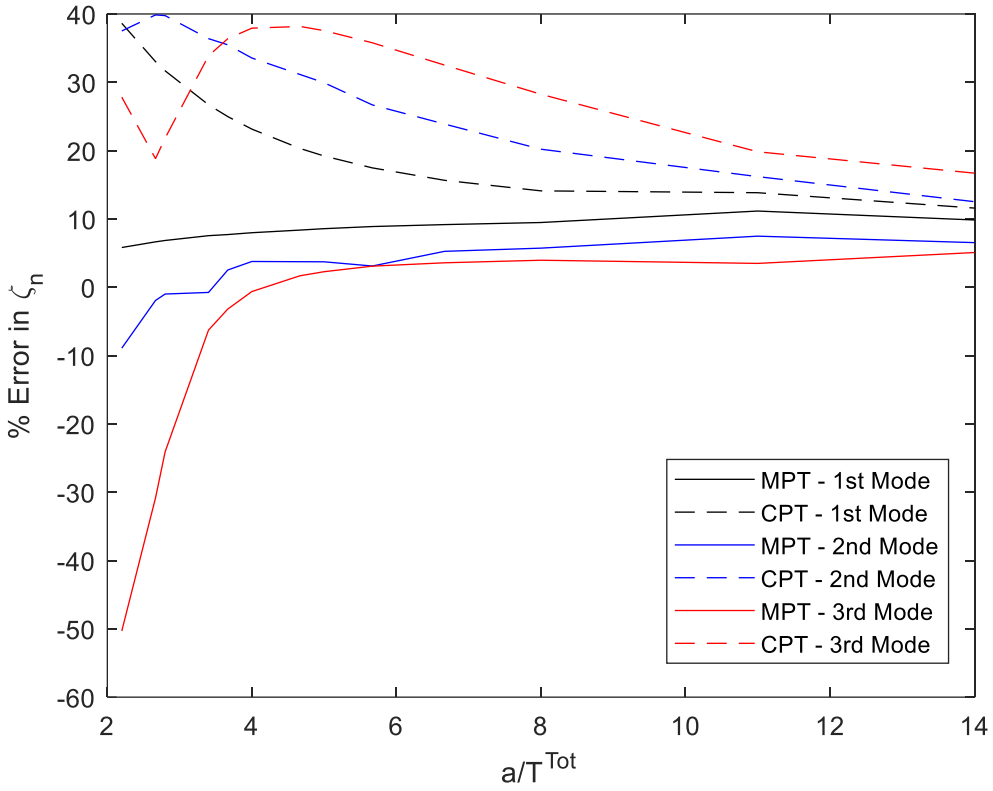

Fig. 7.9 – Percentage error in ζ_n for each of the first 3 flexural mode for both CPT and MPT plate models

As expected, with higher radius to thickness ratios, lower errors are exhibited in each of the four parameters. However, it is important to note that generally, the higher the order of the mode, the greater the percentage error. The estimated ζ_n shows a trend of greater error with higher order of mode for the CPT based model, however, for the Mindlin based model the 3rd mode has the lowest error at radius to thickness ratios greater than 5 (2.3% error). Although, the error in all 3 modes for the MPT based model is comparatively low. Capacitance results in Fig. 7.7, show a complicated trend with radius to thickness ratios. At radius to thickness ratios of greater than 10, all curves trend towards lower error with increases in radius to thickness ratio. However, at lower radius to thickness ratios, except for the first spurious mode, most curves cross through zero error and therefore, for specific combinations of radius to thickness will show almost zero error for both thin and thick plate models.

7.3.2 Multi-layer PT

A second set of COMSOL simulations are performed to analyse the accuracy of both models when used to parameterise PTs with multiple input and output layers. A single PT is first chosen with a radius of 8mm and total thickness of 1mm. For this analysis, the number of

layers (N_{in} and N_{out}) and the total thickness of each section ($T_{\text{in}}^{\text{Tot}}$ and $T_{\text{out}}^{\text{Tot}}$) will be varied. The simulation will be performed in the same manner as the previous section with the 1st and 2nd spurious modes being analysed. L_n and $C_n$will be extracted from the COMSOL simulated input impedance data, then, both models will be used to estimate these parameters and percentage error will be calculated. Additionally, by measuring the output impedance and using method 3 presented in Chapter 3 the turn ratio N_n can be measured. Then, using (5.83) or (6.58) N_n can be estimated using the equivalent circuit models for validation. Finally, input and output capacitance are extracted from the simulated data and estimated using the equations (5.50) and (5.51) respectively. It should be noted that the equations for N_n, C_{in} and C_{out} are the same for both CPT and MPT model. The percentage error (7.2) in the extracted values are shown for the 1st spurious mode in Table 7.2 and 2nd spurious mode in Table 7.3.

Table 7.2 – Percentage error in the extracted equivalent circuit parameters from the 1st spurious mode of various multilayer PTs using both presented models

$a = 8\text{mm}, \text{T}^{\text{Tot}} = 1\text{mm}$								
N_{in}	N_{out}	$T_{\text{in}}/T_{\text{out}}$	Model	L_2 (%)	C_2 (%)	C_{in}(%)	C_{out}(%)	N_2(%)
1	1	1	CPT	9.6	-16.2	-23.0	-23.0	0
		1	MPT	3.7	-14.9	-23.0	-23.0	0
2	1	1	CPT	9.9	-12.4	-22.6	-22.6	0
		1	MPT	3.9	-11.1	-22.6	-22.6	0
2	2	1	CPT	8.6	-6.8	-23.0	-23.0	0
		1	MPT	2.6	-5.6	-23.0	-23.0	0
1	2	1	CPT	9.7	-12.2	-22.7	-22.7	0
		1	MPT	3.7	-10.9	-22.7	-22.7	0
2	1	0.33	CPT	10.8	-25.3	-16.1	-26.8	-0.7
		0.33	MPT	2.9	-23.4	-16.1	-26.8	-0.7
1	2	0.33	CPT	8.1	-8.7	-16.7	-27.7	-0.1
		0.33	MPT	0	-7.1	-16.7	-27.7	-0.1

Table 7.3 – Percentage error in the extracted equivalent circuit parameters from the 2nd spurious mode of various multilayer PTs using both presented models

$a = 8\text{mm}, \mathrm{T}^{\mathrm{Tot}} = 1\text{mm} = \mathrm{T}_{\mathrm{in}}N_{\mathrm{in}} + T_{\mathrm{out}}N_{\mathrm{out}}$								
N_{in}	N_{out}	$T_{\mathrm{in}}/T_{\mathrm{out}}$	Model	L_3 (%)	C_3 (%)	C_{in}(%)	C_{out}(%)	N_3(%)
1	1	1	CPT	24.4	-17.2	-28.0	-28.0	0
		1	MPT	-0.31	-10.1	-28.0	-28.0	0
2	1	1	CPT	23.3	-11.8	-28.4	-28.4	0
		1	MPT	-1.8	-5.0	-28.4	-28.4	0
2	2	1	CPT	22.2	-6.7	-28.7	-28.7	0
		1	MPT	-3.2	-0.25	-28.7	-28.7	0
1	2	1	CPT	23.4	-12.0	-28.3	-28.3	0
		1	MPT	-1.6	-5.2	-28.3	-28.3	0
2	1	0.33	CPT	22.7	-20.8	-19.7	-36.8	-0.2
		0.33	MPT	-4.8	-15.7	-19.7	-36.8	-0.2
1	2	0.33	CPT	23.8	-11.2	-18.0	-33.6	-1.5
		0.33	MPT	-3.3	-6.5	-18.0	-33.6	-1.5

Observing the results in Table 7.2 and Table 7.3, increasing the number of layers and changing the relative layer thicknesses causes minimal change in error when compared to measuring a device with a single input and output section layer. As is expected, at a radius to thickness of 8 (in between a 'thick' and 'thin' plate), the Mindlin based model is significantly more accurate across the range of devices analysed, with percentage errors typically below 5% and 15% for L and C respectively, compared to 24% and 20% in for L and C respectively in the thin plate model.

Both models (as the equations are identical) show around 20% error on average when estimating the input and output capacitance. Horsley also found a similar error when analysing the radial mode of this PT topology [7.2]. Horsley hypothesised that this error was

due to the capacitance in the infinite spurious modes that occur in parallel when estimating this parameter, falsely inflating its value. Finally, the turns ratio estimation was very accurate in all devices simulated with most devices showing 0% error and all devices tested showing $\leq$ 1.5% error.

7.4 Experimental results

Due to the lack of availability of radial mode PTs with accurate material properties, the two presented models will be verified against measurements published by Lin [7.3]. The PT in question is the CK2 PT made from PKI-802 material. A summary of the physical and material properties of the PT are given in Table 7.4.

Table 7.4 – PKI-802 material properties [7.3]

Radius (mm)		**Total Thickness (mm)**	**Total Input Thickness (mm)**	**Output Thickness (mm)**	**Num. of input layers**	**Num. of output layers**
15		6.1	4.06	2.03	2	1
Q_r	Q_s	$d_{31}(\mathrm{m/V})$	$\varepsilon_{33}^{\mathrm{T}}$	$s_{11}^{\mathrm{E}}(\mathrm{m^2/N})$	σ	$\rho\ (\mathrm{kg/m^3})$
356	240	$-1e^{-10}$	1000	$1.04e^{-11}$	0.32	7600

In [7.3], the equivalent circuit parameters of the first two modes are presented. Then, using both the CPT and MPT based models developed in this work the equivalent circuit parameters for the first two modes are then estimated.

For the CPT based model, the input and output capacitance are estimated using (5.50)-(5.51), equations (5.80)-(5.82) are used to estimate the equivalent L_n and C_n of each mode. Finally, equation (5.83) is used to estimate turn ratio for the CPT based model.

For the Mindlin model, equation (6.59) is used to simulate the spurious resonance around the 1st and 2nd spurious modes. Then, using method 2 presented in Chapter 3, the equivalent inductance and capacitance are extracted. As the equations for C_{in}, C_{out} and N_n are the same for both models, these components are estimated using (5.50)-(5.51) and (5.83), respectively. The percentage error in each of the extracted components is then calculated. The results of

this analysis are shown in Table 7.5 for the 1st spurious mode and Table 7.6 for the 2nd spurious mode.

One issue that arises, is that the s_{55}^{E} parameter, required by the MPT model, is typically not published (or measured) for most piezoelectric materials. As a result, we do not have a value for this parameter for the PKI-802 material. Therefore, to combat this issue, the s_{55}^{E} parameter was varied through a range of values chosen based on typical s_{55}^{E} parameters exhibited by piezometric materials [7.4]. Then, for each variation, the equivalent circuit components are estimated, and the percentage error calculated. The results of this analysis are shown in Fig. 7.10 and Fig. 7.11 for the 1st and 2nd spurious modes, respectively.

Table 7.5 – 1st Spurious mode

	L_2 (mH)		C_2(pF)		N_2		C_{in} (nF)		C_{out} (nF)	
Measured [7.3]	112.4		181.2		1.04		5.41		2.74	
	mH	% error	pF	% error	-	% error	nF	% error	nF	% error
CPT based Model	50.7	54.9	277.4	-53.1	1	- 3.8	4.18	22.7	2.09	23.7
Mindlin based Model	See Fig. 7.10				1	-3.8	4.18	22.7	2.09	23.7
	ζ_2 (kΩ)		F_2 (kHz)							
Measured	24.9		35.9							
	kΩ	% error	kHz	% error						
CPT based Model	13.5	45.7	42.5	-20.4						
Mindlin based Model	See Fig. 7.10									

Table 7.6 – 2nd Spurious mode

	L_3 (mH)		C_3 (pF)		N_3		C_{in} (nF)		C_{out} (nF)	
Measured [7.3]	20.4		54.4		1.06		5.41		2.74	
	mH	% error	pF	% error	-	% error	nF	% error	nF	% error
CPT based Model	12.3	39.7	63.5	-16.8	1	-5.6	4.18	22.7	2.09	23.7
Mindlin based Model	See Fig. 7.11				1	-5.6	4.18	22.7	2.09	23.7
	ζ_3 (kΩ)		F_3 (kHz)							
Measured	19.4		151.3							
	kΩ	% error	kHz	% error						
CPT based Model	13.9	28.1	180.3	-19.1						
Mindlin based Model	See Fig. 7.11									

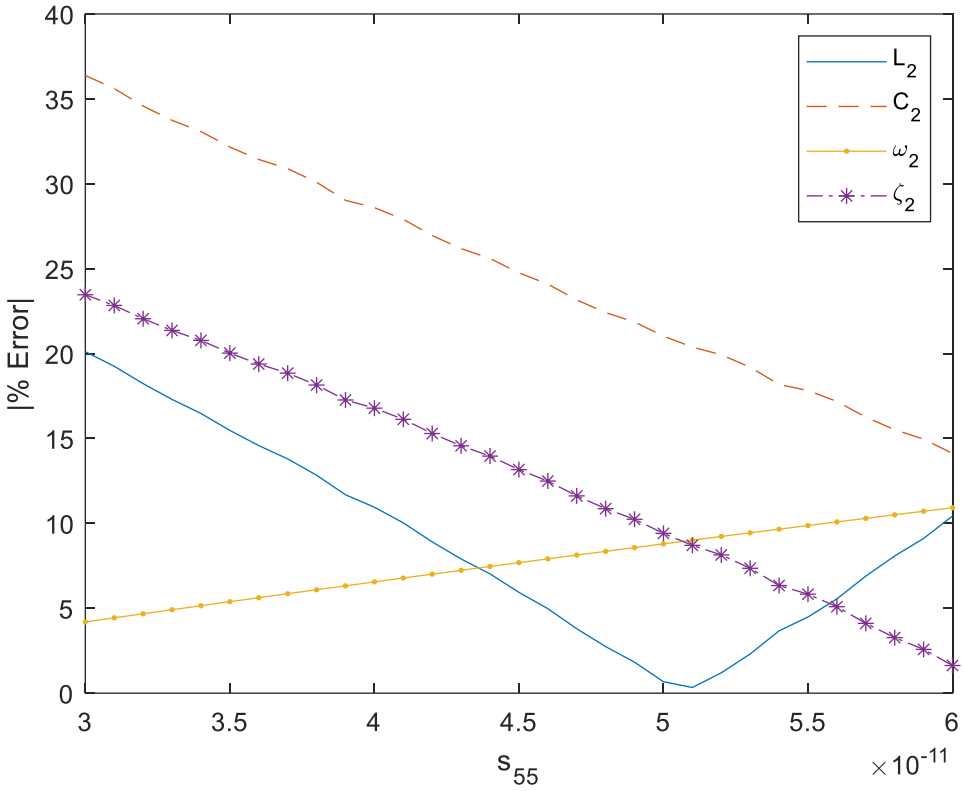

Fig. 7.10 – Percentage error in estimated parameter values against s_{55} parameter for the 1st spurious mode

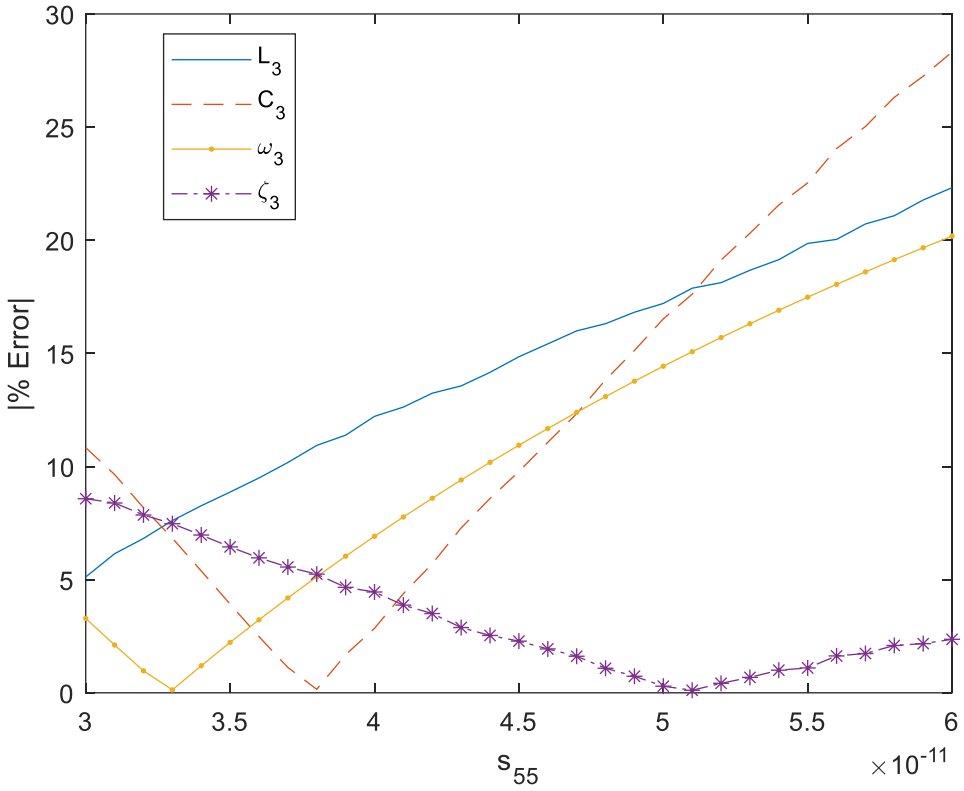

Fig. 7.11 – Percentage error in estimated parameter values against s_{55} parameter for the 2nd spurious mode

Firstly, observing the results in Fig. 7.10 and Fig. 7.11, an estimate for s_{55}^{E} can be made. Unfortunately, from these results there is not an optimum value for s_{55}^{E}which causes minima in the percentage error for each of the parameters analysed. Although, based on the simulated results, this is as expected, especially noting that the PT in question is 'thick' (radius to thickness ratio = 2.5). Therefore, it is likely that each of the estimated parameters will exhibit some error. We can see that at $s_{55}^{\mathrm{E}} = 5 \times 10^{-11}$, similar errors are observed in Fig. 7.10 and Fig. 7.11 to that which were observed in the simulated results in Fig. 7.6 - Fig. 7.9 for all 4 parameters, for a PT with radius to thickness ratio of 2.5. Therefore, this seems like a reasonable estimate for this parameter.

Comparing the results for both CPT and MPT based models, the CPT model is inaccurate, with estimated L and C values having more than 50% error for the first mode and up to 40% error for the second mode. On the other hand, the MPT model is much more accurate, with estimated L and C values only containing up to 22% error for the first mode and only up to 17% error for the second mode. However, as was found in Chapter 4, for the purpose of avoiding interaction between spurious and optimum modes, in many cases only ζ_n and ω_n

are relevant parameters. Both models fared better when estimating these parameters, with ζ_n and ω_n estimated by the CPT based model exhibiting up to 45% error for the first mode and up to 28% for the second mode. The Mindlin plate model exhibits less than 10% error for the first mode and less than 15% error for the second mode, significantly better than the thin plate model and excellent overall.

Finally, the turn ratio N_n is accurately estimated as was expected, however, the estimated input and output capacitances have around 20% error. Again, as Horsley [7.2] discussed, this is likely due to the capacitance in other vibration modes influencing the measured C_{in} and C_{out} and falsely inflating it.

7.5 Discussion

The results of this analysis have shown that while exhibiting some errors, both models derived here are effective at estimating the equivalent circuit parameters of the spurious modes exhibited by the radial mode Transoner PT. However, in almost all circumstances the MPT model is more accurate than the CPT model, with this being most apparent in higher modes at smaller radius to thickness ratios. Both models show large errors in the estimated parameters of the higher modes at very low radius to thickness ratios, with all modes showing minimal error at high radius to thickness ratios for both models.

However, as is discussed in [7.1], at low radius to thickness ratios (between 1-2.5) only the 1st spurious mode is likely to interact with the radial mode. Then, with increasing radius to thickness ratio, the radial mode will shift location with respect to the spurious modes and is able to interact with the higher order 2nd, 3rd and greater modes. Therefore, observing Fig. 3 in [7.1], the 2nd mode will only be likely to interact with the radial mode at radius to thickness ratios greater than 2.5 and in the 3rd mode at radius to thickness ratios greater than 9. Therefore, if we observe Fig. 7.8 and Fig. 7.9, and only consider errors at radius to thickness ratios where modes are likely to interact with the radial mode, then the maximum error in ζ_n and ω_n is 40% for the thin plate model and 10% for the thick plate model across the range of radius to thickness ratios analysed. This is a significant decrease from 160% and 50% for the CPT and MPT models respectively, when considering all modes at all radius to thickness ratios.

Whist it is clear the Mindlin based model is more accurate than the CPT based model, there are some downsides. As the CPT based model is a more simplistic model, explicit equations for L_n and C_n have been derived. However, for the Mindlin based model, only the combined impedance of L_n and C_n can be estimated, therefore, to estimate these parameters using this model requires simulating this impedance across a range of frequencies and then using an equivalent circuit extraction method to determine the parameters. Therefore, it is more complicated and computationally complex to estimate parameters using the thick plate model. Additionally, most commercial materials manufacturers do not include a value for s_{55}^{E} meaning the MPT model cannot be used without estimating this parameter.

7.6 Summary

In this chapter, the lumped equivalent circuit models developed for the spurious modes occurring in the Transoner PT have been verified against FEA simulated and experimental measurements.

7.7 References

[7.1] J. Forrester, J. Davidson, and M. Foster, 'Effect of Spurious Resonant Modes on the Operation of Radial Mode Piezoelectric Transformers', in *PCIM Europe 2018; International Exhibition and Conference for Power Electronics, Intelligent Motion, Renewable Energy and Energy Management*, Jun. 2018.

[7.2] E. Horsley, 'Modelling and Analysis of Radial Mode Piezoelectric Transformers and Inductor-less Resonant Power Converters', University of Sheffield, 2011.

[7.3] R.-L. Lin, 'Piezoelectric Transformer Characterization and Application of Electronic Ballast', *Ph.D. Dissertation*, Nov. 2001, Accessed: Feb. 15, 2018. [Online]. Available: https://vtechworks.lib.vt.edu/handle/10919/29948

[7.4] 'eFunda: Piezo Material Data'. https://www.efunda.com/materials/piezo/material_data/matdata_index.cfm (accessed Oct. 30, 2020).

Chapter 8 - Derivation of a lumped equivalent circuit model of the radial modes of the ring-dot PT

8.1 Introduction

As analysed in the previous chapter the radial mode Transoner PT suffers from issues with spurious modes. The ring-dot PT avoids such issues by using a single layer design, which avoids exciting these unwanted modes, thus avoiding the adverse effects. The ring-dot PT is also simpler to construct than the Transoner and as it uses the same vibration mode as the Transoner, can achieve similar output power densities. However, as frequently discussed in the previous chapters, it is vital to have an accurate lumped equivalent circuit model of the PT to be able to affectively design the PT for a given application.

This chapter presents a full derivation of an improved lumped equivalent circuit model of a galvanically isolated ring-dot PT, including the effect of the 'gap' section, based on Kirchhoff plate theory (CPT). The model is subsequently validated against finite element analysis (FEA) tools and experimental measurements from [8.1].

8.2 Ring-Dot ground electrodes vs full face ground electrode

Although typical ring-dot PTs use a full-face ground electrode, here a ring-dot PT with ring-dot ground electrode is proposed. Whilst this is done to simplify the analysis, this proposed electrode structure provides some advantages over the classic ring-dot design, most notably providing galvanic isolation between the input and output sections of the device. This is vitally important for safety, specifically in applications that use mains power. An additional advantage with this method is ease of manufacture. In ring-dot PTs with the typical electrode pattern (i.e. ring-dot on top face, full face electrode on bottom face), before building the PT, the disc must be poled. Typically, this is done by first applying a full-face electrode to both

top and bottom faces of the disc. The top electrode is then removed by grinding and replaced with a ring-dot electrodes.

In the PT topology presented here, the manufacturer could simply apply the ring-dot electrodes to the upper and lower surface and then use these electrodes to pole the disc. Whilst a single step process could be used for the typical electrode pattern (i.e. ring-dot on top face, full face electrode on bottom face), this could lead to some non-ideal polling patterns in the gap section.

8.3 Scope

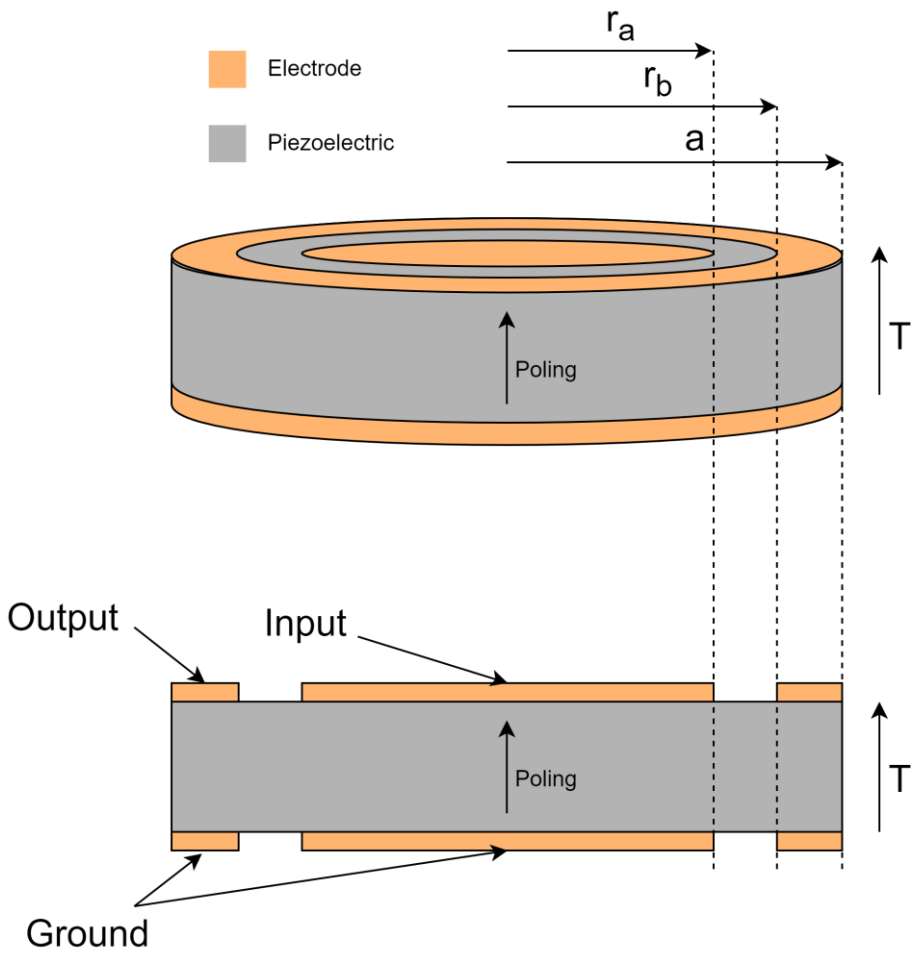

Fig. 8.1 – Ring-Dot PT

The model derived here will be a 1D analysis of a ring-dot device, operating exclusively with radial motion. A diagram of this device is shown in Fig. 8.1. The PT is made of a single disc of piezoelectric material, with a ring-dot electrode on both top and bottom faces. As shown in Fig. 8.1, the top dot electrode provides the input, while the top ring electrode provides the

output. The bottom dot and ring electrodes provide isolated ground connections for the input and output, respectively. The electrodes are assumed to be made of a highly conductive metal (copper, platinum, gold) with negligible thickness.

Initially, it is assumed that the disc is polled only in the volume which is formed by a cylinder of height T and radius r_a that exists between the top and bottom dot electrodes and the top and bottom ring-electrodes. The non-electroded region of the disc - the 'gap' - will be assumed to be made of unpoled piezoelectric and hence will act like an elastic material with the mechanical properties of the unpolled piezoelectric material.

The PT is split into 3 regions, dot (input), inner-ring (gap) and outer-ring (output), as shown in Fig. 8.2. Each section will be analysed separately based on the forces and velocities acting on it, thus allowing an equivalent circuit to be generated for each section. Then, all three equivalent circuits will be combined by equating the forces and velocities on the boundaries of sections. This equivalent circuit will then be simplified to the lumped Mason equivalent circuit form (Fig. 2.13), providing equations for each of the parameters.

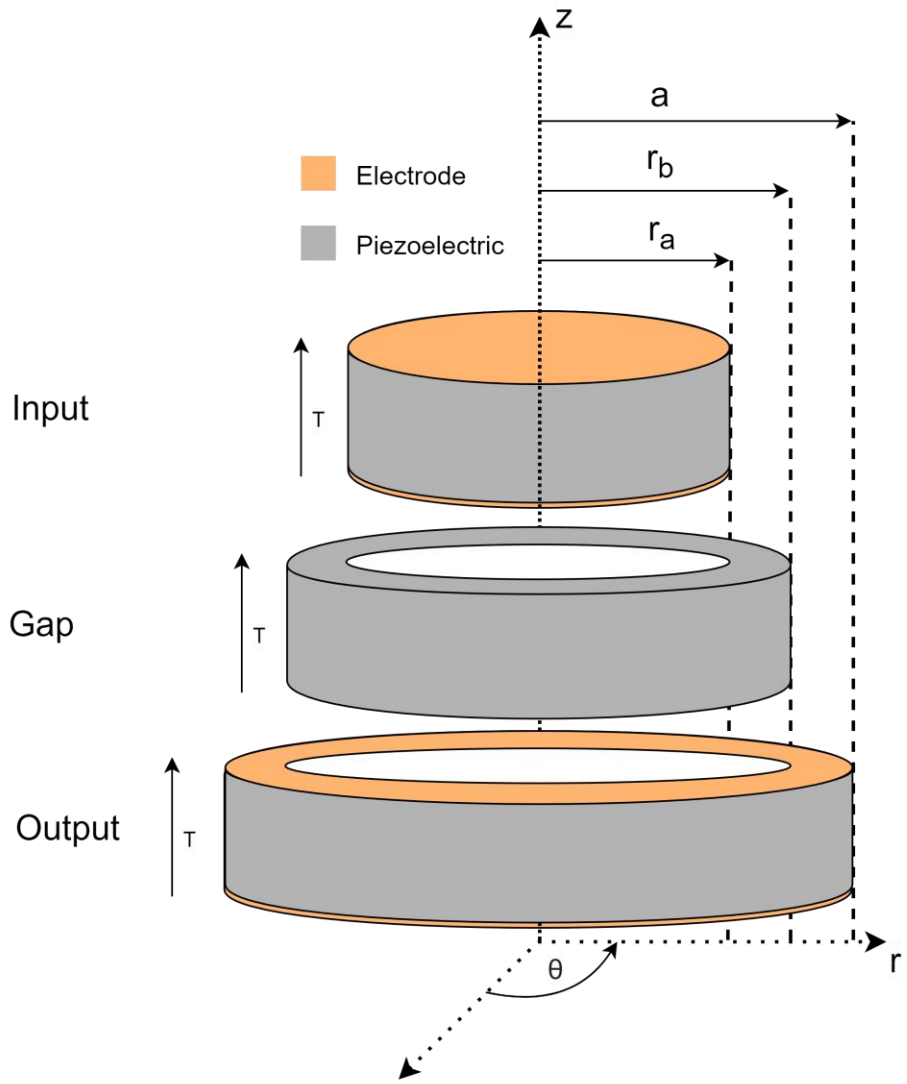

Fig. 8.2 – Ring-dot PT expanded into 3 distinct sections

To facilitate this analysis several assumptions will be made. The main assumption is that the PT follows Kirchhoff's thin plate theory (CPT) and the associated assumptions, which is well discussed in [8.2], [8.3] and Chapter 5.

8.4 Derivation

The derivation will be handled in 3 separate parts for each of the sections of the device. For each section, an equation for the radial displacement will be found. Using this equation, the electrical and mechanical properties of each section will be evaluated, allowing equations for the force on the outer and inner edges of the section to be found, along with the current flowing into/out of each electrode. Based on these equations, equivalent circuits will be found

for each section of the device, then subsequently combined to produce a full device equivalent circuit.

8.4.1 Starting equations

The constitutive equations for a piezoelectric disc polled in the 'z' direction from CPT are given by [8.4],

$$T_{r_{\mathrm{in,out,gap}}} = \frac{S_{r_{\mathrm{in,out,gap}}} + \sigma S_{\theta_{\mathrm{in,out,gap}}}}{(s_{11}^{\mathrm{E}}(1-\sigma^2))} - \frac{d_{31}E_{z_{\mathrm{in,out,gap}}}}{s_{11}^{\mathrm{E}}(1-\sigma)} \tag{8.1}$$

$$T_{\theta_{\mathrm{in,out,gap}}} = \frac{S_{\theta_{\mathrm{in,out,gap}}} + \sigma S_{r_{\mathrm{in,out,gap}}}}{(s_{11}^{\mathrm{E}}(1-\sigma^2))} - \frac{d_{31}E_{z_{\mathrm{in,out,gap}}}}{s_{11}^{\mathrm{E}}(1-\sigma)} \tag{8.2}$$

$$D_{z_{\mathrm{in,out,gap}}} = d_{31}\left(T_{r_{\mathrm{in,out,gap}}} + T_{\theta_{\mathrm{in,out,gap}}}\right) + \varepsilon_{33}^{\mathrm{T}}E_{z_{\mathrm{in,out,gap}}} \tag{8.3}$$

where d_{31} is the piezoelectric strain constant, s_{11}^{E} is the elastic compliance in the radial direction, $\varepsilon_{33}^{\mathrm{T}}$ is the dielectric constant and σ is Poisson's ratio given by

$$\sigma = -\frac{s_{12}^{\mathrm{E}}}{s_{11}^{\mathrm{E}}} \tag{8.4}$$

In this notation used here, '$\mathrm{in, out, gap}$' describes a general-purpose equation that can be applied to all sections of the device. This notation also describes that in each section of the device these equations should be treated separately as the terms in the equations will be different. Throughout the derivation, the subscript will change depending on the section the equation is relevant to. Electric fields $E_{z_{\mathrm{in,out,gap}}}$ in the respective regions are given by,

$$E_{z_{\mathrm{in}}} = \frac{V_{\mathrm{in}}}{T}, E_{z_{\mathrm{out}}} = \frac{V_{\mathrm{out}}}{T}, E_{z_{\mathrm{gap}}} = 0 \tag{8.5}$$

where T is the thickness of the PT, V_{in} and V_{out} are the voltages at the input and output terminals, respectively. From the previous assumptions and assuming perfect axisymmetric motion, strains in the radial (r) and azimuth (θ) direction are given by

$$S_r = \frac{\partial}{\partial r}u_{r_{\mathrm{in,out,gap}}}(r) \tag{8.6}$$

$$S_\theta = \frac{u_{r_{\text{in,out,gap}}}(r)}{r} \tag{8.7}$$

where u_r is radial displacement of a point in the respective section of the device. Finally, the equation of radial motion in each of the sections of the thin disc are given by [8.4],

$$\frac{\partial}{\partial r} T_{r_{\text{in,out,gap}}} + \frac{T_{r_{\text{in,out,gap}}} - T_{\theta_{\text{in,out,gap}}}}{r} = -\rho\omega^2 u_{r_{\text{in,out,gap}}} \tag{8.8}$$

where ω is the frequency (rad/s) and ρ is the density of the piezoelectric material. Solving the equation of radial motion (8.8) for radial displacement and assuming harmonic excitation gives

$$u_{\text{r}_{\text{in,out,gap}}}(r,t) = C1_{\text{in,out,gap}}\,\text{J}_1(\beta r) + C2_{\text{in,out,gap}}\text{Y}_1(\beta r)e^{\text{j}\omega t} \tag{8.9}$$

where $C1_{\text{in,out,gap}}$and $C2_{\text{in,out,gap}}$are constants, J_n and Y_n are Bessel functions of the first and second kind respectively and n$^{\text{th}}$ order, and β is defined as

$$\beta = \omega\sqrt{s_{11}^{\text{E}}\rho(1-\sigma^2)} \tag{8.10}$$

8.4.2 Modelling of the dot (Input) section

The inner-dot (input) section will be analysed first. Fig. 8.3 shows velocity v_1 and force F_1 acting on the outer edge of the inner dot section of the PT.

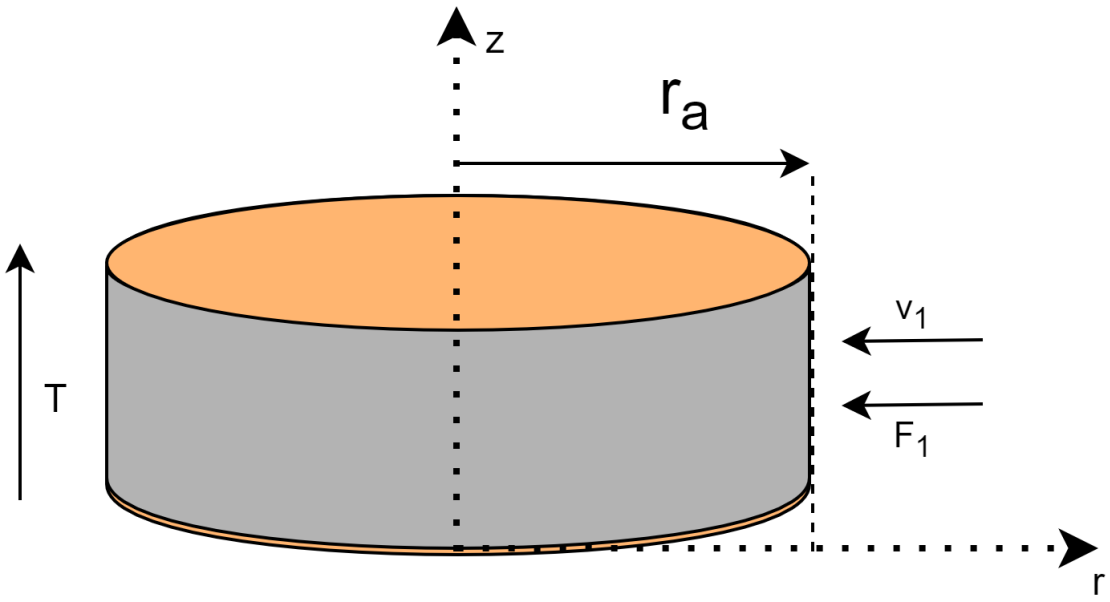

Fig. 8.3 – Inner-dot section, highlighting force acting on the section and velocity on the outer-edge

8.4.2.a) Displacement

Constants, $C1_{\text{in}}$ and $C2_{\text{in}}$ in (8.9), are found using the vibration velocity v_1 of the PT. Firstly, noting that at the centre of the disk ($r = 0$), the displacement must be finite, however, as r approaches 0, $Y_1(\beta r)$ approaches ∞. As a result, $C2_{\text{in}} = 0$. $C1_{\text{in}}$ can then be found by firstly finding the velocity of a particle on the outer edge $r = r_a$ of this section. The vibration velocity is found by differentiating with respect to time, the radial displacement (8.9) at the outer edge of the dot section, giving

$$v_1(t) = \frac{\partial u_{\text{r}}(r_{\text{a}})}{\partial t} = -\text{j}\omega C1_{\text{in}} \text{J}_1(\beta r_{\text{a}}) e^{\text{j}\omega t} \tag{8.11}$$

Note that the minus sign in (8.11) is due to the direction of velocity being defined opposite to the radial coordinate. Therefore, $C1_{\text{in}}$ is given by,

$$C1_{\text{in}} = \frac{\text{j}v_1(t)}{\text{J}_1(\beta r_{\text{a}})\omega e^{\text{j}\omega t}} \tag{8.12}$$

Finally, substituting (8.12) and $C2_{\text{in}} = 0$ into (8.9) gives the displacement of a point in the dot section,

$$u_{r_{\text{in}}}(r,t) = v_1 \frac{\text{j}}{\omega} \frac{\text{J}_1(\beta r)}{\text{J}_1(\beta r_a)} \tag{8.13}$$

8.4.2.b) Electrical equations

Equations for the current into the input section will now be generated. The charge on the input dot electrode, Q_{in} is given by Gauss's law in terms of electric displacement, D_z,

$$Q_{\text{in}} = 2\pi \int_0^{r_a} D_{z_{\text{in}}} r \, \mathrm{d}r \tag{8.14}$$

Substituting equations for T_r, T_θ, D_z (8.1)-(8.3), S_r (8.6) and S_θ (8.7) into Q_{in} (8.14), and with some manipulation, gives

$$\begin{aligned} Q_{\text{in}} = \frac{-2\pi}{(1-\sigma)s_{11}^{\text{E}}} \int_0^{r_a} \Bigg[d_{31} \left(-\frac{\partial u_{r_{\text{in}}}(r,t)}{\partial r} r - u_{r_{\text{in}}}(r,t) \right) \\ + \left(2{d_{31}}^2 - s_{11}^{\text{E}} \varepsilon_{33}^{\text{T}} (1-\sigma) \right) E_{z_{\text{in}}} r \Bigg] \mathrm{d}r \end{aligned} \tag{8.15}$$

The current into the dot electrode I_{in}, is given by,

$$I_{\text{in}} = \frac{\partial \left(Q_{\text{in}} e^{j\omega t} \right)}{\partial t} = \mathrm{j}\omega Q_{\text{in}} \tag{8.16}$$

Substituting Q_{in} (8.15) into I_{in} (8.16), with $E_{z_{\text{in}}}$ (8.5) and u_r (8.13) gives an equation for the input current,

$$I_{\text{in}} = \frac{\mathrm{j}\omega r_a^2 \pi \left(2d_{31}^2 + s_{11}^{\text{E}} \varepsilon_{33}^{\text{T}} (\sigma - 1) \right)}{T(\sigma-1)s_{11}^{\text{E}}} V_{\text{in}} + \frac{(2r_a \pi d_{31})}{(\sigma-1)s_{11}^{\text{E}}} v_1 \tag{8.17}$$

where T is the thickness of the disc. As in the previous chapters, force factor A_{in} can be defined. The force factor describes the conversion from mechanical to electrical energy (or from electrical to mechanical in the A_{out} force factor). The A_{in} force factor is defined as

$$A_{\text{in}} = \frac{(2r_a \pi d_{31})}{(\sigma-1)s_{11}^{\text{E}}} \tag{8.18}$$

Using A_{in}, I_{in} (8.17) can be further simplified to

$$I_{\text{in}} = \mathrm{j}\omega C_{\text{in}} V_{\text{in}} + A_{\text{in}} v_1 \tag{8.19}$$

where the input capacitance, C_{in}, is given by

$$C_{\text{in}} = \frac{r_a^2 \pi \left(2d_{31}^2 + s_{11}^{\text{E}} \varepsilon_{33}^{\text{T}} (\sigma - 1)\right)}{T(\sigma - 1) s_{11}^{\text{E}}} \tag{8.20}$$

8.4.2.c) Mechanical equations

Observing Fig. 8.3, the force F_1 acts inwards on the outer edge of the dot section. This force is given by

$$F_1 = \text{Stress} \cdot \text{Area} = -T_{r_{\text{in}}}(r_a) 2\pi r_a T \tag{8.21}$$

again, noting the minus sign in (8.21) as the force is defined in the opposite direction to the 'r' direction. Substituting T_r (8.1), $E_{z_{\text{in}}}$(8.5), S_r (8.6) and S_θ (8.7) in to F_1 (8.21) gives,

$$F_1(t) = -\frac{2\pi r_a T}{s_{11}^{\text{E}}(1 - \sigma^2)} \left(\frac{\partial u_{r\,\text{in}}(r,t)}{\partial r} + \frac{\sigma u_{r\,\text{in}}(r,t)}{r} - \frac{d_{31} V_{\text{in}}(t)(1 + \sigma)}{T} \right) \tag{8.22}$$

Then substituting u_r (8.13) into F_1 (8.22) and using the A_{in} force factor (8.18), after rearranging gives,

$$F_1(t) = A_{\text{in}} V_{\text{in}}(t) + Z_a v_1(t) \tag{8.23}$$

where the impedance Z_a is defined as

$$Z_a = \frac{2\text{j}T\pi}{s_{11}^{\text{E}}(\sigma^2 - 1)\omega} \frac{\left((\sigma - 1)\text{J}_1(\beta r_a) + \text{J}_0(\beta r_a) r_a \beta\right)}{\text{J}_1(\beta r_a)} \tag{8.24}$$

8.4.2.d) Equivalent circuit

Based on I_{in} (8.19) and F_1 (8.23), and treating force in an analogous way to voltage and velocity in an analogous way to current, an equivalent circuit can be generated. Similar to the techniques used in the previous chapters, A_{in} will be modelled using an ideal transformer. Fig. 8.4 shows the equivalent circuit for the input dot section of the ring-dot PT.

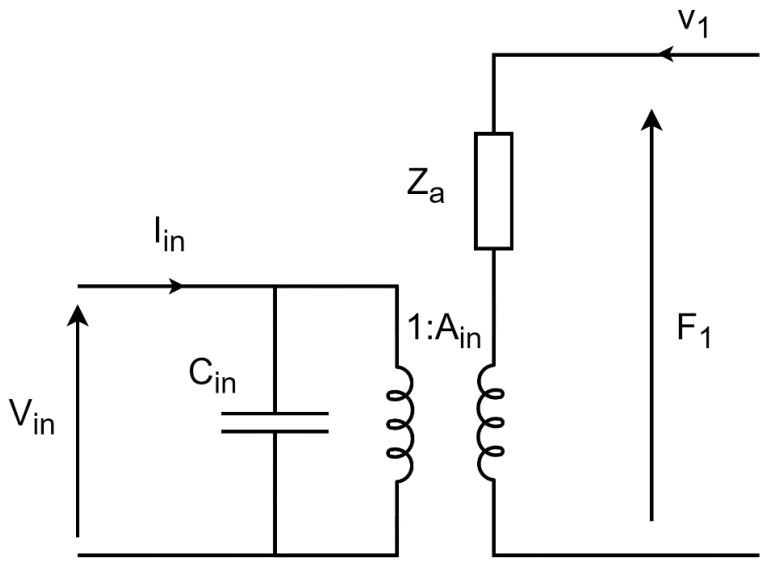

Fig. 8.4 – Equivalent circuit for the dot section of the PT

8.4.3 Modelling of the inactive (Gap) ring section

The inactive ring (gap) section of the PT has no electrodes and is the unpoled piezoelectric material between the input and output sections of the PT. Fig. 8.5 shows vibration velocities, v_{1g} and v_{2g}, and forces, F_{1g} and F_{2g}, acting on the inner and outer edges of the inactive ring section of the PT.

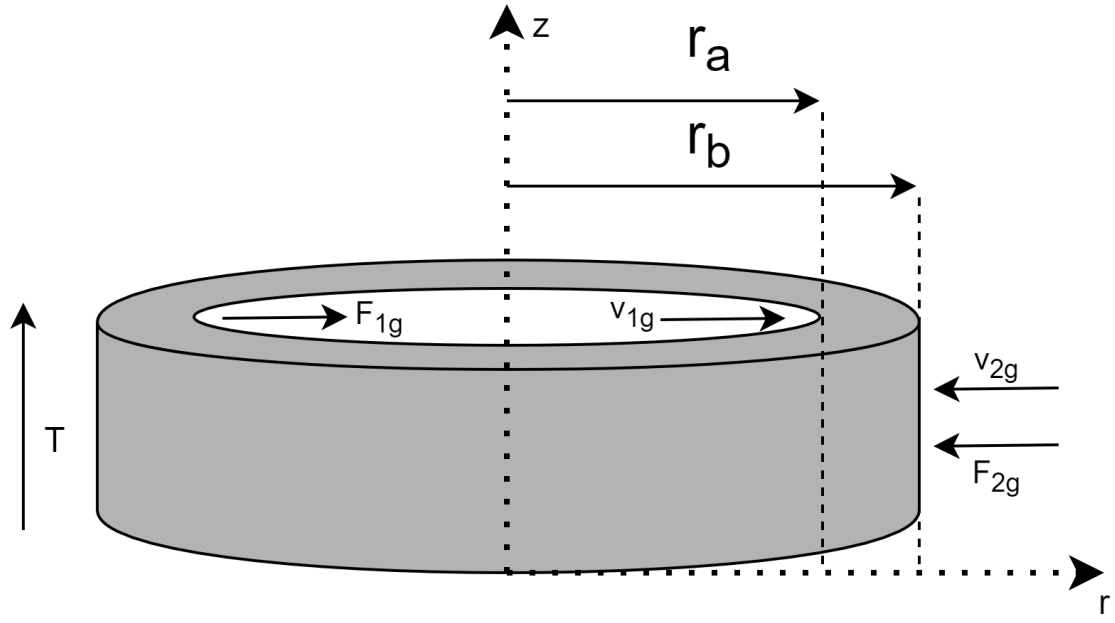

Fig. 8.5 – Forces and velocities acting on the inner-ring section of the PT

It should be noted that $F_{1g} = -F_1$ and $v_{1g} = -v_1$; however, initially it is assumed that these forces and velocities are unrestricted external forces and velocities. Although later the

individual equivalent circuits will be combined by adding restrictions to these forces and velocities that come as a result of the geometry of the device.

8.4.3.a) Displacement

Again, starting from the general solution to the equation of motion (8.9), constants $C1_{\text{gap}}$ and $C2_{\text{gap}}$ are found using the vibration velocities, $v_{1\text{g}}$ and $v_{2\text{g}}$. Observing Fig. 8.5, the vibration velocity acting on the inner edge, v_{1g}, can be found by differentiating the radial displacement at the inner edge ($r = r_a$) with respect to time, giving

$$v_{1g}(t) = \frac{\partial u_r(r_a)}{\partial t} = \text{j}\omega\left(C1_{\text{gap}}\text{J}_1(\beta r_a) + C2_{\text{gap}}\text{Y}_1(\beta r_a)\right)e^{\text{j}\omega t} \tag{8.25}$$

Similarly, vibration velocity on the outer edge, $v_{2\text{g}}$, can be found by differentiating the radial displacement at the outer edge ($r = r_b$), giving

$$v_{2\text{g}}(t) = -\frac{\partial u_r(r_b)}{\partial t} = -\text{j}\omega\left(C1_{\text{gap}}\text{J}_1(\beta r_b) + C2_{\text{gap}}\text{Y}_1(\beta r_b)\right)e^{\text{j}\omega t} \tag{8.26}$$

Again, note the minus sign in (8.26) due to $v_{2\text{g}}$ being defined in the opposite direction to the 'r' direction. As both (8.25) and (8.26) contain two unknowns, they will be solved simultaneously. Solving $v_{1\text{g}}$ (8.25) and $v_{2\text{g}}$ (8.26) for $C2_{\text{gap}}$ gives,

$$C2_{\text{gap}} = \frac{-\text{J}_1(\beta r_a)C1_{\text{gap}}\omega - \text{j}e^{-\text{j}\omega t}v_{1\text{g}}(t)}{\text{Y}_1(\beta r_a)\omega} \tag{8.27}$$

$$C2_{\text{gap}} = \frac{-\text{J}_1(\beta r_b)C1_{\text{gap}}\omega + \text{j}e^{-\text{j}\omega t}v_{2\text{g}}(t)}{\text{Y}_1(\beta r_b)\omega} \tag{8.28}$$

Equating (8.27) and (8.28), and solving for $C1_{\text{gap}}$ gives,

$$C1_{\text{gap}} = \frac{\text{j}\left(v_{1g}(t)\text{Y}_1(\beta r_b) + v_{2g}(t)\text{Y}_1(\beta r_a)\right)e^{-\text{j}\omega t}}{\omega\left(\text{J}_1(\beta r_a)\text{Y}_1(\beta r_b) - \text{Y}_1(\beta r_a)\text{J}_1(\beta r_b)\right)} \tag{8.29}$$

$C2_{\text{gap}}$ is then found by substituting (8.29) into either (8.27) or (8.28) and simplifying,

$$C_{2_{\text{gap}}} = \frac{\mathrm{j}\left(v_{1\text{g}}(t)\mathrm{J}_1(\beta r_b) + v_{2\text{g}}(t)\mathrm{J}_1(\beta r_a)\right)e^{-\mathrm{j}\omega t}}{\omega\left(\mathrm{J}_1(\beta r_a)\mathrm{Y}_1(\beta r_b) - \mathrm{Y}_1(\beta r_a)\mathrm{J}_1(\beta r_b)\right)} \tag{8.30}$$

Finally, substituting (8.29) and (8.30) into the general equation for radial displacement (8.9), gives the equation for the displacement of a particle in the inactive ring section of the device,

$$u_{r_{\text{gap}}}(r,t) = \frac{\mathrm{j}\begin{pmatrix} \mathrm{J}_1(\beta r_a)\mathrm{Y}_1(\beta r)v_{2g}(t) + \mathrm{J}_1(\beta r_b)\mathrm{Y}_1(\beta r)v_{1g}(t) \\ -\mathrm{J}_1(\beta r)\mathrm{Y}_1(\beta r_b)v_{1g}(t) - \mathrm{J}_1(\beta r)\mathrm{Y}_1(\beta r_a)v_{2g}(t) \end{pmatrix}}{\omega\left(\mathrm{J}_1(\beta r_a)\mathrm{Y}_1(\beta r_b) - \mathrm{Y}_1(\beta r_a)\mathrm{J}_1(\beta r_b)\right)} \tag{8.31}$$

8.4.3.b) Electrical equations

As there is no electrode in this section of the device, the external electric field across the gap region is equal to 0. If this region is made of polled piezoelectric materials other authors have found an electric field is generated across the thickness of the device [8.6]. This adds additional complexity but will be explored later (section 8.4.7). Initially, the gap region is assumed to be an elastic material with the same mechanical properties as the piezoelectric material and an electrical insulator. This simplification leads to,

$$D_{z_{\text{gap}}} = 0, E_{z_{\text{gap}}} = 0 \tag{8.32}$$

and, by extension,

$$Q_{\text{gap}} = 0, I_{\text{gap}} = 0 \tag{8.33}$$

8.4.3.c) Mechanical equations

Observing Fig. 8.5, the force F_{1g} acts inwards on the inner radius and F_{2g} acts inwards on the outer radius of the gap section. These forces are given by

$$F_{1g} = -2\pi T r_a T_{r_{\text{gap}}}(r_a) \tag{8.34}$$

$$F_{2g} = -2\pi T r_b T_{r_{\text{gap}}}(r_b) \tag{8.35}$$

Substituting T_r (8.1) into F_{1g} (8.34) and F_{2g} (8.35), using D_z, E_z (8.32) and $Q_{\text{gap}}, I_{\text{gap}}$ (8.33), and the equation for the displacement of a particle in the inactive inner ring (8.31), this gives equations for the forces F_{1g} and F_{2g},

$$F_{1g} = Z_1 v_{1g} + Z_2 v_{2g} \tag{8.36}$$

$$F_{2g} = Z_2 v_{1g} + Z_3 v_{2g} \tag{8.37}$$

where impedances $Z_{1,2,3}$ are defined by,

$$Z_1 = \frac{2\mathrm{j}\pi T}{s_{11}^{\mathrm{E}}\omega(\sigma^2 - 1)} \frac{\begin{pmatrix}\big((\sigma - 1)\mathrm{Y}_1(\beta r_a) + r_a \mathrm{Y}_0(\beta r_a)\beta\big)\mathrm{J}_1(\beta r_b) \\ -\mathrm{Y}_1(\beta r_b)\big((\sigma - 1)\mathrm{J}_1(\beta r_a) + \mathrm{J}_0(\beta r_a) r_a \beta\big)\end{pmatrix}}{\big(\mathrm{J}_1(\beta r_a)\mathrm{Y}_1(\beta r_b) - \mathrm{Y}_1(\beta r_a)\mathrm{J}_1(\beta r_b)\big)} \tag{8.38}$$

$$Z_2 = \frac{4\mathrm{j}T}{s_{11}^{\mathrm{E}}\omega(\sigma^2 - 1)} \frac{1}{\big(\mathrm{J}_1(\beta r_a)\mathrm{Y}_1(\beta r_b) - \mathrm{Y}_1(\beta r_a)\mathrm{J}_1(\beta r_b)\big)} \tag{8.39}$$

$$Z_3 = \frac{2\mathrm{j}\pi T}{s_{11}^{\mathrm{E}}\omega(\sigma^2 - 1)} \frac{\begin{pmatrix}\big((\sigma - 1)\mathrm{Y}_1(\beta r_b) + r_b \mathrm{Y}_0(\beta r_b)\beta\big)\mathrm{J}_1(\beta r_a) \\ -\mathrm{Y}_1(\beta r_a)\big((\sigma - 1)\mathrm{J}_1(\beta r_b) + \mathrm{J}_0(\beta r_b) r_b \beta\big)\end{pmatrix}}{\big(\mathrm{J}_1(\beta r_a)\mathrm{Y}_1(\beta r_b) - \mathrm{Y}_1(\beta r_a)\mathrm{J}_1(\beta r_b)\big)} \tag{8.40}$$

8.4.3.d) Equivalent circuit

As done for the input dot, an equivalent circuit can be created, based on equations for the two forces, F_{1g} and F_{2g}. An equivalent circuit for each force, F_{1g} and F_{2g}, is shown in Fig. 8.6.

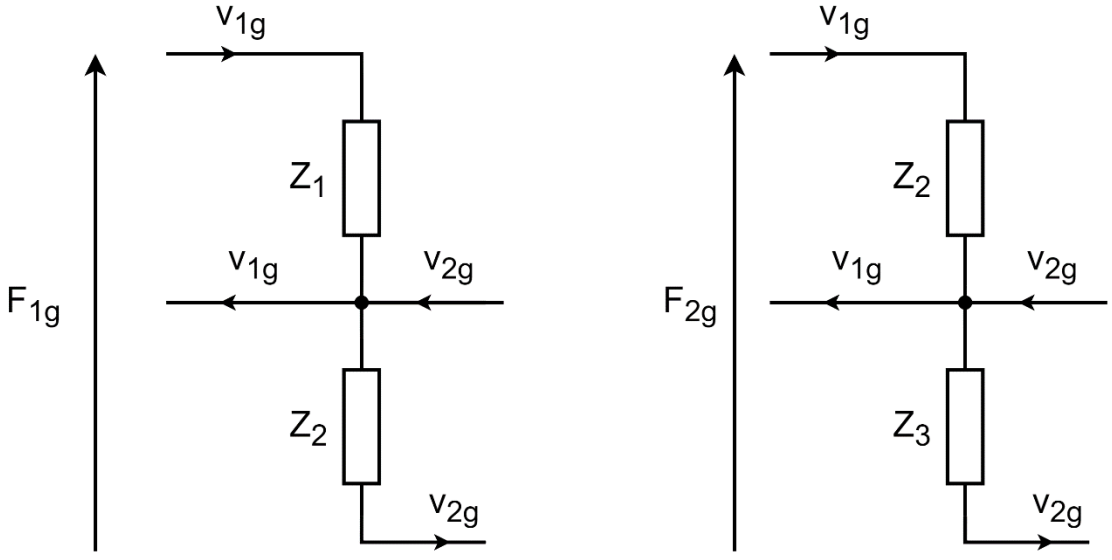

Fig. 8.6 – Equivalent circuits for the inactive inner-ring section of the ring-dot PT

Observing the two circuits in Fig. 8.6, by transforming the impedances, the two circuits can be combined to create a single equivalent circuit. This is shown in Fig. 8.7.

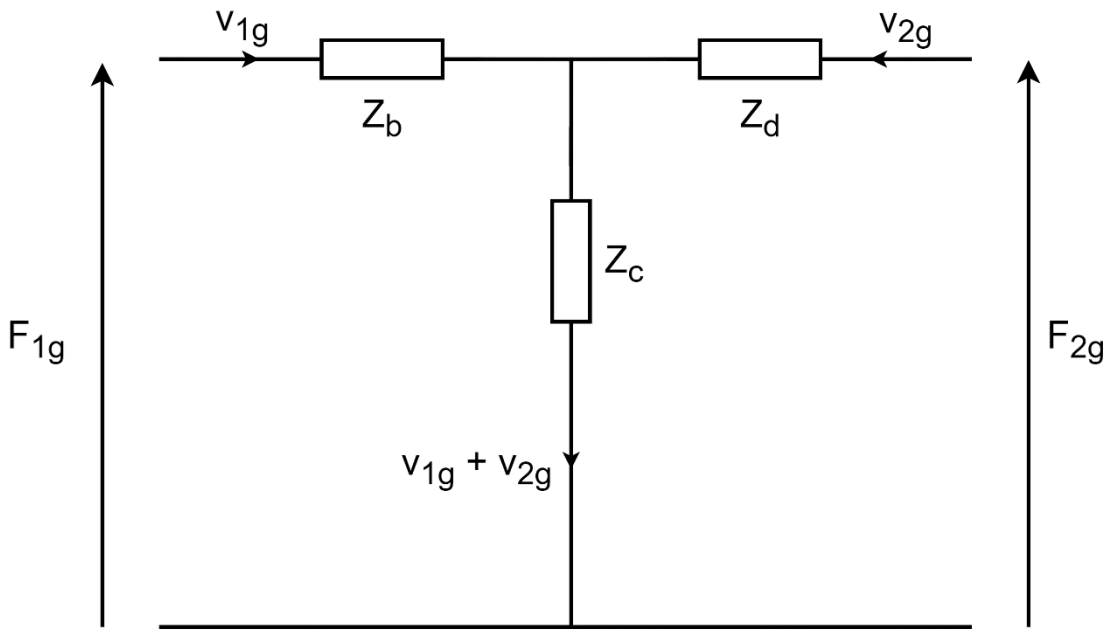

Fig. 8.7 – Combined equivalent circuit for the inactive inner-ring section of the ring-dot PT

where impedances $Z_{b,c,d}$ are defined by

$$Z_b = Z_1 - Z_2 = \frac{2\mathrm{j}T}{\omega s_{11}^{\mathrm{E}}(\sigma^2 - 1)} \frac{\begin{pmatrix}\big((\sigma - 1)\mathrm{Y}_1(\beta r_a) + r_a\mathrm{Y}_0(\beta r_a)\beta\big)\pi\mathrm{J}_1(\beta r_b) - 2 \\ -\pi\big((\sigma - 1)\mathrm{J}_1(\beta r_a) + \mathrm{J}_0(\beta r_a) r_a\beta\big)\mathrm{Y}_1(\beta r_b)\end{pmatrix}}{\big(\mathrm{J}_1(\beta r_a)\mathrm{Y}_1(\beta r_b) - \mathrm{Y}_1(\beta r_a)\mathrm{J}_1(\beta r_b)\big)} \tag{8.41}$$

$$Z_c = Z_2 = \frac{4\mathrm{j}T}{s_{11}^{\mathrm{E}}\omega(\sigma^2 - 1)} \frac{1}{\big(\mathrm{J}_1(\beta r_a)\mathrm{Y}_1(\beta r_b) - \mathrm{Y}_1(\beta r_a)\mathrm{J}_1(\beta r_b)\big)} \tag{8.42}$$

$$Z_d = Z_3 - Z_2 = \frac{2\mathrm{j}T}{\omega s_{11}^{\mathrm{E}}(\sigma^2 - 1)} \frac{\begin{pmatrix}\pi\big((\sigma - 1)\mathrm{Y}_1(\beta r_b) + r_b\mathrm{Y}_0(\beta r_b)\beta\big)\mathrm{J}_1(\beta r_a) - 2 \\ -\pi\big((\sigma - 1)\mathrm{J}_1(\beta r_b) + \mathrm{J}_0(\beta r_b) r_b\beta\big)\mathrm{Y}_1(\beta r_a)\end{pmatrix}}{\big(\mathrm{J}_1(\beta r_a)\mathrm{Y}_1(\beta r_b) - \mathrm{Y}_1(\beta r_a)\mathrm{J}_1(\beta r_b)\big)} \tag{8.43}$$

8.4.4 Modelling of the outer ring (Output) section

The velocity and forces acting on the inner and outer edges of the outer-ring section of the PT are shown in Fig. 8.8 below.

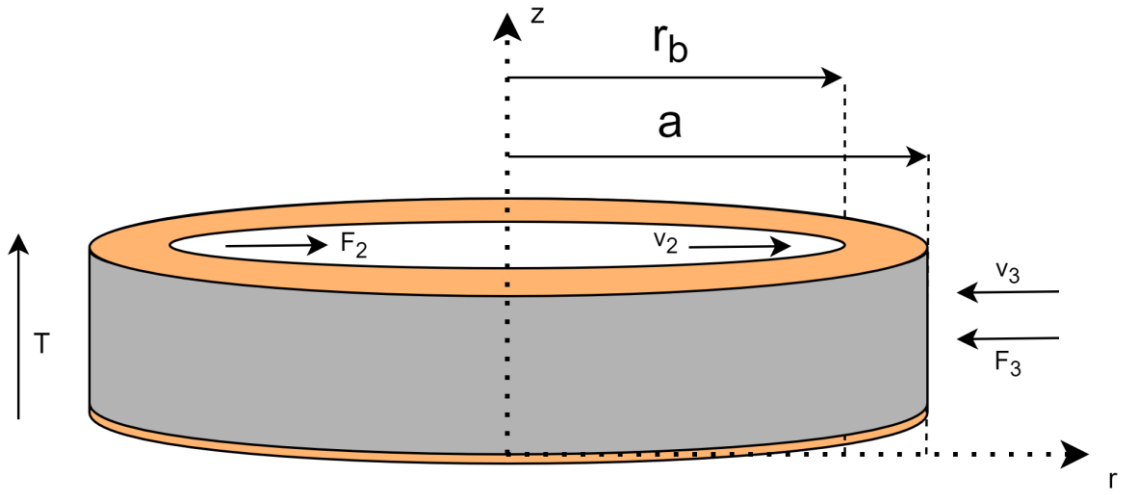

Fig. 8.8 – Forces and velocities acting on the outer-ring section of the ring-dot PT

8.4.4.a) Displacement

From the general solution of the equation of motion (8.9), constants $C1_{\text{out}}$ and $C2_{\text{out}}$, are again found using the vibration velocities, v_2 and v_3. Observing Fig. 8.8, the vibration velocity acting on the inner edge ($r = r_b$), v_2, is given by

$$v_2(t) = \frac{\partial u_{r_{\text{out}}}}{\partial t} = \mathrm{j}\omega\left(C1_{\text{out}}\mathrm{J}_1(\beta r_b) + C2_{\text{out}}\mathrm{Y}_1(\beta r_b)\right)e^{\mathrm{j}\omega t} \tag{8.44}$$

Similarly, vibration velocity on the outer edge ($r = a$), v_3, is given by

$$v_3(t) = -\frac{\partial u_{r_{\text{out}}}}{\partial t} = -\mathrm{j}\omega\left(C1_{\text{out}}\mathrm{J}_1(\beta a) + C2_{\text{out}}\mathrm{Y}_1(\beta a)\right)e^{\mathrm{j}\omega t} \tag{8.45}$$

Solving both v_2 (8.44) and v_3 (8.45) simultaneously for $C2_{\text{out}}$ gives,

$$C2_{\text{out}} = \frac{-\mathrm{J}_1(\beta r_b)C_{1_{\text{out}}}\omega - \mathrm{j}e^{-\mathrm{j}\omega t}v_2}{Y_1(\beta r_b)\omega} \tag{8.46}$$

$$C2_{\text{out}} = \frac{-\mathrm{J}_1(\beta a)C_{1_{\text{out}}}\omega + \mathrm{j}e^{-\mathrm{j}\omega t}v_3}{\mathrm{Y}_1(\beta a)\omega} \tag{8.47}$$

Equating (8.46) and (8.47) and then solving for $C_{1_{\text{out}}}$ gives,

$$C1_{\text{out}} = \frac{\mathrm{j}\left(v_2(t)\mathrm{Y}_1(\beta a) + v_3(t)\mathrm{Y}_1(\beta a)\right)e^{-\mathrm{j}\omega t}}{\omega\left(\mathrm{J}_1(\beta a)\mathrm{Y}_1(\beta r_b) - \mathrm{Y}_1(\beta a)\mathrm{J}_1(\beta r_b)\right)} \tag{8.48}$$

$C2_{\text{out}}$ can then be found by substituting $C1_{\text{out}}$ (8.48) into either (8.46) or (8.47) and simplifying to give,

$$C2_{\text{out}} = \frac{-\text{j}\big(v_2(t)\text{J}_1(\beta a) + v_3(t)\text{J}_1(\beta r_b)\big)e^{-\text{j}\omega t}}{\omega\big(\text{J}_1(\beta a)\text{Y}_1(\beta r_b) - \text{Y}_1(\beta a)\text{J}_1(\beta r_b)\big)} \tag{8.49}$$

Finally, substituting $C1_{\text{out}}$ (8.48) and $C2_{\text{out}}$ (8.49) into the general solution for the equation of motion (8.9), gives an equation for the displacement of a particle in the outer-ring section of the device,

$$u_{r_{\text{out}}}(\text{r},\text{t}) = \frac{\text{j}\begin{pmatrix}\text{J}_1(\beta r)\text{Y}_1(\beta r_b)v_3 - \text{J}_1(\beta a)\text{Y}_1(\beta r)v_2 \\ -\text{J}_1(\beta r_b)\text{Y}_1(\beta r)v_3 + \text{J}_1(\beta r)\text{Y}_1(\beta a)v_2\end{pmatrix}}{\big(\text{J}_1(\beta a)\text{Y}_1(\beta r_b) - \text{Y}_1(\beta a)\text{J}_1(\beta r_b)\big)\omega} \tag{8.50}$$

8.4.4.b) Electrical equations

The charge into the output ring electrode, Q_{out} is given by Gauss's law

$$Q_{\text{out}} = 2\pi\int_{r_b}^{a} D_{z_{\text{out}}} r\,\text{d}r \tag{8.51}$$

Substituting equations for T_r, T_θ, D_z (8.1)-(8.3), S_r (8.6) and S_θ (8.7) into Q_{out} (8.51) gives,

$$\begin{aligned} Q_{\text{out}} = \frac{-2\pi}{(1-\sigma)s_{11}^{\text{E}}}\int_{r_b}^{a}\Bigg[& d_{31}\left(-\frac{\partial u_{r_{\text{out}}}}{\partial r}r - u_{r_{\text{out}}}\right) \\ & + r\left(2d_{31}^2 + s_{11}^{\text{E}}\varepsilon_{33}^{\text{T}}(\sigma-1)\right)E_{z_{\text{out}}}\Bigg]\text{d}r \end{aligned} \tag{8.52}$$

The current into outer ring electrode is then given by,

$$I_{\text{out}} = \frac{\partial\big(Q_{\text{out}}e^{\text{j}\omega t}\big)}{\partial t} = j\omega Q_{\text{out}} \tag{8.53}$$

Substituting Q_{out} (8.52) into I_{out} (8.53), with $E_{z_{\text{out}}}$ (8.5) and u_r (8.50) gives an equation for the magnitude of the output current,

$$I_{\text{out}} = \frac{\text{j}\pi(a^2 - r_b^2)\left(2d_{31}^2 + s_{11}^{\text{E}}\varepsilon_{33}^{\text{T}}(\sigma-1)\right)\omega}{T(\sigma-1)s_{11}^{\text{E}}}V_{\text{out}} - \frac{2\pi d_{31}(r_b v_2 + a v_3)}{(1-\sigma)s_{11}^{\text{E}}} \tag{8.54}$$

As with the input dot section, using the A_{out} force factor allows (8.54) to be further simplified to,

$$I_{\text{out}} = j\omega C_{\text{out}} V_{\text{out}} + A'_{\text{out}}(r_b v_2 + a v_3) \tag{8.55}$$

where A'_{out} is defined as

$$A'_{\text{out}} = \frac{2\pi d_{31}}{(1-\sigma)s_{11}^{\text{E}}} \tag{8.56}$$

and the output capacitance is given by

$$C_{\text{out}} = \frac{\text{j}\pi(a^2 - r_b^2)\left(2d_{31}^2 + s_{11}^{\text{E}}\varepsilon_{33}^{\text{T}}(\sigma - 1)\right)}{T(\sigma - 1)s_{11}^{\text{E}}} \tag{8.57}$$

It's important to note the definition of A'_{out} in (8.56) differs from A_{in} in (8.18), as there are two edges to this section and therefore two velocities, which complicates the definition of A_{out}. This will be revisited in section 8.4.5.

8.4.4.c) Mechanical equations

Observing Fig. 8.8, the force F_2 acts inwards on the inner radius and F_3 acts inward on the outer radius of the outer ring section. These forces are given by,

$$F_2 = -2\pi r_b T_{r_{\text{out}}}(r_b) T \tag{8.58}$$

$$F_3 = -2\pi a T_{r_{\text{out}}}(a) T \tag{8.59}$$

Substituting T_r (8.1) into F_2(8.58) and F_3 (8.59), using $E_{z_{\text{out}}}$ (8.5), S_r (8.6) and S_θ (8.7) and the equation for the displacement of a particle in the outer ring section (8.50), gives equations for the forces F_2 and F_3,

$$F_2 = Z_4 v_2 + Z_5 v_3 + A'_{\text{out}} V_{\text{out}} r_b \tag{8.60}$$

$$F_3 = Z_5 v_2 + Z_6 v_3 + A'_{\text{out}} V_{\text{out}} a \tag{8.61}$$

where $Z_{4,5,6}$ are given by

$$Z_4 = \frac{2\mathrm{j}T\pi}{s_{11}^{\mathrm{E}}(\sigma^2 - 1)\omega} \frac{\begin{pmatrix}\big((\sigma - 1)\mathrm{Y}_1(\beta r_b) + r_b\mathrm{Y}_0(\beta r_b)\beta\big)\mathrm{J}_1(\beta a) \\ -\big((\sigma - 1)\mathrm{J}_1(\beta r_b) + \mathrm{J}_0(\beta r_b)r_b\beta\big)\mathrm{Y}_1(\beta a)\end{pmatrix}}{\mathrm{Y}_1(\beta a)\mathrm{J}_1(\beta r_b) - \mathrm{Y}_1(\beta r_b)\mathrm{J}_1(\beta a)} \tag{8.62}$$

$$Z_5 = \frac{4\mathrm{j}T}{s_{11}^{\mathrm{E}}\omega(\sigma^2 - 1)} \frac{1}{\mathrm{Y}_1(\beta a)\mathrm{J}_1(\beta r_b) - \mathrm{Y}_1(\beta r_b)\mathrm{J}_1(\beta a)} \tag{8.63}$$

$$Z_6 = \frac{2\mathrm{j}T\pi}{s_{11}^{\mathrm{E}}(\sigma^2 - 1)\omega} \frac{\begin{pmatrix}\big((\sigma - 1)\mathrm{Y}_1(\beta a) + a\mathrm{Y}_0(\beta a)\beta\big)\mathrm{J}_1(\beta r_b) \\ -\mathrm{Y}_1(\beta r_b)\big((\sigma - 1)\mathrm{J}_1(\beta a) + \mathrm{J}_0(\beta a)\beta a\big)\end{pmatrix}}{\mathrm{Y}_1(\beta a)\mathrm{J}_1(\beta r_b) - \mathrm{Y}_1(\beta r_b)\mathrm{J}_1(\beta a)} \tag{8.64}$$

8.4.4.d) Equivalent circuit

Similar to the inactive gap sections, several manipulations to the equations (8.60), (8.61) and (8.55) must be performed before a single equivalent circuit can be drawn. Firstly, similarly to [8.5], [8.7] we define,

$$F_2' = \frac{F_2}{r_b}, F_3' = \frac{F_3}{a}, v_2' = v_2 r_b, v_3' = v_3 a. \tag{8.65}$$

Therefore, (8.55) can be re-written as

$$I_{\mathrm{out}} = j\omega C_{\mathrm{out}} V_{\mathrm{out}} + A'_{\mathrm{out}}(v_2' + v_3'), \tag{8.66}$$

and (8.60) and (8.61) can be written as

$$F_2{}' = \frac{Z_4}{r_b^2} v_2' + \frac{Z_5}{r_b a} v_3' + A'_{\mathrm{out}} V_{\mathrm{out}} \tag{8.67}$$

$$F_3' = \frac{Z_5}{r_b a} v_2' + \frac{Z_6}{a^2} v_3' + A'_{\mathrm{out}} V_{\mathrm{out}} \tag{8.68}$$

As done in [8.8] the manipulations defined in (8.65) can be performed using ideal transformers. After performing a similar transformation to that which as used for the inactive gap section, a single equivalent circuit can be formed based on the forces in (8.67) and (8.68), this is shown in Fig. 8.9.

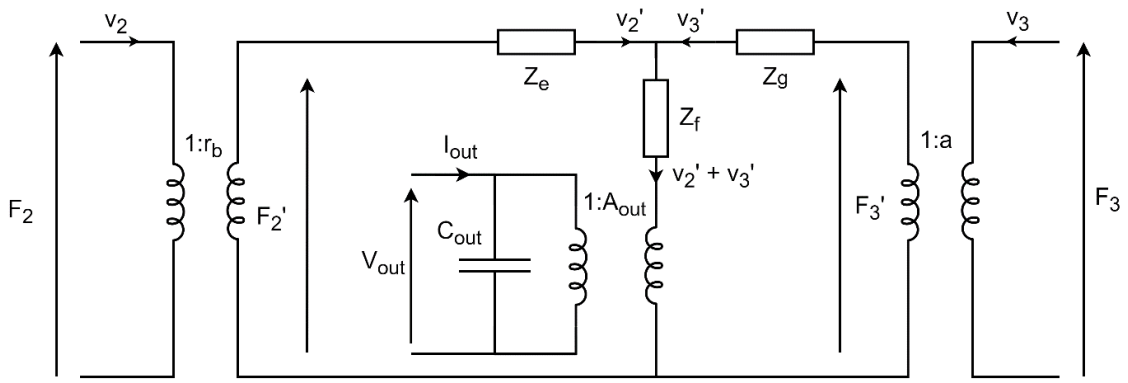

Fig. 8.9 – Equivalent circuit for the outer ring section

The transformed impedances $Z_{e,f,g}$ are defined as,

$$Z_e = \frac{Z_4}{r_b^2} - \frac{Z_5}{r_b a} = \frac{2\mathrm{j}T}{s_{11}^{\mathrm{E}}\omega(\sigma^2-1)r_b^2 a}\frac{\begin{pmatrix} a\pi\big((\sigma-1)\mathrm{Y}_1(\beta r_b)+r_b\mathrm{Y}_0(\beta r_b)\beta\big)\mathrm{J}_1(\beta a) \\ -a\pi\big((\sigma-1)\mathrm{J}_1(\beta r_b)+\mathrm{J}_0(\beta r_b)r_b\beta\big)\mathrm{Y}_1(\beta a)-2r_b \end{pmatrix}}{\mathrm{Y}_1(\beta a)\mathrm{J}_1(\beta r_b)-\mathrm{Y}_1(\beta r_b)\mathrm{J}_1(\beta a)} \tag{8.69}$$

$$Z_f = \frac{Z_5}{r_b a} = \frac{4\mathrm{j}T}{s_{11}^{\mathrm{E}}\omega(\sigma^2-1)r_b a}\frac{1}{\mathrm{Y}_1(\beta a)\mathrm{J}_1(\beta r_b)-\mathrm{Y}_1(\beta r_b)\mathrm{J}_1(\beta a)} \tag{8.70}$$

$$Z_g = \frac{Z_6}{a^2} - \frac{Z_5}{r_b a} = \frac{2\mathrm{j}T}{s_{11}^{\mathrm{E}}\omega(\sigma^2-1)a^2 r_b}\frac{\begin{pmatrix} r_b\pi\big((\sigma-1)\mathrm{Y}_1(\beta a)+a\mathrm{Y}_0(\beta a)\beta\big)\mathrm{J}_1(\beta r_b) \\ -r_b\pi\big((\sigma-1)\mathrm{J}_1(\beta a)+\mathrm{J}_0(\beta a)\beta a\big)\mathrm{Y}_1(\beta r_b)-2a \end{pmatrix}}{\mathrm{Y}_1(\beta a)\mathrm{J}_1(\beta r_b)-\mathrm{Y}_1(\beta r_b)\mathrm{J}_1(\beta a)} \tag{8.71}$$

8.4.5 Full equivalent circuit

Assuming the forces and velocities at the boundaries between sections are equal (i.e. $F_1 = F_{1g}, F_{2g} = F_2, v_1 = -v_{1g}, v_{2g} = -v_2$), the three equivalent circuits can be combined into a single equivalent circuit. Firstly, assuming the PT is free to vibrate (free vibration boundary condition), the force on the outer edge of the PT, F_3, is equal to 0. Applying this condition and simplifying gives the circuit shown in Fig. 8.10.

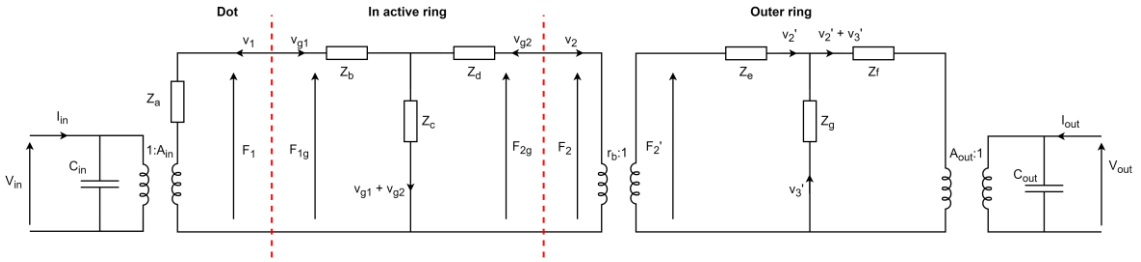

Fig. 8.10 – Full equivalent circuit for the ring-dot PT with $F_3 = 0$

The full equivalent circuit in Fig. 8.10 can now be simplified using several π to T and T to π circuit transformations, some manipulation and the Bessel function identity [8.8],

$$-\frac{2}{\pi} = X\big(\mathrm{J}_0(X)\mathrm{Y}_1(X) - \mathrm{J}_1(X)\mathrm{Y}_0(X)\big) \tag{8.72}$$

The full simplification process is derived in detail in Appendix 11.4. The resulting simplified equivalent circuit is shown in Fig. 8.11,

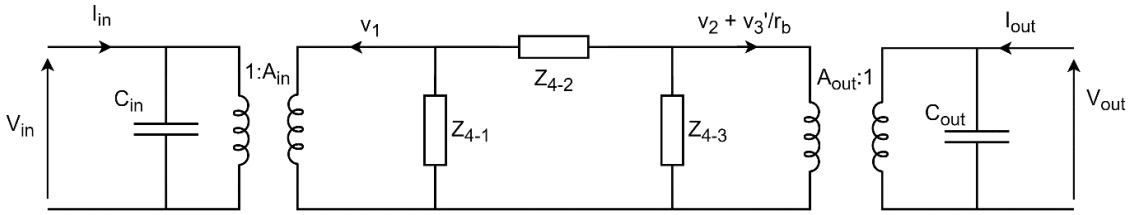

Fig. 8.11 – Simplified the ring-dot equivalent circuit

where impedances Z_{4-1}, Z_{4-2} and Z_{4-3} are defined in terms of the impedances Z_{a-g}

$$Z_{4-1} = \frac{\begin{pmatrix}\big(Z_g r_b^2\gamma + (Z_c+\lambda)\gamma - Z_c^2\big)Z_f \\ -Z_g\big((-Z_c-\lambda)\gamma + Z_c^2\big)\end{pmatrix}}{Z_g\lambda + Z_f\big(Z_g r_b^2 + Z_c + \lambda\big)} \tag{8.73}$$

$$Z_{4-2} = \frac{\begin{pmatrix}\Big(\big(Z_f+Z_g\big)Z_c + \big(Z_f r_b^2 + \lambda\big)Z_g + Z_f\lambda\Big)\gamma \\ -Z_c^2\big(Z_f+Z_g\big)\end{pmatrix}}{Z_g Z_c} \tag{8.74}$$

$$Z_{4-3} = \frac{\left(\begin{pmatrix}(-Z_f-Z_g)Z_c \\ +\big(-Z_f r_b^2 - \lambda\big)Z_g - Z_f\lambda\end{pmatrix}\gamma\right) r_b^2 \\ +Z_c^2\big(Z_f+Z_g\big)}{\big(-Z_g r_b^2 - Z_c - \lambda\big)\gamma + Z_c\big(Z_g r_b^2 + Z_c\big)} \tag{8.75}$$

and λ and γ are defined as

$$\gamma = Z_a + Z_b + Z_c \tag{8.76}$$

$$\lambda = Z_e r_b^2 + Z_d \tag{8.77}$$

And A_{out} is given by

$$A_{\text{out}} = A'_{\text{out}} r_b. \tag{8.78}$$

Substituting impedances Z_{a-g} ((8.24), (8.41)-(8.43), (8.69)-(8.71)) into Z_{4-1}, Z_{4-2} and Z_{4-3}, (8.73)-(8.75) with γ (8.76) and λ (8.77) gives the full expressions for $Z_{4-1,2,3}$ in terms of material and geometrical parameters. The resulting equations have been omitted due to length.

8.4.6 Simplifying the model to lumped form

The circuit shown in Fig. 8.11 could now be used to mathematically simulate the electrical behaviour of a ring-dot PT. However, the circuit is inconvenient to simulate, as each impedance cannot be represented using traditional electrical components as each impedance is in terms of Bessel functions. As a result, it is not possible to simulate such a circuit in software such as SPICE or by building a practical emulator for the circuit. Therefore, in this section, the circuit in Fig. 8.11 will be further simplified to a lumped equivalent circuit form, which can then be simulated and emulated using traditional electronic components.

8.4.6.a) Finding resonant frequencies

Observing the circuit in Fig. 8.11, when driven at the resonant frequency, owing to the π form of the equivalent circuit, the impedance of the three impedances should equal zero. This is not the case for the 'T' form of the circuit as shown in Fig. A.3.

Solving (8.73)-(8.75) equal to zero leads to the same equation for resonance for each of the impedances. The resulting equation for resonance is

$$\sigma\ -1 + \frac{\mathrm{J}_0(\beta a)\beta a}{\mathrm{J}_1(\beta a)} = 0 \tag{8.79}$$

The first positive solution (root) of (8.79) for βa is denoted R. Equation (8.79) is a transcendental equation and must be solved numerically. Using the first positive solution of R, the first radial resonant frequency of the PT can be found using,

$$\omega_0 = \frac{R}{\sqrt{s_{11}^{\mathrm{E}}\rho(1-\sigma^2)}\,a} \tag{8.80}$$

This agrees with the results reported by Horsley [8.5] for the radial mode Transoner PT. It is also notable that the resonant frequency is controlled exclusively by the outer radius of the device, and not by the internal radii.

8.4.6.b) Approximating equivalent circuit

To simplify the circuit in Fig. 8.11 to the traditional Mason equivalent form, an approximation method will be used. First, a Taylor expansion of each impedance in Fig. 8.11 will be performed around the first radial resonance. The first two elements in the Taylor series for each impedance are,

$$Z_{T4-1} \approx 0 + \frac{\chi}{\mathrm{J}_1\left(\frac{Rr_a}{a}\right)\tau R^2\left(r_b\mathrm{J}_1\left(\frac{Rr_a}{a}\right)+\psi\right)} \tag{8.81}$$

$$Z_{T4-2} \approx 0 - \frac{\chi}{R^2\psi\tau\mathrm{J}_1\left(\frac{Rr_\mathrm{a}}{a}\right)} \tag{8.82}$$

$$Z_{T4-3} \approx 0 + \frac{r_2\chi}{R^2\psi\tau\left(r_b\mathrm{J}_1\left(\frac{Rr_\mathrm{a}}{a}\right)+\psi\right)} \tag{8.83}$$

where ψ, τ and χ are defined as,

$$\psi = \mathrm{J}_1(R)a - \mathrm{J}_1\left(\frac{Rr_\mathrm{b}}{a}\right)r_b \tag{8.84}$$

$$\tau = (\sigma-1)\mathrm{Y}_1(R) + R\mathrm{Y}_0(R) \tag{8.85}$$

$$\chi = 4\mathrm{j}\rho r_b\left(\mathrm{J}_1\left(\frac{Rr_b}{a}\right)r_b+\psi\right)T(R^2+\sigma^2-1)a \tag{8.86}$$

Then, using the circuit transformation in [8.8] the circuit in Fig. 8.11, becomes that shown in Fig. 8.12.

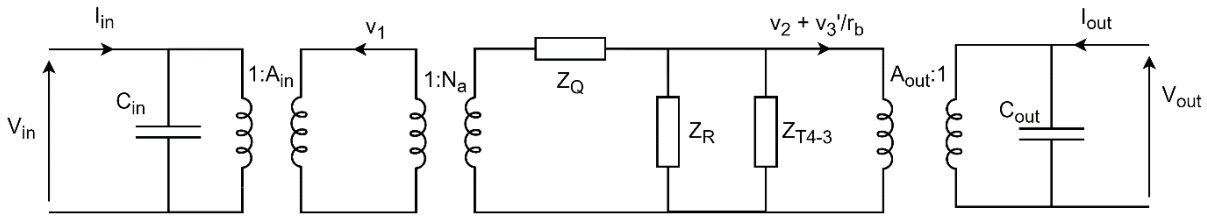

Fig. 8.12 – Simplified ring-dot equivalent circuit after circuit transformation defined in [8.8] is performed

Where impedances Z_R and Z_Q, and turns ratio N_a are given by,

$$Z_R = Z_{T4-1} + Z_{T4-2} \tag{8.87}$$

$$N_a = \frac{Z_R}{Z_{T4-1}} \tag{8.88}$$

$$Z_Q = \frac{Z_{T4-2}(Z_{T4-1} + Z_{T4-2})}{Z_{T4-1}} \tag{8.89}$$

The circuit in Fig. 8.12 can then be simplified by first recognising that,

$$Z_R + Z_{T4-3} = 0 \text{ and } Z_R Z_{T4-3} = \infty \tag{8.90}$$

Therefore, the parallel combination of Z_R and Z_{T4-3} tends to ∞, leaving only the Z_Q impedance. Then, the next obvious simplification to the circuit in Fig. 8.12, would be to combine $1{:}\,A_{\text{in}}$ and $1{:}\,N_a$ transformers. However, it is useful to be able to equate the resonant current in the equivalent circuit to the vibration velocity of the PT. While combining A_{in} and N_a would allow that, the resonant current would be equal to $v_2 + v_3'/r_2$ which is difficult to externally measure. Therefore, the remaining impedance, Z_Q, is referred across the $1{:}\,N_a$ transformer and then the $1{:}\,N_a$ transformer combines with the $A_{\text{out}}{:}\,1$. This simplification means the resonant current is equal to the vibration velocity, v_1 which can be measured at the outer edge of the inner-dot section. This is important as the vibration velocity is a key metric for analysing PTs [8.8]. The resulting circuit is shown in Fig. 8.13.

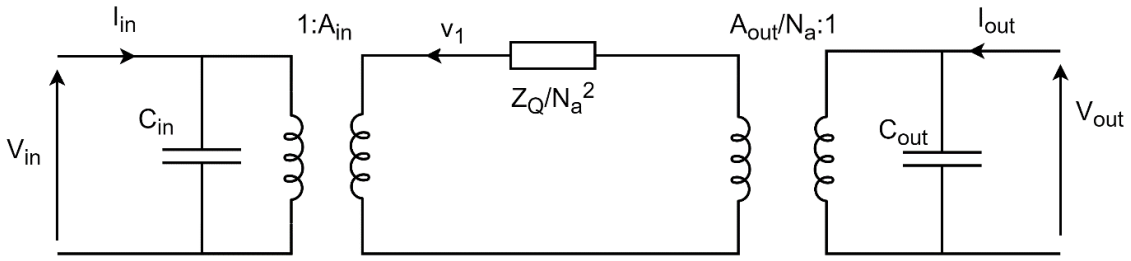

Fig. 8.13 – Fully simplified ring-dot equivalent circuit

Finally, to simplify the circuit in Fig. 8.13 to the Mason equivalent form, the impedance $\left(Z_Q/N_a^2\right)$, should be converted to an LC equivalent circuit. Firstly, the impedance of an LC circuit is defined as,

$$Z_{\mathrm{eq}} = \mathrm{j}\omega L_m - \frac{\mathrm{j}}{\omega C_m} \tag{8.91}$$

where L_m and C_m are the equivalent mechanical inductance and capacitance. Then, as done previously, a Taylor expansion of the equivalent impedance $\left(Z_{\mathrm{eq}}\right)$ is taken around the resonant frequency of the LC circuit $\left(\omega_0 = \frac{1}{\sqrt{L_m C_m}}\right)$, giving

$$Z_{Teq} \cong 0 + 2\mathrm{j}L_m(\omega - \omega_0) \tag{8.92}$$

Equating Z_{Teq} and Z_Q/N_a^2, using equations Z_{T4-1}, Z_{T4-2} and Z_{T4-3} (8.81)-(8.83), N_a (8.88) and Z_Q (8.89), and solving for L_m gives,

$$L_m = \frac{2Ta^2\rho(R^2 + \sigma^2 - 1)}{R^2} \frac{\mathrm{J}_1(R)}{\left((\sigma - 1)\mathrm{Y}_1(R) + R\mathrm{Y}_0(R)\right)\mathrm{J}_1\left(\frac{Rr_a}{a}\right)^2} \tag{8.93}$$

Then, to find C_m, the resonant frequency of the equivalent circuit is used. After substituting in (8.93) and (8.80) to $\left(\omega_0 = 1/\sqrt{L_m C_m}\right)$, and rearranging for C_m gives

$$C_m = \frac{s_{11}^{\mathrm{E}}(1 - \sigma^2)}{2T(R^2 + \sigma^2 - 1)} \frac{\left(R\mathrm{Y}_0(R) + \mathrm{Y}_1(R)\sigma - \mathrm{Y}_1(R)\right)\mathrm{J}_1\left(\frac{Rr_a}{a}\right)^2}{\mathrm{J}_1(R)} \tag{8.94}$$

8.4.6.c) Damping

In the Mason equivalent circuit model, it is typical to use a resistance in series with the LC circuit to model the losses in the system. The value of this damping resistance is influenced

by several factors, including material choice and PT design, but also the physical construction of the device. Therefore, it is difficult to estimate its value. It is common to estimate a value of damping resistance by measuring previous similar devices, made from similar materials. It is also common to define a Q factor for a device, rather than a specific damping resistance, therefore, the value of the damping resistance will be defined in terms of the Q factor of the radial mode in a ring-dot device. Firstly, the Q factor of a series RLC circuit is,

$$Q = \frac{1}{R_m}\sqrt{\frac{L_m}{C_m}} \tag{8.95}$$

where R_m is the damping resistance. Substituting (8.93) and (8.94) into (8.95) and rearranging for R_m gives,

$$R_m = \frac{2}{Q}\sqrt{-\frac{T^2 \mathrm{J}_1(R)^2 a^2 (R^2 + \sigma^2 - 1)^2 \rho}{\left(R\mathrm{Y}_0(R) + \mathrm{Y}_1(R)\sigma - \mathrm{Y}_1(R)\right)^2 R^2 \mathrm{J}_1\left(\frac{Rr_a}{a}\right)^4 s_{11}^{\mathrm{E}}(\sigma^2 - 1)}} \tag{8.96}$$

Using the newly defined L_m, C_m and R_m, the circuit in Fig. 8.13 can be simplified to that shown in Fig. 8.14.

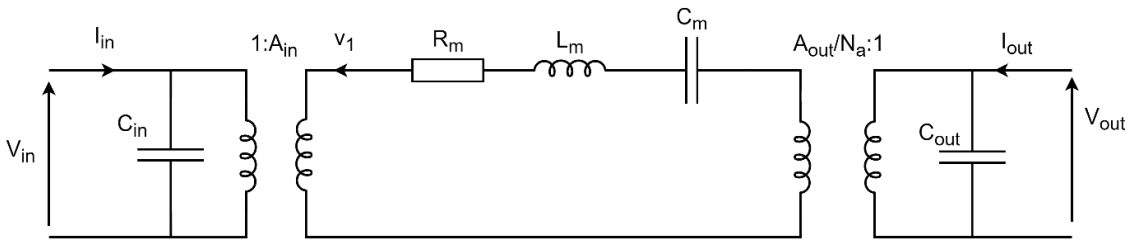

Fig. 8.14 – Ring-dot PT equivalent circuit model simplified to the classic Mason equivalent circuit form

8.4.6.d) Single transformer form

Whilst the circuit in Fig. 8.14 and accompanying equations allow a ring-dot PT to be simulated and emulated, it is often inconvenient to have two transformers in the circuit. This is because it is difficult to experimentally measure the A_{in} and A_{out} force factors and when emulating, it is more difficult to produce two transformers with almost 'ideal' characteristics than it is to produce one. Unless a direct relationship between the resonant current and the vibration velocity is required, it is more convenient to combine A_{in} and A_{out} transformers into a single transformer, N_1.

To achieve this, first the RLC circuit must be referred across the $1: A_{\text{in}}$ transformer. The resulting RLC components are given by

$$R_1 = \frac{R_m}{A_{\text{in}}^2} \tag{8.97}$$

$$L_1 = \frac{L_m}{A_{\text{in}}^2} \tag{8.98}$$

$$C_1 = C_m A_{\text{in}}^2 \tag{8.99}$$

Then combining $A_{\text{in}}, A_{\text{out}}$ and N_a gives N_1

$$N_1 = \frac{A_{\text{in}}}{\left(\frac{A_{\text{out}}}{N_a}\right)} = N_1 = -\frac{r_a \text{J}_1\left(\frac{Rr_a}{a}\right)}{\text{J}_1(R)a - r_b \text{J}_1\left(\frac{Rr_b}{a}\right)} \tag{8.100}$$

The final ring-dot PT equivalent circuit with a single transformer is shown in Fig. 8.15.

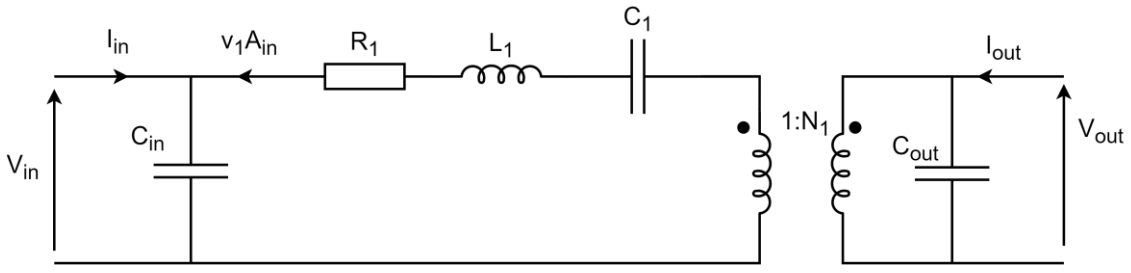

Fig. 8.15 – Single transformer form of the simplified ring-dot PT equivalent circuit

8.4.7 Extension to poled gap PTs

The lumped equivalent circuit model previously developed is for a device in which the 'gap' section of the PT was made from unpolled piezoelectric (i.e. an elastic, insulating material with the mechanical characteristics of the piezoelectric material). However, in many cases a fully poled disk will be used and as a result, this gap region will be poled. Therefore, the previous assumption that $E_z = 0$ in the gapped region, is no longer true. To address this, an equation for the electric field in the 'gap' section will be derived. Two equations for E_z will be derived, a constant E_z approximation between r_a and r_b and a non-linear E_z approximation between these radii.

8.4.7.a) Non-linear $\boldsymbol{E_z}$

Due to there being no electrodes in this region, $D_z = 0$. Setting the equation for the electric displacement field (8.3) equal to 0, then rearranging for $E_{z_{\text{gap}}}$ yields,

$$E_{z_{\text{gap}}} = \frac{\left(\frac{\partial u_{r_{\text{gap}}}}{\partial r} + \frac{u_{r_{\text{gap}}}}{r}\right) d_{31}}{s_{11}^{\text{E}} \varepsilon_{33}^{\text{T}} (\sigma - 1) + 2d_{31}^2} \tag{8.101}$$

Then, substituting $u_{r_{\text{gap}}}$ (8.50) into (8.101) gives,

$$E_{z_{\text{gap}}} = \frac{\text{j}d_{31}\beta \begin{pmatrix} \text{Y}_0(r\beta) v_{2g} \text{J}_1(\beta r_a) + \text{Y}_0(r\beta) v_{1g} \text{J}_1(\beta r_b) \\ -\big(\text{Y}_1(\beta r_a) v_{2g} + \text{Y}_1(\beta r_b) v_{1g}\big) \text{J}_0(r\beta) \end{pmatrix}}{\big(-\text{Y}_1(\beta r_a)\text{J}_1(\beta r_b) + \text{J}_1(\beta r_a)\text{Y}_1(\beta r_b)\big)\omega(\varepsilon_{33}^{\text{T}}(\sigma - 1)s_{11}^{\text{E}} + 2d_{31}^2)} \tag{8.102}$$

8.4.7.b) Constant $\boldsymbol{E_z}$

A second, greatly simplified, equation for E_z is also derived. This time starting with Gauss's equation and setting charge in this region equal to 0,

$$Q = 2\pi \int_{r_a}^{r_b} D_{z_{\text{gap}}} r \, dr = 0 \tag{8.103}$$

Then, substituting in (8.3), evaluating the integral and rearranging for $E_{z_{\text{gap}}}$ gives

$$E_{z_{\text{gap}}} = -\frac{2\text{j}d_{31}\big(r_a v_{1g} + r_b v_{2g}\big)}{\omega(\varepsilon_{33}^{\text{T}}(\sigma - 1)s_{11}^{\text{E}} + 2d_{31}^2)(r_a^2 - r_b^2)} \tag{8.104}$$

Using these two definitions of $E_{z_{\text{gap}}}$, with equations F_{1g} (8.34) and F_{2g} (8.35) allows impedances $Z_{b,c,d}$ to be calculated for a fully polled ring-dot PT. However, these new solutions for $Z_{b,c,d}$ have been omitted due to length. Additionally, this added complexity means the full simplification process can no longer be performed analytically using the newly derived impedances. Therefore, to evaluate the accuracy of these new impedances, an equation for the input impedance of the circuit in Fig. 8.10 will be derived, allowing the input impedance of a PT to be estimated using this newly derived impedances and thus then compared to either FEA simulated results or experimental measurements of the PT.

First, an equation for the input impedance of the ring-dot PT with the output terminal shorted, is derived. Based on the circuit in Fig. 8.10, the input impedance with the output terminals shorted is given by (8.105).

$$Z_{\text{in}} = \frac{\left(-r_b^2(Z_c - \gamma - \lambda)Z_g - Z_c^2 + \gamma Z_c + \gamma\lambda\right)Z_f - Z_g(Z_c^2 - Z_c\gamma - \gamma\lambda)}{A_{\text{in}}^2\left(Z_f\left(Z_g r_b^2 + Z_c + \lambda\right) + Z_g(Z_c + \lambda)\right)} \tag{8.105}$$

Then, using (8.105) with the newly defined impedances $Z_{b,c,d}$ calculated for both non-linear and constant $E_{z_{\text{gap}}}$ approximations, along with impedances $Z_{a,e,f,g}$ (8.24), (8.69)-(8.71) and A_{in} (8.18) allow the input impedance of the ring-dot PT with a poled 'gap' region to be simulated.

8.5 Simulation and experimental validation of multiple radial mode ring-dot PT equivalent circuit models

Validation of the models generated here will be in 2 parts. Initially, COMSOL will be used to simulate several ideal devices, the equivalent circuit components extracted and compared to those generated by the various models. Finally, the various models will be validated against experimental PT data.

8.5.1 Comparison to FEA

To provide a baseline measurement of the accuracy of the model derived here, COMSOL will be used to simulate several ring-dot PTs. For each PT, the equivalent circuit parameters will be estimated using the equivalent circuit model derived. These estimated parameters will then be compared to component values extracted from impedance measurements taken in COMSOL using method 3 from Chapter 3.

For this simulation, a frequency domain study was used to simulate devices with dimensions $a = 8\text{ mm}$, $1\text{mm} < r_a < 7\text{ mm}$, $1.5\text{ mm} < r_b < 7.5\text{ mm}$ and $0.5\text{mm} < T < 1.5\text{ mm}$. PZT-4 material was used with parameters given in Table 8.1. In the inactive section of the PT, the same material is used; however, it is treated as an elastic material with electrostatics and solid mechanics decoupled. The PZT in this section acts as an elastic, electrically insulting material.

Table 8.1 – PZT 4 material properties

$s_{11}^{\mathrm{E}}\ (\mathrm{m^2/N})$	ε_r	$d_{31}(\mathrm{m/V})$	σ	$\rho\ (\mathrm{kg/m^3})$
$1.23x10^{-11}$	1300	$1.23x10^{-10}$	0.329	7500

For each PT, L_1, C_1, C_{in} and N_1 were all extracted from the frequency domain COMSOL analysis input impedance data using method 3 presented in Chapter 3. Then, the same parameters are estimated using the model derived in this chapter, using equations C_{in} (8.20), L_1 (8.98), C_1 (8.99) and N_1 (8.100). The parameters estimated from the model derived here are compared to the extracted parameters from COMSOL and the percentage error (7.2) calculated. The results of this analysis are shown in Table 8.2.

Table 8.2 – Average error and standard deviation in the estimated parameters

Parameter	Average Error (%)	Standard Deviation (%)
L_1	1.6192	1.7770
C_1	1.4094	1.5837
N_1	1.0812	1.1582
C_{in}	54.3844	35.8875
C_{out}	47.7010	21.2229

Observing the results, the equivalent circuit model accurately estimates L_1, C_1 and N_1 across the range of tested values, with an average of less than 2% error in each of the three parameters.

The results also show that both the estimated C_{in} and C_{out} values show significant error in most devices. However, this can be attributed to inaccuracies in the measurement of these parameters, as the measured value is a combination of C_{in} (or C_{out}) and an additional capacitance between the input and output electrodes $C_{\mathrm{dot-ring}}$. This is discussed later in section 8.5.3. It should be noted that the accuracy of C_{out} is slightly greater than C_{in}, this can be attributed to C_{out} being around 2.9x larger on average than C_{in}, therefore, $C_{\mathrm{dot-ring}}$ has a smaller (but still significant) impact on the measurement of C_{out} compared to C_{in}.

8.5.2 Effect of assumptions

As discussed during the derivation, several assumptions have been made to allow simplified models to be created. The following section will evaluate the models derived here against various COMSOL simulations to analyse the impact of these assumptions.

8.5.2.a) Thin PT with elastic inactive section

The main assumptions that were made during the derivation were that the PT followed Kirchhoff's thin plate model (radius >> thickness of disc) and that $E_z = 0$ in the gap section. To get a baseline for how accurate the model is, in this first section a PT is simulated which agrees with these assumptions. The dimensions of the sample 'thin' ring-dot PT are given in Table 8.3.

Table 8.3 – 'Thin' PT dimensions

r_a (mm)	r_b(mm)	a(mm)	T(mm)
3	5	8	0.1

A COMSOL 2D axisymmetric study was used to model this PT, which is made from PZT-4 material with material properties given in Table 8.1, with an elastic 'gap' region. The input impedance of the PT was simulated, and the equivalent components extracted using method 3 presented in Chapter 3. Then, the equivalent parameters of the PT were estimated using the model derived here. The equivalent components were calculated using equations (8.20) C_{in}, (8.98) L_1 and (8.99) C_1.

Additionally, it is also important to consider the impact the Taylor approximation, that was performed during section 8.4.6.b), has on the accuracy of the fully simplified model. Therefore, the input impedance of the PT without the Taylor expansion can be estimated using equation (8.105). Then, similar to the COMSOL impedance data, the equivalent circuit parameters can be extracted using method 3 presented in Chapter 3. This will give us non-approximated values for each of the parameters as estimated by the model.

For ease of comparison between the model derived here and the COMSOL simulated data, its beneficial to plot the impedance responses. To achieve this, an expression for the input impedance of the PT can be derived (see Chapter 3), this is defined as,

$$Z_{\text{in}} = \frac{\text{j} - \text{j}C_1 L_1 \omega^2}{\omega(C_1 C_{\text{in}} L_1 \omega^2 - C_1 - C_{\text{in}})} \tag{8.106}$$

Then, by substituting the estimated values from the approximate (after Taylor expansion) model derived here the input impedance can be simulated and compared to that extracted from the COMSOL simulation and that derived using equation (8.105) (non-approximated). The results of this analysis are shown in Fig. 8.16 and Table 8.4.

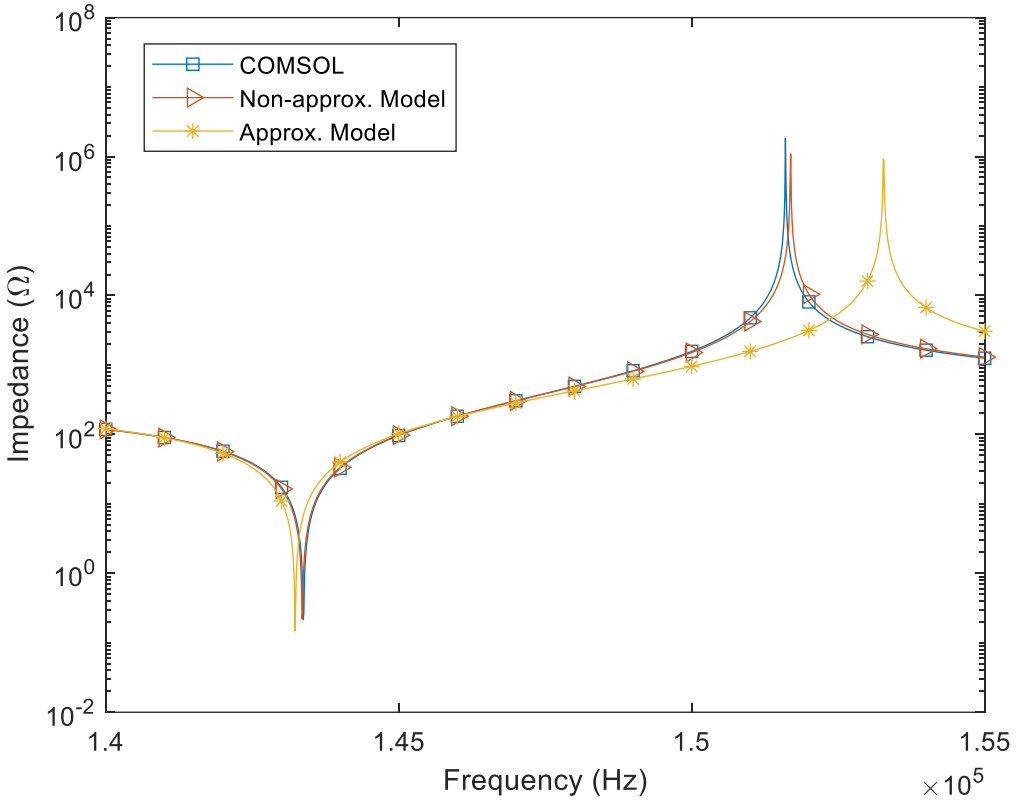

Fig. 8.16 – Simulated and estimated input impedance of the thin PT with elastic in-active section

Table 8.4 – Simulated and estimated parameters of the thin PT with elastic in-active section

	L_1(mH)		C_1(pF)		C_{in}(nF)	
COMSOL	3.82		322.4		2.73	
	mH	**% error**	**pF**	**% error**	**nF**	**% error**
Non-approximated	3.82	0%	322.9	0.2%	2.70	1.1%
Approximate	3.84	0.5%	321.9	0.3%	2.22	19.4%

As Fig. 8.16 shows, both models have very good agreement to the COMSOL simulation around the series resonance. However, at the anti-resonance frequency (peak in the impedance curve) the approximate model has some error when compared to COMSOL. Observing Table 8.4, we can see that this error originates from error in C_{in}, with a 19% error in the estimated value, compared to the 1% error in the non-approximated model. However, both models provide very accurate estimates of L_1 and C_1 showing an average of 0.1% and 0.3% error for the non-approximated and approximate models, respectively.

8.5.2.b) Thicker PT with elastic inactive section

Next, the effect of in-validating Kirchhoff's thin plate assumptions is examined. For this, the PT under test will still have an 'elastic' inactive section, but the thickness of the PT will be increased by an order of magnitude. The 'moderately-thick' ring-dot PT dimensions are given in Table 8.5.

Table 8.5 – 'Moderately-thick' PT dimensions

r_a (mm)	r_b(mm)	a(mm)	T(mm)
3	5	8	1

A similar frequency domain study was performed in COMSOL. Again, both approximate and non-approximated models are used to estimate the equivalent circuit parameters of the PT using the same method as described previously. The results of this analysis are shown in Fig. 8.17 and Table 8.6.

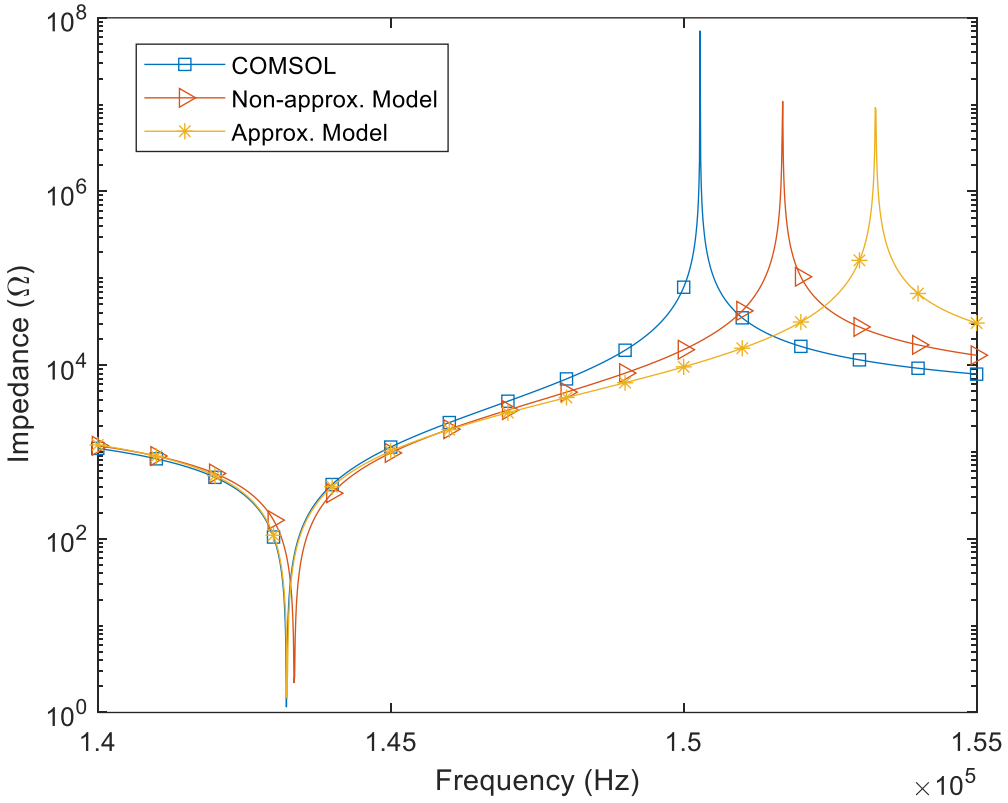

Fig. 8.17 – Simulated and estimated input impedance of the moderately-thick PT with elastic in-active section

Table 8.6 – Simulated and estimated equivalent parameters of the thick PT with elastic in-active section

	L_1(mH)		C_1(pF)		C_{in}(nF)	
COMSOL	38.6		32.0		0.32	
	mH	**% error**	**pF**	**% error**	**nF**	**% error**
Non-approximated	38.2	1.0%	32.3	0.9%	0.27	15.6%
Approximate	38.4	0.5%	32.2	0.625%	0.22	31.3%

As Table 8.6 shows, the results are similar to the previous analysis with good accuracy in L_1 and C_1 but poor accuracy when estimating the value of C_{in} for both non-approximated and approximate models. As a result of the increased thickness, the overall error has also increased. Whilst L_1 and C_1 have an average error of less than 1% for both the non-approximated and approximate models, respectively, C_{in} error has greatly increased in both models with the non-approximated model still being slightly more accurate than the

approximate model, with errors of 16% and 31%, for the non-approximated and approximate models respectively. The increased C_{in} error is likely due to fringing effects accentuated by the increased thickness and the impact of an additional capacitance between input and output electrodes which as discussed previously, has not been included in this model.

8.5.2.c) Thin PT with piezoelectric in-active section

The next simulation will look at the effect of having a polled piezoelectric gap section in the PT. For this, the same 'thin' PT will be used (Table 8.3), however, the in-active section will now include full piezoelectric coupling between solid mechanics and electrostatic physics in COMSOL. The two additional models that were developed in the 8.4.7 section will also be included in the results as they account for the polled 'gap' section. The method of extracting the equivalent circuit values using these additional methods is identical to the non-approximated method described previously, however, with the new definitions for impedances $Z_{b,c,d}$. The results of this simulation are shown in Fig. 8.18 and Table 8.7.

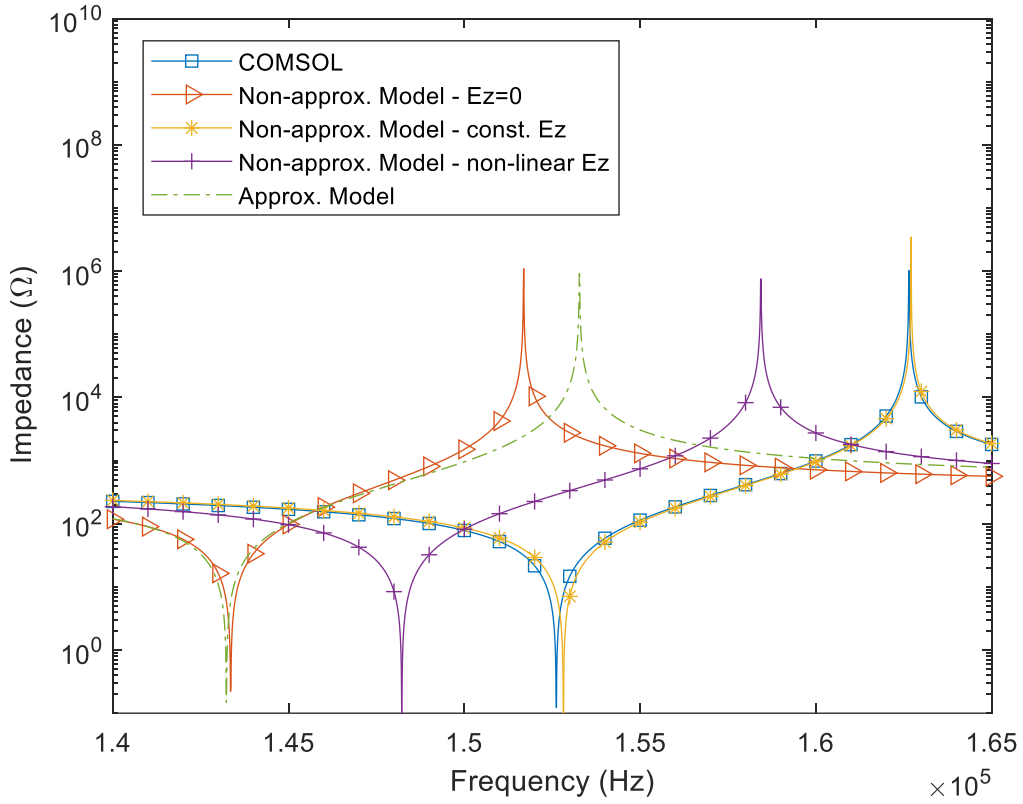

Fig. 8.18 – Simulated and estimated input impedance of the thin PT with piezoelectric in-active section

Table 8.7 – Simulated and estimated parameters of the thin PT with piezoelectric in-active section

		L_1(mH)		C_1(pF)		C_{in}(nF)	
COMSOL		2.95		369.2		2.72	
		mH	**% error**	**pF**	**% error**	**nF**	**% error**
$E_z = 0$	Non-approximated	3.82	29.5%	322.9	12.5%	2.70	0.7%
	Approximate	3.84	30.2%	321.9	12.8%	2.22	18.4%
Constant E_z		3.05	3.4%	355.8	3.6%	2.66	2.2%
Non-linear E_z		3.06	3.7%	376.9	2.1%	2.64	2.9%

Observing the results in Table 8.7, the models with $E_z = 0$ give inaccurate results for this PT, as expected. Both models overestimate the value of L_1 and C_1, with an average of up to 22% error across the 3 estimated parameters. However, the non-approximated model is still able to accurately estimate the value of C_{in}. On the other hand, both of the $E_z \neq 0$ models accurately estimate all three parameters. Achieving 4% and 3% average error for the constant E_z and non-linear E_z respectively. Therefore, if a ring-dot PT is made from a fully polled piezoelectric disc, then it is beneficial to use one of the methods developed in section 8.4.7 when estimating parameters.

8.5.2.d) Thicker PT with piezoelectric inactive section

The final simulation will examine the effect of a 'thick' PT made with a polled 'gap' section. The 'thick' PT will be used with dimensions given in Table 8.5. The 'gap' section of the PT will again have full piezoelectric coupling. Again, all 4 models will be compared to the simulated results using the same methods as described previously. The results of this simulation are shown in Fig. 8.19 and Table 8.8.

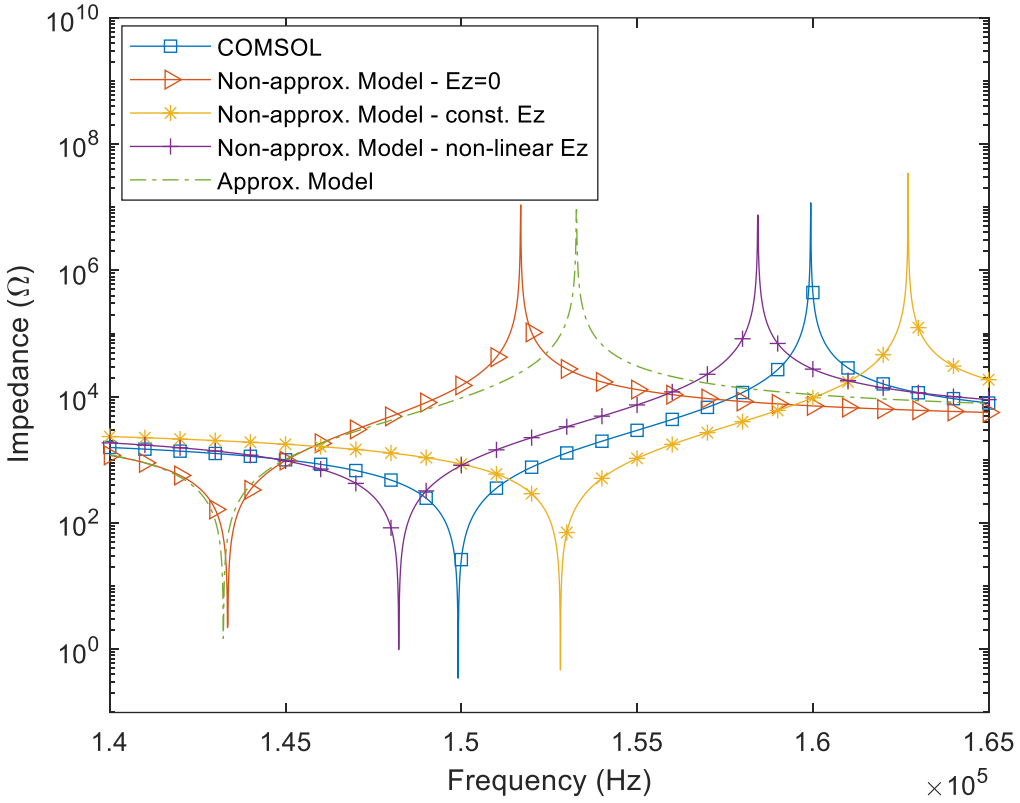

Fig. 8.19 – Measured and estimated input impedance of the thick PT with piezoelectric in-active section

Table 8.8 – Measured and estimated parameters of the thick PT with piezoelectric in-active section

		L_1(mH)		C_1(pF)		C_{in}(nF)	
COMSOL		23.4		48.2		0.35	
		mH	**% error**	**pF**	**% error**	**nF**	**% error**
$E_z = 0$	Non-approximated	38.2	63.2%	32.3	33.0%	0.27	22.9%
	Approximate	38.4	64.1%	32.2	33.2%	0.22	37.1%
Constant E_z		30.5	30.3%	35.6	26.1%	0.27	22.9%
Non-linear E_z		30.6	30.8%	37.7	21.8%	0.26	25.7%

As the results in Table 8.8 show, all methods have significant errors when estimating the parameters of this PT. However, the $E_z \neq 0$ methods show significantly less error than the $E_z = 0$ methods. However, with an average error of 26.6% and 26.1% error for the constant E_z and the non-linear E_z respectively, the percentage error is still large. This shows the

limitations of the approximated E_z model in the gap region for thick devices. Therefore, to be able to achieve more accurate parameter estimations for these devices, a full 3D analysis would need to be performed.

8.5.3 Impact of input-output capacitance

Owing to the 'gap' region between the input and output section, there is a capacitance generated between the input and output electrodes. Estimating this capacitance is a difficult process and has been analysed for similar devices in [8.9], [8.10]. The impact of this capacitance in the operation of a ring-dot PT is beyond the scope of this analysis, however, one clear issue with this capacitance is that it affects the measurement of the input and output capacitance. An equivalent circuit for the ring-dot PT with this additional capacitance is shown in Fig. 8.20.

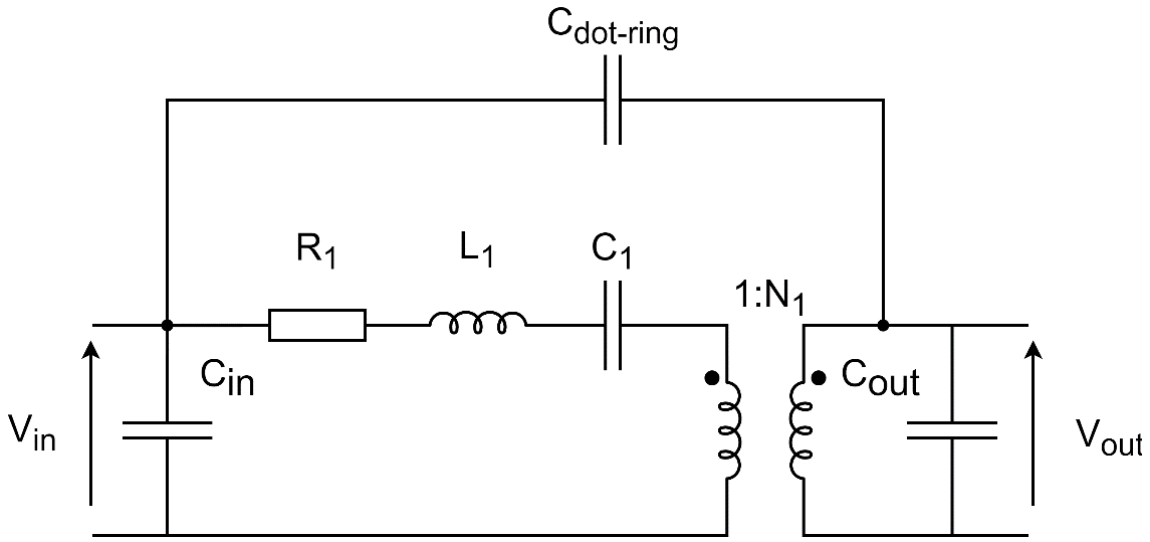

Fig. 8.20 – Mason equivalent circuit with an additional capacitance between input and output electrodes

Typically, the input and output capacitances are measured with the output and input shorted, respectively. However, observing Fig. 8.20, this additional capacitance is then in parallel with the C_{in} (or C_{out}) capacitor, therefore, falsely inflating the apparent input (or output) capacitance value during measurement. This could cause even greater problems in high damping equivalent circuit extraction methods that require accurate C_{in} measurements as shown in Chapter 3.

To investigate the typical size of this capacitance, a COMSOL simulation was used. Extracting this capacitance is non-trivial as measuring directly across the input-output electrodes would

excite the resonant circuit, thus affecting the measurement. Therefore, a similar method to that presented in method 2 presented in Chapter 3 will be used.

In the method described in Chapter 3, the amplitude of the output voltage is set to a value equal to $N_1 V_{\text{in}}$, this forces the voltage across the RLC circuit to equal zero during measurement, removing the influence of the RLC circuit on the measurement of C_{in}. However, whilst using this method in this scenario would cause the voltage across the RLC to equal 0, the voltage across the $C_{\text{dot-ring}}$ capacitance would then be equal to $V_{C_{\text{inout}}} = V_{\text{in}} - N_1 V_{\text{in}}$. Even a PT with $N_1 = 1$, will also not ensure $V_{C_{\text{inout}}} = 0$ (and thus allowing measurement of C_{in} or C_{out} without its influence), as the ideal (1:N_1) transformer causes a 180° phase shift in the signal.

Setting $V_{\text{out}} = N_1 V_{\text{in}}$, means the measured value of C_{in} is equal to,

$$C_{\text{in-measured}_{V_{\text{out}}=N_1 V_{\text{in}}}} = C_{\text{in}} + (1 - N_1) C_{\text{dot-ring}} \tag{8.107}$$

as the voltage across $V_{C_{\text{inout}}} = V_{\text{in}} - N_1 V_{\text{in}}$. However, it is not possible to separate the value of each individual capacitance from this measurement alone. Therefore, a second measurement is used. A capacitance measurement with the output shorted taken at low frequency (1kHz) gives a measured capacitance approximately equal to,

$$C_{\text{in-measured}_{\text{Output short}}} \approx C_{\text{in}} + C_{\text{dot-ring}} + C_1 \tag{8.108}$$

as at 1kHz the RLC impedance $\approx 1/j\omega C_1$ $\left(X_{L_1} \approx 0,\ R_1 \approx 0\right)$. Subtracting the $C_{\text{in-measured}_{V_{\text{out}}=N_1 V_{\text{in}}}}$ from $C_{\text{in-measured}_{\text{Output short}}}$ then gives,

$$-N_1 C_{\text{dot-ring}} - C_1 \approx \left(C_{\text{in-measured}_{V_{\text{out}}=N_1 V_{\text{in}}}} - C_{\text{in-measured}_{\text{Output short}}}\right) \tag{8.109}$$

If a separate method is used to find C_1 such as method 3 presented in Chapter 3, then $C_{\text{dot-ring}}$ can be calculated using,

$$C_{\text{dot-ring}} \approx \frac{\left(C_{\text{in-measured}_{V_{\text{out}}=N_1 V_{\text{in}}}} - C_{\text{in-measured}_{\text{Output short}}}\right) + C_1}{-N_1} \tag{8.110}$$

Using COMSOL, the relevant measurements can be performed on the previous 4 PTs. The $C_{\mathrm{dot-ring}}$ values for each PT estimated using (8.110) are shown in Table 8.9.

Table 8.9 – Estimated $C_{dot-ring}$ capacitance values, along with improved measurements of C_{in}

PT	$C_{\mathrm{in-measured}_{V_{\mathrm{out}}=N_1 V_{\mathrm{in}}}}$ $(\mathbf{nF})$	$C_{\mathrm{in-measured}_{\text{Output short}}}$ $(\mathbf{nF})$	C_1 $(\mathbf{nF})$	N_1	$C_{\mathrm{dot-ring}}$ $(\mathbf{nF})$	C_{in} $(\mathbf{nF})$
1	2.8725	2.9869	0.322	-0.546	0.380	2.28
2	0.34059	0.34199	0.032	-0.545	0.056	0.254
3	2.9059	3.0253	0.369	-0.573	0.436	2.22
4	0.39289	0.38914	0.048	-0.590	0.088	0.253

Observing the results in Table 8.9, the value of $C_{\mathrm{dot-ring}}$ is typically around an order of magnitude smaller than C_{in} (or C_{out}). Whilst the typical value of $C_{\mathrm{dot-ring}}$ in these PTs are comparatively small it is still likely to have an impact on performance. Although the impact of this capacitance has yet to be fully investigated, it is unlikely that this capacitance will have major effect on zero voltage switching (ZVS) performance of the PT but may affect the output voltage and power that a PT can achieve. It should also be noted that whilst a full examination of this capacitance is beyond the scope of this analysis, we can see that this capacitance is controlled by the thickness of the PT but will also most likely also be controlled by the size of the in-active region $(r_b - r_a)$. The C_{in} values in Table 8.9 can then be compared to the estimated C_{in} values using the various models, as shown in Table 8.10.

Table 8.10 – Error in estimated C_{in} value

		PT 1		PT 2		PT 3		PT 4	
C_{in}		2.28nF		0.254nF		2.22nF		0.253nF	
		nF	% **error**	**nF**	% **error**	**nF**	% **error**	**nF**	% **error**
$E_z = 0$	Non-approximated	2.70	18.4%	0.27	6.3%	2.70	21.6%	0.27	6.7%
	Approximate	2.22	2.6%	0.22	13.4%	2.22	0%	0.22	13.0%
Constant E_z						2.66	19.8%	0.27	6.7%
Non-linear E_z						2.64	18.9%	0.26	2.8%

Firstly, Table 8.10 shows that the approximate model is the most accurate in PTs with both elastic and piezoelectric in-active regions, when the PT is thin. This seems to suggest that at larger PT thicknesses there are more fringing affects, effecting the measured C_{in} value.

Whereas in the 3 other models (non-approximated models), the value of C_{in} is very accurately estimated for the thicker PT, so it is clear the fringing affects are accounted for in the higher order components of the impedances included in the non-approximated models. However, in the thinner PTs the non-approximated models seem to overestimate the fringing, leading to overestimated values of C_{in}. Overall, all methods provide acceptable estimates for C_{in}.

8.5.4 Practical PT validation

The PT models generated here will be validated against the ring-dot PT presented in [8.1]. The PT is made from KNN lead-free piezoelectric, with $r_a = 5.5\text{mm}$, $r_b = 6.75\text{mm}$, $a = 17.1\text{mm}$ and $T = 1.9\text{mm}$. The relevant material properties for the KNN material are shown in Table 8.11. It should be noted that the PT in [8.1] uses the inner dot electrode as an output and the outer ring electrode as an input; however, by swapping input and output measurements in [8.1], the results will directly comparable to the ring-dot PT that was modelled in this paper.

Table 8.11 – KNN material properties

$s_{11}^{\mathrm{E}}\ (\mathrm{m^2/N})$	$\varepsilon_r^{\mathrm{T}}$	$d_{31}(\mathrm{m/V})$	σ	$\rho\ (\mathrm{kg/m^3})$	Q
$6.91x10^{-12}$	300	$-33x10^{-12}$	0.27	4650	1500

The equivalent circuit parameters are estimated using various models presented here using the methods described in the previous section. The resulting equivalent circuit components and percentage errors are shown in Table 8.12.

Table 8.12 – Measured and estimated parameters and resulting percentage errors of the PT in [8.1]

		$L_1(\mathrm{mH})$		$C_1(\mathrm{pF})$		$F_1\ (\mathrm{kHz})$		$C_{\mathrm{in}}(\mathrm{nF})$		N_1	
		(mH)	% error	(pF)	% error	(kHz)	% error	(nF)	% error	N_1	% error
[8.1]		374.2	-	5.946	-	106.7	-	0.159	-	-0.26	-
$E_z = 0$	**Non-approximated**	426.0	13.8	4.96	16.6	109.5	2.62	0.122	23.3	-0.23	11.5
	Approximate	424.6	13.3	4.98	16.2	109.5	2.62	0.111	30.2	-0.23	11.5
Constant E_z		415.2	11.0	5.00	15.9	110.4	3.47	0.122	23.3	-0.23	11.5
Non-linear E_z		412.3	10.2	5.05	15.1	110.2	3.28	0.122	23.3	-0.23	11.5

Observing Table 8.12, the models accounting for $E_z \neq 0$ are most accurate in this case as they account for the piezoelectric gap region, showing an average error of 16.7% and 16.2% for the constant and non-linear E_z models, respectively. The models accounting for $E_z \neq 0$ have lower accuracy in this analysis, this is likely because of the full-face ground electrode in this PT, which changes the electric field generated across the in-active piezoelectric region. All the models show high C_{in} error, this is because the measured value in [8.1] is the combination of C_{in} and $C_{\mathrm{dot-ring}}$. Therefore, it's likely the real C_{in} value will be smaller than that presented in [8.1] and as a result the real C_{in} will be much closer to that predicted by these models. Finally, the turn ratio estimations show acceptable accuracy compared to that published in [8.1]. It should be noted that as the method of component extraction from the measured PT data is not known, the accuracy of the parameters published in [8.1] is therefore not known.

8.6 Summary

An equivalent circuit model has been presented for the radial vibration modes occurring in the ring-dot PT, using Kirchhoff plate theory. This model includes the effects of the 'gap' section of the device on the equivalent circuit and investigates several models for this section of the device. Finally, the model is verified against simulated and experimental measurements. In the following chapters, this model will be used to design high temperature PTs and will be used as parts of an automated PT design algorithm.

8.7 References

[8.1] M. Guo, D. M. Lin, K. H. Lam, S. Wang, H. L. W. Chan, and X. Z. Zhao, 'A lead-free piezoelectric transformer in radial vibration modes', *Review of Scientific Instruments*, vol. 78, no. 3, p. 035102, Mar. 2007, doi: 10.1063/1.2712795.

[8.2] E. Ventsel and T. Krauthammer, *Thin plates and shells: theory, analysis, and applications*. New York: Marcel Dekker, 2001.

[8.3] J. N. Reddy, *Theory and analysis of elastic plates*. Philadelphia, PA: Taylor & Francis, 1999.

[8.4] T. Ikeda, *Fundamentals of piezoelectricity*. Oxford ; New York: Oxford University Press, 1990.

[8.5] E. L. Horsley, A. V. Carazo, M. P. Foster, and D. A. Stone, 'A Lumped Equivalent Circuit Model for the Radial Mode Piezoelectric Transformer', in *2009 Twenty-Fourth Annual IEEE Applied Power Electronics Conference and Exposition*, Feb. 2009, pp. 1747–1753. doi: 10.1109/APEC.2009.4802906.

[8.6] Q. Wang, S. T. Quek, C. T. Sun, and X. Liu, 'Analysis of piezoelectric coupled circular plate', *Smart Mater. Struct.*, vol. 10, no. 2, p. 229, 2001, doi: 10.1088/0964-1726/10/2/308.

[8.7] S. Lin, 'Study on the radial composite piezoelectric ceramic transducer in radial vibration', *Ultrasonics*, vol. 46, no. 1, pp. 51–59, Mar. 2007, doi: 10.1016/j.ultras.2006.10.005.

[8.8] E. Horsley, 'Modelling and Analysis of Radial Mode Piezoelectric Transformers and Inductor-less Resonant Power Converters', University of Sheffield, 2011.

[8.9] T. Chen and N. Bowler, 'Analysis of a concentric coplanar capacitive sensor for nondestructive evaluation of multi-layered dielectric structures', *IEEE Transactions on Dielectrics and Electrical Insulation*, vol. 17, no. 4, pp. 1307–1318, Aug. 2010, doi: 10.1109/TDEI.2010.5539703.

[8.10] H. Nishiyama and M. Nakamura, 'Capacitance of disk capacitors', *IEEE Transactions on Components, Hybrids, and Manufacturing Technology*, vol. 16, no. 3, pp. 360–366, May 1993, doi: 10.1109/33.232065.

Chapter 9 - BSPT-based high temperature PTs

9.1 Introduction

As discussed in Chapter 2, owing to the difficultly in designing ring-dot PTs and PTs in general, they have seen few commercial applications. Additionally, even a slight performance improvement over magnetic transformers in typical applications does not warrant their use over traditional magnetic devices, given the additional complexity in designing PTs. However, given the unique properties of PTs, there are several applications where PTs are more suitable than traditional electronics, one of which is in high temperature environments.

In the previous chapter, a lumped equivalent circuit model for the ring-dot PT was presented. This chapter will utilize this model to design a bismuth scandium lead titanate (BSPT) based ring dot PT for use in high temperature resonant converter applications. A BSPT PTs will be fabricated and characterised using impedance and equivalent circuit extraction methods. Additionally, a similar PZT-based PT will also be fabricated and tested for comparison. Then, both PTs will be used as part of a half-bridge resonant inverter, allowing evaluation of the performance of each PT in a typical converter application at high temperatures.

9.2 High temperature PTs

9.2.1 Bismuth Scandium Lead Titanate

Eitel *et al.* first introduced BSPT ((1 – *x*) $BiScO_3$-*x*$PbTiO_3$) as an alternative to PZT materials with similar piezoelectric properties, with its main advantage being an increased curie temperature [9.1]. Eitel *et al.* then further analysed the material and found that with $x = 64\%$, designated as the morphotropic phase boundary, the k_{p}^2, d_{33} and $\varepsilon_{33}^{\mathrm{T}}$ all exhibited properties similar to a hard PZT whilst having a 64°C increase in curie temperature (T_c) over the highest T_c achieved by PZT materials [9.2].

Fei *et al.* validated the use of BSPT for high temp piezoelectric transducers at temperatures up to 200°C [9.3]. They found it to be an excellent material for that application, owing to its

excellent piezoelectric properties. Ji *et al.* and Wu *et al.* both evaluated the use of BSPT in energy harvesting applications, with both authors showing devices with excellent performance even at temperatures greater than 200°C [9.4], [9.5]. These results suggest that BSPT would be an excellent material for PT applications.

9.3 PT design

9.3.1 PT topology

A ring-dot PT topology was chosen for this study. The ring-dot PT is a radial mode device made from a single, unipoled piezoelectric disc with an input dot electrode and an output ring electrode. A 3D perspective diagram of the ring-dot PT is shown in Fig. 9.1.

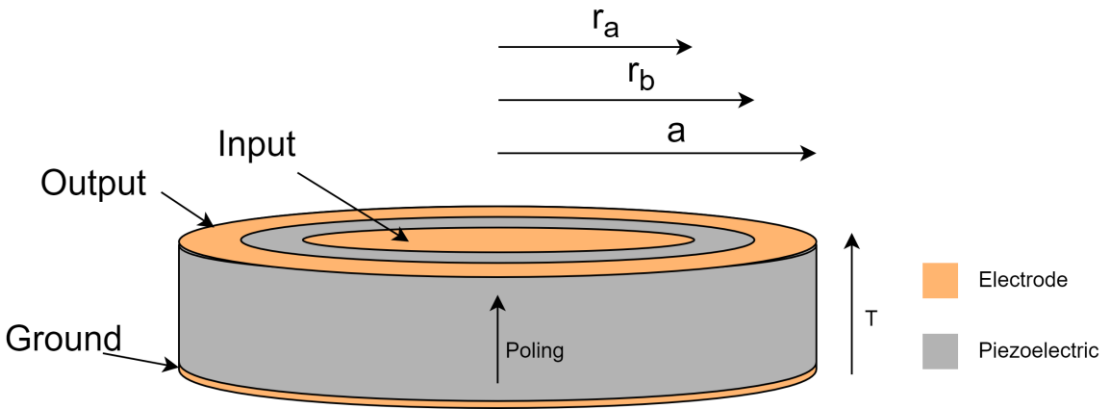

Fig. 9.1 – Model of ring-dot PT, centre dot is the input section and outer ring is the output section. The bottom face is fully covered by an electrode to form a common ground

The following section will detail the design procedure for a high temperature BSPT ring-dot PT for use in an inductorless half bridge resonant inverter.

9.3.2 Geometric design

9.3.2.a) Disc size – Choosing a and T

For radial-mode PTs, it is the radius, a, that predominantly determines the resonant (and hence operating) frequency. A large enough thickness is required to enable robust construction and increase output power capability. Erhart [9.6] found that, due to the electrode structure of the ring-dot PT, no spurious modes occur near to the radial vibration mode. However, the natural vibration modes of the underlying piezoelectric disc will still exist and whilst Erhart found these modes were not excited in the ring-dot topology, it is not known if the underlying modes will still affect performance. Therefore, the PT will still be designed

as if the spurious modes do exist and are excited. As is shown in [9.7], the frequency of spurious vibration modes in radial mode PTs are predominantly determined by radius/ thickness for the disc. Therefore, this ratio must be carefully chosen to avoid spurious modes occurring near the fundamental radial mode. In this application, $a = 8\text{mm}$ and $T = 1.1\text{mm}$ were selected, this gives a radius to thickness ratio of 7.3 and, observing Fig. 3 in [9.7], this ensures the radial mode is at a frequency directly between the second and third spurious resonant modes.

9.3.2.b) Inner radii – r_a and r_b

The radii r_a and r_b, determine the turns ratio, the input capacitance and output capacitance. Foster *et al.* [9.8] showed that when an ideal PT (no loss) is designed with an input to output capacitance ratio (C_N) of $< 2/\pi$ and assuming the converter is driven appropriately, ZVS can be achieved for all loads. However, when a lossy PT is considered, this criterion becomes,

$$C_N = \frac{C_\text{in}}{N_1^2 C_\text{out}} < \frac{2\eta}{\pi} \tag{9.1}$$

where η is the efficiency of the PT. As there is no information as to how a BSPT PT is likely to perform, the efficiency of such a device is unknown. Therefore, in accordance to (9.1), the PT should be designed such that C_N is significantly less than $2/\pi$, to account for less-than-ideal efficiencies. As shown in Fig. 9.1, both input and output sections of the PT have the same thickness between their respective electrodes and ground, therefore based on the equation for the input and output capacitance (9.2), C_N is given by (9.3)

$$C_\text{in} = \frac{\epsilon\pi r_\text{a}^2}{d}\left(1 - k_\text{p}^2\right), C_\text{out} = \frac{\epsilon\pi\left(a^2 - r_\text{b}^2\right)}{d}\left(1 - k_\text{p}^2\right) \tag{9.2}$$

$$C_N = \frac{r_\text{a}^2}{N_1^2\left(a^2 - r_\text{b}^2\right)} \tag{9.3}$$

where k_p^2 is the planar coupling factor. To determine the appropriate r_a and r_b, a parametric sweep was performed, with r_a and r_b varied through a range of $0.5\text{mm} < r_a < 7\text{mm}$ and $1\text{mm} < r_b < 7.5\text{mm}$, with $a = 8\text{mm}$ and $T = 1.1\text{mm}$. For each combination the turns ratio was calculated using equation (8.100) from Chapter 8 and then using (9.3), the capacitance ratio was found. In this application, a $C_\text{N} \ll 2/\pi$ was desired (to allow for $\ll 100\%$ efficiency), whilst also achieving a turns ratio of $0.75 < N_1 <$1.25. Using the results of this analysis, a

graph is created, showing regions where the analysed r_a and r_b values lead to a PT design with parameters that fit the specification. The inequality graph is shown in Fig. 9.2.

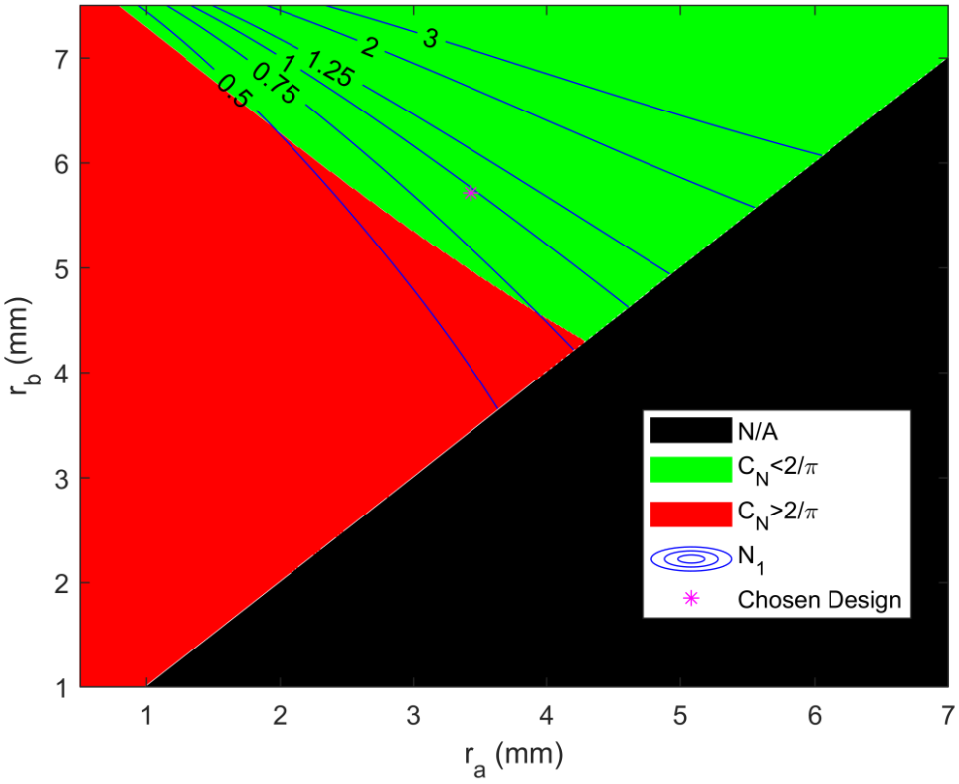

Fig. 9.2 – Inequality and contour plot showing desired design regions, the red and green regions show where ZVS is not achieved and where ZVS is achieved, respectively. The blue lines indicate the regions where acceptable turns ratios are achieved.

Observing Fig. 9.2, firstly, the black region shows PTs that are physically not possible because r_b must be greater than r_a. Secondly, the red region shows where the critical ZVS criterion is not achieved and therefore, should be avoided. The green region corresponds to PTs which meet the critical criterion and therefore, ZVS can be achieved for all loads (assuming correct driving conditions and efficient operation). Then, the blue lines on the graph in Fig. 9.2 show contours of constant turn ratio N_1.

Whilst in theory choosing any dimension in the region between the 0.75 and 1.25 contour lines and in the green region would be acceptable, some choices will lead to better designs. Firstly, as previously mentioned, C_N should be designed to be significantly lower than $2/\pi$ to not only guarantee ZVS but to also account for PT inefficiencies ($\eta < 100\%$). Secondly, in the chosen design, ideally none of the dimensions should be less than 1mm. This includes dot

radius, outer ring radius and the gap between the two electrodes. This is for several reasons, firstly, this ensures that these regions are large enough so that they can be easily physically constructed. Secondly, an additional parasitic capacitance is generated between the input dot and output ring electrodes. Therefore, by ensuring a significant gap between electrodes, reduces the size of this capacitance and thus reduces any additional adverse effects. Therefore, accounting for these constraints and designing for $N_1 \approx 1$, a PT with r_a = 3.4mm and r_b = 5.7mm was chosen, as highlighted on Fig. 9.2. To ensure a fair comparison, both PTs were built to the same specification. The prototype PTs are shown in Fig. 9.3

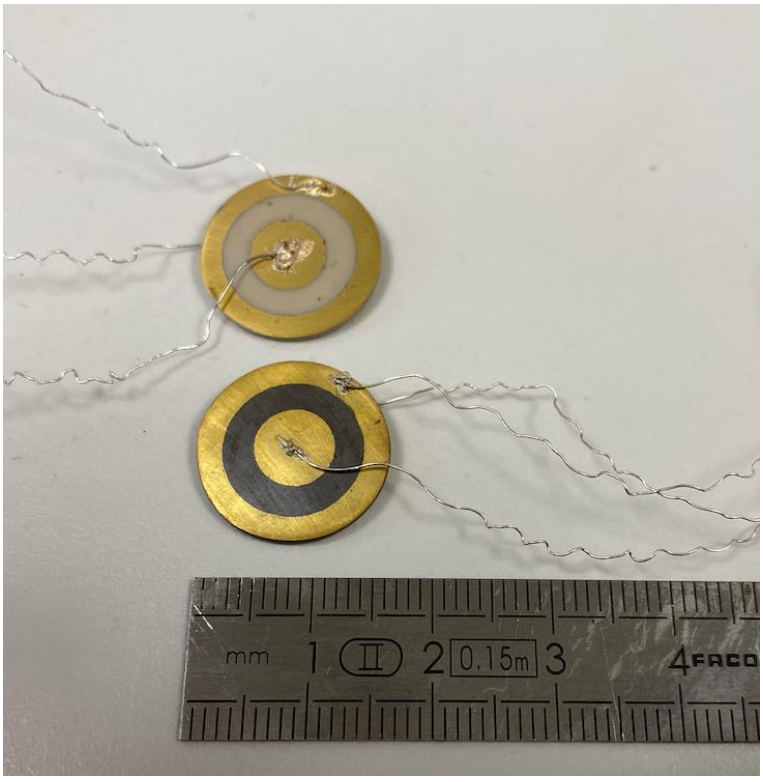

Fig. 9.3 – Fabricated PTs by the Materials Science Department at the University of Sheffield, (top) BSPT and (bottom) PZT

9.4 Experimental testing of prototype PTs

The prototype PTs were then experimentally tested under several different ambient temperatures. First the PTs were characterised to determine their small signal equivalent circuit properties and how they change with increases in ambient temperature. Second, each PT was used as part of an inductorless half-bridge resonant inverter to evaluate the large signal performance of both PTs with changes in ambient temperature.

9.4.1 High temperature experimental setup

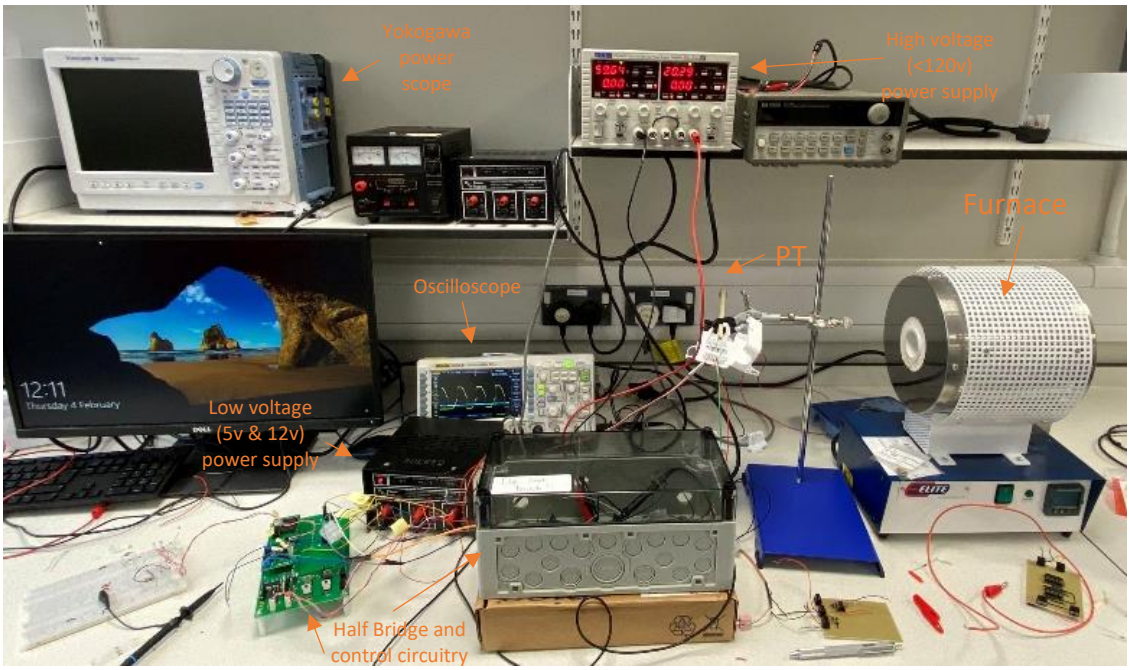

Fig. 9.4 – Full experimental setup

The full experimental setup used for the following experimentation is shown in Fig. 9.4. To control the ambient temperature around the PT sample, an Elite tube furnace was used. This furnace allows the ambient temperature to be quickly controlled to a high precision. In order to allow the PT to vibrate freely whilst inside the furnace, the PT was suspended from a ceramic rod, which was clamped into position allowing the PT to be easily placed inside the oven, this can be seen in Fig. 9.5. The clamp was positioned to ensure the PT was centred within the furnace. A cap was placed other the other end of the furnace's tube to aid thermal stability.

Fig. 9.5 – PT mounted on ceramic rod inside furnace

Three wires were threaded through the ceramic rod (chosen to withstand the heat and low thermal conductivity), providing electrical connections to the PT at one end and then to the testing circuitry at the other. One challenge of this setup was that ordinary solder would not be suitable for attaching the PT to the wires, owing to the high temperatures involved in the testing. Therefore, each of the three wires from the PT was wrapped tightly onto the three wires that are threaded inside the ceramic rod, thus achieving a solid electrical and mechanical connection.

To accurately measure the ambient temperature around the PT, an N-type thermocouple was placed in close proximity to the PT within the oven. The wires for the thermocouple were also threaded through the ceramic rod. The temperature from the thermocouple was measured and logged using a Pico TC-08 datalogger connected to a nearby PC, where the temperature was logged 4 times a second throughout the testing. Before each measurement was taken, the temperature was adjusted, the transient allowed to settle and then the PT was exposed for at least 20 mins to ensure the PT had reached the desired temperature.

9.4.2 Characterisation of high temperature PTs

9.4.2.a) Experimental setup

The small-signal input impedance, Z_{in}, of both PTs was measured using an Omicron Bode 100 vector network analyser. This is done by shorting the output electrode to ground, and then

measuring the impedance at the input electrode with respect to ground, as shown in Fig. 9.6. Similarly, the small signal output impedance, Z_{out}, was measured between the output electrode and ground, with the input electrode shorted to ground. Each impedance measurement was taken at a range of frequencies around the radial resonance. These measurements were then repeated at a range of temperatures, from room temperature up to a maximum of 250°C for the BSPT and up to 200°C for the PZT PT. For each measurement, the equivalent circuit components are extracted using the high damping extraction method presented in Chapter 3.

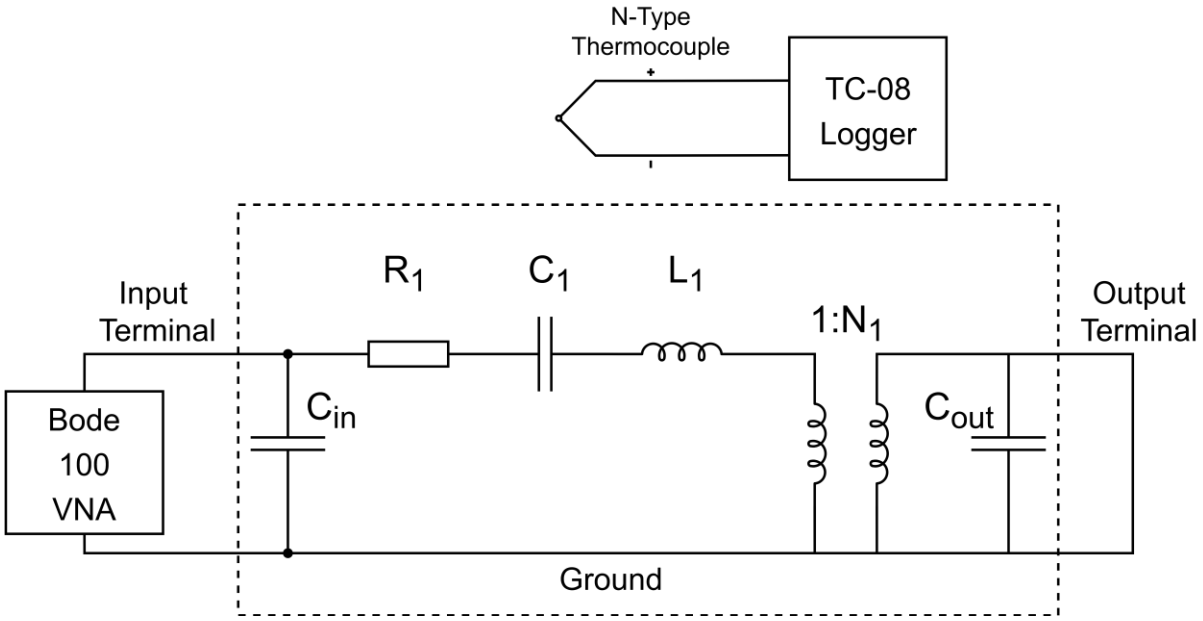

Fig. 9.6 – Circuit setup for input impedance measurements, dashed region highlights the Mason equivalent circuit model for the ring-dot PT

9.4.2.b) Results

9.4.2.b.i) Damping and Q factor

Observing Fig. 9.7, the PZT PT exhibits damping significantly lower than the BSPT PT across the 25°C-200°C temperature range. However, unlike the PZT PT, the BSPT PT's damping resistance decreases logarithmically with temperature. Whilst, at room temperature the PZT's damping resistance is an order of magnitude lower, at higher temperatures the BSPTs damping resistance is only approximately twice as large. Additionally, this decrease in damping carries on to 250°C, past what is possible with the PZT. Therefore, with improvements to the construction of the BSPT PT allowing it to reach 300°C, it is possible that the BSPT and the PZT would have similar damping resistances.

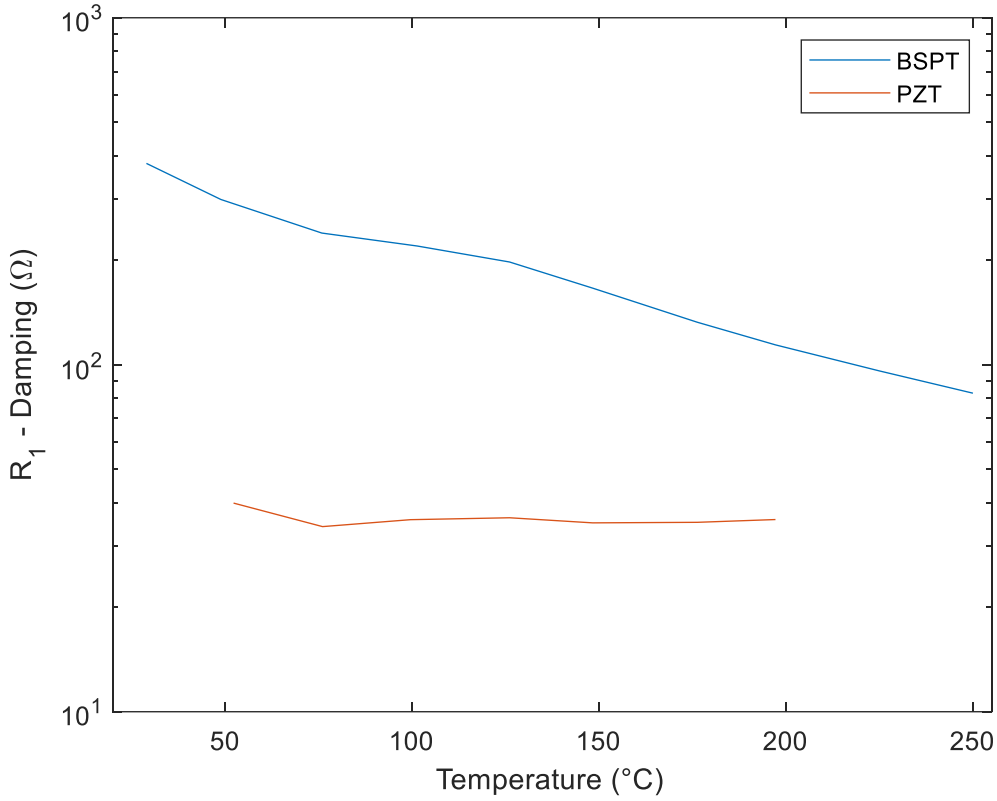

Fig. 9.7 – Damping resistance against temperature

From the extracted equivalent circuit properties, the electrical Q factor can be calculated using,

$$Q = \frac{1}{R_1}\sqrt{\frac{L_1}{C_1}} \tag{9.4}$$

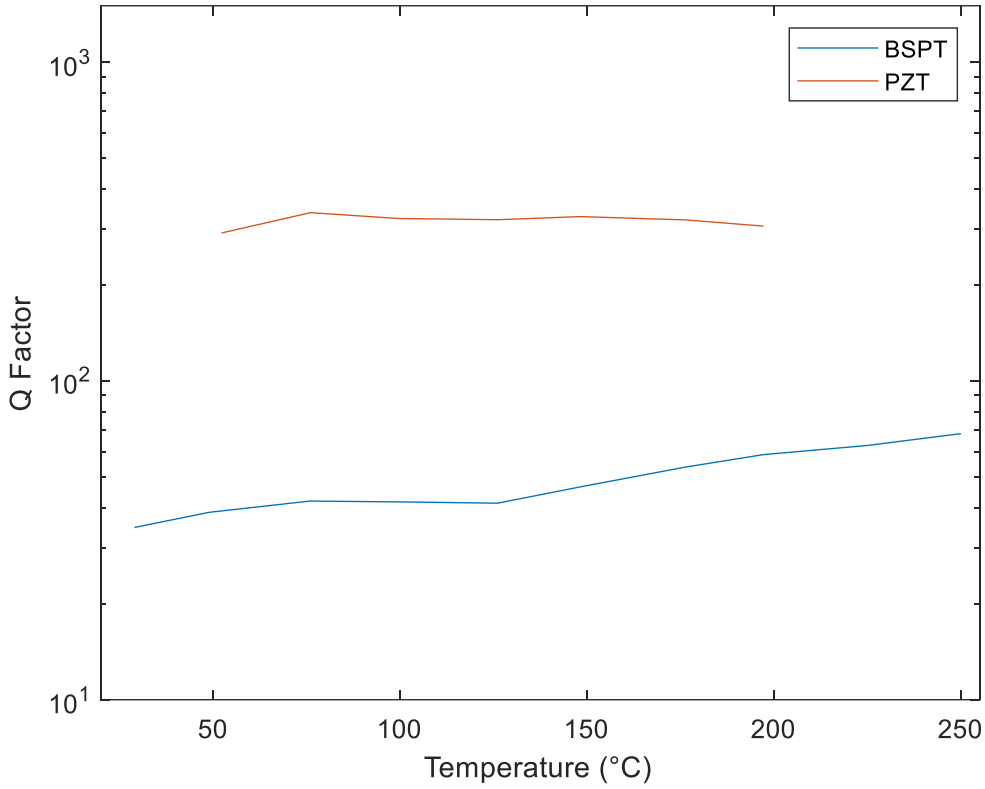

Fig. 9.8 – Q factor against temperature

Fig. 9.8 shows the electrical Q factor of both the PZT and BSPT PTs against temperature. As to be expected after observing Fig. 9.7, the Q factor of the PZT PT is much higher than the BSPT PT. Again, the PZT's Q factor slightly decreases with temperature, conversely the BSPT PT's Q factor increases with temperature. However, unlike the damping, even at the highest temperatures, the Q factor of the PZT is significantly larger than the BSPT. Whilst both are high when compared to traditional electronic circuits, when using the BSPT device in a resonant converter application, it is possible that fewer harmonics will be filtered by the PT, giving a less than ideal output voltage waveform. This may cause issues and additionally may make modelling of these devices using fundamental mode analysis techniques less accurate. Wu *et al.* presented a BSPT based energy harvester which had a similar Q factor (~25) to the BSPT PT presented here, supporting the results collected here [9.5].

9.4.2.b.ii) Input and output capacitance - $\boldsymbol{C_{\mathrm{in}}}$ and $\boldsymbol{C_{\mathrm{out}}}$

The normalised input and output capacitance is shown in Fig. 9.9, where the parameters are normalised to the lowest temperature measurement of that parameter. Additionally, the value of $\varepsilon_{33}^{\mathrm{T}}$ is measured from a disc of BSPT material and is shown for comparison.

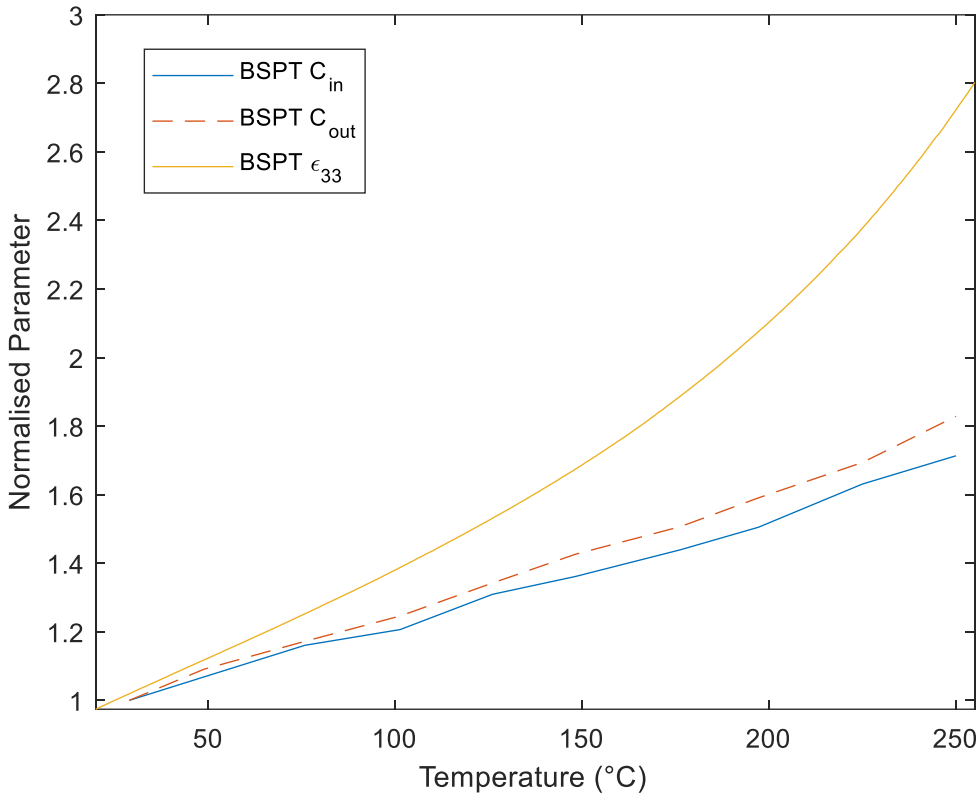
BSPT C_{in}
BSPT C_{out}
BSPT ϵ_{33}
Normalised Parameter
Temperature (°C)
3
2.8
2.6
2.4
2.2
2
1.8
1.6
1.4
1.2
1
50
100
150
200
250

a)

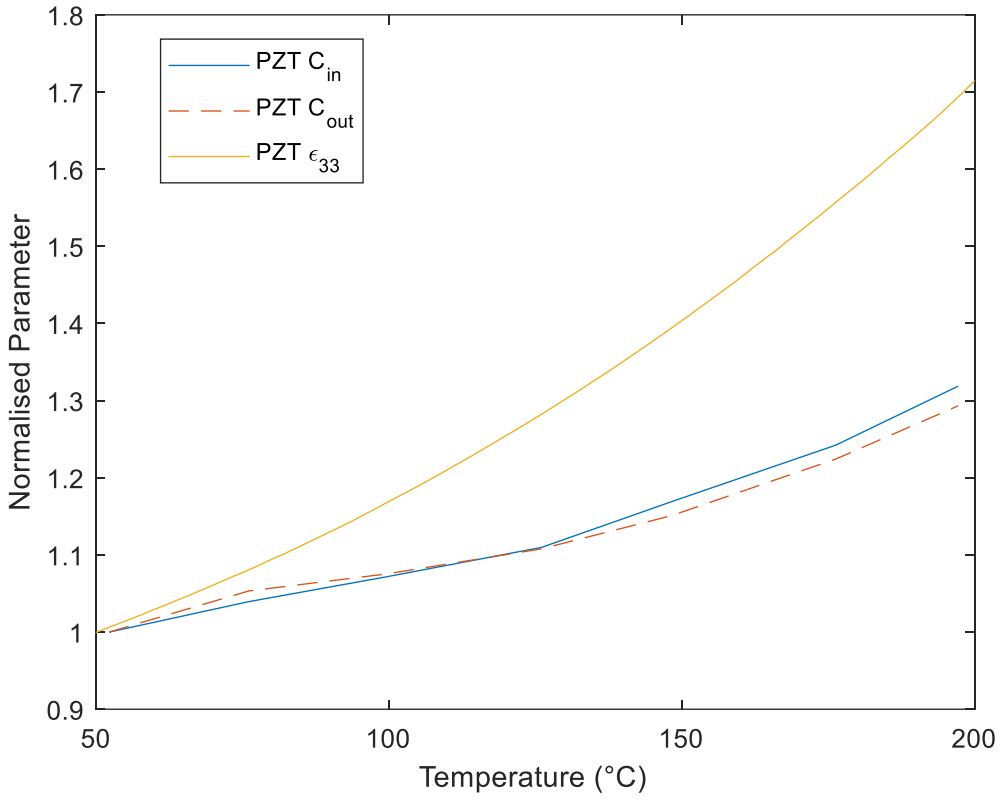

b)

Fig. 9.9 – Normalised change in C_{in} and C_{out} against temperature, (a) BSPT and (b) PZT. Measurements normalised to lowest temperature measurement of each parameter

Observing Fig. 9.9, capacitances C_{in} and C_{out} increase with temperature for both devices, as expected, owing to the increase in $\varepsilon_{33}^{\mathrm{T}}$ with temperature as is common in piezoelectric materials. Fig. 9.9 additionally shows normalised permittivity against temperature for both BSPT and PZT. As expected, the capacitances follow a similar trend to changes in $\varepsilon_{33}^{\mathrm{T}}$ with temperature; however, they increase at a slower rate with temperature. Observing the capacitance equations (9.2), this difference is likely due to an increase in coupling factor with temperature, similar to that found by Zhang *et al.* for a similar BSPT based device [9.9].

Additionally, in both devices there exist slight differences between the percentage change in the input and output capacitances. Whilst this cannot be explained simply by the equations modelling these capacitances, the difference is likely due to measurement error specifically at the low temperature ranges, slight heterogeneity in the construction of the devices and potentially differing rates of expansion in the input and output section of the device with temperature.

Comparing both Fig. 9.9a and Fig. 9.9b, the BSPT PT's capacitance increase at approximately twice the rate with temperature as the PZT PT does. One issue that arises with large output capacitance, is a reduction in both output power and efficiency, as discussed by Horsley [9.10] and in Chapter 4.

9.4.2.b.iii) Resonant frequency

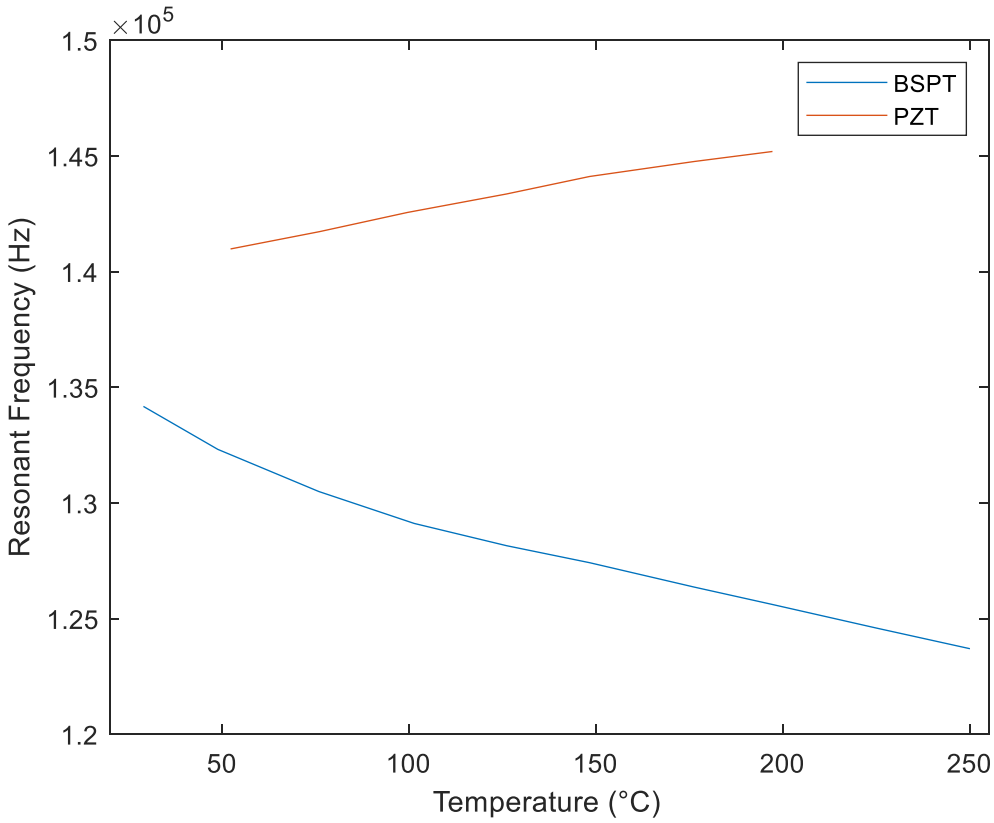

Fig. 9.10 – Changes in resonant frequency against temperature for both BSPT and PZT based PTs

Observing Fig. 9.10, both devices experience changes in resonant frequency with temperature. Whereas the PZT PT's resonant frequency increases with temperature, the BSPT PT's resonant frequency decreases with temperature. Additionally, even considering the temperature range, 25°C-200°C, the BSPT has approximately double the change in resonant frequency of the PZT, potentially making control of BSPT based converters more difficult.

9.4.3 Characterisation of PTs as part of a half-bridge resonant inverter

This section describes large-signal characterisation of both PTs excited using an inductorless half-bridge allowing the performance of the high-temperature PTs to evaluated under real-world conditions.

9.4.3.a) Inverter

The inductor less half-bridge (Fig. 9.11) inverter topology was chosen due to its suitability for step-down applications, soft-switching ability [9.11] and to avoid the aforementioned difficulties associated with high-temperature magnetics. The half-bridge circuit is shown in Fig. 9.11 with switches S1 and S2 forming a half-bridge and with the dashed box highlighting the Mason equivalent circuit for the ring-dot PT.

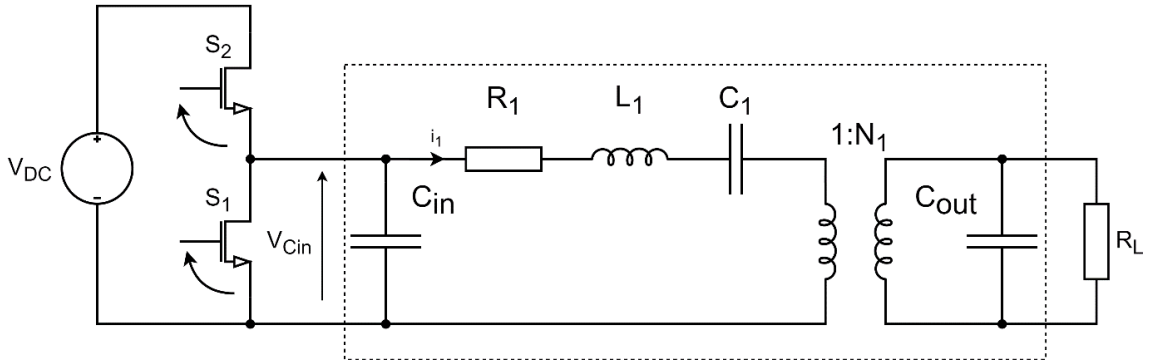

Fig. 9.11 – Inductor less half bridge inverter, dashed region highlights the Mason equivalent circuit model for the ring-dot PT

The half-bridge-based inverter uses 2 switches to chop a DC voltage into a high frequency square wave. The MOSFETS are switched in anti-phase, with a deadtime (both switches off) between. The high frequency trapezoidal waveform is filtered by the RLC circuit of the PT. Due to the high Q factor of the PT, most (if not all) additional harmonics are attenuated, allowing only the fundamental of the input trapezoidal wave to the PT to pass to the output. Therefore, the output of the converter (across the load) is a high frequency sine wave which, if desired, can then be rectified and filtered to produce a DC output. However, in the following analysis rectification and filtering will be omitted.

9.4.3.a.i) Zero voltage switching

Dead-time is an essential requirement in bridge type circuits to avoid simultaneous conduction of S1 & S2 in what is commonly known as a “shoot-through” event. In resonant power supplies, zero-voltage switching (ZVS) is often used to achieve high efficiency by reducing switching losses. ZVS takes advantage of the resonance of the PT and uses the current flowing through the resonant tank to charge/discharge the input capacitance during the deadtime, allowing the MOSFETs (S1 and S2) to be switched with no voltage across them, leading to minimal switching losses.

The operation of a half-bridge converter with an optimised (for ZVS) PT can be described by only 3 modes:

Mode 1:

Assuming initially $V_{C_{in}} = 0$ (or V_{DC}), S1 and S2 are both off. The resonant current, i_1, charges (red) (or discharges (green)) the input capacitor towards V_{DC} (or 0).

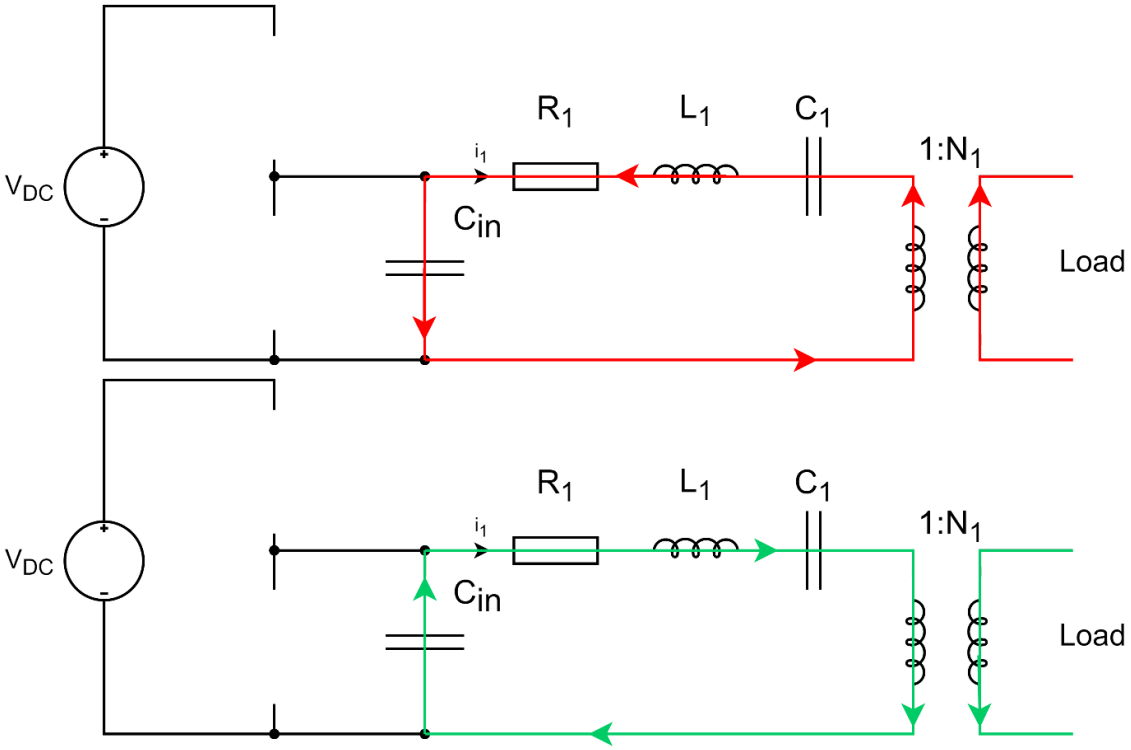

Fig. 9.12 – Mode 1 operation of the inductor less half bridge resonant converter, (top) shows the current flow after S1 turn off and (bottom) shows current flow after S2 turn off

Mode 2:

$V_{C_{in}} > V_{DC}$ (red) (or $V_{C_{in}} < 0$ (green)), the body diode of S2 (or S1) begins to conduct, clamping $V_{C_{in}} = V_{DC} + V_{DF}$ (or $V_{C_{in}} = -V_{DF}$)

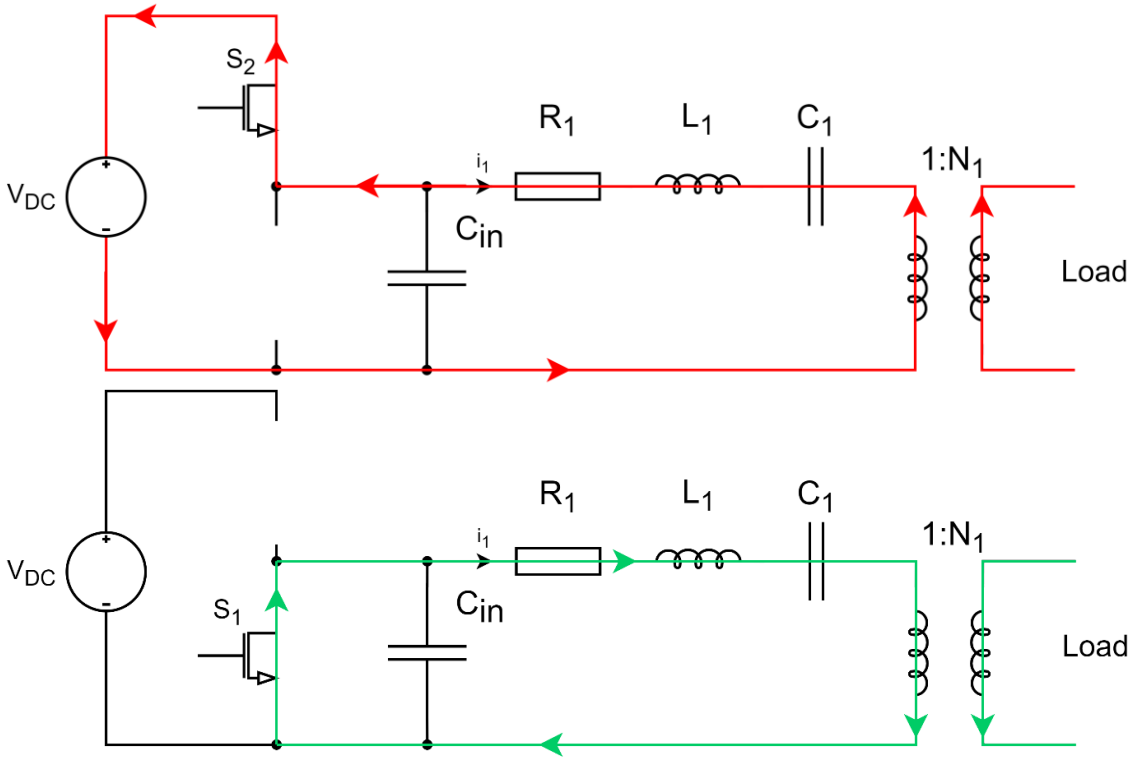

Fig. 9.13 – Mode 2 operation of the inducto rless half bridge resonant converter, (top) shows current flow during S2 body diode conduction and (bottom) shows current flow during S1 body diode conduction

Mode 3:

S2 (or S1) is turned on, $V_{C_{in}}$ is clamped at V_{DC} (or 0)

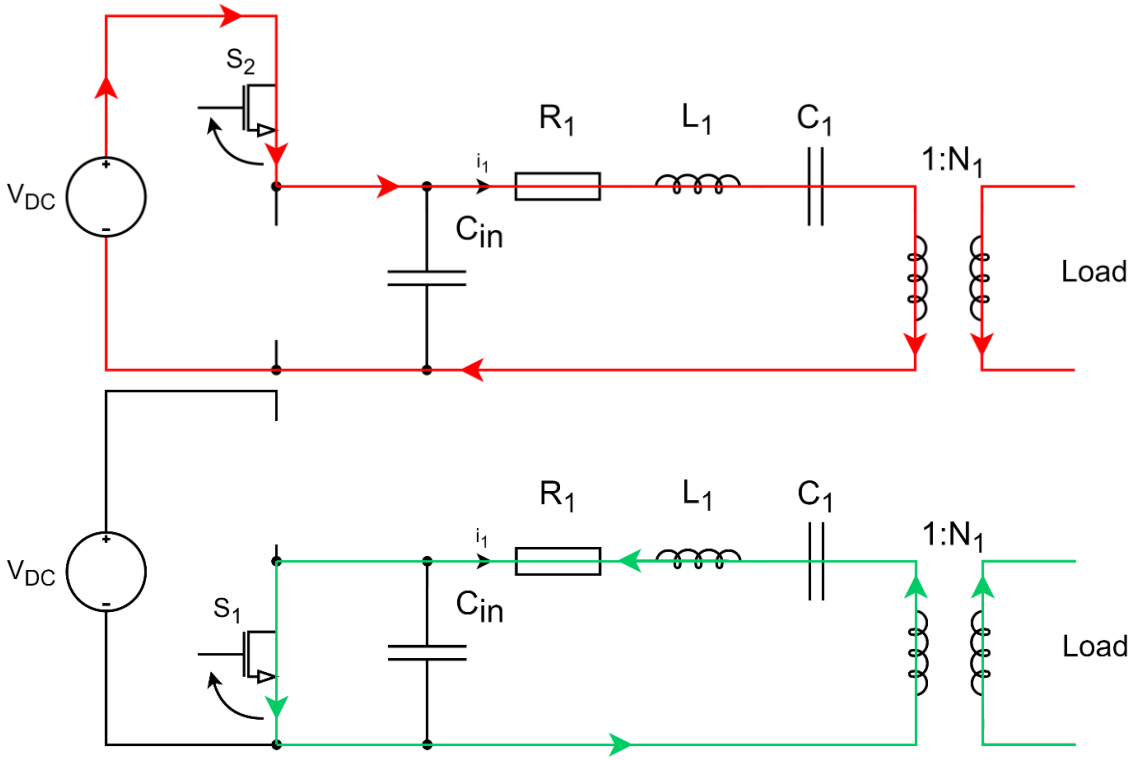

Fig. 9.14 – Mode 3 operation of the inductor less half bridge resonant converter, (top) shows current flow during S2 conduction and (bottom) shows current flow during S1 conduction

The PT input voltage ($V_{C_{\text{in}}}$) waveform during ZVS operation is shown in Fig. 9.15. Additionally, the gate drive signals, and the resonant current are also shown in Fig. 9.15.

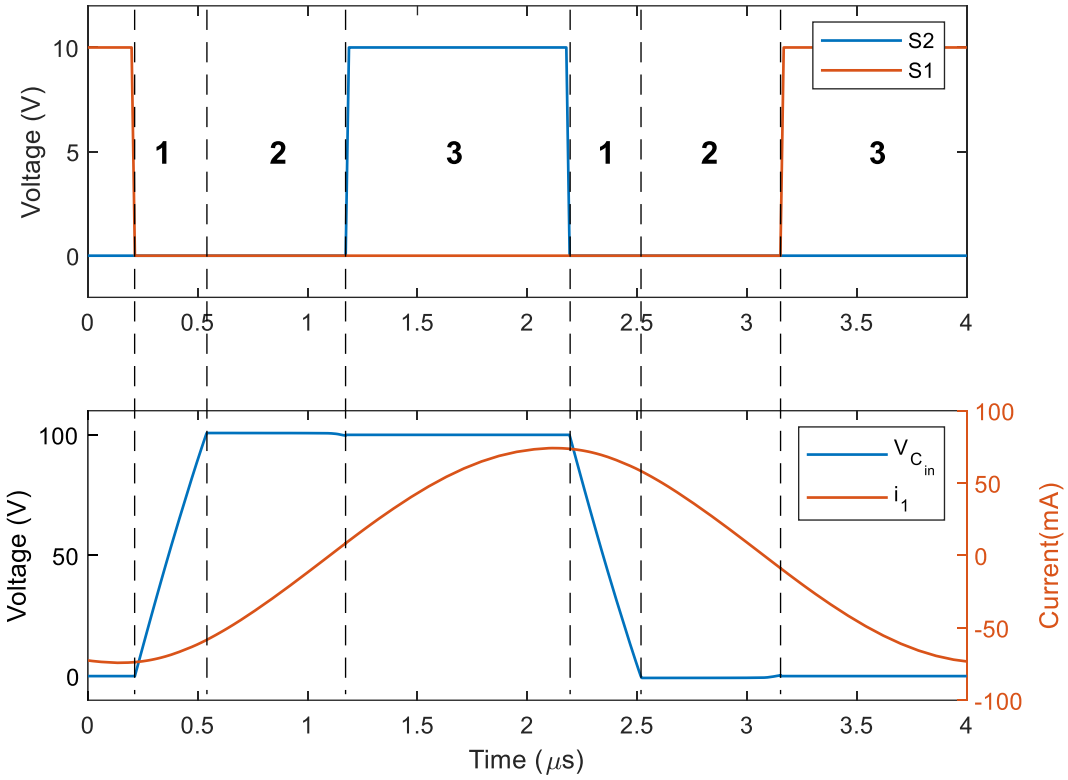

Fig. 9.15 – Simulated waveforms from the half-bridge converter during ZVS operations

If ZVS is achieved, the converter will follow a repeating mode sequence of Mode 1 -> Mode 2 -> Mode 3, as shown in Fig. 9.15. However, if the converter (PT or drive circuitry) is not designed correctly, the PT will follow a repeating pattern of Mode 1 -> Mode3 -> Mode 1, meaning the $V_{\mathrm{C_{in}}}$ has not reached V_{DC} (or 0) during the deadtime, and so ZVS is not achieved. If ZVS is not achieved, there will be some switching loss across the MOSFET, reducing converter efficiency.

For the testing performed here, IRF740B MOSFETs were chosen, owing to their low C_{DS} capacitance ($\sim 60\mathrm{pF}$) and high V_{DS} voltage rating (400V).

9.4.3.b) Resonant current estimation

A typical PT based converter controller aims to achieve a $\pi/2$ phase difference between the resonant current and the input voltage, as at the frequency the PT is being operated at resonance which is optimum for achieving ZVS. However, unlike traditional resonant converters featuring discrete components, the resonant current is not easily measurable in PTs. An estimator circuit provides a simple, low-cost method of estimating this quantity. A

simple anti-parallel diode current estimator proposed by Yang *et al.* [9.12] was used. The half-bridge converter with this additional circuit is shown in Fig. 9.16.

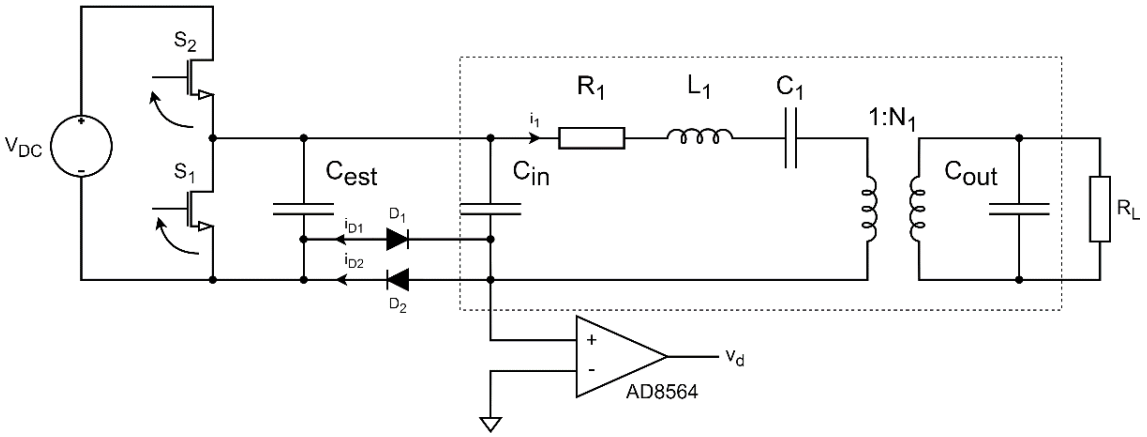

Fig. 9.16 – Inductor less half-bridge with anti-parallel diode resonant current estimator

Idealised waveforms for the circuit are shown in Fig. 9.17. The value of the current estimation capacitor C_{est} is set to be much smaller than the input capacitance of the PT to minimise it effect on the ZVS performance of the converter. As described in [9.12], the current flowing through the diode D_2, i_{D2}, is in phase with the resonant current i_1. Thus, a square wave voltage, v_{d}, is measured at the output of the comparator, which is in-phase with the resonant current.

This square wave signal is processed using a PLL and frequency divider logic as described by Yang *et al.* [9.12] to produce the gate drive signals for S1 and S2. A full description of this circuitry is available in [9.12].

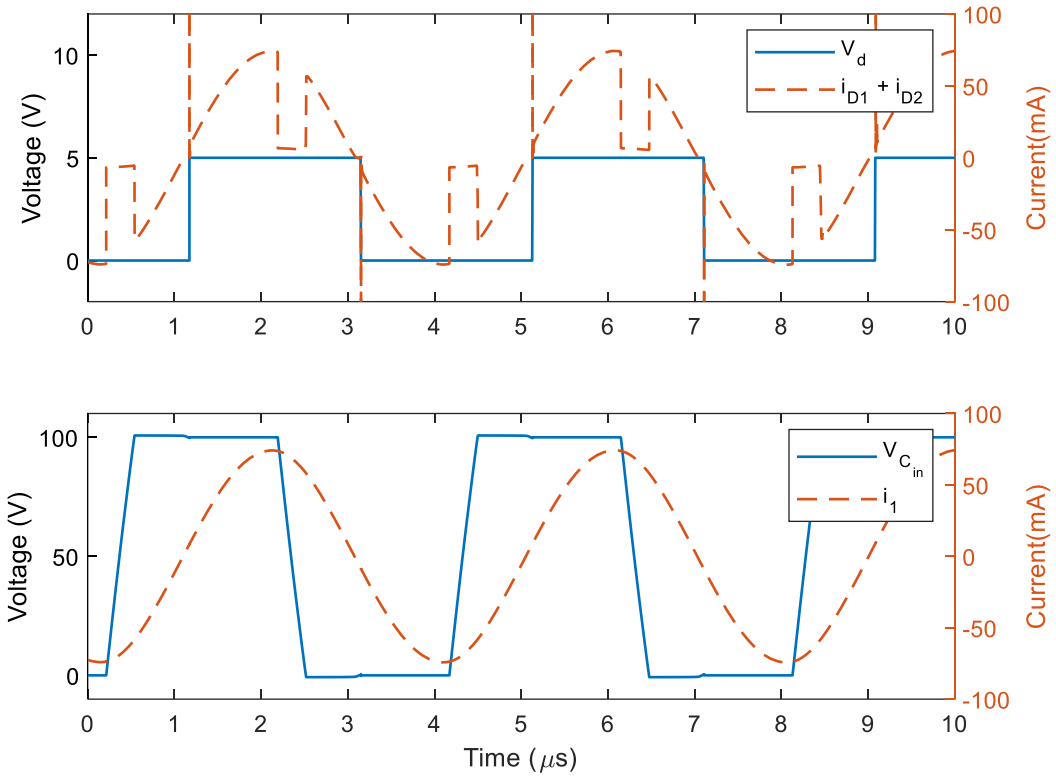

Fig. 9.17 – Simulated waveforms from the resonant current estimator and half-bridge converter

9.4.3.c) Experimental setup

A circuit diagram for the experimental setup is shown in Fig. 9.18 and Fig. 9.19.

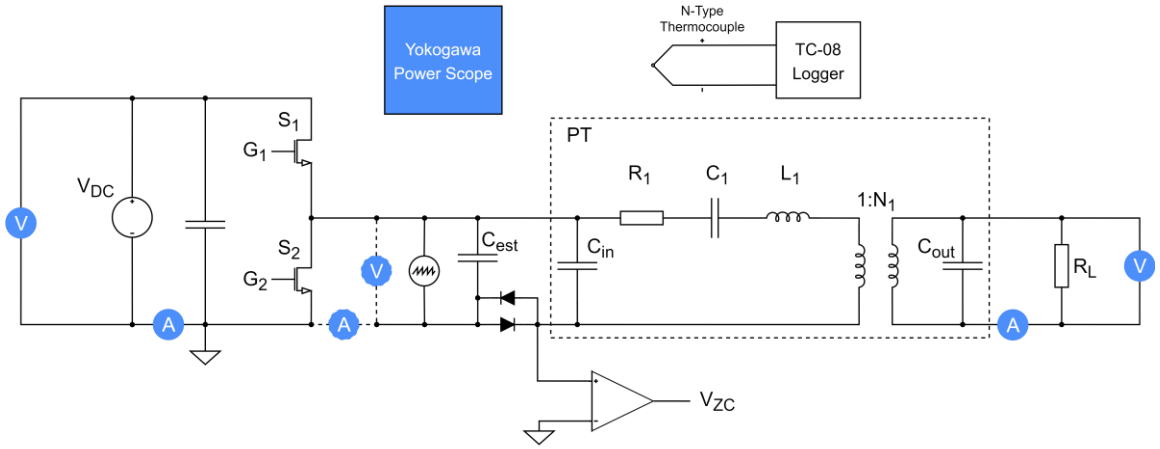

Fig. 9.18 – Inductor less half-bridge and measurement setup for high temperature measurements

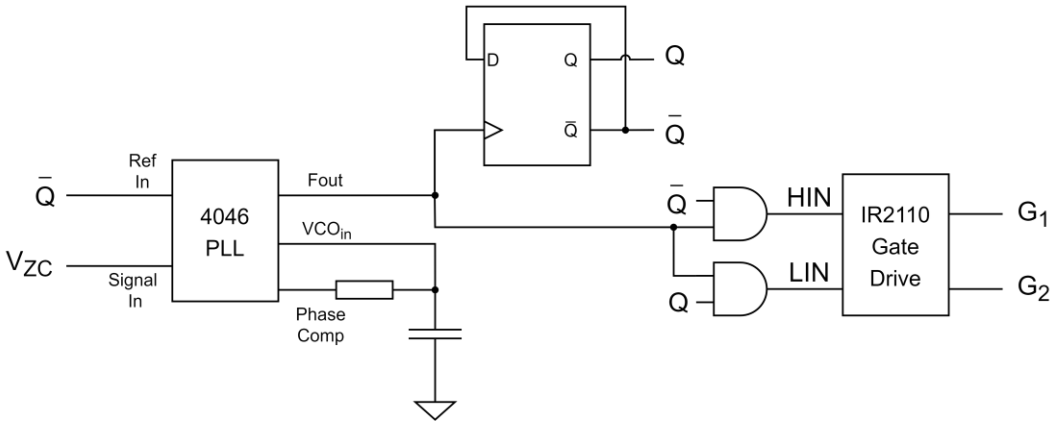

Fig. 9.19 – Phase locked loop, logic and gate drive circuitry for inductorless half-bridge

The input electrode and ground of the PT were connected to the half-bridge circuit, and the output electrode and ground of the PT connected to a load resistance. The converter was then operated with an 80V DC input, with the half-bridge switches driven in antiphase with a 25% duty cycle. The frequency doubler and PLL control system described in [9.12] ensures the resonant current is $\pi/2$ out of phase with the input voltage by controlling the operating frequency. The input power to the half-bridge and the output power to the load were measured using a Yokogawa PX8000 power scope, allowing the efficiency to be calculated.

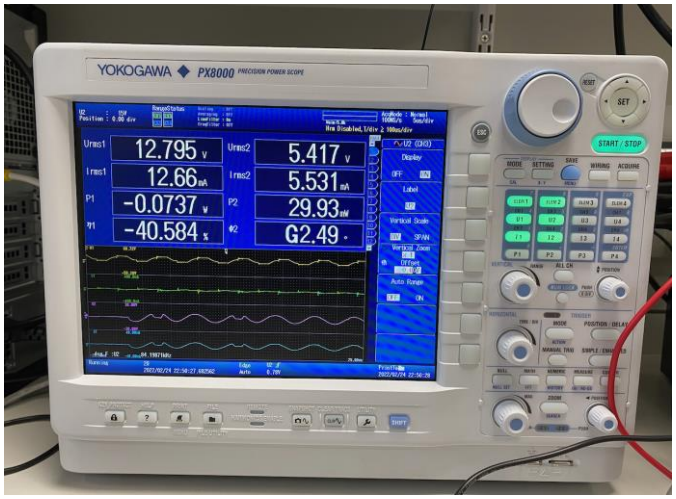

Fig. 9.20 – Yokogawa PX8000 power scope

Additionally, a second measurement is taken, measuring the input power to the PT and the output power to the load. This second measurement allows the efficiency of exclusively the PT to be measured during operation. Then, comparing the converter efficiency from the first measurement and the PT efficiency from the second measurement, allows the losses to be broken down into PT losses and loss in the switches (conduction and switching), at each operating point. Measurements were taken just after the converter was switched on, to avoid

self-heating affects. Again, measurements were taken at a range of temperatures, from room temperature up to 250°C for the BSPT and up to 200°C for the PZT PT.

9.4.3.c.i) Load

To fairly evaluate the performance of each PT, a was matched load should be used to compensate for the capacitance variation with temperature. The matched load is calculated using,

$$R_{\mathrm{L_{Matched}}} = \frac{1}{\omega C_{\mathrm{out}}} \tag{9.5}$$

However, observing (9.5) and the characterisation results in the previous section, the capacitance and resonant frequency of each PT changes with temperature; therefore, so will the matched load. Fig. 9.21 shows the estimated matched load for both PTs based on the characterisation results as a function of temperature.

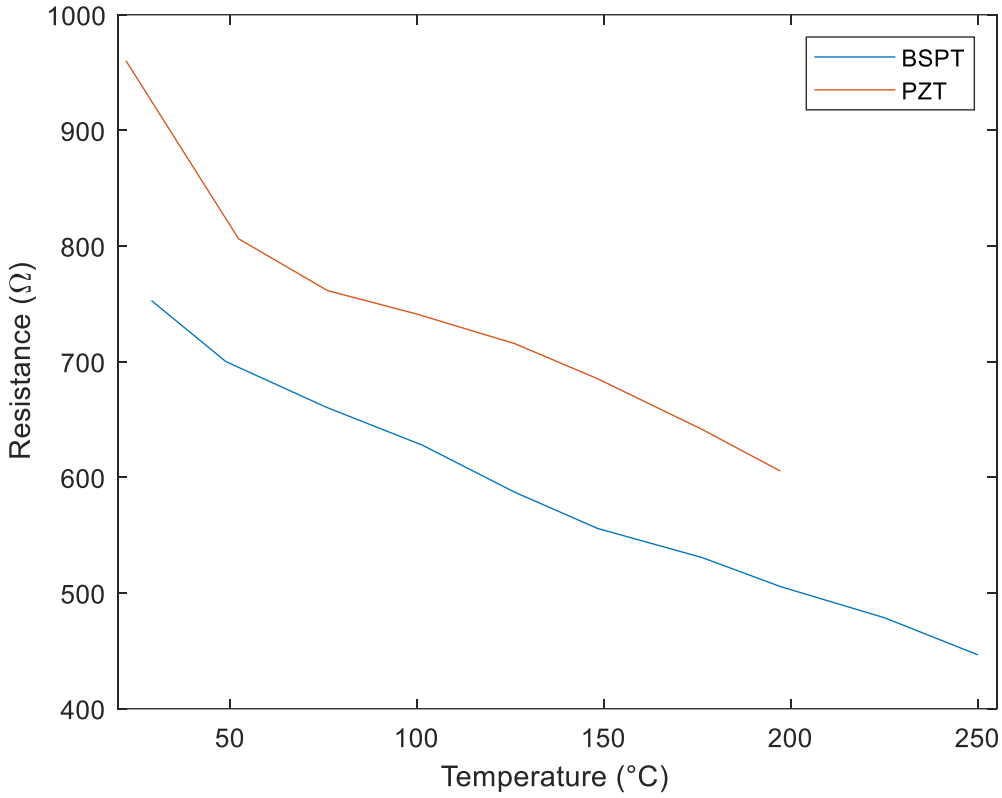

Fig. 9.21 – Matched load against temperature for both the BSPT PT and the PZT PT

To account for the changing matched load, each converter was measured with 3 different load values, chosen to span the full range of exhibited matched loads as highlighted in Fig. 9.21, values of 1 kΩ, 500 Ω and 220 Ω loads were used for the experimental testing.

9.4.3.d) Simulation

An important aspect in PT based resonant converter design is how accurately the performance of the converter can be predicted based on its equivalent circuit components. In addition to the experimental converter testing, a similar simulated test will also be performed. The converter will be simulated using LTSpice and using the equivalent circuit component values extracted from the characterisation step performed previously. For each temperature step, the input and output power and efficiency will be extracted for comparison to the experimental results.

9.4.3.e) Results

9.4.3.e.i) Output power and efficiency

Fig. 9.22 shows the output power and Fig. 9.23 shows the efficiency of both resonant converters when driving the most efficient load at each temperature step. Where the most

efficient load is the load resistance where the converter achieves the highest efficiency, typically when the load resistance that is used is close to theoretical matched load

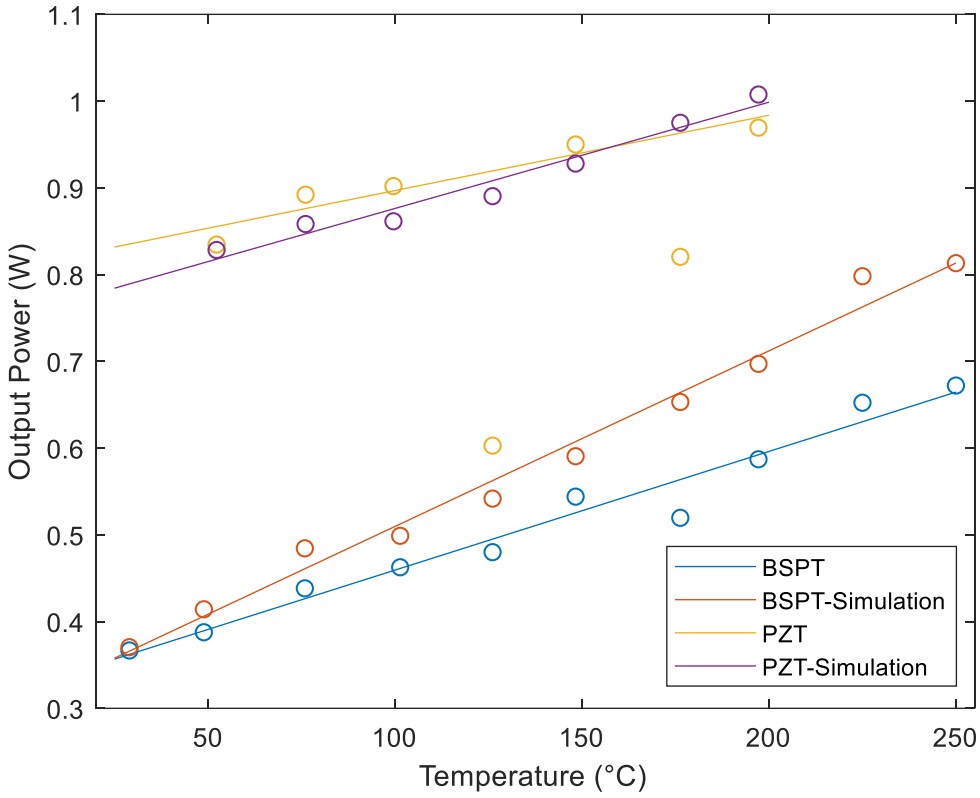

Fig. 9.22 – Output Power of both BSPT and PZT based resonant converter against PT ambient temperature when driving the most efficient load, lines of best fit are also shown.

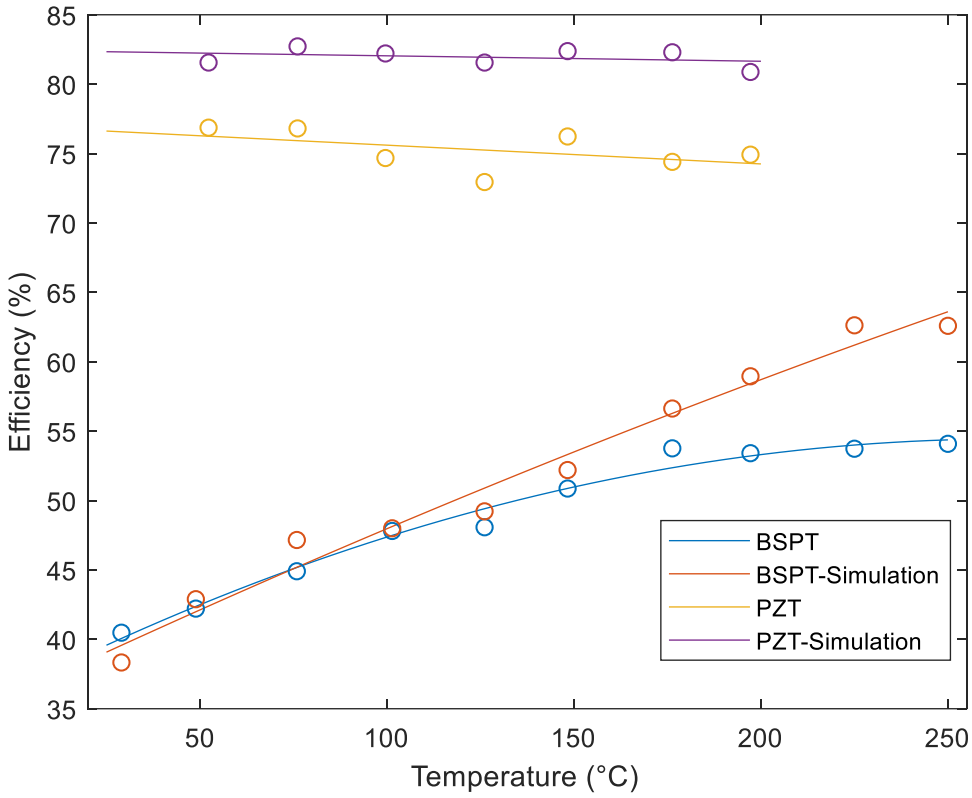

Fig. 9.23 – Efficiency of both BSPT and PZT based resonant converter against PT ambient temperature when driving the most efficient load, lines of best fit are also shown

Observing Fig. 9.22 and Fig. 9.23, the PZT PT achieves significantly higher output power and efficiency when operating under the same conditions as the BSPT PT. The PZT PT achieves a very similar output power across the range of temperatures tested, with output power slightly increasing with temperature. However, as can be predicted based on the decrease in damping resistance, the BSPT has a roughly linear increase in output power with temperature. The efficiency of the PZT based converter slightly decreases with temperature in agreement with a slight increase in damping and output capacitance that was observed in the characterisation measurements. Again, for the BSPT, owing to the significant reduction in damping in the BSPT PT with increasing temperature, the BSPT based converter exhibits a notable increase in efficiency with temperature.

At room temperature, the PZT based converter significantly outperforms the BSPT based converter, achieving just less than three times the output power at approximately double the efficiency. Although, at 200°C, whilst the PZT based converter still outperforms the PZT based converter, the output power is only twice that of the BSPT based converter and at an efficiency of only around 1.3x greater. However, and most importantly, the BSPT still sees

improvements in performance at temperatures greater than 200°C, past what is possible to achieve with the PZT based converter.

9.4.3.e.ii) Ability to achieve zero voltage switching

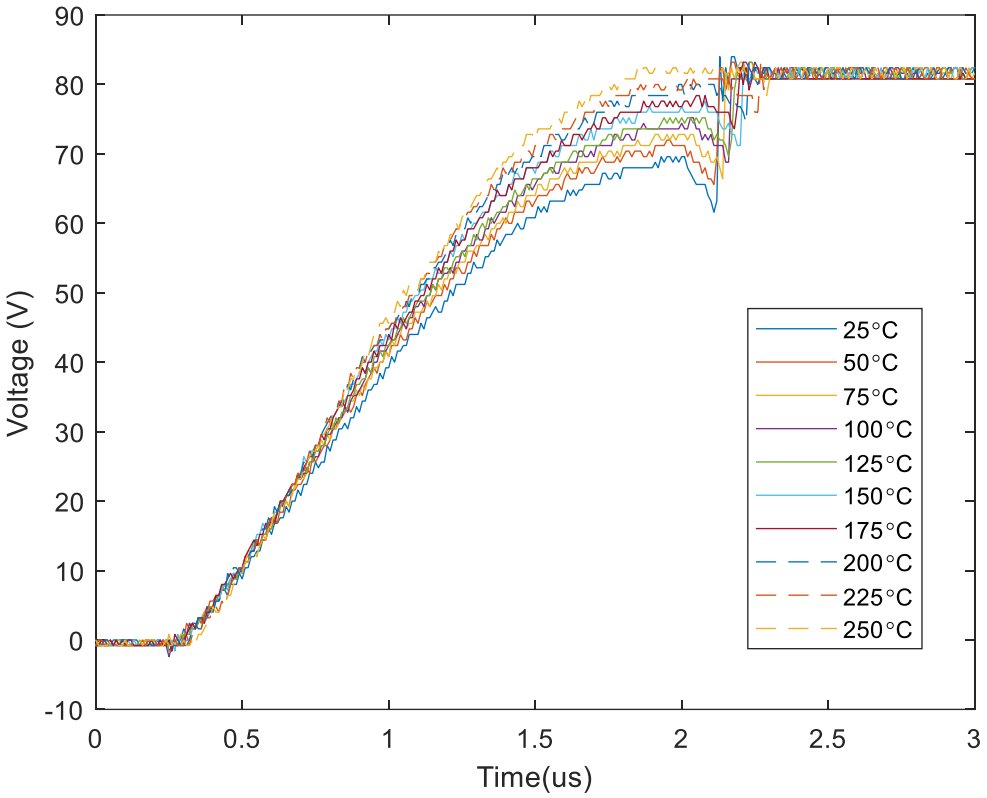

Fig. 9.24 – Vc_{in} voltage to the BSPT PT during the deadtime, with a 500Ω load at several ambient tempatures

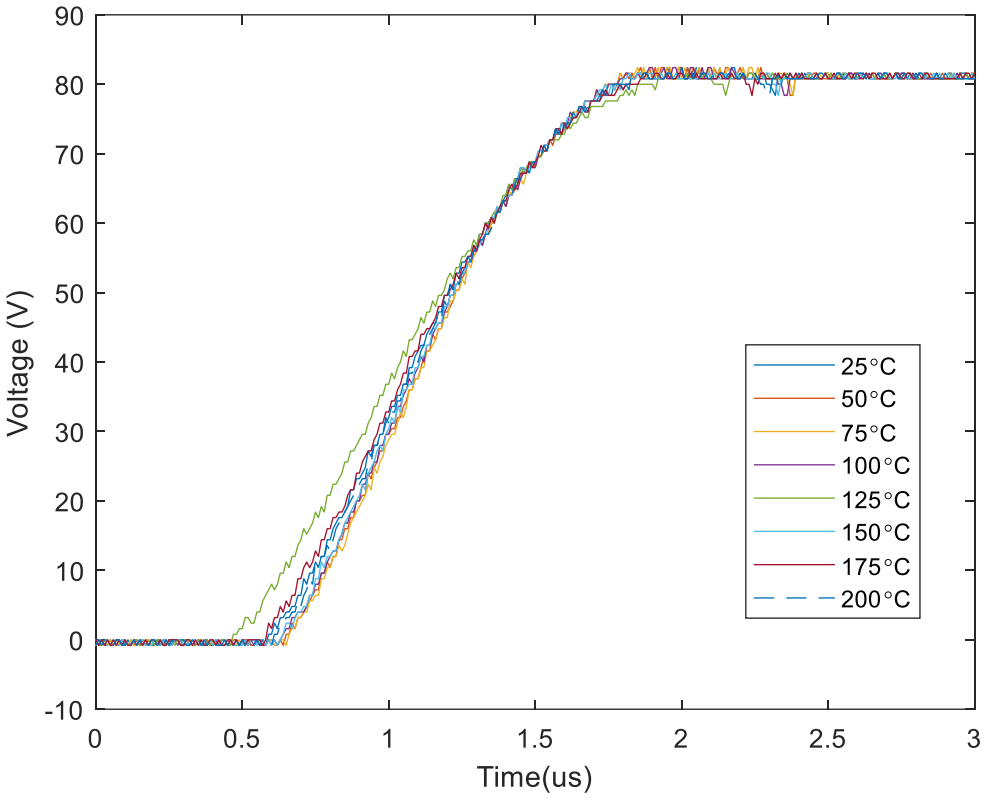

Fig. 9.25 – $V_{C_{in}}$ voltage to the PZT PT during the deadtime, with a 500Ω load at several ambient tempatures

As expected, Fig. 9.24 shows $V_{C_{\text{in}}}$ at the point of S2 turn on increasing with a rise in ambient temperature for the BSPT based converter, thus meaning K_{ZVS} increases with a rise in ambient temperature. As Foster *et al.* discuss, the ZVS characteristics of the PT based converter will depend on the capacitance ratio and efficiency [9.8]. Whilst capacitance ratio is fixed for a PT, the efficiency of the BSPT PT increases with temperature and as a result, increases the K_{ZVS} value that is achieved in the BSPT based converter. In contrast, owing to the greater efficiency of the PZT PT at all temperatures, the PZT based converter achieves ZVS ($K_{\text{ZVS}} \geq 1$) across the full temperature range.

9.4.3.e.iii) Loss breakdown

Fig. 9.26 and Fig. 9.27 show the percentage of the input power that is lost across the PT and the half bridge switches, and the percentage of power delivered to the load for the BSPT and PZT converters respectively. These results are calculated when driving the most efficient load.

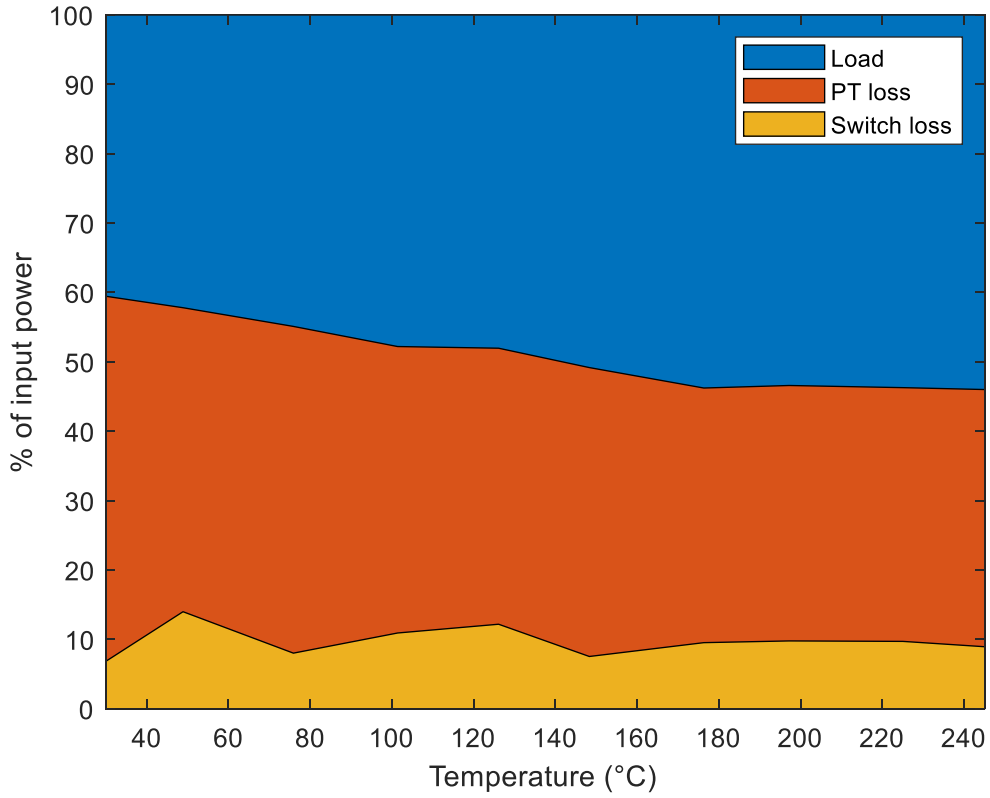

Fig. 9.26 – Percentage of input power lost / provided to each section of the BSPT based converter whilst operating with the most efficient load, at temperatures from 30°C to 250°C

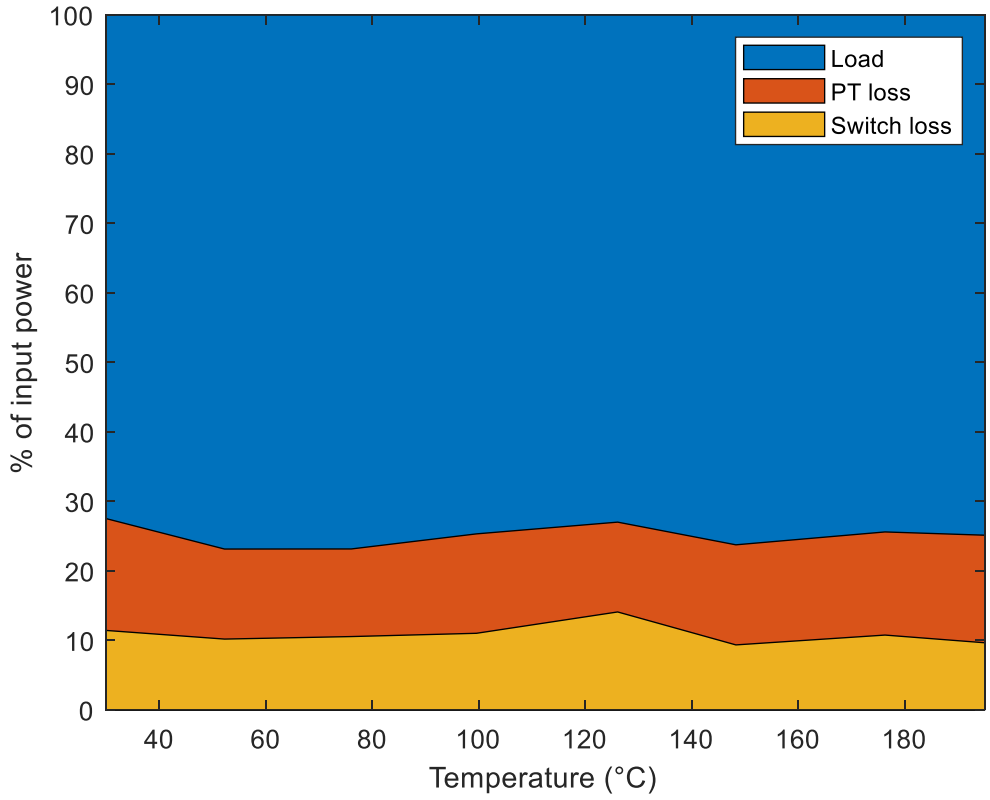

Fig. 9.27 – Percentage of input power lost / provided to each section of the PZT based converter whilst operating with the most efficient load, at temperatures from 30°C to 200°C

Observing Fig. 9.26, for the BSPT based converter, the percentage of input power delivered to the load increases with temperature, as expected with the efficiency of the converter increasing with temperature. Most of the increase in output power percentage comes from a decrease in the losses across the PT. Whilst, Fig. 9.24 shows that the converter achieves greater K_{ZVS} with increasing temperature and as a result decreases the switching losses, this reduction in loss has a negligible effect on increasing converter efficiency. Although, as Fig. 9.24 shows, the PT achieved a relatively high K_{ZVS} at room temperature $K_{\mathrm{ZVS}} = 0.87$ and so only a minor improvement in switching losses is achieved at higher temperatures.

Observing Fig. 9.27, for the PZT based converter, the percentage of input power delivered to the load is relatively constant across the temperature range, as expected. Similar to the BSPT based converter, around 10% of the input power is lost across the switches, which given the excellent ZVS performance of the PZT based converter, this can be attributed to conduction loss. However, in contrast to the BSPT based converter, only around 10% of the input power is lost across the PT, with the BSPT PT loss accounting for between 30-50% of the input power.

9.5 Discussion

This analysis shows that a PT made from BSPT can be effectively used in a power converter and validates the performance of BSPT PTs at temperatures of up to 250°C. Converters made with BSPT PTs show both improved output power and efficiency at elevated temperatures when compared to room temperature, due to improvements in PT efficiency which subsequently improves the K_{ZVS} of the converter. However, PZT PTs clearly outperform the BSPT PTs in this application at temperatures less than 200°C. This is due mostly to the low damping these PTs exhibit, giving rise to lower losses, higher K_{ZVS} and increased output power.

BSPT PTs have one clear advantage over PZT PTs in their ability to be used at temperatures of up to 300°C, around 100°C greater than PZT, owing to BSPT's higher curie temperature. Therefore, for temperatures in the range 200°C -300°C, BSPT is an excellent material for PTs. As typical passive components cannot operate at such temperatures, industries such as aerospace or oil, where temperatures in the range 200°C -300°C are common, could present several applications for BSPT based devices.

The BSPT's properties also show improvement with increases in temperature; therefore, it is likely that at even greater temperatures, BSPT performance would further improve. The BSPT PT based converter presented here achieves around 60% efficiency at just under 0.7W output power at 250°C, achieving results similar to high temperature power supplies presented in literature, whilst being much simpler to implement.

During the power converter testing, the switches accounted for around 10% of the overall losses across the full temperature range, therefore, further improvements can be made by choosing a MOSFET with a lower $R_{\mathrm{DS_{ON}}}$value than the IRF740B (0.5Ω) used here. However, whilst this may allow the efficiency to increase to around 65%, in the case of the BSPT PT, the PT is still responsible for most of the loss. This loss is due to the relatively high damping resistance of the PT (causing I^2R losses) and the large output capacitance that is exhibited at high temperatures. These issues can be attributed to the low Q factor (~ 50) of BSPT and the rapid increase in dielectric constant with temperature of the BSPT. Therefore, this offers potential for further improvements to the BSPT material to improve on these characteristics. As shown by Eitel *et al.* using a different BSPT composition ($x = 70\%$) increases the Curie

temperature and lowers the dielectric constant in the temperature range of interest. However, this composition gives increased tan δ losses and inferior piezoelectric properties (lower k_p^2 and d_{33}) compared to the $x = 64\%$ composition used in this study. Therefore, a careful balance is required to further optimise the material for this application.

It should be noted that traditional silicon-based components were used for the additional circuitry in the experimental work and as these components cannot perform at high temperatures (>150°C), only the PT was kept in the furnace during testing. Consequently, lengthy wires were used to connect the PT to the main circuitry and testing equipment. This causes unwanted resonances and additional parasitic elements which likely harmed the performance of both converters. Therefore, it is likely that a converter made from high temperature suitable components, therefore allowing reduced connection lengths, could improve converter performance.

Finally, the simulated results show good correlation with experimental results, especially for PZT measurements. Both simulated power and efficiency curves are slightly higher for both converters, but both show a similar trend to the experimental results. The slight difference can be attributed to several factors include inaccuracies in the current estimation and gate drive circuitry therefore operating the converter at a different point; inaccuracies in the experimental efficiency measurements due to the challenges involved in such measurements and the non-ideal characteristics of the experimental setup including long wires and unmodelled parasitic properties in the PT itself.

However, there are some notable differences between the experimental and simulated BSPT measurements. The simulated efficiency of the BSPT based converter is approximately linear with temperature; however, the experimental results show a quadratic relationship. The BSPT-based converter exhibits a drop in efficiency at high temperatures compared to simulated results. This can again be attributed to numerous factors; however, it is most likely that there are parasitic elements, which are not included in the simulated model which cause the efficiency to drop. These parasitics would also explain the discrepancy in the output power measurements. Therefore, further work should be done to characterise these parasitics to allow more informed BSPT PT designs.

9.6 References

[9.1] R. E. Eitel, C. A. Randall, T. R. Shrout, P. W. Rehrig, W. Hackenberger, and S.-E. Park, 'New High Temperature Morphotropic Phase Boundary Piezoelectrics Based on Bi(Me)O_3–$PbTiO_3$ Ceramics', *Jpn. J. Appl. Phys.*, vol. 40, no. 10R, p. 5999, Oct. 2001, doi: 10.1143/JJAP.40.5999.

[9.2] R. E. Eitel, C. A. Randall, T. R. Shrout, and S.-E. Park, 'Preparation and Characterization of High Temperature Perovskite Ferroelectrics in the Solid-Solution (1-x)$BiScO_3$–x$PbTiO_3$', *Jpn. J. Appl. Phys.*, vol. 41, no. 4R, p. 2099, Apr. 2002, doi: 10.1143/JJAP.41.2099.

[9.3] C. Fei *et al.*, '0.36$BiScO_3$-0.64$PbTiO_3$ piezoelectric ceramics for high temperature ultrasonic transducer applications', *Journal of Alloys and Compounds*, vol. 743, pp. 365–371, Apr. 2018, doi: 10.1016/j.jallcom.2018.01.393.

[9.4] J.-H. Ji, D.-J. Shin, J. Kim, and J.-H. Koh, '$BiScO_3$-$PbTiO_3$ piezoelectric ceramics with Bi excess for energy harvesting applications under high temperature', *Ceramics International*, vol. 46, no. 4, pp. 4104–4112, Mar. 2020, doi: 10.1016/j.ceramint.2019.10.117.

[9.5] J. Wu, H. Shi, T. Zhao, Y. Yu, and S. Dong, 'High-Temperature $BiScO_3$-$PbTiO_3$ Piezoelectric Vibration Energy Harvester', *Advanced Functional Materials*, vol. 26, no. 39, pp. 7186–7194, 2016, doi: https://doi.org/10.1002/adfm.201602645.

[9.6] J. Erhart, P. Pulpán, R. Dolecek, P. Psota, and V. Lédl, 'Disc Piezoelectric Ceramic Transformers', *IEEE Transactions on Ultrasonics, Ferroelectrics, and Frequency Control*, vol. 60, no. 8, pp. 1612–1618, Aug. 2013, doi: 10.1109/TUFFC.2013.2742.

[9.7] J. Forrester, J. Davidson, and M. Foster, 'Effect of Spurious Resonant Modes on the Operation of Radial Mode Piezoelectric Transformers', in *PCIM Europe 2018; International Exhibition and Conference for Power Electronics, Intelligent Motion, Renewable Energy and Energy Management*, Jun. 2018, pp. 1–8.

[9.8] M. P. Foster, J. N. Davidson, E. L. Horsley, and D. A. Stone, 'Critical Design Criterion for Achieving Zero Voltage Switching in Inductorless Half-Bridge-Driven Piezoelectric-Transformer-Based Power Supplies', *IEEE Transactions on Power Electronics*, vol. 31, no. 7, pp. 5057–5066, Jul. 2016, doi: 10.1109/TPEL.2015.2481706.

[9.9] S. Zhang, R. E. Eitel, C. A. Randall, T. R. Shrout, and E. F. Alberta, 'Manganese-modified $BiScO_3$–$PbTiO_3$ piezoelectric ceramic for high-temperature shear mode sensor', *Appl. Phys. Lett.*, vol. 86, no. 26, p. 262904, Jun. 2005, doi: 10.1063/1.1968419.

[9.10] E. Horsley, 'Modelling and Analysis of Radial Mode Piezoelectric Transformers and Inductor-less Resonant Power Converters', University of Sheffield, 2011.

[9.11] M. Ekhtiari, Z. Zhang, and M. A. E. Andersen, 'State-of-the-art piezoelectric transformer-based switch mode power supplies', in *IECON 2014 - 40th Annual Conference of the IEEE Industrial Electronics Society*, Oct. 2014, pp. 5072–5078. doi: 10.1109/IECON.2014.7049271.

[9.12] Z. Yang, J. Forrester, J. N. Davidson, M. P. Foster, and D. A. Stone, 'Resonant current estimation and phase-locked loop feedback design for piezoelectric transformer-based power supplies', *IEEE Transactions on Power Electronics*, pp. 1–1, 2020, doi: 10.1109/TPEL.2020.2976206.

Chapter 10 - Genetic algorithm approach to PT design for inductorless resonant converters

10.1 Introduction

In Chapter 8, a lumped equivalent circuit model for the ring-dot PT is derived, allowing the equivalent circuit components to be estimated for a given ring-dot PT design. The models derived in Chapter 5 and Chapter 6 for the flexural spurious modes supplements the work done by Horsely *et al.* [10.1], and thus allows both the radial and spurious mode equivalent circuit components to be estimated for a given Transoner PT. Whilst these models allow a given PT design to be converted to an equivalent circuit, during the design stage a reverse process is required, with an application providing a desired electrical specification, leading to desired component values, and then a suitable PT design should be formulated to achieve these values. The process often requires expert knowledge, expensive design tools and trial and error to achieve a suitable PT design.

This chapter presents a genetic algorithm approach to PT design for resonant converter applications, allowing an engineer to provide an electrical converter specification and then an optimised PT design is found through several iterations of improvement. Unlike previous approaches, ring-dot PTs will also be designed using the model derived in Chapter 8 and spurious modes can also be accounted for using the analysis in Chapter 4. Additionally, this method considers circuit performance metrics rather than PT performance metrics, and thus a PT is optimised specifically for use in a resonant converter.

10.2 PT based half-bridge resonant converter design

The genetic algorithm presented here will be tasked with designing a PT that is optimal for use as part of a half-bridge resonant converter. The following section will introduce the half-bridge inverter and the two PT topologies.

10.2.1 Circuit design

10.2.1.a) Inductor-less half-bridge

The half-bridge topology is a popular topology for building PT based resonant converters, owing to its simplicity and its ability to achieve ZVS without additional magnetic components [10.2]. The circuit diagram for the PT based inductor-less half-bridge inverter is shown in Fig. 10.1.

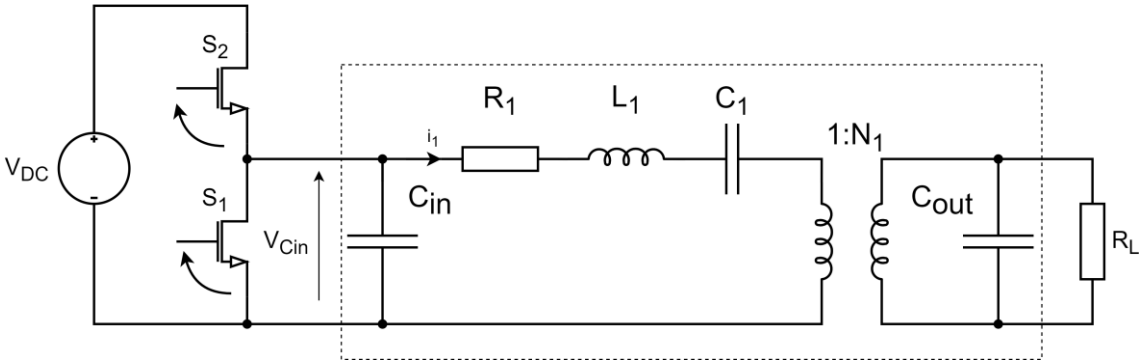

Fig. 10.1 – PT based inductor-less half-bridge resonant inverter, dotted section highlights the PT equivalent circuit

Achieving ZVS is vital for high efficiency operation, as it minimises switching losses. A detailed description of ZVS and the criteria for designing PTs to achieve ZVS with this circuit is discussed in detail in Chapter 9. The resulting trapezoidal signal that occurs at the input to the PT ($V_{C_{\text{in}}}$) is then filtered by the high Q-factor RLC tank, thus only allowing the fundamental component of the trapezoidal wave to pass, achieving a sinusoidal output across the load. In this implementation, an AC output will be assumed (i.e. no rectification and filtering of the output voltage) and thus a simple resistive load is used. The design algorithm will be tasked with designing a PT which allows ZVS to be achieved in this circuit, whilst simultaneously achieving the desired output voltage and maximising PT efficiency.

10.2.2 PT Design

Unlike previous genetic algorithm approaches (as discussed in section 2.7), the presented method will evaluate PT performance based on electrical characteristics rather than typical PT metrics, such as electromechanical coupling factor. To allow computation of these electrical characteristics, each PT must be converted to its electrical equivalent circuit. The following section will introduce each PT topology, describe the equivalent circuit extraction,

and discuss the physical limitations in the construction of each PT that should be factored into the design algorithm.

10.2.2.a) Ring-dot PT

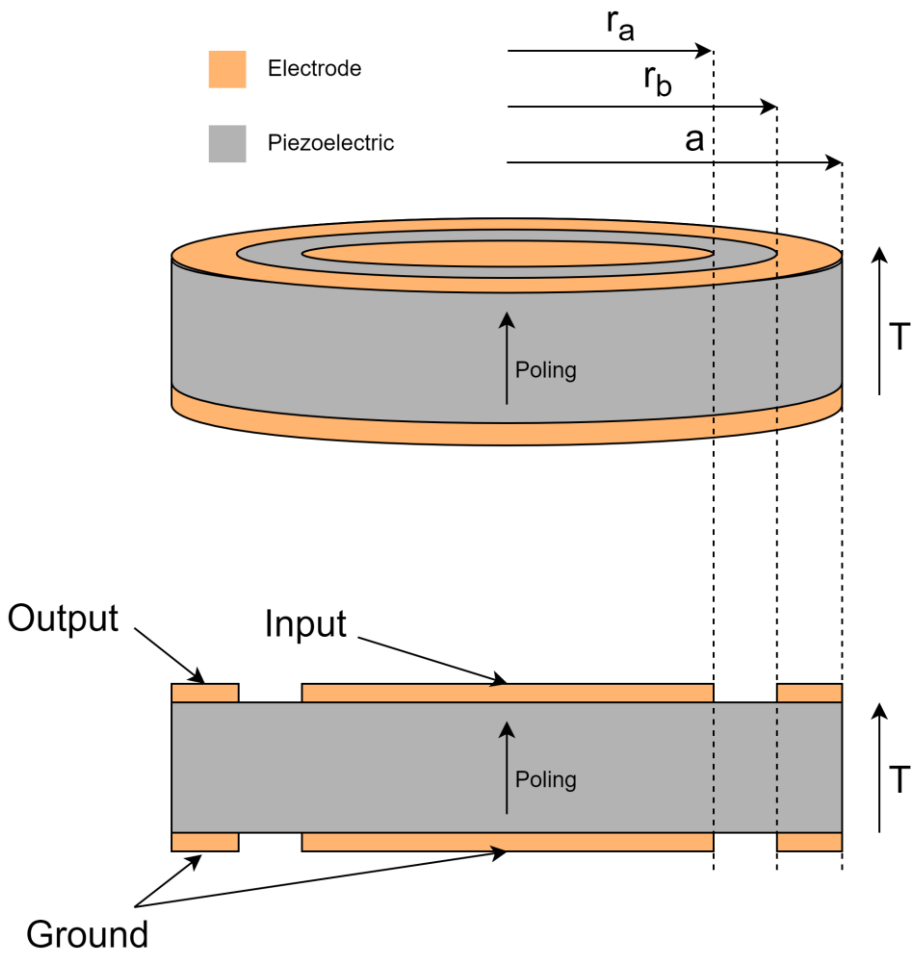

Fig. 10.2 – Ring-dot PT

Fig. 10.2 shows a schematic diagram of a ring-dot PT. As discussed previously, the ring-dot PT is a radial mode device, thus the design algorithm will design the PT and converter for operation at the PTs radial resonant frequency. The relationship between the material and dimensions of the PT on the one hand, and the electrical properties of the PT on the other, was derived in Chapter 8. Equations for the equivalent circuit parameters of this topology of PT when operated at the radial mode are thus given by (8.20)(8.57)(8.93)(8.94)(8.96)(8.97)(8.98)(8.99)(8.100),

$$L_1 = \frac{a^2 T \mathrm{J}_1(R)\rho(R^2+\sigma^2-1){s_{11}^{\mathrm{E}}}^2(\sigma-1)^2}{\Big(2\big((\sigma-1)\mathrm{Y}_1(R)+R\mathrm{Y}_0(R)\big)\Big)R^2\mathrm{J}_1\left(\frac{Rr_a}{a}\right)^2 r_a^2 d_{31}^2\pi^2} \tag{10.1}$$

$$C_1 = -\frac{\big(2(1+\sigma)\big)d_{31}^2\mathrm{J}_1\left(\frac{Rr_1}{a}\right)^2 r_a^2\pi^2\big((\sigma-1)\mathrm{Y}_1(R)+R\mathrm{Y}_0(R)\big)}{(\sigma-1)(R^2+\sigma^2-1)\mathrm{J}_1(R)Ts_{11}^{\mathrm{E}}} \tag{10.2}$$

$$R_1 = \frac{1}{Q}\sqrt{\frac{L_1}{C_1}} \tag{10.3}$$

$$C_{\mathrm{in}} = \frac{\pi r_a^2\left(2d_{31}^2+s_{11}^{\mathrm{E}}\varepsilon_{33}^{\mathrm{T}}(\sigma-1)\right)}{T(\sigma-1)s_{11}^{\mathrm{E}}} \tag{10.4}$$

$$C_{\mathrm{out}} = \frac{\pi(a^2-r_b^2)\left(2d_{31}^2+s_{11}^{\mathrm{E}}\varepsilon_{33}^{\mathrm{T}}(\sigma-1)\right)}{T(\sigma-1)s_{11}^{\mathrm{E}}} \tag{10.5}$$

$$N_1 = -\frac{r_a\mathrm{J}_1\left(\frac{Rr_a}{a}\right)}{\mathrm{J}_1(R)a-r_b\mathrm{J}_1\left(\frac{Rr_b}{a}\right)} \tag{10.6}$$

where R is the first positive solution of

$$\sigma - 1 + \frac{\mathrm{J}_0(R)R}{\mathrm{J}_1(R)} = 0 \tag{10.7}$$

One of the main challenges of designing a ring-dot PT, is that both capacitance ratio C_N, which should be carefully designed to optimise the ZVS performance of the converter (as discussed by Foster *et al*. [10.3]) and the turn ratio N_1, which should be carefully designed to achieve the desired output voltage, are controlled by changing the same physical dimensions (r_a, r_b, a). Therefore, the design space for these elements will be constricted. Due to manufacturing tolerances, there will be a minimum size of electrode and spacing between electrodes, this should be factored into the design. Additionally, as disc radii are typically only available in discrete sizes (typically whole millimetres), this should also be factored into the design algorithm.

10.2.2.b) Radial mode Transoner PT design

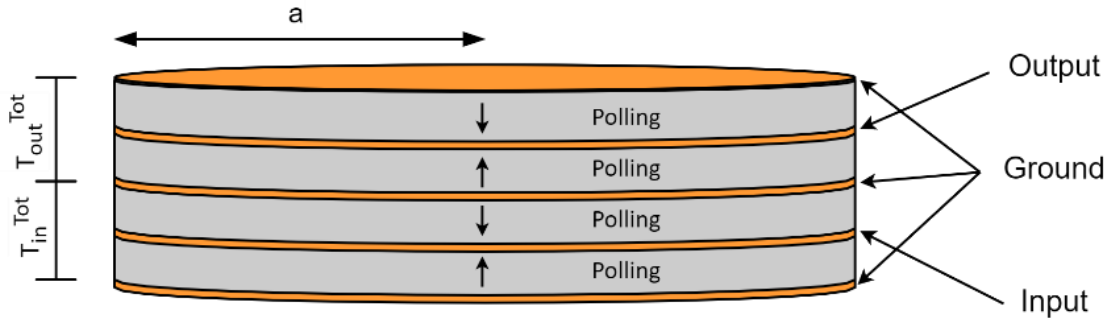

Fig. 10.3 – Radial mode Transoner PT

Fig. 10.3 shows a schematic diagram of a radial mode Transoner PT. Similar to the ring-dot PT, the Transoner is most optimally operated at the first radial vibration mode, thus this design algorithm will optimise the design of the PT for radial mode operation. Horsley *et al.* [10.1] derived equations for the equivalent circuit parameters of this PT when it is driven at the first radial vibration mode. Equations for the equivalent circuit parameters of the Transoner PT are given in equations (10.8)-(10.12).

$$L_1 = \frac{\left(T_{\text{in}}^{\text{Tot}} + T_{\text{out}}^{\text{Tot}}\right)\rho(R^2+\sigma^2-1)s_{11}^{\text{E}\,2}(\sigma-1)^2}{4\pi R^2 d_{31}^2 N_{\text{in}}^2} \tag{10.8}$$

$$C_1 = \frac{4N_{\text{in}}^2 d_{31}^2 a^2(\sigma+1)\pi}{(1-\sigma)(R^2+\sigma^2-1)s_{11}^{\text{E}}\left(T_{\text{in}}^{\text{Tot}} + T_{\text{out}}^{\text{Tot}}\right)} \tag{10.9}$$

$$C_{\text{in}} = \frac{\pi a^2 N_{\text{in}}^2 \varepsilon_{33}^{\text{T}}\left(1 - \frac{2d_{31}^2}{\varepsilon_{33}^{\text{T}} s_{11}^{\text{E}}(1-\sigma)}\right)}{T_{\text{in}}^{\text{Tot}}} \tag{10.10}$$

$$C_{\text{out}} = \frac{\pi a^2 N_{\text{out}}^2 \varepsilon_{33}^{\text{T}}\left(1 - \frac{2d_{31}^2}{\varepsilon_{33}^{\text{T}} s_{11}^{\text{E}}(1-\sigma)}\right)}{T_{\text{out}}^{\text{Tot}}} \tag{10.11}$$

$$N_1 = \frac{N_{\text{in}}}{N_{\text{out}}} \tag{10.12}$$

$$R_1 = \frac{1}{Q}\sqrt{\frac{L_1}{C_1}} \tag{10.13}$$

R has identical equations for both PT topologies. Although the model in [10.1] contains insulating and electrode layers, for simplicity they will be omitted in this design as their influence in most cases is negligible. Unlike the ring-dot PT, N_1 and C_{N}, can be controlled by different physical dimensions, thus allowing more freedom in the design than the ring-dot PT. However, unlike the ring-dot PT, the radial mode Transoner has several spurious modes that can occur around the radial resonance, which can influence the PTs performance as discussed by Erhart [10.4] and in Chapter 4. Therefore, control of spurious modes should also be considered in the design algorithm. Similar to the ring-dot PT, disc radii come in discrete sizes and therefore, this should be considered in the design. Although the layer thicknesses can be easily controlled to a high resolution, the number of layers in each section will be limited due to manufacturing constraints.

10.3 Genetic algorithm

A genetic algorithm is an optimisation tool. The GA here works to reduce the value of a cost (fitness) function which represents the performance of a design. The GA operates on a fixed population of candidate solutions with the design parameters encoded in a chromosome, where a chromosome in this context is a collection of PT design parameters. The performance of each candidate solution is then ranked, and then evolutionary concepts of breeding (crossover and mutation) are used to ensure the qualities of the best solutions are passed on to the next generation while still allowing a degree of search space exploring to avoid becoming caught up in a local minimum. Crossover is the process of combining two chromosomes to produce a subsequent child chromosome and mutation which allows a slight random variability of the parameters within a chromosome. After many generations the population will (if the problem is properly defined) converge to the optimal solution. In this implementation, a ‘continuous’ genetic algorithm was designed based on that presented in [10.5].

The input parameters to the genetic algorithm are:

- Electrical
    - DC input voltage
    - RMS output voltage
    - Output Power
    - Q factor or Damping resistance
    - Minimum K_{zvs} (see [10.3] and 10.3.1.e) for more details)
    - MOSFET output capacitance
- Mechanical
    - Min/Max PT total thickness
    - Min/Max PT radius
    - Minimum electrode size and resolution (ring-dot only)
    - Max number of layers (radial mode Transoner only)
- Material
- Simulation options
    - Population (see 11.5.1)
    - Reproductive rate (see 11.5.3.a)
    - Maximum mutation and mutation rate (see 11.5.5)
    - Number of generations (see 11.5.7)
    - Max number of stagnant generations (see 11.5.7)

Based on these inputs, the genetic algorithm will then execute based on the simulation options and should then return a PT which is within the mechanical bounds set by the user and when used in a resonant converter will aim to achieve the electrical specification.

Full details of the genetic algorithm can be found in Appendix 11.5. The following section will detail the key element of the genetic algorithm, the fitness function.

10.3.1 Fitness

The fitness of a PT is a measure of how well the PT will perform in the given application. The fitness function in this implementation is comprised of the following elements:

- Output voltage error compared to the specification
- Maximizing efficiency
- Minimizing vibration velocity
- Ability to achieve ZVS ($K_{\mathrm{zvs}} > 1$)

Additionally, as radial mode Transoner PTs contain spurious modes which can occur near the radial mode and affect performance, their impact is also considered. As Chapter 4 describes, spurious mode ill-effects can be avoided in most cases through achieving a large frequency

difference between optimum and spurious modes, and by maximising $\zeta_2\left(=\sqrt{L_2/C_2}\right)$ in the spurious modes. Therefore, these elements will be included in the fitness calculation for radial mode PTs.

10.3.1.a) Equivalent circuit parameter extraction

The first step to calculating a devices fitness, is to estimate the electrical equivalent circuit parameters using equations (10.1)-(10.6) for ring-dot and (10.8)-(10.12) for radial mode.

10.3.1.b) Operating frequency and output voltage error

Each PT is then evaluated to find the frequency (if any) at which the desired output voltage is achieved when the PT is used as part of a half-bridge converter. To do this, several assumptions are made.

Firstly, it will be assumed that the converter is being driven with a $\pi/2$ deadtime, ZVS is achieved (i.e. PT has been designed appropriately) and therefore the waveforms for $V_{C_{\mathrm{in}}}$ and i_1 will those shown in Fig. 10.4. Secondly, owing to the high Q-factor of the PT, we assume that only the fundamental of the input voltage passes through the RLC circuit to the output of the PT.

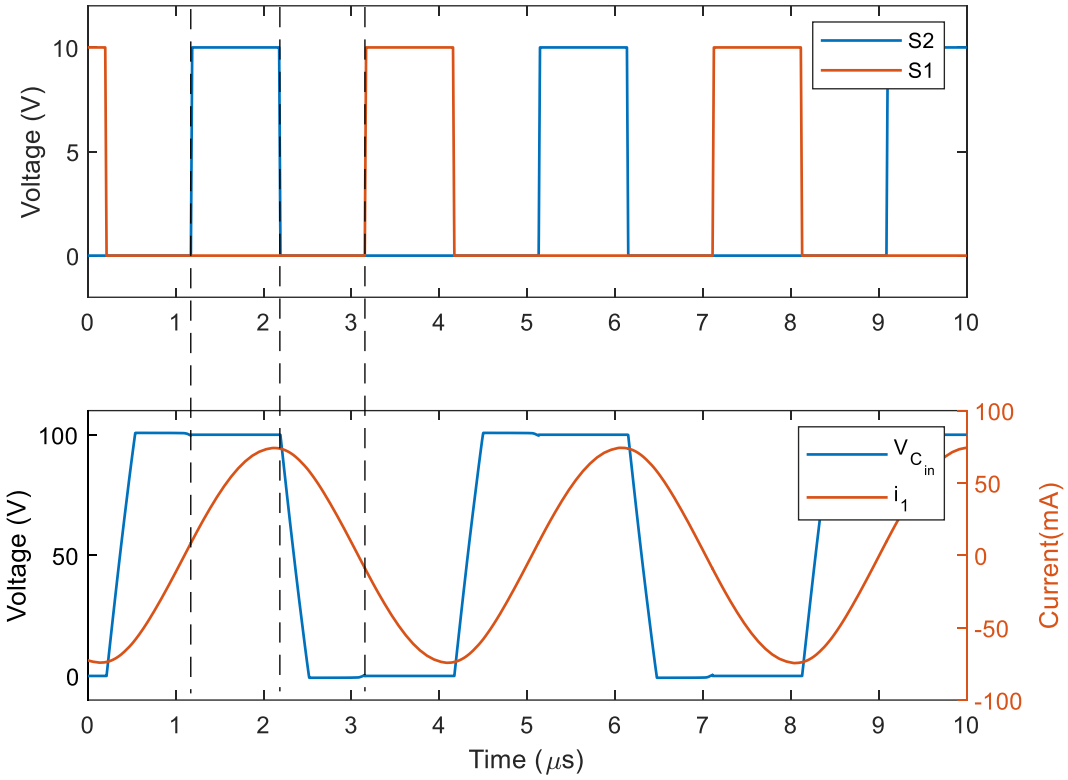

Fig. 10.4 – Waveforms $V_{C_{in}}$, i_1, and gate drive signals (S1 and S2) for the inductorless half bridge during ZVS operation

To determine the optimal (for accurate output voltage) operating frequency, first the amplitude of the voltage at the input of the PT, $V_{C_{\text{in}}}$, should be estimated. The trapezoidal input voltage to the PT can be approximated using only the fundamental component. The amplitude of the fundamental component of the trapezoidal input waveform is given by,

$$V_{\text{C}_{\text{in}}<1>} \approx \frac{4\sqrt{2}}{\pi^2} V_{\text{DC}} \tag{10.14}$$

where V_{DC} is the input DC link voltage to the half-bridge and $< 1 >$ signifies the first harmonic of a Fourier series. Therefore, the effective input voltage to the PT can be estimated as

$$v_{\text{in}}(\omega t) = V_{\text{C}_{\text{in}}<1>} \sin(\omega t) \tag{10.15}$$

Then, applying circuit analysis on the Mason equivalent circuit, the output voltage of the PT can be derived as follows.

The output voltage of a PT with a load R_L is defined as

$$V_{\text{out}} = I_{\text{out}} R_L \tag{10.16}$$

where I_{out} is given by,

$$I_{\text{out}} = \frac{I_1}{N_1} - I_{C_{\text{out}}} \tag{10.17}$$

and $I_{C_{\text{out}}}$ is given by,

$$I_{C_{\text{out}}} = \text{j} V_{\text{out}} \omega C_{\text{out}} \tag{10.18}$$

Then, substituting $I_{C_{\text{out}}}$(10.18) into I_{out} (10.17) and the result into V_{out} (10.16) gives,

$$V_{\text{out}} = \frac{I_1 R_L}{\text{j} N_1 \omega C_{\text{out}} \left(R_L - \frac{\text{j}}{\omega C_{\text{out}}} \right)} \tag{10.19}$$

Next, an equation for the resonant current, I_1, is derived. First, the input impedance of the PT and load is given by,

$$Z_{\text{in}} = R_1 + \text{j}\omega L_1 - \frac{\text{j}}{\omega C_1} + \frac{R_s}{N_1^2} - \frac{\text{j}}{\omega C_{\text{s}} N_1^2} \tag{10.20}$$

where R_{s} and C_{s} are the equivalent series RC representation of C_{out} and R_L evaluated at a frequency ω, they are given by,

$$R_s = \frac{R_L}{C_{\text{out}}^2 R_L^2 \omega^2 + 1} \tag{10.21}$$

$$C_{\text{s}} = \frac{C_{\text{out}}^2 R_{\text{L}}^2 \omega^2 + 1}{R_{\text{L}}^2 C_{\text{out}} \omega^2} \tag{10.22}$$

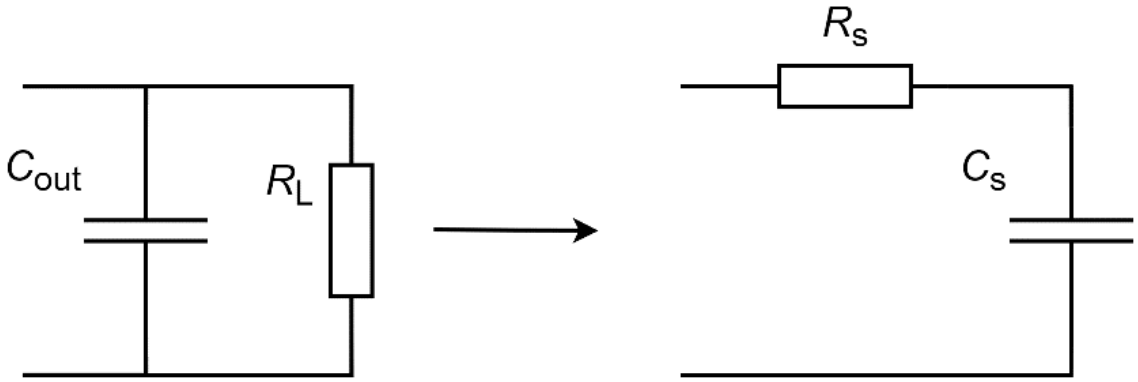

Fig. 10.5 – Output of PT, conversion of parallel to series circuit

For this algorithm, the user will supply a desired output voltage and a desired output power, rather than a specific load. The load can then be calculated as

$$R_L = \frac{V_{\text{out}_{\text{RMS}}}^2}{P_{\text{out}}} \tag{10.23}$$

Then, using Z_{in} (10.20) and $V_{C_{\text{in}}<1>}$ (10.14) the current, I_1, through the resonant circuit can be determined using,

$$I_1 = \frac{V_{\text{in}}}{Z_{\text{in}}} \approx \frac{V_{C_{\text{in}}<1>}}{Z_{\text{in}}} \tag{10.24}$$

Finally, the output voltage error is then calculated using,

$$V_{\text{out-err}} = \left| \frac{-\text{j}I_1 R_L}{N_1 \omega_{\text{op}} C_{\text{out}} \left(R_L - \frac{j}{\omega_{\text{op}} C_{\text{out}}} \right)} - V_{\text{out-spec}} \right| \tag{10.25}$$

where $V_{\text{out-spec}}$ is the desired output voltage and ω_{op} is the operating frequency (ω_{op} should occur at frequency close to the first radial vibration mode for both PT topologies). Using (10.25), ω_{op} can be found as the frequency which minimises $V_{\text{out-err}}$. Ideally, this should be achieved using a numerical solving function to achieve an accurate solution; however, to increase the speed of the fitness function computation, an approximate method will be used.

A linear search is performed over a range of frequencies to determine the frequency at which $V_{\text{out-err}}$ is minimised. The range of frequencies should be carefully selected to strike a balance between accuracy and execution speed. However, if possible, ZVS should always be achieved

at $\omega \geq \omega_1$ (where ω_1 is the resonant frequency of the radial mode). Additionally, it is known that maximum voltage gain occurs with $\omega \geq \omega_1$. Therefore, the frequency range $\frac{\omega_1}{2\pi}$ to $\left(\frac{\omega_0}{2\pi} + f_{\max}\right)$ was to be analysed. In this implementation, an $f_{\max}$ of 50 kHz was chosen. This value of $f_{\max}$ is suitable for radial mode PTs as typical resonant frequencies are within 50 kHz-250 kHz. For higher frequency PT (such as thickness mode PTs) a larger range of frequencies should be selected [10.6].

10.3.1.c) Efficiency

The efficiency of each PT when driving R_L at the operating frequency can then be estimated. An equation for the efficiency of a PT when driving a load of R_L (not including the effects of spurious modes) was derived in Chapter 4,

$$\eta_1 = \frac{R_L}{\left(C_{\text{out}}^2 R_L^2 \omega_{\text{op}}^2 + 1\right) N_1^2 R_1 + R_L} \tag{10.26}$$

10.3.1.d) Vibration velocity

Vibration velocity is another important factor to consider and is often neglected in PT design algorithms. The larger the vibration velocity, the greater the loss ($v_1 \propto I_1, \text{Power loss} \propto I_1^2 R_1$) and heat that is generated by the PT. As was found in [10.7] the damping resistance typically increases with heat, thus causing further increases in loss and heat. Additionally, there is also a limit to the maximum vibration velocity that a piezoelectric disc can handle before the disc will become cracked or damaged. Therefore, it is important that vibration velocity is minimised.

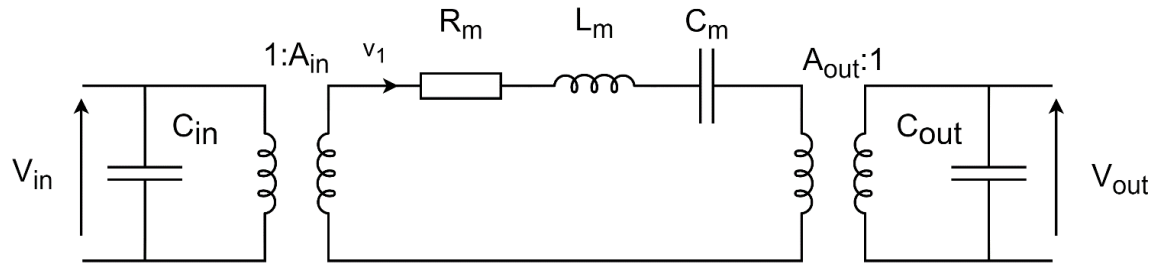

Fig. 10.6 – Two transformer Mason equivalent circuit

Based on the two-transformer form of the Mason equivalent circuit in Fig. 10.6, an equation for the vibration velocity can be derived in terms of P_{out} and R_{s},

$$v_{1_{\mathrm{RMS}}} = \sqrt{\frac{P_{\mathrm{out}}}{A_{\mathrm{out}}^2 R_{\mathrm{s}}}} \tag{10.27}$$

The force factor A_{out} for the ring-dot PT is given by

$$A_{\mathrm{out}} = \frac{2\pi d_{31}\left(a\mathrm{J}_1(R) - r_b\mathrm{J}_1\left(\frac{Rr_{\mathrm{b}}}{a}\right)\right)}{s_{11}^{\mathrm{E}}(\sigma - 1)\mathrm{J}_1\left(\frac{Rr_{\mathrm{a}}}{a}\right)} \tag{10.28}$$

and for the radial mode PT A_{out} is given by,

$$A_{\mathrm{out}} = \frac{2\pi a d_{31} N_{\mathrm{out}}}{s_{11}^{\mathrm{E}}(1-\sigma)} \tag{10.29}$$

Then, by substituting A_{out} (10.28) or (10.29) (depending on the topology) into $v_{1_{\mathrm{RMS}}}$ (10.27), the vibration velocity can be found.

10.3.1.e) ZVS factor K_{ZVS}

Achieving ZVS is one of the most difficult tasks in PT design and, as a result, is a widely discussed topic. Foster *et al.* [10.3] presented the most important contribution to this topic, with their criterion, stating that with a fixed 90° (25%) deadtime and if the $C_{\mathrm{N}} = \frac{C_{\mathrm{in}}}{N_1^2 C_{\mathrm{out}}}$ ratio of the PT is less than $2/\pi$, then ZVS is guaranteed for all loads. Whilst this does simplify the problem and provides a definitive starting point for designs, there are still several design decisions to be made. Additionally, in most cases the desired load will not be equal to the matched load, therefore, in some cases $C_{\mathrm{N}} > 2/\pi$ can still lead to a PT which will achieve ZVS. Finally, the criterion ensures ZVS can be achieved for a given PT but does not state the exact frequency at which ZVS is achieved, therefore, this may not be the operating frequency determined earlier.

For this algorithm, we will determine if or how close to achieving ZVS a PT based converter is when driving a specific load at the operating frequency as determined earlier. To do this we will use the K_{ZVS} parameter described by Foster et at [10.3]. K_{ZVS} is described as the voltage across the input capacitor, $V_{C_{\mathrm{in}}}$, just before the high side MOSFET switches on, normalised to the DC input voltage. For example, $K_{\mathrm{ZVS}} \geq 1$ means that $V_{C_{\mathrm{in}}}$ has exceeded the DC supply

voltage during the deadtime and therefore ZVS is achieved, whereas $K_{\mathrm{ZVS}} < 1$ means that ZVS has not been achieved. To calculated K_{ZVS} for each PT, the model derived in [10.3] will be used.

Firstly, the phase angle (ϕ) between v_{in} and i_1 needs to be found. As described by Foster *et al.* a numerical method should be used to solve equation 27 in [10.3] for ϕ. Typically, the Nelder-Mead simplex method is used. Nevertheless, to again improve the speed of the fitness computation, an approximation will be used in this work. Similar to the operating frequency estimation, a range of phase angles $-\pi > \phi > \pi$, will be tested in equation 27 of [10.3] and the value which minimises the output of equation 27, will then be assumed to be the best estimate of ϕ.

Once ϕ has been found, K_{ZVS} can be estimated using equation 18 in [10.3]. For this, the load resistance is set to that found from (10.23) R_L, rather than the matched load and the frequency is set to the operating frequency found from (10.25). The result of this computation is the K_{ZVS} value for these specific operating conditions.

10.3.1.f) Spurious mode avoidance

Unlike the ring-dot PT [10.4], one of the issues plaguing radial-mode Transoner PT designs is the impact of spurious modes. As discussed in detail in Chapter 4, spurious modes cause the efficiency to decrease, and reliability and longevity of the device to be reduced. In Chapter 4, methods for spurious mode avoidance are discussed, with large frequency difference and large ζ_2 $\left(\zeta_2 = \sqrt{L_2/C_2}\right)$ being the most critical. Again, it should be noted that the subscript '2' from the analysis in Chapter 4 is referring to the spurious mode of interest (closest spurious mode) rather than the 2nd mode (the first spurious mode).

Therefore, these quantities will be included in the fitness score, with better PTs maximising both quantities. Whilst the efficiency degradation (efficiency loss from spurious modes) could be calculated for each PT and this then used in the fitness score, the efficiency degradation is highly dependent on the loss in the spurious mode (R_2), which currently there is no method of accurately estimating. However, maximising both frequency difference and ζ_2, with good quality device construction and high *Q* materials, minimises loss in both operating and spurious modes and should ensure minimal efficiency degradation.

Based on the work in Chapter 5 and Chapter 6, there are two methods for estimating the equivalent parameters of the spurious modes in the radial mode PT, either using the classic plate theory (CPT) or Mindlin plate theory (MPT). Whilst the model based on MPT is much more accurate, especially when estimating the parameters of a thick (radius/thickness < 10) PTs, it is much more computationally complex and therefore, time consuming to estimate the relevant parameters using this method compared to the CPT method. Whilst more time consuming than the CPT, it is still significantly faster than using an FEA approach. Therefore, in this implementation we will present the user with a choice of using either model or no spurious mode approximation.

10.3.1.f.i) Classic plate model

Frequency difference

To find the frequency difference, the optimum mode resonant frequency and the spurious mode frequencies of the radial mode PT will first be found. As derived in [10.1], the radial resonant frequency of the radial-mode Transoner is found using,

$$\omega_1 = \frac{R}{a}\sqrt{\frac{1}{s_{11}^{\mathrm{E}}(1-\sigma^2)\rho}} \tag{10.30}$$

where R is the first positive root of (10.7). As discussed in [10.8], only the first 3 flexural spurious modes typically interfere with the radial mode when accounting for the typical range of piezoelectric discs currently available on the market. Therefore, the first 3 spurious mode resonant frequencies will be calculated; however, this could easily be extended if required to account for high order spurious modes. Similar to the radial vibration mode, as described in Chapter 5 the spurious resonant frequencies are found using,

$$\omega_{\mathrm{n}} = \frac{R_{s_{\mathrm{n}}}^2\sqrt{D}}{a^2\sqrt{\rho(\mathrm{T}^{\mathrm{Tot}})}} \tag{10.31}$$

where n is the order of the spurious resonant mode (i.e 1st spurious mode, $n = 2$) and D is the flexural rigidity given by

$$D = \frac{\mathrm{T}^{\mathrm{Tot}^3}}{12s_{11}^{\mathrm{E}}(\sigma^2-1)} \tag{10.32}$$

and R_{s_n} is the n^{th} positive root of,

$$\sigma + \frac{\left(\mathrm{I}_1(R_{s_n})\mathrm{J}_0(R_{s_n})R_{s_n} + \mathrm{I}_0(R_{s_n})\mathrm{J}_1(R_{s_n})R_{s_n} - 2\mathrm{J}_1(R_{s_n})\mathrm{I}_1(R_{s_n})\right)}{2\mathrm{J}_1(R_{s_n})\mathrm{I}_1(R_{s_n})} \tag{10.33}$$

As was found in Chapter 4, only the closest spurious mode to the radial mode (in terms of resonant frequency) needs to be considered. Therefore, the minimum frequency difference between radial (ω_1) and closest spurious mode is found using

$$\Delta\omega = \frac{\min\left((|\omega_1 - \omega_2|), (|\omega_1 - \omega_3|), (|\omega_1 - \omega_4|)\right)}{\omega_1} \tag{10.34}$$

Additionally, m is defined as the value of n for the closest spurious mode.

Calculating ζ_2

ζ_2 can be calculated using the CPT model derived in Chapter 5. Equations for L_m and C_m are combined and ζ_2 can be calculated using,

$$\zeta_2 = \sqrt{\frac{L_m}{C_\mathrm{m}}} = \frac{\sqrt{\sigma^2 - 1}\left(\psi\sqrt{\rho}\sqrt{(\sigma - 1)}\left(\mathrm{T}^{\mathrm{Tot}}\right)^2 s_{11}^{\mathrm{E}\,\frac{3}{2}}\sqrt{3}\right)}{12N_{\mathrm{in}}^2 T_{\mathrm{out}}^{\mathrm{Tot}\,2} d_{31}^2 \mathrm{I}_1\left(R_{\mathrm{s_m}}\right)^2 R_{\mathrm{s_m}}^2 (1+\sigma)\pi} \tag{10.35}$$

where m is the mode of minimum frequency difference and ψ is given by

$$\psi = (2\sigma^2 - 2\sigma)\mathrm{I}_1\left(R_{\mathrm{s_m}}\right)^2 + 2R_{\mathrm{s_m}}\mathrm{I}_0\left(R_{\mathrm{s_m}}\right)(\sigma - 1)I_1\left(R_{\mathrm{s_m}}\right) + R_{\mathrm{s_m}}^2\mathrm{I}_0\left(R_{\mathrm{s_m}}\right)^2 \tag{10.36}$$

10.3.1.f.ii) Mindlin plate model

Extracting the relevant parameters using the Mindlin plate model presented in Chapter 6, is significantly more complex. In order to first extract L_m and C_m in the spurious mode equivalent circuit, thus allowing ζ_2 and frequency difference to be calculated, the input impedance of the PT must first be simulated around the offending spurious resonance. Then, using an extraction method, such as those presented in Chapter 3, the equivalent components can be determined. However, this method requires simulating the input impedance of many devices at several frequency ranges, which owing to the large number of devices analysed, would lead to slow operation (but still significantly faster than FEA).

To optimise the operational speed, first, the approximate resonant frequencies of each spurious mode occurring at a frequency in the vicinity of the radial mode are determined.

Firstly, the roots of equation (6.57) are found, in order to give an equation that can be numerically solved for the resonant frequencies,

$$\frac{\begin{pmatrix}[(1-\sigma)(\sigma_1-\sigma_2)\mathrm{J}_1(\delta_2 a)-\mathrm{J}_0(\delta_2 a)a\delta_2(B-\sigma_2)(B-\sigma_1+1)]\mathrm{J}_1(\delta_1 a)\\ +\mathrm{J}_0(\delta_1 a)\mathrm{J}_1(\delta_2 a)a\delta_1(B-\sigma_2+1)(B-\sigma_1)\end{pmatrix}}{\mathrm{J}_1(\delta_1 a)\mathrm{J}_1(\delta_2 a)(\sigma_1-\sigma_2)} \qquad (10.37)$$

where $\sigma_1, \sigma_2, \delta_1, \delta_2$ and B are defined in Chapter 6. Then, an array of frequencies in the range $0.4\omega_1 < \omega < 1.6\omega_1$, are substituted into $\sigma_1, \sigma_2, \delta_1, \delta_2$ and B. Finally, the resulting $\sigma_1, \sigma_2, \delta_1, \delta_2$ and B arrays are substituted into (10.37), where the zero crossings (non-asymptotic) in the resulting output array highlight frequencies at which a spurious mode occurs. A graph of the output of (10.37) for a sample PT is shown in Fig. 10.7.

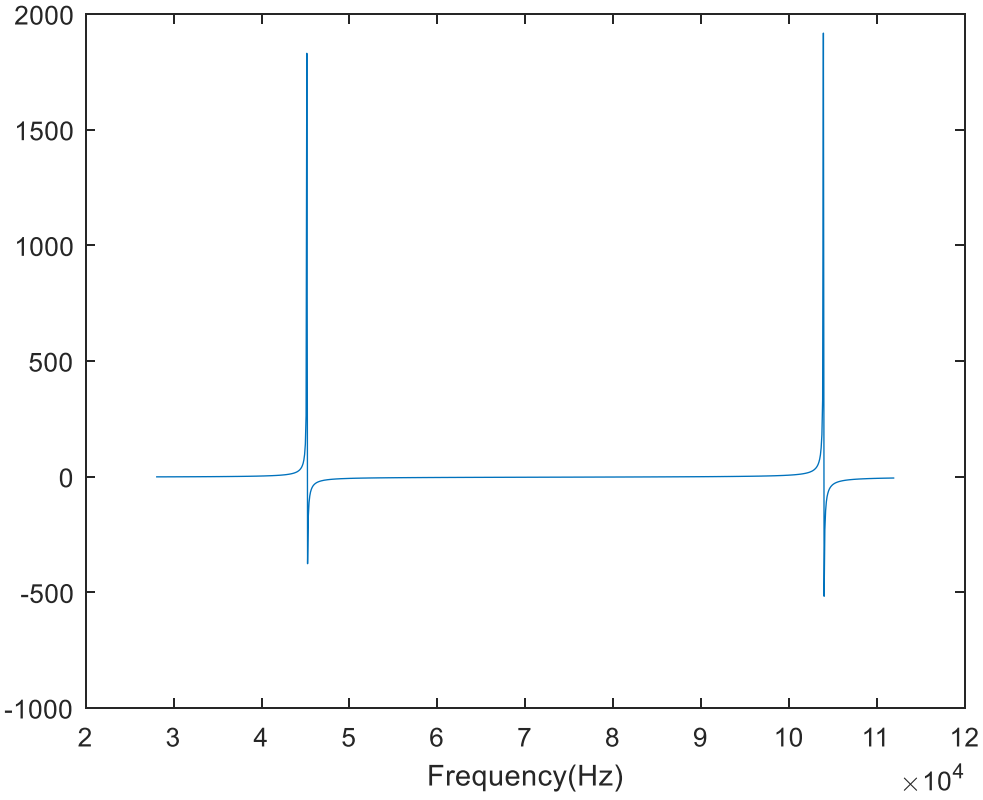

Fig. 10.7 – Output of (10.37) for a sample PT

Once the approximate locations of the spurious modes are known, then the nearest spurious mode to the radial mode can now be determined. This is achieved by first finding the roots of (10.37), which gives the approximate spurious resonant frequencies. The frequency difference with the radial mode is then computed for each mode, with the minimum frequency difference indicating to the closest mode. Whilst the approximate resonant

frequencies could then be used to compute the frequency difference, due to the lack of frequencies evaluated (for increased speed), the resulting spurious resonant frequency might be imprecise. Therefore, a second simulation is performed. However, this time a concentrated frequency selection can be made, as the approximate location of each mode is known. A frequency range $\omega_{\mathrm{spur}_{\mathrm{approx}}} - 10\pi < \omega < \omega_{\mathrm{spur}_{\mathrm{approx}}} + 10\pi$ was selected. The range of 5kHz above and below the approximate resonant frequency was chosen though trial and error. Again, this frequency array was substituted into $\sigma_1, \sigma_2, \delta_1, \delta_2$ and B and then into,

$$Z_{\mathrm{in}} = \frac{Z_{C_{\mathrm{in}}}\left(\frac{Z}{A_{\mathrm{in}}^2}\right)}{Z_{C_{\mathrm{in}}} + \left(\frac{Z}{A_{\mathrm{in}}^2}\right)} \tag{10.38}$$

where $Z_{C_{\mathrm{in}}}$ is given by,

$$Z_{C_{\mathrm{in}}} = \frac{1}{\mathrm{j}\omega C_{\mathrm{in}}} \tag{10.39}$$

Z is defined as,

$$Z = \frac{2\mathrm{j}\pi D\left(\begin{pmatrix} -(\sigma-1)(\sigma_1-\sigma_2)\mathrm{J}_1(\delta_2 a) \\ -\mathrm{J}_0(\delta_2 a)a\delta_2(B-\sigma_2)(B-\sigma_1+1) \end{pmatrix}\mathrm{J}_1(\delta_1 a) + \mathrm{J}_0(\delta_1 a)\mathrm{J}_1(\delta_2 a)a\delta_1(B-\sigma_2+1)(B-\sigma_1)\right)}{\mathrm{J}_1(\delta_1 a)\mathrm{J}_1(\delta_2 a)(\sigma_1-\sigma_2)\omega} \tag{10.40}$$

and where C_{in} is defined in (10.10) and D given by,

$$D = \frac{\mathrm{T}^{\mathrm{Tot}^3}}{12(1-\sigma^2)s_{11}^{\mathrm{E}}} \tag{10.41}$$

Thus, allowing the input impedance spectra of the spurious mode occurring nearest to the radial mode to be estimated. The frequencies of the impedance maxima (f_{m_a}) and minima (f_{m}) of this mode are extracted. This allows L_m and C_m of the spurious mode to calculated using method 2 presented in Chapter 3,

$$C_m = C_{\mathrm{in}}\frac{{f_{m_a}}^2 - {f_{\mathrm{m}}}^2}{{f_{\mathrm{m}}}^2} \tag{10.42}$$

$$L_m = \frac{1}{\left(4{f_{m_a}}^2\pi^2 - 4{f_{\mathrm{m}}}^2\pi^2\right)C_{\mathrm{in}}} \tag{10.43}$$

Finally, the frequency difference and ζ_2 are calculated using

$$\Delta\omega = \frac{\left|\omega_1 - \frac{1}{\sqrt{L_2 C_2}}\right|}{\omega_1} \tag{10.44}$$

$$\zeta_2 = \sqrt{\frac{L_m}{C_{\mathrm{m}}}} \tag{10.45}$$

It should be noted that the 'm' notation is used throughout, however, ζ_2 is used to ensure the notation here agrees with the analysis in Chapter 4, in which these parameters are relevant to. Again, as discussed, the subscript '2' is referring to the spurious mode of interest not the first spurious mode.

10.3.1.f.iii) No spurious mode calculation

In some scenarios, a user may not require or desire spurious mode avoidance. This may be for a several reasons, such as the error in the spurious mode model negatively impacting the results or for increased computation speed. In these cases, ζ_2 and $\Delta\omega$ are not computed and thus they are not included in the fitness score.

10.3.1.g) *Fitness score*

To be able to quantify how well each PT performs, a single fitness score will be generated combining each of the quantities previously derived. Firstly, some adjustments should be made to each parameter to avoid a single quantity having an overly significant impact of the overall fitness score.

As V_{out} is roughly approximated (the linear search used to determine $V_{\mathrm{out\text{-}Err}}$ has limited frequency resolution), it is likely that the $V_{\mathrm{out\text{-}Err}}$ that is calculated is likely to be imprecise. Therefore, PTs could be unfairly penalised due to this imprecision.

A solution to this issue is to increase the frequency resolution; however, this would decrease computation speed. Therefore, the $V_{\mathrm{out\text{-}Err}}$ value for each PT will be capped to account for this. First, V_{tol} is defined as the maximum acceptable output voltage error, which in this

implementation is set to 0.1V. For each PT, if $V_{\text{out-Err}} < V_{\text{tol}}$ then $V_{\text{out-Err}} = V_{\text{tol}}$, thus meaning the lowest achievable $V_{\text{out-Err}}$ is V_{tol}. This can be written as,

$$V_{\text{out-Err}} = V_{\text{out-Err}}[V_{\text{out-Err}} < V_{\text{tol}}] = V_{\text{tol}} \tag{10.46}$$

By rounding $V_{\text{out-Err}}$, PTs are not penalised for not being able to achieve exact $V_{\text{out-spec}}$ values in our approximation, whilst still ensuring devices that are only able to produce very inaccurate output voltages are penalised in the score.

This same process is performed for spurious mode frequency difference and ζ_2 as to avoid over optimising these parameters,

$$\zeta_2 = \zeta_2\left[\zeta_2 > \zeta_{2_{\text{tol}}}\right] = \zeta_{2_{\text{tol}}} \tag{10.47}$$

$$\Delta\omega = \Delta\omega[\Delta\omega > \Delta\omega_{\text{tol}}] = \Delta\omega_{\text{tol}} \tag{10.48}$$

Using the adjusted quantities, the fitness score for a ring-dot PT is then given by

$$\text{Fit} = (1-\eta)V_{\text{out-Err}}|v_1| \tag{10.49}$$

whereas, for a radial mode Transoner PT including adjusted ζ_2 and $\Delta\omega$ values, the fitness score is calculated using

$$\text{Fit} = (1-\eta)V_{\text{out-Err}}|v_1|\,\frac{1}{\Delta\omega}\frac{1}{\zeta_2} \tag{10.50}$$

with smaller fitness values signifying better devices. It should be noted that K_{ZVS} does not feature in these fitness scores. Whilst $K_{\text{ZVS}}$is an important quantity to consider, to the authors knowledge there is no advantage to having $K_{ZVS} \gg 1$. However, K_{ZVS} should be included in the design algorithm, therefore, an adjustment to the fitness is made

$$\text{Fit} = \text{Fit}[K_{\text{ZVS}} < \min K_{\text{ZVS}}] = [\,] \tag{10.51}$$

where [ ] signifies the removal of this PT from the current generation of devices. Therefore, devices which do not achieve at least the $\min K_{\text{ZVS}}$ spec will be removed. However, especially in cases with small population sizes (P) and in early generations is it possible that all devices will not achieve the desired K_{ZVS} value. In this case, the population stage is repeated until at

least 1 device is suitable. In some cases, based on the electrical spec it may not be possible to design a suitable device, therefore, the algorithm will exit after $\mathrm{maxFail}$ generations with no suitable PT.

10.4 Implementation

The algorithm described in the previous section was implemented as part of a web application. The genetic algorithm and backend of the website were implemented in Python, due its wide array of libraries for both mathematical computation and web development. The web app will be developed with the Flask framework in Python 3.

10.4.1 Algorithm

Due to the relatively slow execution of Python, several optimised libraries were used to expedite the mathematical computations. The NumPy library was used for most of the computations. NumPy provides a large array of mathematical functions optimised to run on large vectors/matrices. To take advantage of NumPy, the algorithm was written in a 'vectorized' format, therefore reducing the number of loops used and allowing computations on vectors/matrices which execute much faster (as NumPy is implemented in C). Additionally, SciPy was used for Bessel functions and numerical solving algorithms and the python cMath library for computations on complex numbers. However, even with the optimised NumPy library, some operations such as solving for $V_{\mathrm{out-err}}$, ϕ and K_{ZVS} still are performed slowly owing to the large, multidimensional matrices involved. To further expedite these computations, the NumExpr [10.9] library was used. This library has several functions which are similar to those in the NumPy library, however, the computation is executed across multiple threads allowing better use of modern server hardware, therefore, speeding up computation.

10.4.2 Web application

The Flask framework was chosen, owing to the fact it is lightweight and easy to use. The frontend of the app was written in plain HTML with styling done using Twitter Bootstrap 4. The desktop user interface is shown in Fig. 10.8 and the mobile user interface is shown in Fig. 10.9.

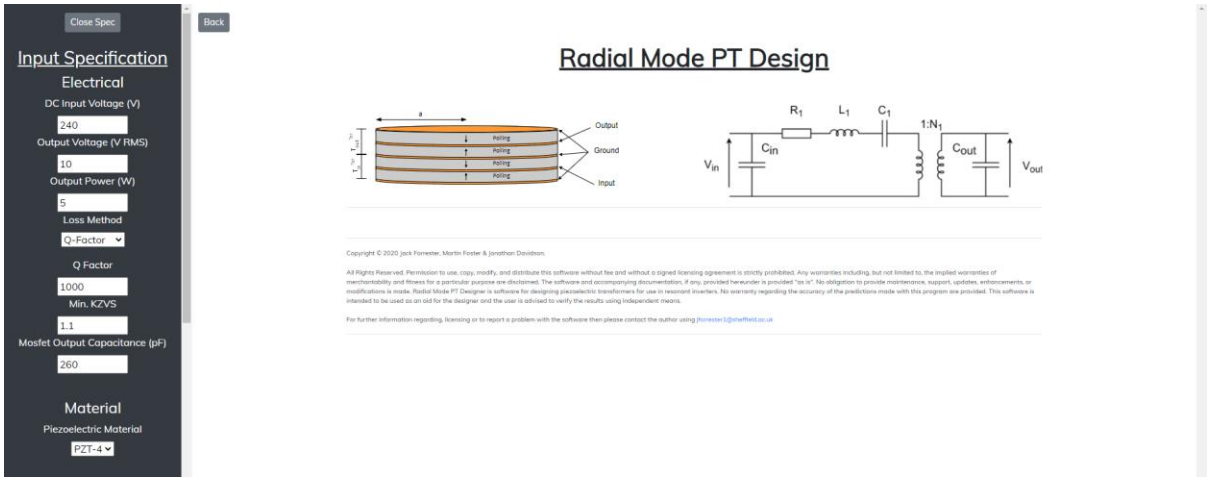

Fig. 10.8 – Desktop UI for the radial mode PT genetic algorithm web application

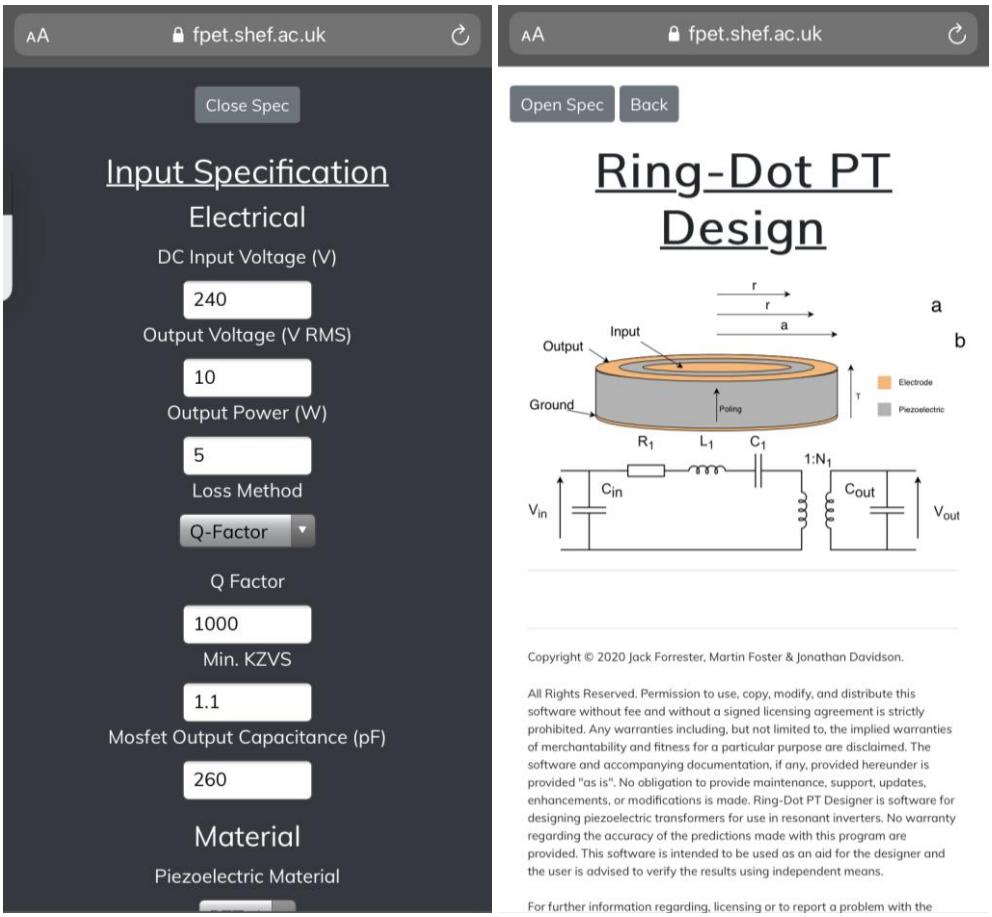

Fig. 10.9 – Mobile UI for the ring-dot PT genetic algorithm web application, specification (left) and content (right)

In the desktop version of the web application, the user supplies inputs on the left-hand side panel, then the results are presented in the main central section of the page. To account for the smaller screen size, the mobile version of the app presents the input section and the main

section using the full screen width, with a toggle between the two, as is shown in Fig. 10.9. This makes both entering input and visualising results easier on a smaller screen.

The top of the page shows a schematic diagram of a ring-dot/radial mode PT and a diagram of the Mason equivalent circuit, to give context to the returned design variables. The main body of the page contains the chosen PT's physical and electrical properties, along with efficiency, vibration velocity, K_{ZVS} and the operation frequency (and ζ_2 and $\Delta\omega$ in the cases of the radial mode PT). Finally, there are several plots which show Z_{in}, $V_{C_{\mathrm{in}}}$, i_1 and V_{out}. These plots are generated using the Plotly.js library. Additionally, another Plotly.js plot is presented which shows the how the fitness of the best PT changes per generation for diagnostic purposes.

As running the algorithm and producing the simulated graphs take considerable computation time, it is more appealing to return the data to the user asynchronously. This allows the page to be loaded first, then upon pressing submit, data is passed between the front and backend without reloading the page. This means that parts of the page can be loaded before others, allowing data to be returned to the user much quicker. To achieve this, Asynchronous JavaScript and XML (AJAX) calls were used, which was done through jQuery. The flow of data is as follows:

1. Upon the user pressing submit, form data is converted to JSON format and is passed to the flask backend through an AJAX call. The form data is parsed and passed into the genetic algorithm, which is then executed.
2. The results of the genetic algorithm are then returned to the frontend as part of the AJAX call in a JSON format. The JSON data is parsed and presented to the user. Additionally, the fitness data is loaded into a Plotly.js graph using jQuery.
3. A second AJAX call is then used to retrieve simulation data for the resulting PT. Relevant data (equivalent circuit parameters, load and input voltage) is passed from the frontend to the backend in JSON format. The flask backend parses the JSON data and runs a function to simulate the PT. The simulated data is again JSON formatted and returned to the frontend.
4. Finally, the data is loaded into the Plotly.js graphs using jQuery.

10.4.3 Simulation of PT

To confirm the validity of the resulting PT to the user, a simulation will be performed to show relevant electrical waveforms. A SPICE simulation could be used; however, a more efficient approach is to derive equations for the relevant electrical quantities. Equations for V_{out}, $V_{C_{\text{in}}}$ and i_1 are derived in Appendix 11.6 and are then used to simulate the relevant waveforms.

10.4.4 Deployment

The final application is deployed on a local IIS webserver using WSGI and FastCGI [10.10]. The application can be accessed (at the time of writing) at https://fpet.shef.ac.uk/PTDesigner/RingDotGenetic for the ring-dot PT and https://fpet.shef.ac.uk/PTDesigner/RadialMode for the radial mode Transoner PT.

10.5 Validation

To validate the design algorithm, a ring-dot PT will be designed for a sample application. The input impedance spectrum of the PT will then be simulated in COMSOL and from this input impedance spectrum, the electrical equivalent circuit for the PT will be extracted using method 3 presented in Chapter 3. Finally, using the electrical equivalent circuit, the half-bridge-based inverter is simulated in LTSpice, where the electrical specifications of the resulting inverter can be verified. The desired electrical specification of the resonant inverter is shown in Table 10.1, the mechanical specification is shown in Table 10.2 and the simulation settings are shown in Table 10.3.

Table 10.1 – Desired electrical specification

V_{DC} (V)	V_{out} (V_{RMS})	P_{out}(W)	η	K_{ZVS}
240	10	5	85%+	>1

Table 10.2 – Mechanical specification

Min-Max Thickness $(\mathbf{mm})$	Min-Max Radius $(\mathbf{mm})$	Min. electrode radius $(\mathbf{mm})$	Electrode resolution $(\mathbf{mm})$
0.75 - 3	4 - 15	1	0.2

Table 10.3 – Simulation settings

Max mutation amount (MutAm) $(\mathbf{mm})$	Reproductive rate (%) (X)	Max generations	Population (P)	Max number of stagnant generations
0.1	50	2000	200	1000

Using these specifications and PZT-4 material with a Q-factor of 1000, the ring-dot genetic algorithm is executed using the online web app. The resulting PT and circuit performance metrics are extracted for comparison with COMSOL.

10.5.1 Results

The results of the simulation using the presented ring-dot genetic algorithm are shown in Table 10.4, Table 10.5 and Table 10.6.

Table 10.4 – Resulting PTs physical specifications from genetic algorithm

$a\ (\mathbf{mm})$	$r_a\ (\mathbf{mm})$	$r_b\ (\mathbf{mm})$	$T\ (\mathbf{mm})$
14	4.02	5.79	1

Table 10.5 – Resulting PTs electrical equivalent circuit parameters estimated from genetic algorithm

$R_1(\Omega)$	$L_1\ (\mathbf{mH})$	$C_1\ (\mathbf{pF})$	$C_{\mathbf{in}}\ (\mathbf{nF})$	$C_{\mathbf{out}}\ (\mathbf{nF})$	N_1
43	84.4	45.85	0.532	5.347	0.197

Table 10.6 – Resulting circuit specification

V_{out} (V_{RMS})	η (%)	Vibration Velocity $v_1(\text{m/s})$	K_{ZVS}	Operating Frequency (kHz)
10	92.3	0.269	1.1	81.71

The resulting PT exhibits the desired output voltage whist achieving a K_{ZVS} value equal to the minimum specification. Additionally, the resulting PT exhibits high efficiency and relatively low vibration velocity, proving the effectiveness of the algorithm. To validate the results, the PT is then simulated in COMSOL, using a 2D axisymmetric model and performing a frequency domain study at frequencies around the radial resonant frequency. The resulting input and output impedance spectra (with output and input shorted respectively) from the simulation are shown in Fig. 10.10.

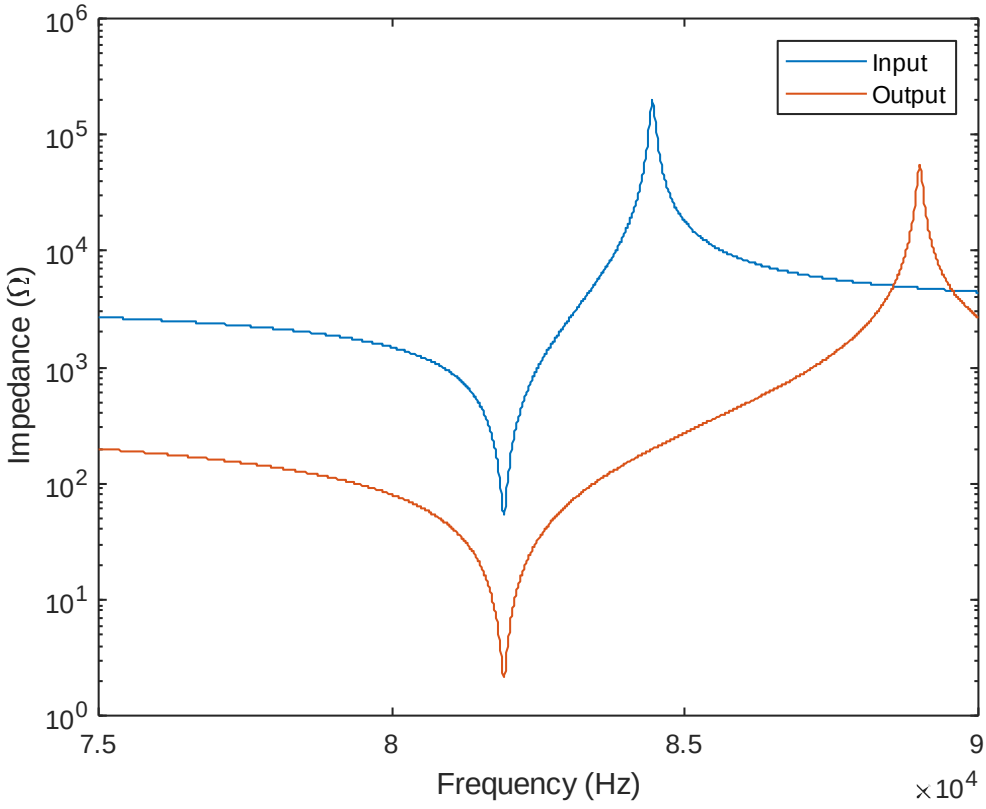

Fig. 10.10 – Input and output impedance spectra of resulting PT from COMSOL

From these impedance spectra the equivalent circuit parameters of the PT can be accurately estimated using method 3 presented in Chapter 3. The resulting equivalent circuit parameters are shown in Table 10.7.

Table 10.7 – Resulting PT electrical specification from COMSOL simulation and extraction using method presented in section 3.4

$R_1(\Omega)$	$L_1(\mathrm{mH})$	$C_1(\mathrm{pF})$	$C_{\mathrm{in}}(\mathrm{nF})$	$C_{\mathrm{out}}(\mathrm{nF})$	N_1
54.5	106.0	35.6	0.568	5.07	0.197

Comparing Table 10.7 with Table 10.5, in general the estimated parameters are accurate to those achieved through COMSOL simulation. Whilst N_1 exhibits 0% error and C_{in} and C_{out} exhibit 5.9% on average, L_1 and C_1 have an average error of 24.5% compared to COMSOL simulated results.

Finally, simulating a half-bridge-based PT inverter in LTSpice using the extracted equivalent circuit allows the electrical performance of the inverter to be evaluated. The half-bridge was made from two IRF510 MOSFETs. The operating frequency of the inverter was minimally adjusted to ensure the PT based inverter achieves the correct output voltage and thus power. Table 10.8 shows key electrical performance metrics for the inverter and Fig. 10.11 shows the output voltage and input voltage ($V_{C_{\mathrm{in}}}$) to the PT.

Table 10.8 – Resulting PT converter circuit specification

V_{out} $(\mathrm{V_{RMS}})$	$P_{\mathrm{out}}(\mathrm{W})$	η_{PT} (%)	η_{Circuit} (%)	Operating Frequency (kHz)
9.99	4.99	92.3	92.3	82.3

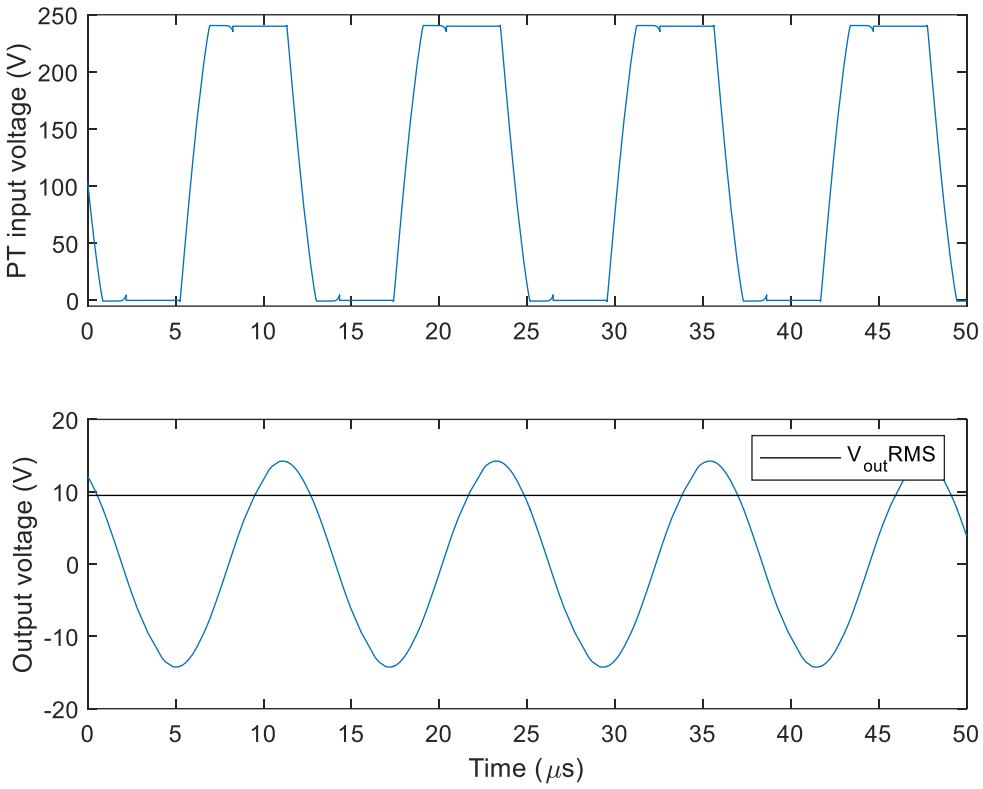

Fig. 10.11 – $V_{C_{in}}$ and V_{out} of the resulting converter from LTSpice

Firstly, the results in Table 10.8 show that the PT based converter can achieve the correct output voltage and correct output power, whilst operating at a frequency with only a 0.71% error compared to that presented by the algorithm. Additionally, as shown in Fig. 10.11 the converter also achieves ZVS as predicted by the genetic algorithm. As a result, the overall circuit efficiency is the same as the PT efficiency and therefore, the loss across the switches is negligible, confirming ZVS is achieved. Finally, the estimated PT efficiency by the genetic algorithm is the same as that given by the LTSpice simulation. Whilst it is not possible to say the resulting PT is the most optimal PT for this application, the PT design produced by the genetic algorithm is proven to be an excellent PT for this application.

10.6 Summary

In summary, an automated ring-dot and Transoner PT designer for resonant circuit applications has been presented. The automated PT designer uses a genetic algorithm to determine the most optimal PT. The genetic algorithm optimises the PT design based on a fitness score which is derived from several important parameters of resonant circuit design,

including efficiency, output voltage accuracy, ZVS performance and spurious mode avoidance. The resulting automated design algorithm is verified against finite element and circuit simulations.

10.7 References

[10.1] E. L. Horsley, A. V. Carazo, M. P. Foster, and D. A. Stone, 'A Lumped Equivalent Circuit Model for the Radial Mode Piezoelectric Transformer', in *2009 Twenty-Fourth Annual IEEE Applied Power Electronics Conference and Exposition*, Feb. 2009, pp. 1747–1753. doi: 10.1109/APEC.2009.4802906.

[10.2] M. Ekhtiari, Z. Zhang, and M. A. E. Andersen, 'State-of-the-art piezoelectric transformer-based switch mode power supplies', in *IECON 2014 - 40th Annual Conference of the IEEE Industrial Electronics Society*, Oct. 2014, pp. 5072–5078. doi: 10.1109/IECON.2014.7049271.

[10.3] M. P. Foster, J. N. Davidson, E. L. Horsley, and D. A. Stone, 'Critical Design Criterion for Achieving Zero Voltage Switching in Inductorless Half-Bridge-Driven Piezoelectric-Transformer-Based Power Supplies', *IEEE Transactions on Power Electronics*, vol. 31, no. 7, pp. 5057–5066, Jul. 2016, doi: 10.1109/TPEL.2015.2481706.

[10.4] J. Erhart, P. Pulpán, R. Dolecek, P. Psota, and V. Lédl, 'Disc Piezoelectric Ceramic Transformers', *IEEE Transactions on Ultrasonics, Ferroelectrics, and Frequency Control*, vol. 60, no. 8, pp. 1612–1618, Aug. 2013, doi: 10.1109/TUFFC.2013.2742.

[10.5] R. L. Haupt and S. E. Haupt, *Practical genetic algorithms*, 2nd ed. Hoboken, N.J: John Wiley, 2004.

[10.6] V. Carazo and Alfredo, 'Piezoelectric Transformers: An Historical Review', *Actuators*, vol. 5, no. 2, p. 12, Apr. 2016, doi: 10.3390/act5020012.

[10.7] T. Andersen, M. A. E. Andersen, O. C. Thomsen, M. P. Foster, and D. A. Stone, 'Nonlinear effects in piezoelectric transformers explained by thermal-electric model based on a hypothesis of self-heating', in *IECON 2012 - 38th Annual Conference on IEEE Industrial Electronics Society*, Oct. 2012, pp. 596–601. doi: 10.1109/IECON.2012.6388760.

[10.8] J. Forrester, J. Davidson, and M. Foster, 'Effect of Spurious Resonant Modes on the Operation of Radial Mode Piezoelectric Transformers', in *PCIM Europe 2018; International Exhibition and Conference for Power Electronics, Intelligent Motion, Renewable Energy and Energy Management*, Jun. 2018.

[10.9] *pydata/numexpr*. Python for Data, 2020. Accessed: Sep. 30, 2020. [Online]. Available: https://github.com/pydata/numexpr

[10.10] M. Corporation, *wfastcgi: An IIS-Python bridge based on WSGI and FastCGI.* Accessed: Nov. 03, 2020. [Online]. Available: http://aka.ms/python

Chapter 11 - Summary, conclusion, and further work

11.1 Summary

Three novel general-purpose methods for extracting the Mason equivalent-circuit components of a PT have been presented. Each method has been compared in several areas, including the implementation difficulty and extraction accuracy. The results of the comparison have shown that all methods provide acceptable extraction accuracy, with methods 1 and 3 proving to be more accurate in certain situations. Although method 2 is the least accurate of all the methods, it requires less expensive measurement equipment to perform than methods 1 and 3 and has the lowest computational complexity. Proving that all three methods have their advantages. Additionally, a novel approach to equivalent circuit parameter extraction from high-damping/low-capacitance PTs was presented. The proposed method removes a key assumption used in the initial 3 methods and in previous literature. The method is experimentally verified against the three general purpose methods and shows increased accuracy of parameter extractions, particularly for PTs with high damping and whilst exhibiting comparatively similar noise resilience.

A detailed analysis of the impact of spurious modes on the efficiency of piezoelectric transformers was presented. Circuit analysis was performed on PT equivalent circuits with both a single resonant branch and with a second resonant branch. This allows equations for the efficiency of each model and subsequently allows the efficiency degradation arising from the spurious mode to be modelled. Using this novel efficiency degradation model, multiple sensitivity analyses were then performed and ζ_2 was highlighted as a critical design consideration. The value of ζ_2 required for minimal efficiency degradation in all devices was found. Furthermore, analysis of the combined effect of ζ_2 and $\Delta\omega$ was performed. This analysis was repeated with the parameter space of all other materials restricted in various scenarios. Results of this analysis provide a method of estimating the extent to which a

spurious mode will degrade efficiency and consequently, through the results of the sensitivity analyses, provide a method for improving PT designs.

A derivation of a lumped equivalent circuit model for the spurious flexural vibration modes occurring in radial mode Transoner PTs has been performed using both Kirchhoff and Mindlin plate models. An explanation of the assumptions made for both models is presented and the differences between each method explored. Finally, each model is verified against FEA simulations in COMSOL and against experimental PT measurements. Both models exhibit acceptable accuracy across the range of devices tested during verification, with the MPT based model providing excellent accuracy in almost all cases.

A lumped equivalent circuit model for a galvanically isolated ring-dot PT was presented. Unlike previous attempts, this model includes the effect of the 'gap' region that occurs between the input dot and output ring electrodes. The new model is then further extended to include non-ideal scenarios, in which the 'gap' section is made from a polled material. The resulting models are then validated against COMSOL simulations, showing excellent accuracy in the extracted parameters. Finally, the models were validated against experimental measurement of a practical PT.

BSPT was analysed for use in high temperature PTs for power converter applications. A ring-dot PT design was developed, and sample PTs made from both BSPT and a hard PZT material were fabricated. Impedance testing was performed, showing the properties of the BSPT PT improving with temperature, the opposite of the PZT PT. Power converter testing showed a similar pattern, with performance of the BSPT based converter improving with temperature. Although the PZT PT based converter outperforms the BSPT PT converter at temperatures less than 200℃, the BSPT PT converter performs acceptably at these temperatures and was proven to work at temperatures up to 250℃ with potential for further improvements in performance at even higher temperatures. Therefore, this analysis has highlighted the effectiveness of BSPT as a material for use in PTs for high temperature power converter applications.

A novel genetic algorithm approach to designing both ring-dot and radial mode Transoner PTs has been presented. A detailed description of the genetic algorithm is shown and the nuances of implementing this algorithm on both ring-dot and radial mode Transoner PTs is discussed.

This algorithm uses the newly derived models presented in Chapter 5, Chapter 6 and Chapter 8, rather than FEA methods, thus allowing increased speed compared to previous approaches. Additionally, PTs are designed specifically to an electrical converter specification, unlike previous approaches which have optimised PT parameters such as coupling factor. This algorithm was then implemented in python and integrated into a python-based web application, which was then deployed on a local server. Finally, the designs produced by the algorithm were verified using COMSOL and LTSpice circuit simulations, with results showing the algorithm was able to produce an optimal PT design for the given application.

11.2 Conclusion

The main aim of the work presented in this thesis is to help simplify the PT design process, with the intention of increasing the commercial adoption of PTs in the future. The main element of this work is the genetic algorithm-based PT designer. This presents a great leap forward in PT design, as this provides an excellent starting point for PT designs without any knowledge of the complex characteristics of PTs and in many cases will produce a PT which is ideally suited for a particular converter application without human intervention. Unlike previous attempts, the algorithm is fast to execute and due to the genetic algorithm-based approach analyses a wider array of devices than other methods. Importantly, the work presented here is a framework which can be built upon to further improve the algorithm in the future, with more accurate PT models, additional design considerations or even new PT topologies.

Whilst spurious modes had been discussed in passing, this thesis presents a much more detailed analysis of these modes than that previously published. Further to this analysis, with the equivalent circuit modelling of the spurious modes for the Transoner PT, this work shows how this spurious mode analysis can be incorporated into the design algorithm, something that would typically require an expert in PT design and expensive FEA tools to incorporate at the design stage. Furthermore, the Mindlin plate theory used in the modelling, to the authors knowledge, has never been previously used for PT analysis. This new method of PT analysis provides much greater accuracy than the Kirchhoff plate theory, thus producing more accurate equivalent circuit estimations of these spurious modes and further increasing the effectiveness of the design algorithm.

Finally, the prototype high temperature BSPT PT developed in this work helps to show some of the advantages of PTs and the potential applications of this technology in the future. Whilst at the moment this materials performance is not quite that of PZT, the work presented here shows the excellent performance of BSPT and provides both electrical engineers and materials scientists a starting point for improvements in the future. Additionally, this work starts the discussion around high temperature PTs, something that previous to this work have been theorised but now have been proven to work and with excellent results.

11.3 Further work

11.3.1 Extraction techniques

The proposed extraction techniques presented in Chapter 3 have all proven to work excellently under ideal conditions. However, in higher damping PTs, previously unmodelled parasitic elements have a larger effect on the impedance spectra. Therefore, further improvements to the high damping / low capacitance extraction technique should include the effect of parasitic elements. This would both not only improve the simulation accuracy of these devices but would also increase the accuracy of the extracted circuit elements. Additionally, based on the impressive noise performance of the estimation methods, a genetic algorithm-based approach to equivalent circuit component extraction may further improve on performance.

11.3.2 Equivalent circuit modelling

Equivalent circuit models were developed for both ring-dot PTs and for the flexural, spurious modes occurring in radial mode PTs. Whilst the accuracy of the ring-dot model was excellent compared to simulated PTs, it requires experimental validation against a PT with an unpolled gap region to fully assess the model's accuracy. Additionally, even with the additional electric field models across the gap region for the fully polled PT example, accuracy was poor in comparison, especially for thicker PTs. Therefore, further work should be done on developing a higher order model for the electric field across the gap region to increase accuracy of the equivalent circuit model. Similarly, the higher order electric field model developed by Wang *et al.* [11.1] could be applied to the spurious mode model of the Transoner PT. This along with a higher order shear deformation model, such as that discussed by Reddy [11.2] would help to increase the accuracy of the estimated component values.

Whilst all three models developed in Chapter 5, 6 and 8 are verified against experimental measurements of PTs, in all cases the experimental PT has a turn ratio of 1:1. Although these models are verified against simulated PTs with $N \neq 1$ with good agreement, further analysis could be performed to verify these models are accurate when verified against experimentally measured PTs with $N \neq 1$.

Additionally, as mentioned when validating the ring-dot PT model, a parasitic capacitance occurs between the input and output electrodes. Further work could be done to model this capacitance and an analysis performed looking into the impact it has on key PT performance metrics.

11.3.3 High temperature PTs and high temperature converters

Chapter 9 verifies the use of BSPT as a high temperature PT material, with excellent success. Next steps, would be to produce a high temperature PT based converter, including a high temperature half-bridge, drive circuity and logic. Additionally, as the power density of PTs is typically limited by temperature rise (and to some extent vibration velocity), further work should be done to find the limit of high temperature PTs. As unlike PZT, the performance of BSPT improves with temperature, so traditional methods of determining output power density, such as evaluating the output power achieved whilst the PT experiences a 30°C temperature rise, is potentially no longer valid. This could subsequently lead to better methods of determining power density of PTs that is applicable to all materials.

As with all PTs, further improvements should then come from materials improvement, producing materials and subsequently PTs that can operate at higher temperatures with lower losses, giving rise to higher power and more efficient converters. This is especially true of the BSPT material, which with some further improvements would be an ideal PT material.

11.3.4 PT design algorithm

The genetic algorithm developed in Chapter 10 provides an excellent framework which can be easily applied to other PT topologies. When a lumped equivalent circuit model is developed for a particular PT, then that topology can be easily incorporated into the algorithm and thus that PT can be designed for certain applications using the genetic algorithm presented here. Similarly, with further improvements in the accuracy of equivalent circuit modelling, there is a greater chance that a physical PT built to a design produced by the genetic algorithm will

perform as predicted. As more complex converter topologies or more complex PT requirements are developed, additional metrics should be included into the fitness function to greater the chance of producing an ideal PT for that application.

11.3.5 References

[11.1] Q. Wang, S. T. Quek, C. T. Sun, and X. Liu, 'Analysis of piezoelectric coupled circular plate', *Smart Mater. Struct.*, vol. 10, no. 2, p. 229, 2001, doi: 10.1088/0964-1726/10/2/308.

[11.2] J. N. Reddy, *Theory and analysis of elastic plates*. Philadelphia, PA: Taylor & Francis, 1999.

A) Appendix

11.4 Appendix 1 - Simplifying the equivalent circuit

To simplify the equivalent circuit model in Fig. 8.10 to the traditional Mason equivalent circuit form, several circuit transformations will be used. Firstly, impedances $Z_{e,g,f}$ will be referred across the $r_b{:}\,1$ transformer. This transformer will then be combined with the $A'_{\mathrm{out}}{:}\,1$ transformer, this then gives A_{out} (A.6) a similar definition to A_{in}. Additionally, Z_a and $Z_b$will be combined, as will Z_d and Z_e (after referring across r_b) impedances. The resulting circuit is shown in Fig. A.1.

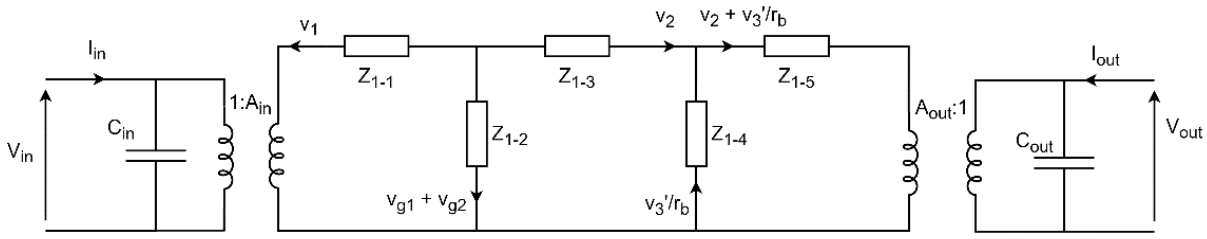

Fig. A.1 – First stage of simplifications to the ring-dot equivalent circuit

The impedances $Z_{1-(1-5)}$ in Fig. A.1 are given by

$$Z_{1-1} = Z_a + Z_b \tag{A.1}$$

$$Z_{1-2} = Z_c \tag{A.2}$$

$$Z_{1-3} = Z_d + Z_e r_b^2 \tag{A.3}$$

$$Z_{1-4} = Z_g r_b^2 \tag{A.4}$$

$$Z_{1-5} = Z_f r_b^2 \tag{A.5}$$

and A_{out} is now defined as

$$A_{\mathrm{out}} = A'_{\mathrm{out}} r_b. \tag{A.6}$$

The next stage of simplification requires transforming Z_{1-2}, Z_{1-3} and Z_{1-4} from a $'\pi'$ circuit to a 'T'circuit. This resulting circuit is shown in Fig. A.2.

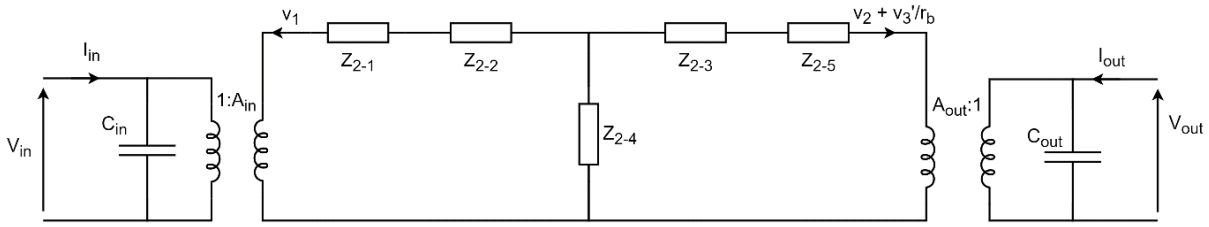

Fig. A.2 – Second stage of simplifications to the ring-dot equivalent circuit

The impedances $Z_{2-(1-5)}$ in Fig. A.2 are given by

$$Z_{2-1} = Z_{1-1} \tag{A.7}$$

$$Z_{2-2} = \frac{Z_{1-2}Z_{1-3}}{Z_{1-2} + Z_{1-3} + Z_{1-4}} \tag{A.8}$$

$$Z_{2-3} = \frac{Z_{1-2}Z_{1-4}}{Z_{1-2} + Z_{1-3} + Z_{1-4}} \tag{A.9}$$

$$Z_{2-4} = \frac{Z_{1-3}Z_{1-4}}{Z_{1-2} + Z_{1-3} + Z_{1-4}} \tag{A.10}$$

$$Z_{2-5} = Z_{1-5} \tag{A.11}$$

Then, combining impedances $Z_{2-1} + Z_{2-2}$ and $Z_{2-4} + Z_{2-5}$, leads to the equivalent circuit given in Fig. A.3.

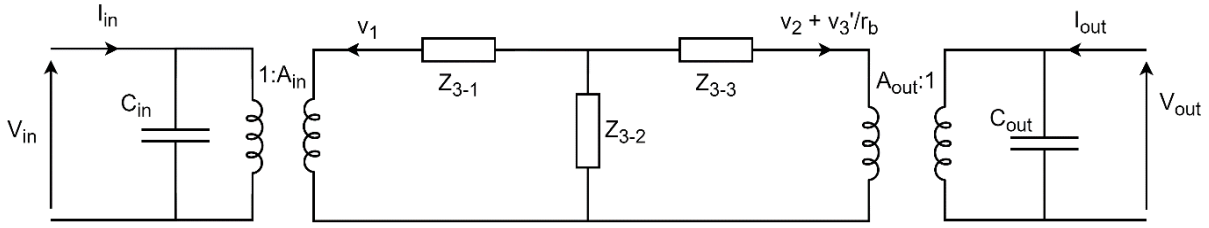

Fig. A.3 – Third stage of simplification of the ring-dot equivalent circuit

The impedances $Z_{3-(1-3)}$ in Fig. A.3 are given by

$$Z_{3-1} = Z_{2-1} + Z_{2-2} \tag{A.12}$$

$$Z_{3-2} = Z_{2-3} \tag{A.13}$$

$$Z_{3-3} = Z_{2-4} + Z_{2-5}. \tag{A.14}$$

Again, a 'T' to $'\pi'$ conversion will be performed on the three impedances $Z_{3-(1-3)}$ to give each impedance the same resonant frequency. This leads to the circuit shown in Fig. A.4.

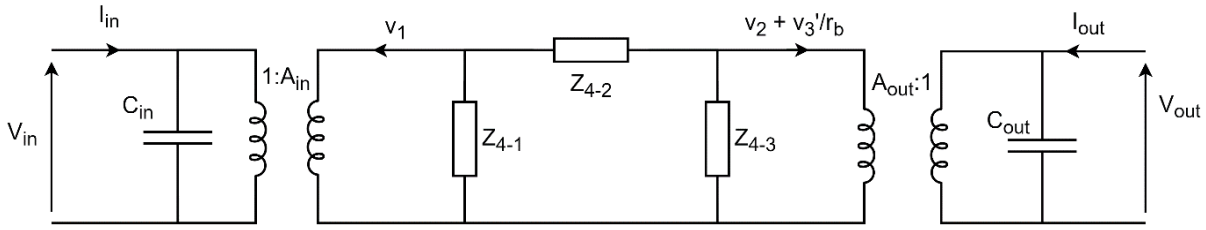

Fig. A.4 – Fourth stage of simplification of the ring-dot equivalent circuit

The impedances $Z_{4-(1-3)}$ are given by

$$Z_{4-1} = \frac{(Z_{3-1}Z_{3-2}) + (Z_{3-1}Z_{3-3}) + (Z_{3-2}Z_{3-3})}{Z_{3-3}} \tag{A.15}$$

$$Z_{4-2} = \frac{(Z_{3-1}Z_{3-2}) + (Z_{3-1}Z_{3-3}) + (Z_{3-2}Z_{3-3})}{Z_{3-2}} \tag{A.16}$$

$$Z_{4-3} = \frac{(Z_{3-1}Z_{3-2}) + (Z_{3-1}Z_{3-3}) + (Z_{3-2}Z_{3-3})}{Z_{3-1}} \tag{A.17}$$

11.5 Appendix 2 - Details of the genetic algorithm

This appendix details the continuous genetic algorithm implemented in the PT designer. A flowchart for the genetic algorithm implemented in Chapter 9 is shown in Fig. A.5.

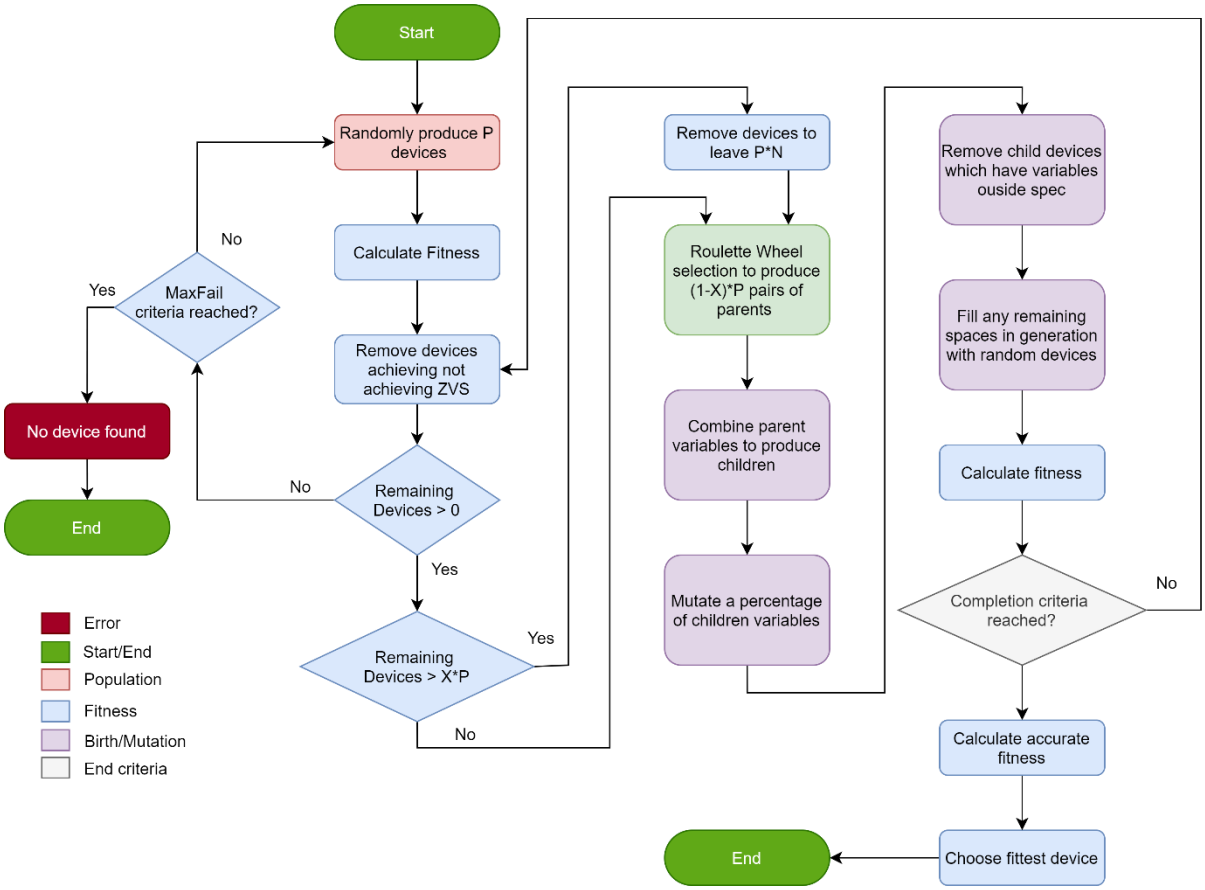

Fig. A.5 – Flowchart for the continuous genetic algorithm

The flowchart in Fig. A.5 is split into several sections as indicated by the colour of the block (see the key bottom left), the following sections will explain in detail the function of each of these sections and the intricacies for each of the PT topologies.

11.5.1 Population

The population operation is tasked with generating P chromosomes, with each chromosome being the parameters of a single PT. For each chromosome, a uniformly distributed random function is used to generate values for each of the variables, r_{a}, r_{b}, a and T for the ring-dot PT, and a, $T_{\mathrm{in}}^{\mathrm{Tot}}$, $T_{\mathrm{out}}^{\mathrm{Tot}}$, N_{in} and N_{out} for the radial mode Transoner PT. The values for each variable must be in the bounded range which the user will specify. These devices will be our initial population of candidate PT devices.

11.5.2 Fitness

The P devices in the current generation, are then evaluated to determine their fitness. The fitness function is described in detail in section 10.3.1.

11.5.3 Selection

Selection has two main parts, firstly, removing non optimal chromosomes and second, selecting parent chromosomes for the next generation of devices.

11.5.3.a) Removal of PTs

Firstly, a percentage $(1-X)$ of the P chromosomes that are in the current generation need to be removed to make space for new chromosomes. The chromosomes in the current generation are sorted by fitness and the top $X\%$ of chromosomes are kept, whilst the other devices are removed. If less than X% of the P chromosomes remain in the current generation, all devices will be kept.

11.5.3.b) Roulette wheel selection

Roulette wheel selection is a common technique for selecting parents to produce new chromosomes in genetic algorithms and is discussed in detail in [10.5]. In this method, the better the fitness of the device, the larger the section of the theoretical roulette wheel the device is given and therefore, the better chance that device has of being selected (spinning of the wheel) to be a parent for new devices.

To determine the percentage of the roulette wheel each device occupies, firstly, the fitness values for each chromosome are inverted thus providing a higher score value for a better rated device. Thus, for device d the inverse fitness is given by,

$$\mathrm{Fit}^{-1}(d) = 1/\mathrm{Fit}\,(d) \tag{A.18}$$

Then, all the inverse fitness values are summed together,

$$\mathrm{TotInvFit} = \sum_{d=1}^{P} \mathrm{Fit}^{-1}(d) \tag{A.19}$$

where P is the population size. For each PT d, the inverted fitness as a proportion of the $\mathrm{TotInvFit}$ is then found. This provides the proportion of the roulette wheel taken up by the chromosome.

$$RW(d) = \frac{\mathrm{Fit}^{-1}(d)}{\mathrm{TotInvFit}} \tag{A.20}$$

The roulette wheel defines the probability distribution from which the parents are chosen for breeding thus,

$$\sum_{d=1}^{P} RW(d) = 1$$

Table A.1.shows a breakdown of this process for a four-device population, P = 4.

Table A.1 – Example roulette wheel for selection of parents

Device	Fitness	1/Fitness	% of roulette wheel	Random number selection
1	0.1	10	26.14%	$0 \leq x < 0.2614$
2	0.8	1.25	3.27%	$0.2614 \leq x < 0.2941$
3	0.04	25	65.36%	$0.2941 \leq x < 0.9477$
4	0.5	2	5.23%	$0.9477 \leq x \leq 1$
Total		38.25	100%	

11.5.3.c) Breeding process: selection of parent chromosomes

Once the roulette wheel is constructed, selection is then performed. $((1 - X)P)$ pairs of parent chromosomes should be chosen. Choice of parents is performed by 'spinning the roulette wheel' and the chromosome which the roulette wheel lands on, is chosen as the parent. This process is then repeated until all parents have been chosen.

To do this, each PT is assigned a range of values between 0-1, corresponding to the percentage of the roulette wheel the chromosome takes up, as shown in the last column of Table A.1. This is done by starting from 0, and commutatively summing up the roulette wheel percentages. Then, the 'spinning' action is performed by a uniform random number generator giving a number between 0-1, the device which has this random value within its range is the device selected. This is repeated until $((1 - X)P)$ pairs of parent chromosomes have been selected. This method ensures that all chromosomes have a chance of being a parent, however, optimal chromosomes have a better chance of being selected (natural selection).

11.5.4 Birth of new chromosomes

After selecting $(1 - X)P$ pairs of parents; these parents should be combined to produce new chromosomes. This is done using one of the blending method presented in [10.5],

$$c_{V_x} = p_{V_x}^{\text{Father}}\gamma + p_{V_x}^{\text{Mother}}(1 - \gamma) \quad \text{(A.21)}$$

where c and p, denote child and parent chromosomes respectively, V_x is the Xth variable to be chosen and γ is a random number between 0-1, generated using a uniform random number generator. This means that each child chromosome is a blend its parents' parameters. This process is repeated for each variable and for each set of parents, with a new γ value generated for each set of parents.

11.5.5 Mutation

Mutation is the process of minimally changing the variables of child chromosome, to avoid premature convergence and to also avoid converging on local minima. Mutation is performed by adding/subtracting a small random number from each variable for a child chromosome. Typically, only a subset of the child chromosomes in a generation should be mutated, therefore, first we generate a random number (between 0 and 1) for each device, if said random number is less than $MutRate$ then mutation will be performed for that chromosome. The mutation process is then performed by,

$$c_{V_x} = c_{V_x} + (\alpha \times \text{MutAm} \times \text{ShouldMut}) \quad \text{(A.22)}$$

where MutAm is the maximum mutation to be added (or removed) from each variable, ShouldMut is a Boolean variable describing if the chromosome should be mutated and α is a uniformly generated random number between -1 and 1. An issue that arises from this mutation method is that for integer variables (radius and number of layers) the small mutations added by this operation will be negligible after rounding. Therefore, to include a chance of mutation of the integer variables, MutAm was increased to a value which will allow these variables to mutate.

11.5.6 Rounding, boundary checking and repopulation

Before progressing to a new generation, it is important to ensure each variable is still within the mechanical bounds set by the user and to round certain quantities that can only be

integers. In both PT topologies, the disc radius (a) should be rounded, as typically discs are only available in discrete, integer sizes. Additionally, the number of layers in each section of the radial mode PT are rounded to the nearest integer for obvious reasons. If a chromosome has at least one variable outside the bounds set by the user, this child chromosome will be respawned with randomly generated values.

At this point in the process, it is likely that some chromosomes have been removed from the generation, either at the fitness stage if they do not achieve $K_{ZVS} > \min K_{\mathrm{ZVS}}$ or at the birth stage due to variables having values outside the desired bounds. However, each generation should start with P chromosomes. To account for this, new chromosomes will be randomly generated as was done in the initial population section, to ensure P chromosomes are in the current generation.

11.5.7 Completion conditions

For this algorithm there are two completion conditions, a maximum similarity completion condition and an exceeding of the maximum number of generations condition. The maximum similarity condition sets the maximum number of generations that pass where the same chromosome is the most optimal. This condition allows the algorithm to prematurely exit once an optimal chromosome has been found, thus reducing computation time. However, the maximum number of similar generations must be carefully set as to avoid early termination of the algorithm before an ideal PT has been found (finding a local minima). Depending on the speed of the implementation, this completion condition can often save negligible time, whilst having detrimental results and, therefore, should be avoided. However, this condition is useful in situations where the maximum number of generations is high or where generations are slow to process, such as with the Mindlin based spurious mode estimation for the Transoner PT.

The second completion condition is an exceeding of the maximum generation condition. This determines the maximum number of generations that the algorithm will be run through, if the maximum similarity condition has not been triggered. This again should be carefully set to allow enough generations to be evaluated to ensure the best chromosome is found.

11.5.8 Final device selection

Once at least one of the completion conditions have been triggered, the next stage is determining which device in the final generation is optimum. If the max similarity condition has been met, then the best chromosome is clearly obvious; however, if the max generation condition is met then a selection must be made.

First, the fitness function evaluation is performed again, however, this time with greater frequency resolution when determining the operating frequency and subsequent computations, and in the K_{ZVS} calculation greater ϕ resolution is used, producing more precise fitness scores at the cost of longer computation time. Then, the chromosome with the lowest (best) fitness is extracted and is chosen as the most optimum chromosome and thus relates to the most optimum PT. This optimum PT is then presented back to the user.

11.6 Appendix 3 - Derivation of key circuit parameters

To validate the performance of the resulting PT from the PT design algorithm, the user is to be provided with several waveforms from the resulting resonant circuit. This could be achieved using a SPICE simulation; however, it is more efficient to analytically derived equations for the relevant properties. In this appendix, equations for V_{out}, $V_{C_{\mathrm{in}}}$ and $i_1(\theta)$ are derived.

11.6.1 V_{out}

V_{out} is calculated by first using (10.14) and (10.15) to first determine the amplitude of the output voltage waveform. Then, by using the i_1 phase angle (ϕ) calculated as part of the K_{ZVS} computation, the output voltage can be simulated using

$$V_{\mathrm{out}} = V_{\mathrm{out\text{-}peak}} \sin(\theta + \phi). \tag{A.23}$$

11.6.2 $V_{C_{\mathrm{in}}}$

To find $V_{C_{\mathrm{in}}}$, as done previously, the model generated in [10.3] will be used as a starting point. However, to further improve on this model, two more modes of operation will be added, these are the MOSFET reverse diode conduction modes. A piecewise description of the $V_{C_{\mathrm{in}}}$ voltage is given by,

$$V_{C_{\text{in}}} = \begin{cases} \dfrac{i_1\left(-\cos(\phi) + \cos(\theta + \phi)\right)}{\omega C_{\text{in}}} & , \quad \theta < \beta \\ V_{DC} + V_{DF} & , \quad \beta \le \theta < \delta \\ V_{DC} & , \quad \delta \le \theta < \pi \\ \dfrac{\left(V_{DC}\omega C_{\text{in}} + i_1\cos(\theta + \phi) + i_1\cos(\phi)\right)}{\omega C_{\text{in}}} & , \quad \pi \le \theta < \pi + \beta \\ -V_{DF} & , \quad \pi + \beta \le \theta < \pi + \delta \\ 0 & , \quad \pi + \delta \le \theta < 2\pi \end{cases} \tag{A.24}$$

where V_{DF} is the forward voltage of the MOSFETs diode, β is the angle at which the diode begins to conduct in the cycle. To evaluate (A.24), the two unknowns β and i_1 are found simultaneously. The conduction angle β is the value of θ at which the MOSFET reverse diode starts conducting during the deadtime. First, taking the first equation in (A.24) and solving for θ when the output equals V_{DC}, gives an equation for β

$$\beta = -\mathrm{j}\ln\left(\frac{2V_{DC}\omega C_{\text{in}}e^{(j\phi)} + I_1e^{(j\phi)^2} + I_1 - \sqrt{\left(\begin{matrix}4C_{\text{in}}^2e^{(j\phi)^2}V_{DC}^2\omega^2 + 4C_{\text{in}}I_1e^{(j\phi)^3}V_{DC}\omega + I_1^2e^{(j\phi)^4} \\ + 4C_{\text{in}}I_1e(j\phi)V_{DC}\omega - 2I_1^2e(j\phi)^2 + I_1^2\end{matrix}\right)}}{2I_1e^{j\phi}}\right) - \phi. \tag{A.25}$$

where I_1 is the peak current through the resonant circuit. Next an equation for the resonant current will be derived. This is achieved by equating the energy supplied to the circuit with the energy dissipated in the load and the loss resistance, and the energy required to charge and discharge C_{in} during a cycle, similar to the method used in [10.3]. However, in this case, the equations will account for the new conduction modes included here. Firstly, an equation for the energy provided to the PT is found. This occurs when $V_{C_{\text{in}}} > V_{DC}$, i.e. during the second mode of operation in (A.24). The energy into the PT is defined as

$$E_{\text{in}} = \frac{1}{\omega}\int_{\beta}^{\pi}(V_{DC}I_1\sin(\theta + \phi) = \frac{\left(V_{DC}I_1\cos(\beta + \phi) + V_{DC}I_1\cos(\phi)\right)}{\omega} \tag{A.26}$$

It should be noted that $V_{DF} = 0$ was assumed. Then, the energy supplied to the load and dissipated in the loss resistance are the same as defined in [10.3],

$$E_{\text{out}} = \frac{I_1^2 R_L \pi}{\omega N^2 (C_{\text{out}}^2 R_L^2 \omega^2 + 1)} \tag{A.27}$$

$$E_{R_1} = \frac{I_1^2 R_1 \pi}{\omega} \tag{A.28}$$

Finally, the energy used to charge/discharge C_{in} is found. The energy used to charge the input capacitor during the first deadtime ($\theta < \beta$), is given by

$$E_{C_{\text{in}}}^{CHA} = \frac{C_{\text{in}}}{2}\left(V_{C_{\text{in}}}(\beta)^2 - V_{C_{\text{in}}}(0)^2\right) = \\ = \frac{I_1^2 \left(\left(\frac{1}{2}\right) e^{\text{j}\phi} + \left(\frac{1}{2}\right) e^{-\text{j}\phi} - \left(\frac{1}{2}\right) e^{\text{j}(\beta+\phi)} - \left(\frac{1}{2}\right) e^{-\text{j}(\beta+\phi)}\right)^2}{2C_{\text{in}}\omega^2} \tag{A.29}$$

Then, the energy used to discharge the input capacitor during the second deadtime ($\pi \leq \theta < \pi + \beta$) is given by

$$E_{C_{\text{in}}}^{DIS} = \left(\frac{1}{2}\right) C_{\text{in}}\left(V_{C_{\text{in}}}(\pi+\beta)^2 - V_{C_{\text{in}}}(\pi)^2\right) \\ = -\frac{I_1\left(4V_{DC}\omega C_{\text{in}}\cos(\beta+\phi) - 4V_{DC}\omega C_{\text{in}}\cos(\phi)\right)}{4C_{\text{in}}\omega^2} \\ -\frac{I_1(I_1 cos(2\phi) - I_1\cos(2\beta+2\phi) + 2I_1\cos(\beta+2\phi) + 2I_1\cos(\beta) - 2I_1)}{4C_{\text{in}}\omega^2} \tag{A.30}$$

The energy balance equation is defined as

$$E_{\text{in}} = E_{\text{out}} + E_{R_1} + E_{C_{\text{in}}}^{CHA} + E_{C_{\text{in}}}^{DIS} \tag{A.31}$$

Substituting (A.26)-(A.30) into (A.31) gives an equation including I_1 and β, which is subsequently solved for I_1, giving

$$I_1 = \frac{4C_{\text{in}}N_1^2 V_{DC}\omega(C_{\text{out}}^2 R_L^2\omega^2 + 1)\cos(\beta+\phi)}{\begin{pmatrix} N_1^2(C_{\text{out}}^2 R_L^2\omega^2 + 1)\cos(2\beta+2\phi) \\ -2N_1^2(C_{\text{out}}^2 R_L^2\omega^2 + 1)\cos(2\phi+\beta) \\ +N_1^2(C_{\text{out}}^2 R_L^2\omega^2 + 1)\cos(2\phi) \\ -2N_1^2(C_{\text{out}}^2 R_L^2\omega^2 + 1)\cos(\beta) \\ +2(C_{\text{out}}^2 R_L^2\omega^2 + 1)(C_{\text{in}}\pi R_1\omega + 1)N_1^2 + 2R_L\pi\omega C_{\text{in}} \end{pmatrix}} \tag{A.32}$$

Finally, substituting (A.32) into (A.25) then allows β to be solved numerically. The result of which can then be substituted back into (A.32) to find I_1. Using the numerically computed values for β and I_1, $V_{C_{\text{in}}}$(A.24) can then be evaluated across a whole cycle.

11.6.3 $i_1(\theta)$

As I_1 has been found previously during the $V_{C_{\text{in}}}$computation, i_1 is then given by

$$i_1 = I_1 \sin(\theta + \phi) \tag{A.33}$$